UNIVERSITAT POLITÈCNICA DE CATALUNYA
BARCELONATECH

The design and implementation of a spectrally tuneable LED-based light source: towards a new era of intelligent illumination

Wim Hertog

A thesis presented for the degree of Doctor of Philosophy in Optical Engineering at the Department of Optics and Optometry of the Universitat Politècnica de Catalunya

Thesis Supervisor

Dr. Josep Maria Carreras Molins

IREC
Institut de Recerca en Energia de Catalunya
Catalonia Institute for Energy Research

Internal Examiner

Dr. José Arasa Martí

Barcelona, December 2016

UNIVERSITAT POLITÈCNICA DE CATALUNYA
BARCELONATECH
Escola de Doctorat

Acta de calificación de tesis doctoral	Curso académico:

Nombre y apellidos

Programa de doctorado

Unidad estructural responsable del programa

Resolución del Tribunal

Reunido el Tribunal designado a tal efecto, el doctorando / la doctoranda expone el tema de la su tesis doctoral titulada _____

_____.

Acabada la lectura y después de dar respuesta a las cuestiones formuladas por los miembros titulares del tribunal, éste otorga la calificación:

☐ NO APTO ☐ APROBADO ☐ NOTABLE ☐ SOBRESALIENTE

(Nombre, apellidos y firma) Presidente/a		(Nombre, apellidos y firma) Secretario/a
(Nombre, apellidos y firma) Vocal	(Nombre, apellidos y firma) Vocal	(Nombre, apellidos y firma) Vocal

_____, _____ de _____ de _____

El resultado del escrutinio de los votos emitidos por los miembros titulares del tribunal, efectuado por la Escuela de Doctorado, a instancia de la Comisión de Doctorado de la UPC, otorga la MENCIÓN CUM LAUDE:

☐ SÍ ☐ NO

(Nombre, apellidos y firma) Presidente de la Comisión Permanente de la Escuela de Doctorado	(Nombre, apellidos y firma) Secretario de la Comisión Permanente de la Escuela de Doctorado

Barcelona a _____ de _____ de _____

Acknowledgements

I still remember my first torch: a yellow Playskool flashlight with a built-in red-green colour filter. It was my absolute favourite toy as a toddler. The love for lights did not let go. From scrounging around markets in far-away countries to setting up a lighting company, illumination has always been a fervent hobby. At the end of my studies, this hobby turned into a full time job that, later on, led to the start of this PhD.

Thanks, mom, dad and Joachim for the years and years of encouragement that fuelled my passion. Without you I would not be where I am now.

My sincere gratitude goes towards Dr. Carreras, whom I met for the first time during a CIE conference in Gent, Belgium. Thank you, Josep, for introducing me in IREC, accepting me as your PhD student and giving me the chance to meet countless like-minded people all over the world. Charles, Francisco, Jordi, Jorge, Oscar, Mariano and especially Jesús: thanks for being such helpful colleagues and more importantly, good friends.

Didem, keeping the most important one for the end, thank you for sharing all my happy and sad moments. Thank you for all those far-away adventures. Our time together is my number one energy resource.

Wim Hertog
Barcelona, 2015

Abstract

Rising population numbers place ever increasing demands on energy resources. A large percentage of the worldwide energy production is reserved for the generation of electricity and a significant portion of the electrical energy generation is used for illumination purposes. At the same time, people demand brighter light sources that provide better light quality. The luminaire of today is not just a simple lamp, but a complex, intelligent piece of technology designed for a specific purpose.

This doctoral dissertation aims to provide a link between the theoretical universe surrounding the physics of electromagnetic radiation and the practical illumination world. A theoretical framework presents the physical properties of light and connects, through the human visual system, to a number of perceptual models. Based on these perceptual models, the colourimetric qualities of an illumination spectrum are analysed and a theoretical framework that aims to optimise the balance between colour fidelity and energy efficiency is proposed. The result of this optimisation is a spectrum that needs to be implemented into a light source.

Recent advancements in semiconductor technology led to the development of highly efficient light emitting diodes. The monochromatic nature of these light sources offers the possibility of creating a spectrally tuneable luminaire that is able to reproduce these optimised illumination spectra. A fully integrated spectrally tuneable light engine combines knowledge on characterising and driving LEDs, optical design and thermal management. Each group of monochromatic LEDs needs a variable current source that ensures predictable behaviour regardless of their dimming level or temperature. An advanced optical solution enables efficient light extraction from the LEDs, provides excellent luminance and chroma homogenisation and, finally, delivers a suitable beam pattern for the intended illumination application. Proper thermal management establishes sufficient heat extraction to guarantee low semiconductor temperatures.

Finally, the LED light engines created during this doctoral research are incorporated into three spectrally tuneable illumination devices, each designed for a specific purpose. A set of spectrally tuneable downlights installed in the laboratories of the lighting group of the Catalonia Institute for Energy Research (IREC) in Barcelona, Spain and the department of neuroscience of the University of Newcastle in the United Kingdom serves as a valuable tool for experiments that evaluate both physical and psychovisual properties of selected illumination spectra. A compact spotlight, used during the “Making Colour” exhibition of the National Gallery in London, is optimised to provide a set of specific illumination spectra to illuminate art reproductions. Lastly, a high power luminaire was designed to generate specialised spectra to irradiate greenhouse plants, steering their morphology and the production of plant-specific compounds.

List of abbreviations and symbols

AC	Alternating Current
E_e	irradiance in watt per square metre
$I_{e,\Omega}$	radiant intensity in watt per solid angle
$L_{e,\Omega,v}$	radiance in watt per solid angle . surface area
M_e	radiant exitance in watt per square metre
$V'(\lambda)$	sensitivity function of the rods of the human eye
k_B	Boltzmann´s constant
Φ_e	radiant flux in watt
ΔE	colour difference / energy difference
ΔT	temperature difference
A	amplitude
a*	a* coordinate of the CIELAB colour space
AIC	Association Internationale de Couleur
AM	Amplitude Modulation
B	magnetic field in teslas
b*	b* coordinate of the CIELAB colour space
BC	Before Christ
BDI	Beck Depression Inventory
C	capacitance in farads / celsius, a unit of measurement for temperature
c	speed of light in metres per second / impact of surrounding in CIECAM02
CAD	Computer Aided Design
CAM	Colour Appearance Model
CAT	Chromatic Adaptation Transform
CBE	Chemical Beam Epitaxy
CCD	Charge-Coupled Device
CCFL	Cold-Cathode Fluorescent Lamp
CCR	Constant Current Reduction
CCT	Correlated Colour Temperature
cd	candela, SI unit of luminous intensity
CDI	Colour Discrimination Index
CFL	Compact Fluorescent Lamp
CMF	Colour Matching Function
CGL	Charge Generation Layer
CIE	Commission Internationale de l'Eclairage
CMS	Colour Matching System
CMYK	Cyan, Magenta, Yellow, Black
COB	Chip On Board
CQS	Colour Quality Scale
CRC	Colour Rendering Capacity
CRI	Colour Rendering Index
CRM	Colour Rendering Map
CT	Colour Temperature
D	diode / degree of chromatic adaptation to the reference white in CIECAM02
D65	CIE standard illuminant D65

DALI	Digital Addressable Lighting Interface
DC	Direct Current / chromaticity distance
DE	Germany
DH	Double Heterojunction
E	electric field in newtons per coulomb / flux in watt
EBL	Electron Blocking Layer
EL	Electroluminescence
EMI	ElectroMagnetic Interference
EML	Emission Layer
ErP	Energy related Products
ES	España
E_{sp}	electric field generated by the space charge
ETL	Electron Transport Layer
eV	electronvolt, a unit of energy
E_v	illuminance in lux
F	factor determining the degree of adaptation in CIECAM02
f	frequency in hertz
FCI	Feeling of Contrast Index
FET	Field-Effect Transistor
FM	Frequency Modulation
FP7	Seventh Framework Programme for Research and Technological Development
FSCI	Full Spectrum Colour Index
FWHM	Full Width at Half Maximum
GSM	Global System for Mobile communications
$\hat{H}$	hamiltonian operator
HBL	Hole Blocking Layer
HID	High Intensity Discharge
HIL	Hole Injection Layer
HI-LED	Human – centric Intelligent LED engines for the take up of SSL in Europe
HPS	High Pressure Sodium
HTL	Hole Transport Layer
I	current in amperes
i(t)	induced current in amperes
IC	Integrated Circuit
IES	Illuminating Engineering Society
I_f	forward current of an LED in amperes
ipRGC	Intrinsically Photosensitive Ganglion Cell
IR	Infrared
IRC	Infrared Coated
IREC	Institut de Recerca en Energia de Catalunya
IRTA	Institut de Recerca i Tecnologia Agroalimentàries
I_s	source current / reverse bias saturation current in amperes
ISBN	International Standard Book Number
ITO	Indium Tin Oxide
I_v	luminous intensity in candela
J	current density in amperes per square metre
JND	Just Noticeable Difference
K	kelvin, SI unit of temperature

KSS	Karolinska Sleepiness Scale
L	inductance in henries
L*	L* coordinate of the CIELUV and CIELAB colour space
L_A	absolute luminance of the adapting field in CIECAM02
LCD	Liquid Crystal Display
LED	Light Emitting Diode
LER	Luminous Efficacy of Radiation
L_{mes}	Luminance under mesopic conditions in candela per square metre
LPS	Low Pressure Sodium
LTE	Long Term Evolution
L_v	luminance in candela per square metre
lx	lux, SI unit of illuminance
MBE	Molecular Beam Epitaxy
MCPCB	Metal Core Printed Circuit Board
MCRI	Memory Colour Rendering Index
MEQ	Morningness – Eveningness Questionnaire
MH	Metal Halide
MOVCD	Metalorganic Vapour Deposition
MQW	Multiple Quantum Well
MV	Mercury Vapour
n	index of refraction
N_c	chromatic induction factor in CIECAM02
NHC	N-Heterocyclic Carbenes
º	symbol for degree
OLED	Organic Light Emitting Diode
OSA	The Optical Society
p	purity of a spectrum
PANAS	Positive and Negative Affect Scale
PAR	Photosynthetically Active Radiation
PC	Phosphor Converted / Polycarbonate
PCB	Printed Circuit Board
P_D	power dissipation in watt
PET	Polyethylene Terephthalate
PLED	Polymer Organic Light Emitting Diode
PMMA	Poly(Methyl Methacrylate)
POF	Plastic Fibre Optic
P_{opc}	flux of a phosphor-converted LED in watt
P_{opp}	flux of a phosphor pump in watt
PSQI	Pittsburgh Sleep Quality Index
PSU	Power Supply Unit
PVN	Paraventricular Nucleus
PWM	Pulse Width Modulation
Q	thermal flux in watt
Q_e	radiant energy in joule
Q_v	luminous energy in lumen . seconds
qV_a	electrostatic potential energy of a charge q in point a
R	resistance in ohms
R_a	the CIE general colour rendering index

RAM	Random Access Memory
RCRI	Rank-order Colour Rendering Index
R_f	feedback resistance in ohms
RGB(W)	Red, Green, Blue(, White)
RHT	Retinalhypothalamic Tract
R_i	colour rendering of test sample i
RoHS	Restriction of Harmful Substances
$R_{th,\,x\text{-}y}$	thermal resistance between point x and point y
S	field-effect transistor
SCN	Suprachiasmatic Nuclei
SD	Secure Digital
SMOLED	Small Molecule Organic Light Emitting Diode
SP	Serial Port
SPD	Spectral Power Distribution
SSL	Solid State Lighting
STAI	State – Trait Anxiety Inventory
T	temperature in Kelvin / period in seconds
t	time in seconds
TC	Technical Committee
TIM	Thermal Interface Material
TIR	Total Internal Reflection
TS	Transparent Substrate
U^*	U* coordinate of the CIE 1964 UCS colour space
u^*	u* coordinate of the CIELUV colour space
u'	u´coordinate of the CIE u´,v´, Y colour space
UART	Universal Asynchronous Receiver/Transmitter
UCS	Uniform Chromaticity Scale
UHP	Ultra High Pressure
$U_{i,r}{}^*$	U* coordinate of the adapted ref. sample under the adapted ref. light source
$U_{i,t}{}^*$	U* coordinate of the adapted ref. sample under the test light source
u_i'	adapted u chromaticity coordinate of the test sample
UK	United Kingdom
UMTS	Universal Mobile Telecommunications System
UoN	University of Newcastle
$u_{s,r}$	u chromaticity coordinate of the reference source
$u_{s,t}$	u chromaticity coordinate of the source-under-test
$u_{s,t}'$	adapted u chromaticity coordinate of the source-under-test
USA	United States of America
USD	United States Dollar
UV	Ultraviolet
V	voltage in volts
$v(t)$	induced voltage in volts
V^*	V* coordinate of the CIE 1964 UCS colour space
v^*	v* coordinate of the CIELUV colour space
v'	v´coordinate of the CIE u´,v´, Y colour space
V_D	voltage across a junction
V_f	forward voltage of an LED in volts
$V_{i,r}{}^*$	V* coordinate of the adapted ref. sample under the adapted ref. light source

$V_{i,t}^*$	V* coordinate of the adapted ref. sample under the test light source
v_i'	adapted v chromaticity coordinate of the test sample
V_{mes}	human eye sensitivity function under mesopic conditions
V_s	source voltage in volts
$v_{s,r}$	v chromaticity coordinate of the reference source
$v_{s,t}$	v chromaticity coordinate of the source-under-test
$v_{s,t}'$	adapted v chromaticity coordinate of the source-under-test
V_T	thermal voltage
W^*	W* coordinate of the CIE 1964 UCS colour space
$W_{i,r}^*$	W* coordinate of the adapted ref. sample under the adapted ref. light source
$W_{i,t}^*$	W* coordinate of the adapted ref. sample under the test light source
WPE	Wall-Plug Efficiency
x	normalised X tristimulus value of the CIE XYZ system
X	X tristimulus value of the CIE XYZ system
y	normalised Y tristimulus value of the CIE XYZ system
Y	Y coordinate of the CIE u´,v´, Y colour space
Y	Y tristimulus value of the CIE XYZ system
YAG	Yttrium Aluminium Garnet
Y_b	relative luminance of the background in CIECAM02
z	normalised X tristimulus value of the CIE XYZ system
Z	Z tristimulus value of the CIE XYZ system
λ	wavelength in metres
λ_p	peak wavelength in metres
Φ_v	luminous flux in lumen
Ω	solid angle
$V(\lambda)$	combined sensitivity function of the S-, M- and L- cones of the human eye
h	Planck´s constant
n	semiconductor ideality factor
v	wave phase velocity
η_{ext}	external quantum efficiency
Ψ	wave function of a quantum system
ε	permittivity in farads per metre
η	efficiency / efficacy
θ	angle of refraction in degrees
μ	permeability in henries per metre
ρ	charge density in coulombs per unit volume of space
σ	Stefan-Boltzmann constant

Table of contents

1. Physics of light – particles and waves

In ancient times there were two theories aiming to explain the workings of our vision. A first school advocated the so called *emission theory* which explains that objects can be seen because of infinitely fast travelling light rays emitted by the eye. An opposing school taught that vision was possible through something representative from an object entering the eye. The *intra-mission theory* was the beginning of modern day studies of light and optics.

1.1 A brief history of light

After the renaissance of the 12th century, science started to progress again in Europe. In 1637 the French philosopher René Descartes published his sine wave of refraction theory, more commonly known as *Snell's law*, after his original discoverer Willebrord Snellius.

23 years later, Italian physicist Francesco Grimaldi showed that when light is shone through a very narrow slit, an interference pattern is created. This diffraction pattern was an extremely important discovery to support the wave theory of light as it proved that light did not go through the slit as a particle, but rather spread out.

A year after Grimaldi published his findings on diffraction, British physicist Isaac Newton started his work to disprove the wave theory of light. Newton argued that Grimaldi´s diffraction was just another kind of refraction, and that refraction and reflection could only be explained when light was a stream of particles. He demonstrated through a series of three experiments that white light is composed of different colours.

1. Sunlight is separated into its colour components by a glass prism
2. These colour components recombine once again to white light by focusing them into a second prism
3. A single colour, which has a unique angle of refraction, cannot be separated further

Newton concluded that light is composed of coloured particles or *corpuscles* and that each corpuscle has its own unique colour.

Grimaldi´s diffraction studies were further elaborated by Christiaan Huygens, resulting in his *Traité de la Lumière* where he developed the concept of the wavefront. Huygens proposed that every point of a wavefront can be considered as a source of secondary, spherical wavelets which spread out in the forward direction at the same speed of the source wave as seen in Fig. 1.1. Huygens, who believed that light waves were of a longitudinal nature, stated that they need a medium to propagate (5).

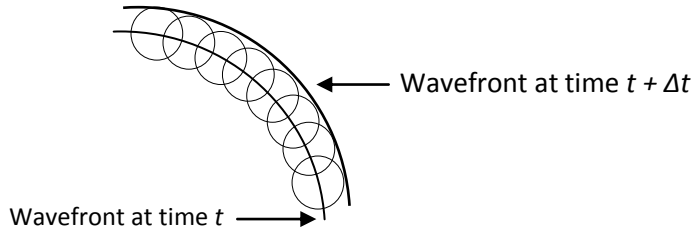

Fig. 1.1. Huygen´s principle

In the early 1800s, Thomas Young, at that time professor at the British Royal Institution, demonstrated the validity of the wave theory of light by letting light pass through a card with a narrow slit followed by another card with two slits placed close to each other. The result was two spread-out light beams with an alternating interference pattern of bright and dark rings in the area of overlap. Young explained the rainbow of colours in soap bubbles and Newton rings based on his experimental finding and firmly believed they were the ultimate proof for a wave-like behaviour of light.

In the mid 19th century, Michael Faraday did another important discovery: Faraday found that when a beam of polarized light was directed through a piece of lead-containing glass, the polarization of the light could be rotated by applying an external magnetic field. This interconnection between light and magnetism, or electromagnetic induction, was proof that light consists of electromagnetic radiation (1-4).

Faraday´s experiments paved the road for the theoretical basis for electromagnetic radiation developed by James Clerk Maxwell and later on, the famous Maxwell equations (Eq. 1.1,1.2,1.3,1.4) linking electricity and magnetism. With his *A Dynamical Model of the Electromagnetic Field* Maxwell proved that light was an electromagnetic phenomenon.

$$\nabla . E = \frac{\rho}{\varepsilon_0} \qquad \text{(Eq. 1.1)}$$

$$\nabla . B = 0 \qquad \text{(Eq. 1.2)}$$

$$\nabla X E = -\frac{\partial B}{\partial t} \qquad \text{(Eq. 1.3)}$$

$$\nabla X B = \mu_0 \left(J + \varepsilon_0 \frac{\partial E}{\partial t}\right) \qquad \text{(Eq. 1.4)}$$

where E is the electric field, B the magnetic field and J the current density. ρ represents the electric charge density, ε_0 the permittivity of free space and μ_0 the permeability of free space (6).

Heinrich Hertz proved the electromagnetic nature of light with the discovery of the photo-electric effect where light interacts with materials to free electrons.

By the end of the 19th century traditional insights of the interaction between light and matter made place for modern quantum mechanics. Although studied extensively, many phenomena could not be explained. No one knew how light could travel through a vacuum, either as a particle or a wave. The

relationship between the temperature of an object and the black-body spectrum was not understood and the nature of spectral lines was a mystery.

Calculating the black-body spectrum proved to be a major challenge, one that was solved in 1901 when Max Planck presented his now famous law, showing the spectral radiance of matter at a certain temperature (Eq. 1.5).

$$B_v(v,T) = \frac{2hv^3}{c^2}\frac{1}{e^{\frac{hv}{k_BT}}-1} \quad \text{(Eq. 1.5)}$$

Where k_B is Boltzmann´s constant and h the Planck constant.

Describing the behaviour of a black-body emitter as a source of quantised energy packets gives birth to the Planck relation which relates energy to frequency (Eq. 1.6).

$$E = hv \quad \text{(Eq. 1.6)}$$

In *Concerning* a *Heuristic Point of View towards the Emission and Transformation of Light* Albert Einstein explains how the photoelectric effect (the emission of electrons by certain metals when irradiated with light) is caused by the absorption of quanta of light, not completely unlike Newton´s corpuscles. Later on, Einstein proved that these quanta also have momentum, which means they are particles. The photon, and the wave-particle duality of light, was a fact (7).

1.2 Light as a wave

Light is a form of electromagnetic radiation that propagates in the form of two mutually coupled vectors. These two vectors, perpendicular to each other, represent a synchronized oscillation of an electrical and a magnetic field. The variable electrical fields generate magnetic fields and vice versa. Together they form a so called transverse wave.

Electromagnetic waves are sinusoidal and are characterized by three parameters common to all sinusoidal disturbances:

- An amplitude (A)
- A period (T)
- A wavelength (λ)

The wavelength of light can be calculated by

$$\lambda = \frac{c}{nf} \quad \text{(Eq. 1.7)}$$

With c equal to the speed of light in a vacuum (299792458 m/s) and n the refractive index of the material of propagation.

Several phenomena can be attributed to the wave-like behaviour of light:

- Diffraction

When light meets an object in its path, it is not simply blocked by that object. Light slightly bends around the object´s edges. This phenomenon is called diffraction.

- Interference

Two waves travelling in the same medium have the tendency to interfere with each other. Constructive interference occurs when two in-phase waves interact, leading to an increase in amplitude while destructive interference is the result from an out-of-phase interaction. Young's double slit experiment illustrates this behaviour.

When monochromatic light is propagated through a narrow slit, the wavelike behaviour projects an interference pattern of alternating dark and light bands on a screen. Young argued that this behaviour clearly shows that light does not adhere to the classic particle theory. Later studies, however, demonstrated that particles such as electrons create a similar pattern when subjected to double slit experiments, illustrating the wave-particle duality of electromagnetic radiation (chapter 1.4).

- Refraction

Refraction occurs when light passes from one medium to another. The change in propagation speed of light causes a change of propagation direction. Refraction of light is described by Snell´s law

$$\frac{\sin\theta_1}{\sin\theta_2} = \frac{v_1}{v_2} = \frac{n_1}{n_2} \qquad \text{(Eq. 1.8)}$$

Where $\theta_1$is the angle of incidence, $\theta_2$the angle of refraction, v_1 and v_2 the speed of light in each medium and n its refractive index. The refractive index of materials is wavelength dependent, an effect called dispersion.

- Polarization

As mentioned before, light is a transverse electromagnetic wave. Normal, non-polarized light sources, such as the sun or common light bulbs, emit light with magnetic and electrical fields that vibrate in all directions. Light sources such as lasers emit polarized light where both the electrical and magnetic field vibrate in one specific plane.

1.3 Light as a particle

Plank's theory of light being a stream of quantised particles and Einstein´s explanation of the photoelectric effect proved that light does not only behave like a wave, but must consist of particles. These elementary particles are called photons.

- Photons move, in vacuum, at a constant velocity equal to the speed of light.
- They have zero rest mass and energy
- Photons carry momentum

The energy of a photon is directly related to its frequency (eq. 1.6).

1.4 The wave-particle duality

Depending on which characteristics are observed, light can be characterized as having a wave-like or particle-like behaviour. While one phenomenon is explained better through the wave theory, another experiment fits the particle theory.

The Schrödinger equation below describes how a quantum wave function evolves over time. The wave function itself is the distribution of probabilities that a quantum system will be in any given quantum state.

$$i\hbar \frac{\partial}{\partial t}\Psi = \hat{H}\Psi \qquad \text{(Eq. 1.9)}$$

where $\hbar = \frac{h}{2\pi}$, Ψ is the wave function of the quantum system and $\hat{H}$ the hamiltonian operator characterizing the total energy of the wave function.

This can be interpreted as the Schrödinger equation giving the probability of finding a given particle at a given point. The probability equations can exhibit wave-like behaviours giving way to a final wave function that exhibits these properties as well.

While theoretically the wave-particle behaviour of light is well explained, grasping the idea on a practical level is much harder. Their union is still one of the major debates in modern day quantum physics.

1.5 Summary and conclusions

In the early days, Grimaldi believed that light behaves as a wave. Not much later, Newton concluded that light must consist out of corpuscles or small particles. In the early 19th century, Young proved with his double-slit experiment that light has a definite wavelike behaviour. At the same time, Faraday's experiments laid down a basis for the famous Maxwell equations that link light and magnetism. In the beginning of the 20th century, modern quantum theories tackled phenomena that could only be explained through the wave-particle duality of light. While diffraction, interference and polarisation can be explained through the wavelike properties of light, Einsteins insights in the photoelectric effect proved that light must consist out of individual photons.

2. Spectrometry and colourimetry

2.1 The electromagnetic spectrum

Electromagnetic waves are described by an amplitude (A), period (T) and wavelength (λ). Their frequency ranges from very energetic 2 x 10^{27} Hz cosmic gamma rays until wavelength as long as the universe itself at the opposite end of the spectrum. In between, several boundaries mark the division between different bands of the spectrum. Fig. 2.1 shows the electromagnetic spectrum and its most common wavelength bands.

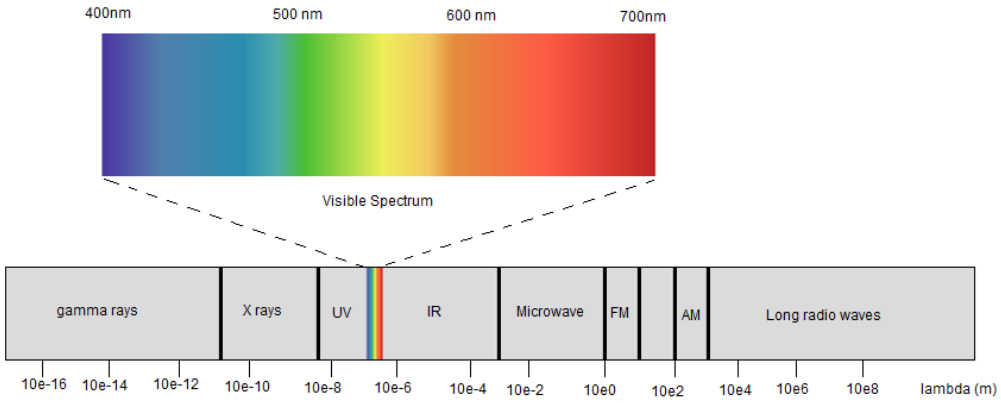

Fig. 2.1. The electromagnetic spectrum.

The longer, less energetic end of the spectrum is made up of radio waves. Groundwave radio transmitters where historically used to provide long distance communication channels as waves with frequencies in the low KHz range use the space between the earth´s surface and the D layer of the ionosphere as a waveguide, effectively making the radiowave follow the earth´s curvature. The medium wave band between 500 and 1600 MHz, widely used during the "Golden Age of Radio" between the 1920´s and 1950´s, could be propagated further than longer wavelengths by using the *skywave effect.* Skywaves bounce between the earth´s surface and the ionosphere and can cover distances of several thousands of kilometres. Short wavelength radio waves, such as the ones used in the common FM-band with frequencies between 75 and 108 MHz, have to use multiple point-to-point transmitters to cover a certain area.

Further increasing the frequency brings us into the territory of microwaves. With wavelengths ranging between one meter and one millimetre, microwaves provide a highly effective directional point-to-point communication channel. Both mobile phone (GSM[1], UMTS[2] and LTE[3]) and Wi-Fi wireless network systems use microwaves. Microwave ovens use the same microwaves to heat food. When generating an oscillating electromagnetic field, dipole molecules such as water try to continuously align themselves

[1] Global System for Mobile communications
[2] Universal Mobile Telecommunications System
[3] Long Term Evolution

with that field. This causes collisions with other water molecules resulting in a transfer of kinetic energy which is released as heat.

The longer wavelengths of the visible spectrum are flanked by infrared radiation (IR). IR rays where discovered by William Herschel in 1800 when he found out that, when shining sunlight through a prism, there was an invisible radiation extending beyond the red colours of the spectrum that heated his thermometer more than the rest of the spectrum did. The infrared spectrum covers a wavelength range from 1 mm at the far end to 700 nm at the short end[4]. IR light is used extensively in industrial processes ranging from high powered lasers to cut steel to thermal imaging systems to monitor the heat generated by electronic components to infrared spectroscopy. Molecules absorb or emit IR light when changing their rotational-vibrational movements. This makes infrared spectroscopy a useful tool to analyze their structure. Weather satellites are equipped with thermal imaging systems that record infrared light. Based on their measurements, different cloud heights, sea and land temperatures and the amount of water vapour in the atmosphere can be quantified. Controlled experiments have shown that the human retina is sensitive up to wavelengths of 1050 nm (8).

The visible light spectrum, spanning wavelengths between 750 and 380 nm (Fig. 2.2), covers only a small part of the electromagnetic spectrum. Newton was the first to divide the spectrum into 7 separate colour ranges and name each range: *Red, Orange, Yellow, Green, Blue, Indigo and Violet*. Newton´s Indigo corresponds to today´s blue (around 450 nm) while his Blue resembles cyan (490 nm). Young and Helmholtz developed the theory of colour vision in the early 19th century and explained the relation between colour vision and the visible light spectrum.

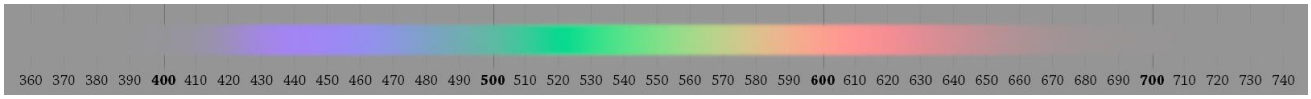

Fig. 2.2. The visible spectrum, desaturated to accurately show pure spectral colours on a gamut-limited sRGB monitor.

Note that not all visible colours are represented in the visible spectrum. Each point in the spectrum shown in Fig. 2.2 contains only 1 wavelength, resulting in a saturated, pure spectral colour. Less saturated colours such as pink or sky blue consist of a mix of multiple different wavelengths. One particular colour is magenta. Magenta, a so called extra-spectral colour, even though seen as very saturated and pure, is not found anywhere in the visible spectrum of light. This red-blue hue is observed when both the long and short wavelength cones on the retina are stimulated (chapter 2.6).

The short wavelength edge of the visible spectrum transits to the ultraviolet (UV) range. UV light was discovered in the beginning of the 19th century when Johann Ritter found out that paper strips saturated with silver chloride discoloured faster under the invisible part just before the violet part of the sun spectrum. UV radiation produces very energetic photons and is therefore damaging to living cells. Short wavelength UV-C radiation (< 290 nm) is completely blocked by O_2 molecules in the upper atmosphere. Most of the UV-B radiation (290 nm – 320 nm) is further absorbed by the ozone layer while a large part of the longer wavelength UV-A radiation (320 nm – 400 nm) reaches the earth´s surface. Ultraviolet light

[4] IR-C to IR-A according to the CIE

has widespread applications in industrial processes: extreme shortwave UV light with a wavelength of 13.5 nm produced by excimer lasers is used for modern photolithography where structures as small as 10 nm are exposed onto silicon (9). The wavelength band between 240 – 280 nm is used extensively for disinfection purposes because of the peak absorption of DNA at 260 nm. UV-B radiation has applications in the printing industry to polymerise inks in large-format printers while near-UV broadband sources are used in insect-trapping equipment. Both UV-B and UV-C light are often used as a source to excite wavelength converters such as phosphors or UV dyes (chapter 8) which have applications ranging from imaging displays and visible light sources to forensics, security and even detergents to wash clothes.

Extreme shortwave UV-radiation transits into X-rays or Röntgen radiation, named after Wilhem Röntgen who discovered the radiation in the late 19th century. Short wavelength X-ray photons (< 0.1 nm) have a high penetration power and are used to image the inside of objects or bodies during (medical) examinations. X-rays have the energy necessary to ionize atoms. Ionizing radiation is harmful to living organisms making Röntgen rays a hazard with serious long-term effects. Controlled, concentrated doses of X-rays are used to selectively threat and kill malignant tumours in radiation therapy. While X-rays are usually produced by making high-velocity electronics collide with a metal target, an interesting discovery by the University of California, Los Angeles, showed that peeling sticky tape in a vacuum produces a steady X-ray flux through a process called triboluminescence (10).

The highest frequency electromagnetic waves produce gamma radiation with extremely energetic photons. Gamma radiation on earth usually results from radioactive decay processes. Recent studies hint at the danger of gamma-rays produced during heavy lightning storms, especially for plane passengers (11, 12). Gamma radiation is used for targeted cancer treatments and is detected during positron emission tomography imaging. The largest gamma ray sources are pulsars and quasars or supernova and hypernova events which can emit gamma bursts releasing up to 8.8×10^{47} J, almost 5 times the sun´s mass turned to energy[5] in a time span of just 23 minutes.

2.2 Black body radiation

Black body radiation is a continuous spectrum that is emitted by any object when it has a temperature above 0 K. A black body itself is a piece of idealized physical matter that absorbs all incident electromagnetic radiation. When the black body is heated, it will emit a black body spectrum containing all wavelengths. A blackbody is usually represented by a hollow body whose walls are at identical temperatures. A small opening in one of the walls will be a perfect black body emitter. Any incident radiation will be absorbed within the cavity of the body. This makes the opening, besides a perfect emitter, also a perfect absorber.

The total radiation emitted by a black body can be calculated by Stefan´s law

$$E = \sigma T^4 \qquad \text{(Eq. 2.1)}$$

[5] Gamma ray burst 080916C, September 16, 2008

With σ = 10^{-8} $Wm^{-2}K^{-4}$

Wien´s law allows us to calculate the peak wavelength of the radiator (λ_m) in relation to its temperature (T)

$$\lambda_m = \frac{2.89789 \,.\, 10^6}{T} \qquad \text{(Eq. 2.2)}$$

Wien´s law shows that the peak wavelength of a black body shifts towards shorter wavelengths with increasing temperatures.

The spectrum in thermal equilibrium can be calculated using Plank´s law (with spectral radiance per unit wavelength)

$$B_v(v,T) = \frac{2hv^3}{c^2} \frac{1}{e^{\frac{hv}{k_B T}} - 1} \qquad \text{(Eq. 2.3)}$$

Where k_B is Boltzmann´s constant and h the Planck constant.

Note that a black body emits a continuous spectrum that contains all wavelengths from 0 to infinity. Fig. 2.3 illustrates the shift in spectral shape and peak wavelength with rising temperatures (13).

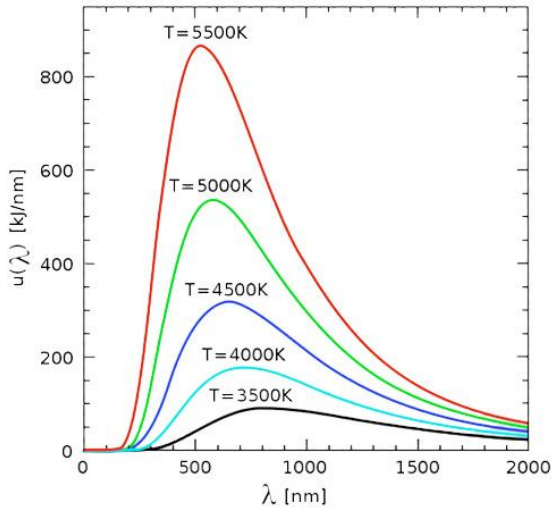

Fig. 2.3. Black body spectra according to Plank´s law at different temperatures.

2.3 Radiometric quantities and units

- Radiant energy

The total amount of energy (Q_e) emitted by a source of electromagnetic radiation is called the radiant energy, measured in Joule (J)

- Radiant flux

When time is factored into the equation, radiant energy becomes radiant flux, measured in watt (W).

$$\Phi_e = \frac{dQ_e}{dt} \quad \text{(Eq. 2.4)}$$

- Radiant intensity

Radiant flux emitted in a certain direction is called radiant intensity (W/sr)

$$I_{e,\Omega} = \frac{d\Phi_e}{d\Omega} \quad \text{(Eq. 2.5)}$$

Where Φ_e is the radiant flux and Ω the solid angle.

- Radiance

Radiance is radiant flux *emitted* in a certain direction by a *surface* and indicates how much of the total energy emitted by a source will be received by an observer (W/(sr.m^2))

$$L_{e,\Omega,v} = \frac{\partial^2 \Phi_e}{\partial\Omega\partial A cos\theta'} \quad \text{(Eq. 2.6)}$$

Where Φ_e is the radiant flux, Ω the solid angle and $A\cos\theta$ the projected area

- Irradiance

Radiant flux *received* by a surface is called irradiance and describes the total energy falling upon an area (W/m^2).

$$E_e = \frac{d\Phi_e}{dA} \quad \text{(Eq. 2.7)}$$

Where Φ_e is the flux received and A the area of the receiving surface.

- Radiant exitance

The radiant flux *emitted* by a *surface* is called the radiant exitance (W/m^2)

$$M_e = \frac{d\Phi_e}{dA} \quad \text{(Eq. 2.8)}$$

With Φ_e the flux received and A the area of the receiving surface.

Note

All the above quantities also have a spectral variant where the quantity is given per unit wavelength. This is often used when only a part of the electromagnetic spectrum is of interest during measurements, analyses and calculations.

2.4 *Measuring light*

Over the course of this PhD, IREC has set up a laboratory to measure light sources and characterize luminaires. Two types of instruments saw extensive use when testing new light emitting materials, optical arrangements and assembled light engines.

- Integrating sphere

An integrating sphere, also called Ulbricht sphere, is an instrument used to measure, in conjunction with a spectrophotometer, the radiant flux and spectrum of a light source. The light source itself is placed within a hollow sphere that is coated with a highly reflective barium sulphate coating with an extremely high (>98%) and flat reflectivity function from the near UV to near IR range of the spectrum. The integrated light output is coupled to a baffled fibre and analysed by a spectrophotometer that compares the raw fibre output to the output of a known calibration standard.

IREC's lighting laboratory has 2 different integrating spheres (Fig. 2.4)

- An Instrument Systems sphere with a diameter of 50 cm in combination with an Instrument Systems Spectro 320 scanning spectrophotometer with a wavelength resolution of 0.3 nm for measurements of Light Emitting Diodes (LEDs). The LED mounting system has a temperature controlled base plate which allows accurate characterisations with controlled semiconductor junction temperatures.
- An Instruments Systems 200 cm sphere combined with an Instrument Systems CAS 120 CCD based spectrophotometer with a resolution of 2.7 nm. This combination allows characterizations of large light sources and luminaires.

Besides radiometric and photometric characterisation systems, the laboratory is equipped with a goniophotometer to perform measurements of the beam pattern of sources and luminaires (Fig. 2.5).

Goniophotometers characterize the angular radiation pattern of light sources. In this case, a dual-sensor equipped TechnoTeam RiGO801 *luminaires* can be configured to measure in the far-field (small objects, illuminance meter only) or in the near field (sources up to 2 m long) by using a CCD camera that moves around the fixed light sources on spherical surface. A smaller model, RiGO801 *LED* is equipped with only a CCD camera and can be used to measure (LED) sources up to 200 mm wide. The measurements from each sensor are converted into *ray-data* which contains the radiant intensity of the source for each solid-angle step of the goniophotometer. Ray files can be used to calculate the total radiant flux of the light source or luminaire and are used as input data for illumination calculation and simulation software.

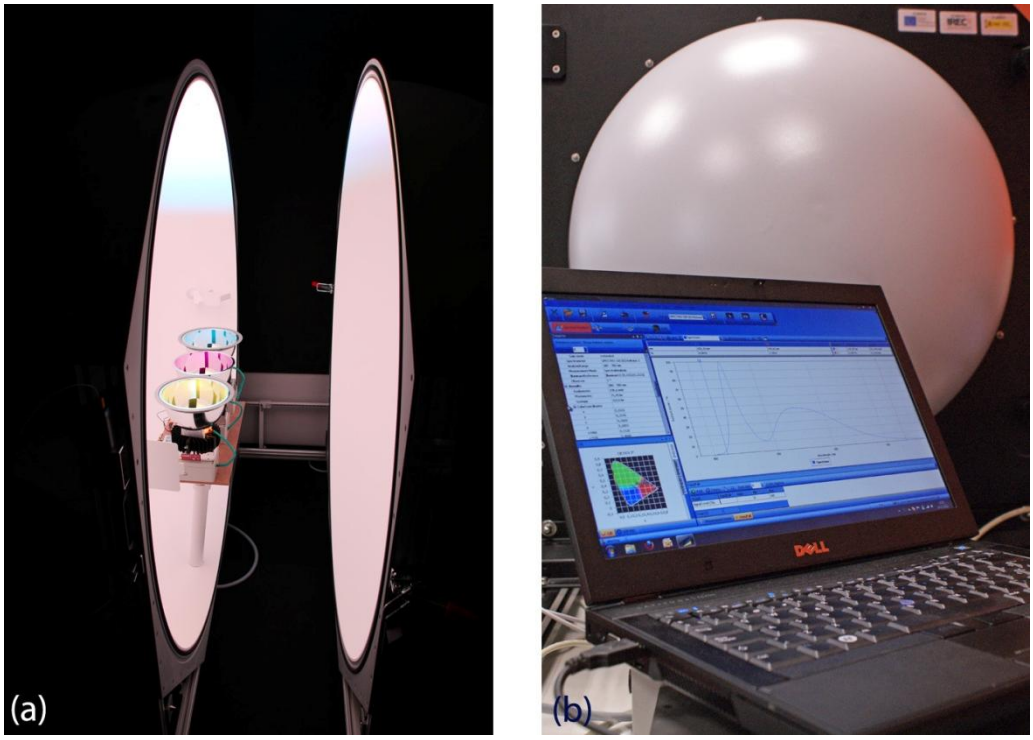

Fig. 2.4. Integrating sphere measurements. 200 cm sphere measuring the output of 3 spectrally tuneable LED luminaires (a) and the output spectrum of a white LED measured by the IS Spectro 320 and 50cm sphere (b).

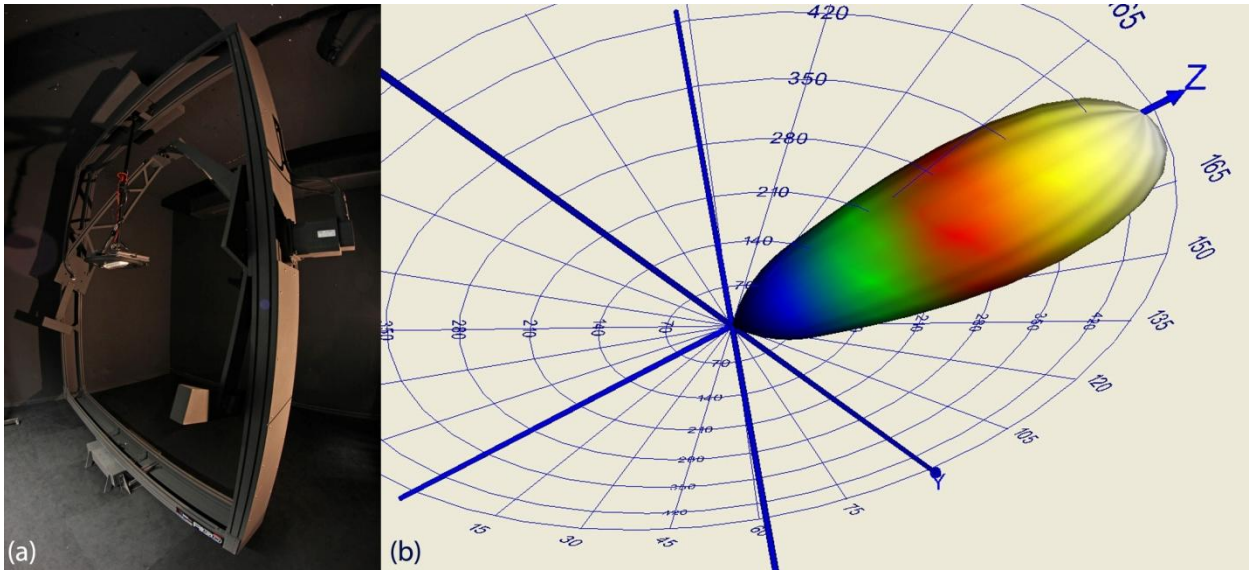

Fig. 2.5. Goniophotometer. TechnoTeam RiGO801 l*uminaires* (a), the resulting ray-data visualised in a polar diagram (b) is used in Dialux, a lighting design software package (chapter 4.5.6 and 4.5.7).

2.5 The visual system

The eyes, in combination with the brain, are responsible for one of our primary sensory functions: vision. Primates and humans have their eyes frontally mounted, providing them with predatory sight. This close mounting introduces a wide overlapping field of view which can be processed by the brain to provide stereopsis or 3-dimensional sight. Animals, depending on their evolutionary needs, have their eyes placed in different positions that provide either a wider angular coverage (prey animals) or a wider stereoscopic field of view (hunters). The visual perception within the eye´s field of view depends on the angular deviation from the centre of vision or the gaze direction, with the ability to resolve the smallest details at 0 º (Fig. 2.6).

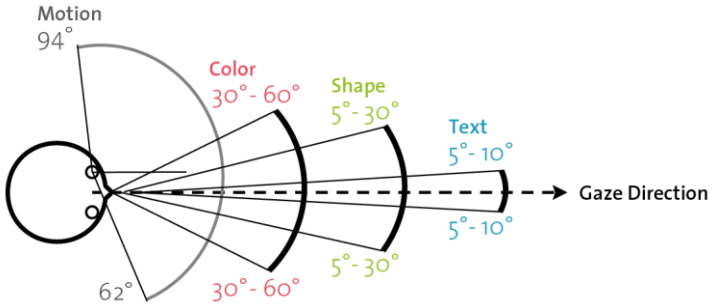

Fig. 2.6. Human visual perception in function of the centre of vision.

While many animals lack the ability to move the eyes, higher developed species and humans can enlarge their (binocular) field of view by moving the eyes in the head. Eye movements are usually done in so called *saccades.* A saccade is a rapid jump of both eyes to a certain fixation point. Only in very specific conditions, for example when following a slow moving object, non-saccadic smooth eye movements take over.

The image forming part of the eye resembles a simple, spherical single-lens camera system (Fig. 2.7). Light enters the eye through a transparent part of the sclera, the outer layer of the eyeball called the cornea. The second layer, the choroid, contains a network of blood vessels that supplies the retina. When the choroid approaches the cornea it forms the ciliary body that produces the oxygen carrying fluid between the cornea and the lens. The ciliary body transforms into the iris which functions like the aperture in a photographic camera. The opening formed by the iris is called the pupil. After passing through the pupil, light reaches the crystalline lens of the eye. The lens itself can be deformed by a set of muscles, either being flattened or more rounded when accommodating for nearby or far-away objects. It has to be noted, however, that most of the light bending is not done by the lens itself but through the cornea and aqueous fluid between the cornea and lens. The light passes through another layer of transparent material before reaching the image recording part of the eye: the retina. The retina consists out of 3 layers (from outside to inside): a layer with photoreceptors, a second layer of collector cells and a final layer of ganglion cells. The place where the optic nerve leaves the eye creates a blind spot on the retina.

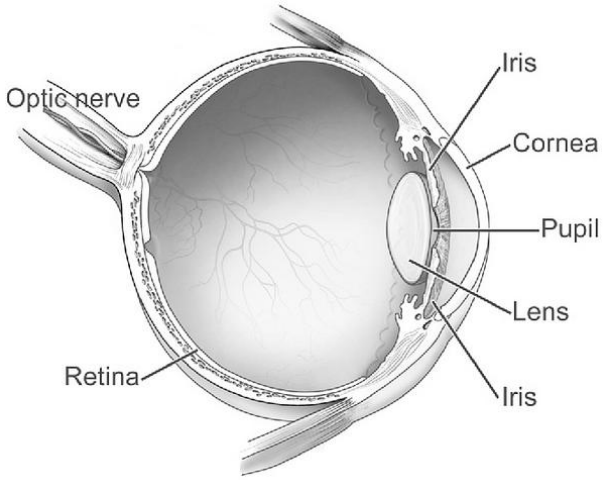

Fig. 2.7. Diagram of the main image-forming parts of the human eye.

The retina itself is part of the central nervous system where the electrical signals from the different photoreceptors are converted into action potentials and sent to the brain via axons. There are five types of neurons in the retina: photoreceptors, bipolar cells, ganglion cells, horizontal cells and amacrine cells. There are four types of photoreceptors, grouped into rods and cones. The on average 90 million rods, spread between 20 º and 100 º from the centre region of the retina, are around 100 times more sensitive to light than the cones and are mainly used for scotopic or night vision (less than 10^{-3} cd/m^2). Rods contain only one type of photosensitive pigment and thus do not enable colour vision. The figure below shows the sensitivity curve for human rods, peaking at 507 nm. As rods are concentrated around the central retinal region they play an important role in peripheral vision.

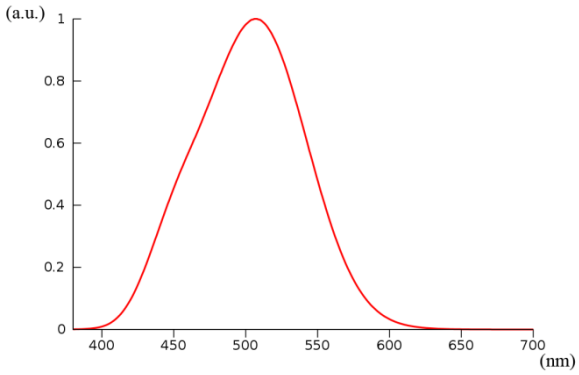

Fig. 2.8. Rods sensitivity or $V'(\lambda)$ function.

The around 8 million cones are located mainly in the central part of the retina or the fovea. There are three types: L-cones, M-cones and S-cones, each containing a different pigment that makes them sensitive to a different spectral region (Fig. 2.9).

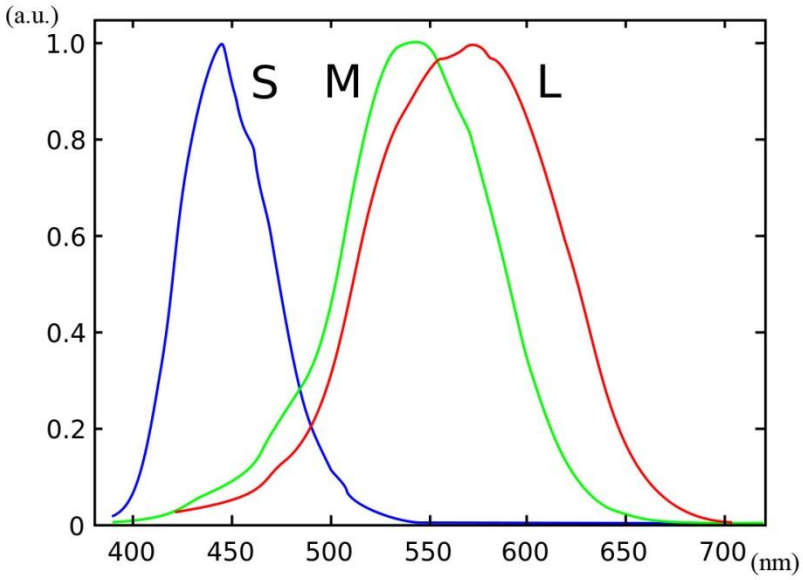

Fig. 2.9. Normalised spectral sensitivities of the S-, M- and L-cones.

The combined spectral responses of the three cones allow the discrimination of wavelengths between 380 and 750 nm, with their combined sensitivity peaking at 555 nm. Although the total number of cones is far less than the total number of rods (8 versus 90 million), the extremely high cone density in combination with other anatomical features such as the absence of blood vessels favour a far higher resolving power in the central fovean region of the retina compared to the peripheries. The optic nerves of the two eyes are joined at the optic chiasm in the brain. This junction ensures that each of the two visual cortices receive signals from the same side of the two eyes (14, 15).

2.5.1 Colour vision

Colour vision requires at least two photoreceptors sensitive to different wavelength bands. Many invertebrates, such as insects, have UV-blue-green trichromacy with variations in the absorption peaks between different species (16). Most lower vertebrates, including fish, have at least trichromatic vision with one of the cones sensitive to UV light. Many mammals possess dichromatic vision with cones sensitive to short and middle-long wavelengths and are unable to see deep red wavelengths. Most old world primates have redeveloped trichromatic vision and have eyesight very similar to that of humans. One of the most striking examples of colour vision in nature is the eye of the mantis shrimp, carrying up to 16 different cones. The retina of the mantis shrimp has cones covering the UV-B to deep red wavelengths and can even differentiate types of polarized light. Such a sophisticated eye does not, however, guarantee that the mantis shrimp has better colour discrimination than humans. Their relatively weak visual cortex means that the brain does not have enough processing power to extract the needed amount of information, making their colour differentiation rather limited (17).

2.5.2 Human vision

Human vision is trichromatic with cones sensitive in the blue wavelength region (S-cones), green wavelength region (M-cones) and yellow wavelength region (L-cones) (fig. 10). Neurologically, their outputs are arranged in two colour opponent chromatic channels and one achromatic channel. The achromatic channel receives signals from M- and L-cones only. One colour opponent channels gives the difference between the output of the M-cones and the sum of the outputs of the L- and S-cones (L-M+S) resulting in a red-green channel while the second colour opponent channel differentiates between the signal of the S-cones and the sum of the M- and L-cones (L+M-S), resulting in the blue-yellow channel. The combination of these three channels allows us to see the world in full colour. Any abnormality in either the presence of the cones or their spectral sensitivity leads to a certain colour vision anomaly. Rod monochromats are completely color blind and see only luminance differences. Cone monochromats are either true dichromats (one of the cones missing) or have a trichromatic anomaly. About 8 percent of the male population and 0.4% of the females have a colour vision deficiency.

2.6.3 Adaptation mechanisms

The human visual system has a number of adaptation mechanisms to ensure optimal sight under a wide range of viewing conditions.

- Luminance adaptation

The eye has a rather limited dynamic range (the maximum difference between the lowest and highest perceivable luminance), but the whole visual system can differentiate a very large luminance range (> 1, 000,000,000,000:1) (18) through three different mechanisms. A first, obvious mechanism is a change in pupil diameter. The eye of an average young person has a pupil diameter ranging from 8 mm to 2 mm, which translates in a 16:1 adjustement range. It is clear that the pupil alone plays a minor role in brightness adjustements. A second mechanism, neural adaptation is active under moderate luminance levels (< 600 cd/m^2) and has an adaptation range of around 1000:1. The largest adaptation range comes from photochemical bleaching of the pigment in the photoreceptors. When a bright image is projected onto the retina, the irradiated photoreceptors become less sensitive and give a lower neural signal compared to surrounding, non-adapted receptors. This is a relatively slow process, especially during recovery from bright sources (18).

The illuminance levels of the surroundings and the adaptation state of the visual system determine which photoreceptors are active.

Scotopic vision

Only rods are active when the eye is dark adapted to luminance values lower than 0.001 cd/m^2. This means that vision is now limited to a gray scale image with lower resolving power than during mesopic and photopic regimes.

Photopic vision

At luminance levels higher than 3 cd/m^2 our vision is dominated by responses from the cones, enabling full colour vision at high spatial resolution.

Mesopic vision

When luminance levels fall in between the scotopic and photopic region, both the cones and the rods are active allowing for limited colour vision.

- Colour constancy

Colour constancy describes the effect that the colours of a scene remain constant for the observer while the spectrum of the illumination is changing (19). When light reflected off an object reaches the eye, it stimulates cone receptors in a certain way. A different spectrum reaching the eye will directly result in a different cone response. For example, the spectrum reflected by a red flower in a field will change quite drastically over the course of the day because of the change in illuminant spectrum (in this case the sun). While we do realise that in the early morning the flower will have a colder, blue-shifted colour, we still perceive or judge the flower as being red. The double-opponent colour-sensitive cells in the primary visual cortex (V1) process localised areas or cone activity to achieve colour constancy (20).

2.5.4 The circadian system

Living creatures are synchronised to a natural day and night cycle. Animals, as well as human beings go to sleep in the evening and wake up again in the morning. Since the early 20th century it was suggested that light plays a crucial role in regulating and modifying these rhythms (21).

The circadian system begins with the eye. Unlike the visual system, the circadian pathway leads via the retinalhypothalamic (RHT) tract to the suprachiasmatic nuclei (SCN) continuing along the paraventricular nucleus (PVN) and superior cervical ganglion to the pineal gland. The pineal gland is responsible for the production of *melatonin,* a key hormone involved in the synchronisation of the circadian rhythm. Only recently the key link between the eye and melatonin production was found. In 1998 a new light sensitive pigment called melanopsin was discovered (22). Not long after the discovery that the same photopigment was present in the retina of mice and that their axons are send to the SCN, definite proof was found that intrinsically photosensitive ganglion cells (ipRGCs) are also present in the human retina (23). There are far fewer ipRGCs compared to rods and cones on the retina and they are much less sensitive to light than the other photoreceptors. Furthermore, the action spectrum of melanopsin, while overlapping with both the cone and rod receptors, has a distinct peak sensitivity of 482 nm. Melanopsin plays a crucial role in photoentrainment which aligns the activity of an organism to the natural 24-hour day-night cycle. This means that blind people that have no means to see light and dark patterns can still synchronise their circadian rhythm, albeit more slowly than people with normal vision (24).

2.6 Basic photometry

The combined sensitivity curves of the S-, M- and L-cones of the eye (Fig. 2.9) determine the relative sensitivity of our visual system to a certain light spectrum. A transfer function describing the sensitivity of the cone receptors and visual system to visible wavelengths in the electromagnetic spectrum lays the basis for the standard photometric observer.

2.6.1 The standard photometric observer

Depending on its radiant energy, radiation near the edges of the visible spectrum becomes progressively less visible. The response of the eye is not determined by a direct measurement, but rather by an experimentally obtained brightness function. The brightness of two different light sources can be determined in two ways:

- A direct comparison method whereby a light source with a certain wavelength is directly compared with a light source of another wavelength. Although this method is simple, its highly subjective rating scheme leads to large fluctuations between results.
- Flicker photometry alternately introduces a reference light source and test light source within the visual field of the observer. Increasing the flicker frequency above the flicker fusion threshold (around 15 Hz, although at very large amplitudes the threshold can be as high as 60 Hz (25)) the two wavelengths of the reference and test light source blend in to one single colour. However, if the two light sources differ in brightness, the difference in brightness remains as a flicker. This phenomenon can be used to match the brightness of two sources with different spectral characteristics.

The latter method was used by the CIE in the early 1920s to determine the spectral luminous efficiency for photopic vision, resulting in the $V(\lambda)$ function illustrated in Fig. 2.10. The $V(\lambda)$ curve represents the perceived brightness of light with a certain wavelength and radiometric power and provides the link between radiometric and photometric units.

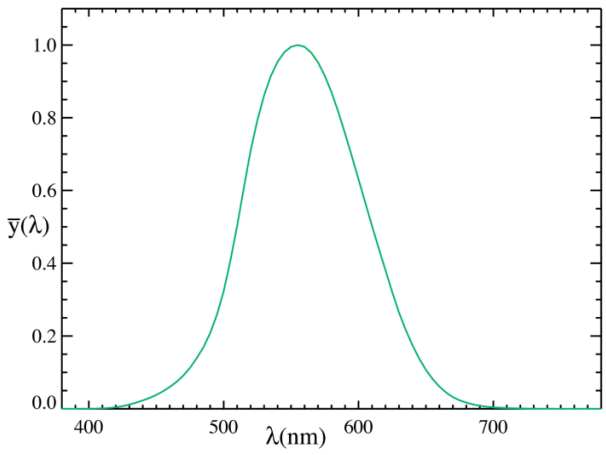

Fig. 2.10. CIE $V(\lambda)$ curve.

The “average” in average observer comes from the 7 studies involving 251 people with normal colour vision involved in determining the $V(\lambda)$ curve.

More recently, the CIE also provided a standard, bridging the gap between the scotopic and photopic functions (26). In the mesopic region both the cones and rods are active. The perceived brightness or V_{mes} function can be calculated as follows:

$$V_{mes}(\lambda, m) = \frac{1}{M(m)} \{mV(\lambda) + (1-m)V'(\lambda)\} \quad \text{(Eq. 2.9)}$$

With

$L_{mes} \geq 5$ cd/m^2, $m = 1$

$L_{mes} \leq 0.005$ cd/m^2, $m = 0$

2.6.2 Photometric quantities and units

- Luminous energy

Luminous energy, Q_v, is the quantity of light that is perceived by our visual system expressed in $lm \,.\, s$

- Luminous flux

The luminous flux of a light source measures the perceived power of light expressed in $cd \,.\, sr$, or more common in *lumen* (lm).

$$\Phi_v = \frac{dQ_v}{dt} \quad \text{(Eq. 2.10)}$$

With Φ_v the luminous energy of the source

From a given spectrum the luminous flux can be calculated as follows:

$$\Phi_v = 683 \,.\, \int_0^\infty V(\lambda) \,.\, P(\lambda) \,.\, d(\lambda) \quad \text{(Eq. 2.11)}$$

Where $V(\lambda)$ is the CIE spectral luminous efficiency curve for photopic vision and $P(\lambda)$ the spectral power distribution. In practice the integration interval lies between 380 and 780 nm.

- Luminous intensity

Luminous intensity measures the perceived power emitted by a light source in a particular direction per unit solid angle. The unit of luminous intensity is candela (cd).

$$I_v = \frac{d\Phi_v}{d\Omega} \quad \text{(Eq. 2.12)}$$

Where Φ_v is the luminous energy of the source and Ω the solid angle

- Luminance

Luminance measures the luminous intensity emitted by a surface in a given direction per unit area of that surface. It describes how bright a surface appears to the eye from a particular point of view. The unit of luminance is *cd/m²* or *nit*.

$$L_v = \frac{d^2\Phi_v}{(dA.\cos\theta\ .d\Omega)} \quad \text{(Eq. 2.13)}$$

Where Φ_v is the luminous flux, A is the area of the surface, θ is the directional angle and Ω is the solid angle.

- Illuminance

The luminous flux per unit area received by a surface is called the illuminance or luminous exitance, expressed in *lm/m²* or *Lux* (lx). The illuminance determines how bright an illuminated surface is perceived and is one of the main units used in illumination design calculations.

$$E_v = \frac{d\Phi_v}{dA} \quad \text{(Eq. 2.14)}$$

With Φ_v the luminous flux and A the area of the illuminated surface.

- Luminous efficacy

The luminous efficacy (η) shows how efficient a light source is in converting power to visible light. This power can either be the radiant flux of the source itself, in which case it is called the *luminous efficacy of radiation (LER)*, or it can be the power consumed by the source resulting in the *luminous efficacy of a source*.

$$\eta = \frac{d\Phi_v}{dE} \quad \text{(Eq. 2.15)}$$

with Φ_v the luminous flux and E the energy either radiated by the source (radiant flux) or consumed.

- Luminous efficiency

The luminous efficiency shows the radiometric power emitted by a light source limited to the visible range of the electromagnetic spectrum compared to the power consumed.

$$\eta = \frac{d\Phi_{ev}}{dE} \quad \text{(Eq. 2.16)}$$

where Φ_{ev} is the radiometric power emitted by the light source confined within the visible range and E the total energy consumed by the source.

2.7 Basic colourimetry

2.7.1 The origin, classification and representation of colours

When colours are named, sorted and classified, a colour system is born. From its earliest moments, mankind tried to find ways to sort colours into categories. Newton, for example, decided that there were seven individual colour groups in his rainbow: red, orange, yellow, green, blue, indigo and violet, a remarkably familiar naming scheme. He proposed to display these colours in a circular way, thereby creating the first colour system (27). It was not until much later that the theories of light and visual perception were sufficiently developed that the origin of colours and the spectral interaction of light with objects could be explained.

The perceived colour of an object is determined by three factors:

- The spectrum of the light incident on the object
- The reflection spectrum of the object itself
- The observer (usually the human eye, but possibly a device such as an imaging sensor)

When sunlight illuminates a ripe tomato, we see the tomato bright red. The reflection spectrum of that tomato absorbs most of the short wavelength light, while reflecting the longer wavelengths of sunlight. On the retina of the eyes, this reflected spectrum stimulates the L-cones telling the brain that the object seen is red. When the illumination spectrum is changes drastically, the appearance of the object changes as well. If, instead of sunlight, a monochromatic blue light source is used, the once bright red tomato will appear black because of the absorption of all the radiation from the light source. These conditions also apply when the observer is not a human eye, but for example a colour camera sensor. Full-colour image sensor mimic the cone-responses of the human eye by using specifically tuned red, green and blue colour filters over an array of light sensitive pixels. The combination of the illumination spectrum, the reflection spectrum of the object and the transmission characteristics of those filters determine the final signal that will be registered by the photosites on the imaging sensor.

2.7.1.1 Colour models and spaces for lighting applications

A colour model describes the appearance of a colour. Colour appearance systems are subjective as they are based on the psychological sensation of a colour. This may include several elements which are not directly related to colour itself, such as the texture of the item. To make things worse, names such as Sunglow, Razzmatazz or Tickle-Me-Pink are highly subjective and might mean nothing at all. It is clear that to accurately describe a colour, a scientific, non-subjective colour classification method has to be introduced.

One of the first colour models was introduced by Albert Henry Munsell in 1905. Munsell designed a colour system that was based on patches arranged and ordered using a cylindrical coordinate system. Munsell value *V* was used to denote *lightness* (or whiteness) as the ordinate, *H* referred to the *hue* (tint)

value as a circumferential angle and *C*, the *chroma* (vividness) of that hue, as the radius. The V axis is divided into 10 lightness values ranging from ideal black (V = 0) to ideal white (V =10). Munsell selected 10 different hues: Red, Yellow-Red, Yellow, Green - Yellow, Green, Blue - Green, Blue, Purple - Blue, Purple and Red – Purple. The chroma values range from 0 (achromatic) to infinity (Fig. 2.11).

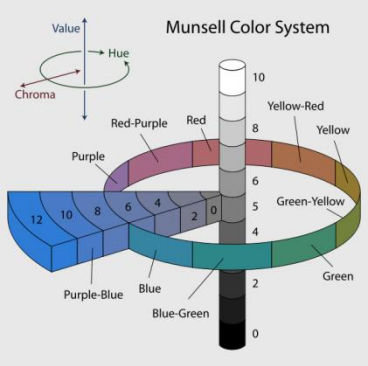

Fig. 2.11. The Munsell colour system describing its 10 hue (H), 10 lightness (V) and, in theory, an infinite number of chroma (C) values.
Source: "Munsell-system". https://commons.wikimedia.org/wiki/File:Munsell-system.svg#/media/File:Munsell-system.svg

The physical Munsell set contains 1250 pigment colour patches which should be viewed under CIE illuminant C. Each patch has its own unique H, V, C code, for example: 10GY, 5, 12 refers to a saturated grass-green coloured patch. A similar and widespread system is the Pantone Color Matching System (CMS) that not only provides a wide range of coded colours, but also aims to standardize colour reproduction by, for example, specifying the exact pigments to be used for CMYK printing processes.

The large advantage of both the Munsell system and Pantone CMS is that they are based on real pigments. This means that the colours are reproducible on different substrates and can be used for (psycho)visual testing and evaluations. The disadvantages, however, are that both systems rely on a limited set of available pigments and colour patches. This limits their reproducible range of colours or colour gamut and poses problems when a colour to be matched falls in between 2 consecutive patches.

Both models discussed above rely on subtractive colour mixing: pigments absorb certain wavelength and reflect others which results in a particular reflectance spectrum.

- CIE RGB

Colours can also be created by additive colour mixing. Mathematically, each and every colour can be formed through additive mixing:

$$I_\lambda + I_r = I_b + I_g \quad \text{(Eq. 2.17)}$$

$$I_\lambda + I_g = I_r + I_b \quad \text{(Eq. 2.18)}$$

$$I_\lambda + I_b = I_r + I_g \quad \text{(Eq. 2.19)}$$

Where I represents the intensity of three monochromatic red, green and blue reference stimuli and I_λ the intensity of the created spectral colour. This can be rewritten as

$$I_\lambda = I_r + I_g + I_b \quad \text{(Eq. 2.20)}$$

To be able to measure, define and calculate colours in an accurate way, the CIE established the 1931 RGB Colour Matching Functions (CMFs). These functions are based on the average data from a total of 17 observers with normal colour vision who performed colour matching experiments led by John Guild and William Wright (28, 29), based on the principles below:

1. The monochromatic red, green and blue reference stimuli have a wavelength of, respectively, 700 nm, 546.1 nm and 435.8 nm.
2. The basic stimulus is an equal-energy spectrum corresponding to a ratio of 1.0000:4.5907:0.0601 for respectively the red, green and blue reference stimulus, given in photometric units.
3. The results are valid within a 2 degree arc inside the fovea.

A narrow field-of-view of only 2 º was chosen because of two reasons:

1. The central fovea contains the highest concentration of colour sensitive cones and thus has the highest visual acuity
2. That same region is covered with the macular pigment which influences the response of those cones.

Because of reported discrepancies between the perceived colour and calculations using the 2-degree CMFs when using a larger field-of-view, new colour matching experiments where started aiming to develop a new set of CMFs for a 10-degree observer (30). The results are published in the CIE 1964 Standard Colorimetric System which contains a new set of CMFs recommended for viewing angles exceeding 4 º.

Fig. 2.12 shows the resulting CMFs which lay the basis for modern colour science.

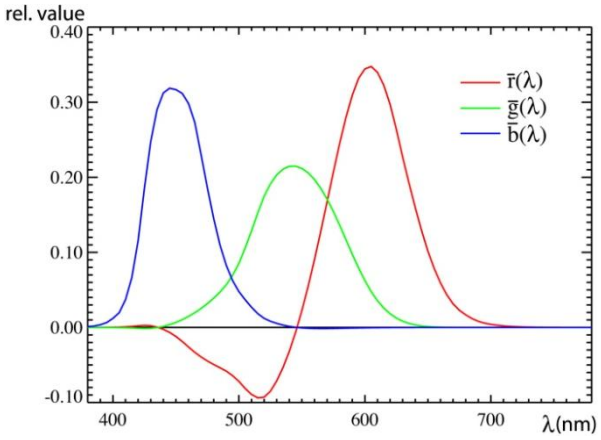

Fig. 2.12. The CIE 1931 standard colorimetric observer $\bar{r}(\lambda)$, $\bar{g}(\lambda)$ and $\bar{b}(\lambda)$ colour matching functions.

While mathematically it is possible to generate any visible colour with a combination of the reference stimuli, this would require negative stimuli for some combinations, something that is physically impossible. In practice, it was found that the red, green and blue primaries located at, respectively, 700 nm, 546.1 nm and 435.8 nm could not generate all visible colours. Some colours, situated mostly in the cyan region of the visible spectrum, required a slight amount of the red primary to be added to the test source in order to match. The result of this added primary is reflected in the negative values of the $\bar{r}(\lambda)$ function.

- CIE XYZ

The colour matching functions can be recalculated for a different set of RGB primaries which allows the CIE RGB colour system to be represented in such a way that there are no negative values in the colour matching functions. The resulting CMFs, shown in Fig. 2.13, are known as the CIE 1931 Standard Observer Colour Matching Functions.

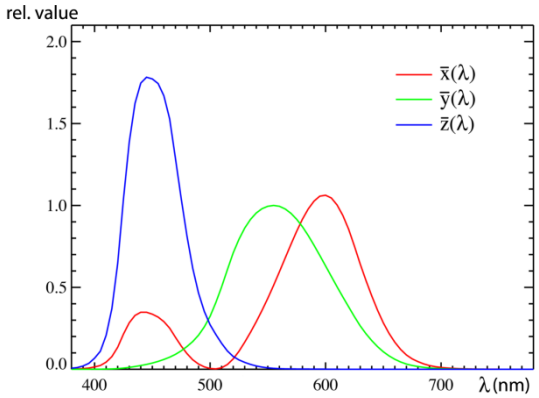

Fig. 2.13. CIE 1931 Standard Observer Colour Matching Functions $\bar{x}(\lambda), \bar{y}(\lambda), \bar{z}(\lambda)$ of the XYZ colour system. Note that the $\bar{y}(\lambda)$ curve is identical to the $V(\lambda)$ curve.

With the tristimulus values equal to

$$X = \int_{380}^{780} \Phi(\lambda)\bar{x}(\lambda)d\lambda \qquad \text{(Eq. 2.21)}$$

$$Y = \int_{380}^{780} \Phi(\lambda)\bar{y}(\lambda)d\lambda \qquad \text{(Eq. 2.22)}$$

$$Z = \int_{380}^{780} \Phi(\lambda)\bar{z}(\lambda)d\lambda \qquad \text{(Eq. 2.23)}$$

RGB tristimulus values can be converted in XYZ tristimulus values using the following relation:

$$\begin{pmatrix} X \\ Y \\ Z \end{pmatrix} = \begin{pmatrix} 2.7689 & 1.7517 & 1.1302 \\ 1.0000 & 4.5907 & 0.0601 \\ 0.0000 & 0.0565 & 5.5943 \end{pmatrix} \begin{pmatrix} R \\ G \\ B \end{pmatrix} \qquad \text{(Eq. 2.14)}$$

With the inverse matrix resulting in the XYZ to RGB conversion:

$$\begin{pmatrix} \mathrm{R} \\ G \\ B \end{pmatrix} = \begin{pmatrix} 2.7689 & 1.7517 & 1.1302 \\ 1.0000 & 4.5907 & 0.0601 \\ 0.0000 & 0.0565 & 5.5943 \end{pmatrix}^{-1} \begin{pmatrix} X \\ \mathrm{Y} \\ Z \end{pmatrix} \quad \text{(Eq. 2.25)}$$

Knowing the XYZ colour matching functions a corresponding colour space can be derived. The XYZ values can be normalized as follows:

$$x = \frac{X}{X+Y+Z} \quad \text{(Eq. 2.26)}$$

$$y = \frac{Y}{X+Y+Z} \quad \text{(Eq. 2.27)}$$

$$z = \frac{Z}{X+Y+Z} \quad \text{(Eq. 2.28)}$$

These three coordinates, called the chromaticity coordinates, define the x,y,Y colour space that forms the basis for representing colours in modern colour science. When only the hue and chroma of a colour is important, the x,y,Y colour space can be represented in its 2-dimensional form known as the CIE 1931 chromaticity diagram where the x and y coordinate combination determines the exact hue and chroma value of a particular colour.

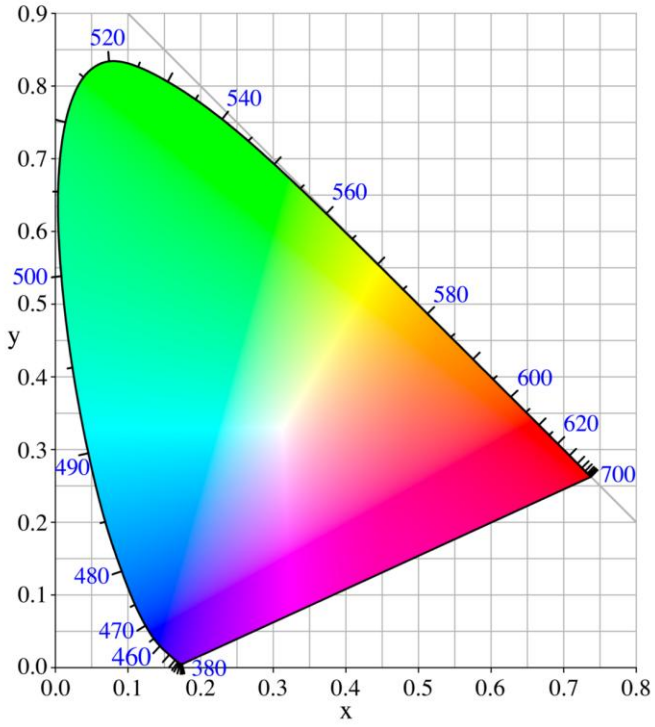

Fig. 2.14. The 1931 CIE chromaticity diagram with its spectral locus showing the corresponding wavelengths in nm.

Fig. 2.14 shows the CIE 1931 chromaticity diagram. Inside the diagram the full gamut of visible colours is represented. Spectral colours (colours composed of one single wavelength) are located on the edges while less saturated colours are found in the interior of the x, y diagram. White light is located in the centre region of the diagram. The line connecting both edges of the visible spectrum is called the line of purples where none of the chromaticity coordinates can be represented by a pure spectral colour.

Note that it is impossible to cover the full visible colour gamut using only three real primaries as the colour gamut of human vision is not a triangle. The more different sources are used, the wider the gamut coverage but it would take an infinite number of primaries to cover the full visible gamut.

While the 1931 x, y chromaticity diagram is accepted and used widely in the field of colour science, there are a few fundamental flaws. One of the major problems is the non-uniformity of the diagram. A certain geometric distance in, for example, the green part of the diagram does not represent an equal perceived difference in colour as the same distance does in the blue part of the diagram. In 1942, David MacAdam did a series of colour matching experiments to determine the just noticeable differences (JND) of chromaticity (31). Although his results can be disputed as he only used one observer for the matching experiments, MacAdam shows the resulting JND plotted in the x, y colour space are in fact ellipses with widely varying size depending on their location in the chromaticity diagram (Fig. 2.15).

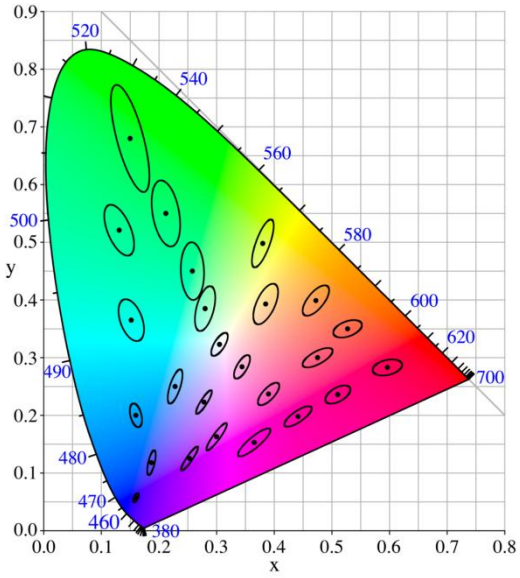

Fig. 2.15. MacAdam ellipses (10 times enlarged) plotted in the x, y colour space show that perceivable colour differences and geometrical distances between colour coordinates depend on the location in the diagram itself.

Several newer colour spaces attempt to represent colours in a more perceptual uniform way:

- CIE u´,v´,Y

The CIE u´, v´, Y colour space is a transformed 1931 CIE XYZ colour space that aims to provide a more perceptual uniform representation of the visible colour gamut. CIE XYZ coordinates can be translated in to the u´,v´ system using the formula below.

$$u' = \frac{4X}{(X+15y+3Z)} \quad \text{(Eq. 2.29)}$$

$$y' = \frac{9Y}{(X+15Y+3Z)} \quad \text{(Eq. 2.30)}$$

While the extreme perceptual inhomogeneities of the x, y colour space have been reduced it is far from perceptually uniform. The uniformity of the chromaticity coordinates is improved, but the uniformity of the lightness scale is not. A linear increase in the Y tristimulus value does not correspond to a perceived linear increase in brightness.

- CIELUV

The CIE 1976 (L*, u*, v*) colour space further improves the CIE u′, v′, Y system by making the lightness scale uniform.

$$L^* = 116\left(\frac{Y}{Y_n}\right)^{\frac{1}{3}} - 16 \text{ if } \frac{Y}{Y_n} > 0.008856 \quad \text{(Eq. 2.31)}$$

$$L^* = 903.3\left(\frac{Y}{Y_n}\right) \text{ if } \quad \frac{Y}{Y_n} \leq 0.008856$$

$$u^* = 13L^*(u' - u_n') \quad \text{(Eq. 2.32)}$$

$$v^* = 13L^*(v' - v_n') \quad \text{(Eq. 2.33)}$$

With u', v' and Y the tristimulus values of the object to be evaluated and u_n', v_n' and Y_n the tristimulus values of a perfect diffuser under a reference illuminant that defines the white point.

Both the CIELUV and CIE u′, v′ colour models are represented in the two-dimensional (u′, v′) chromaticity diagram shown in Fig. 2.16.

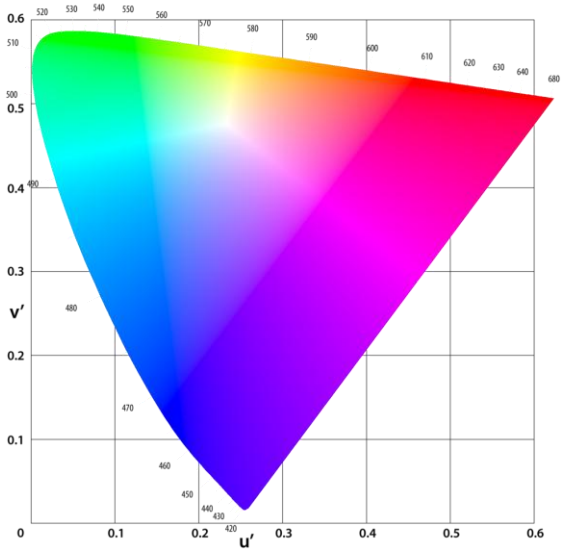

Fig. 2.16. The CIE (u´, v´) chromaticity diagram representative for the CIE u´, v´ and CIELUV colour models.

- CIELAB

At the same time of the introduction of the CIELUV colour model, the CIE presented CIE (L*, a*, b*). The LAB colour space is based on a lightness component, L*, and 2 colour-opponent coordinates: a* and b*. Similar to the cone responses, the a* coordinate represents a green (negative a* values) to magenta (positive a* values) variation while the b* coordinate represents a blue (negative b* values) to yellow (positive b* values) axis. The three coordinates can be calculated using the following transformations

$$L^* = 116\left(\frac{Y}{Y_n}\right)^{\frac{1}{3}} - 16 \text{ if } \frac{Y}{Y_n} > 0.008856 \quad \text{(Eq. 2.34)}$$

$$L^* = 903.3\left(\frac{Y}{Y_n}\right) \text{ if } \quad \frac{Y}{Y_n} \leq 0.008856$$

$$a^* = 500\left\{\left(\frac{X}{X_n}\right)^{\frac{1}{3}} - \left(\frac{Y}{Y_n}\right)^{\frac{1}{3}}\right\} \quad \text{(Eq. 2.35)}$$

$$b^* = 200\left\{\left(\frac{Y}{Y_n}\right)^{\frac{1}{3}} - \left(\frac{Z}{Z_n}\right)^{\frac{1}{3}}\right\} \quad \text{(Eq. 2.36)}$$

With X, Y and Z representing the tristimulus values of the object to be evaluated while X_n, Y_n and Z_n are the XYZ tristimulus values of a perfect reflecting diffuser under the reference white point.

- CIECAM02

Since the introduction of more perceptually linear colour models and spaces, the CIE has strived to incorporate more colour appearance phenomena in to their models. The CIELUV and CIELAB models formed the basis to more complex colour appearance models such as CIECAM02.

CIECAM02 provides a means to transform tristimulus coordinates into a colour system that takes viewing conditions and perceptual attributes into account (32, 33). While a full study of the model is outside the scope of this thesis, the main attributes are discussed below.

There are two main parts in the model:

- A chromatic adaptation transform (CAT) ensures correct white-balancing as the eye perceives a white surface as white under a large range of illumination spectra
- A set of equations to calculate the effects of a number of perceptual phenomena

The first step in CIECAM02 model is obtaining the R, G and B cone responses. A slightly modified XYZ to RGB transformation helps the following chromatic adaptation predictions.

While both CIELUV and CIELAB have a basic chromatic adaptation scheme (and many more complex CATs have been developed later on), CIECAM goes back to the simple Von Kries chromatic adaptation. Von Kries states that colour constancy, or the ability of the visual system to adapt to different illumination spectra while keeping the perceived colour of objects the same, is achieved by adapting the gains of the individual cone responses. A factor *D* sets the desired degree of chromatic adaptation based on guidelines provided by the CIE.

At this point, the conditions surrounding the 2 º stimulus (10 º background) are taken in to account. There are three surround conditions defined by the CIE: *Average*, *Dim* or *Dark*. The chosen surround condition depends on the luminance ratio between the reference white measured in the surround field to the display area (which is the 2-degree stimulus plus the 10-degree background), the degree of adaptation, the impact of the surrounding and the chromatic induction factor.

The resulting chromatically adapted R, G and B coordinates are then transformed to the Hunt-Pointer-Estévez colour space and a luminance level adaptation factor is brought in to the equation.

Finally, the colour coordinates are used to calculate the CIECAM02 appearance correlates

- Brightness
- Lightness
- Colourfulness
- Chroma
- Hue

The CIECAM02 input parameters and guidelines to use them are largely based on empirical data, which makes the CAM relatively complicated to use, but does provide a standard that models the workings of the human visual system much more accurately than previous colour systems could ever do.

2.7.2 Metamerism

Two or more stimuli having identical chromaticity coordinates, but a different spectrum, are called metamers. The stimuli can be either light sources or objects reflecting or transmitting a certain illumination spectrum.

Metamerism exist because the retinal cones are tristimulus receptors, which means that for one set of chromaticity coordinates there are an infinite number of matching spectra.

Metameric failure occurs when a change of the *illuminant spectrum*, the *observer*, the *field-of-view* or the *angle-of-view* causes a change in colour coordinates.

- Illuminant metameric failure

Occurs when a change in the illuminant causes a difference in chromaticity between two items viewed under that light source

- Observer metameric failure

Observer metameric failure is caused by the difference in the visual system between 2 observers (typically colour blindness versus normal vision).

- Field-of-view metameric failure

When a stimulus is viewed with the central fovea, due to a difference in concentration in cones, the colour sensation is slightly different than when the same stimulus is registered outside the central fovean region of the retina.

- Angle-of-view metameric failure

Depending on the gloss and other gonio-dependant characteristics of certain materials, the chromaticity changes depending on the viewing angle.

2.7.3 The correlated colour temperature

An ideal black body emits a specific spectrum that depends on its temperature (chapter 2.2). This temperature dependant spectrum results in a very specific set of chromaticity coordinates, which means its behaviour can be represented by a single variable: the *colour temperature (CT in K)*. Low CTs (< 3000 K) are equal to warm, yellow tinted light while high CTs (> 6500 K) are represented by blue-tinted colours.

Colour temperature is defined only for light sources that emit a spectrum resulting in chromaticity coordinates equal to the chromaticity coordinates of a black body emitter emitting at the same temperature. For light sources that emit a spectrum resulting a chromaticity coordinates near but not equal to the chromaticity of a black body, the *correlated colour temperature (CCT in K)* has to be used. For some quasi-black body light sources, such as incandescent lamps or other thermal radiators, the actual filament temperature is equal to the colour temperature. Non-black body radiators such as fluorescent light sources and light-emitting diodes (LEDs) have a CCT that has no relation to their actual temperature.

The line connecting the chromaticity coordinates of all black body temperatures, ranging from 0K to ∞, is called the black body locus. As the sun is a near-black body emitter that has a varying CT depending on the time of the day and the atmospheric conditions, our visual system has evolved to perceive light with chromaticities near the black body locus as white light. The CCT is defined by the CIE within a range of chromaticity coordinates called isotherms, located both above and below the black body locus and perpendicular to the black body locus itself (Fig. 2.17).

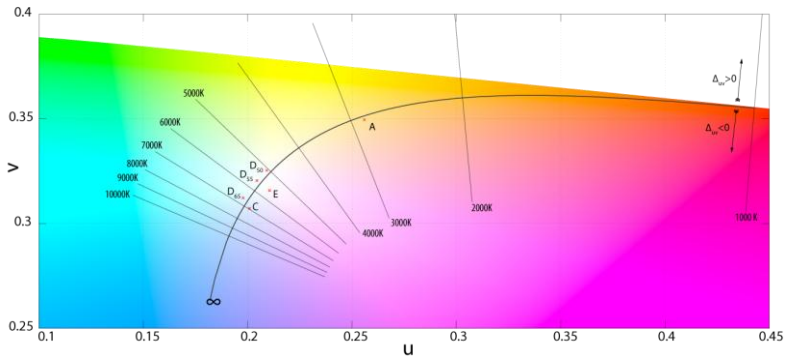

Fig. 2.17. The black body locus with isotherms for a selection of colour temperatures represented in a slice of the CIE 1960 UCS. The letters A to E show the chromaticity coordinates corresponding to a number of CIE standard illuminants.

In practice, not all light that falls within this definition is perceived as being achromatic or neutral white. In 1941 Kruithof showed through psychophysical experiments that, depending on the illuminance levels, only certain CTs are perceived as being pleasant whereas others were regarded as being unnatural or uncomfortable. His data resulted in the famous *Kruithof curve* (Fig. 2.18) that shows the luminance region where a certain CT appears pleasing, reddish or blueish (34).

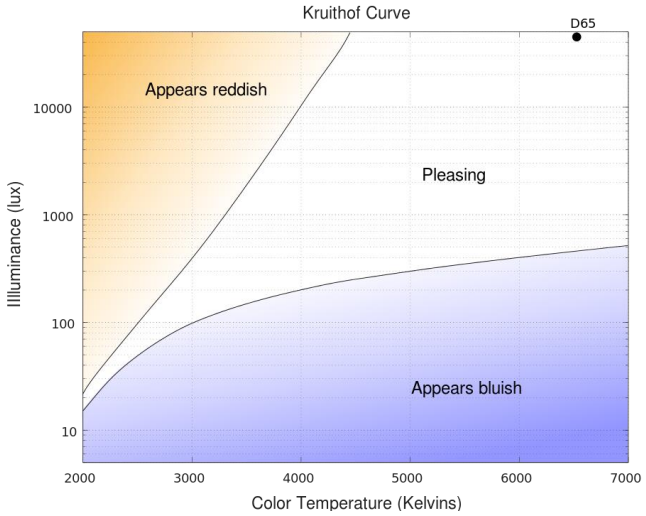

Fig. 2.18. The Kruithof curve showing pleasing CTs in function of the illuminance level.

Under low illuminance levels, light sources with a lower colour temperature are regarded as more pleasing while sources with higher colour temperatures appear bluish. At the same time low CT sources appear reddish under high illuminance levels. The results of his experiments are a direct consequence of the increasing sensitivity of the visual system to blue light with decreasing luminance levels (Purkinje effect).

While Kruithof showed that CT and illuminance levels have a definite impact on the perception of white light, more recent experiments show that also the deviation from the black body locus itself has its effects. Freyssinnier et al. conducted experiments to explore the effects of light sources not located on the black body and the achromatic sensation of white light. He subjected 20 people to a psychovisual

test carried out in a dark environment with each subject looking into a neutral grey viewing booth. Freyssinnier concluded that, under a constant illuminance of 300 lux, sources with a CCT below 4000 K are perceived as achromatic white when their chromaticity coordinates fall slightly below the black body locus (slight magenta tint). The opposite is true for sources with a CCT higher than 4000 K (a slight green tint is preferred) (35).

The results agree well with our evolutionary adaptation to natural light sources: the chromaticity of daylight is located slightly above the black body locus. There are, however, two fundamental issues with the setup and execution of the experiment.

- Freyssinier´s experiment takes place in a dark room with subjects focusing in to a viewing booth that has a very homogeneous illumination. This means that the luminance contrast between the central fovean region of the eye and the background is very small while the contrast between the background and the completely dark surroundings of the viewing area is very large. This is hardly a realistic setting.
- The light sources used to generate stimuli of different CCTs had significant differences in their spectra (a mix of fluorescent and incandescent sources was used).

2.7.4 Colour rendering

The colour rendering properties of a light source describe the effect of an illumination spectrum on the *perceived* colours of objects. Perceived is the keyword here as colours can look very appealing and pleasant but not resemble the real colour of an object. At the same time the object´s colour might be rendered very accurately when compared to a reference light source such as the sun, but still look unpleasant.

Colour rendering is a key property of light sources and a hot topic of debate in recent years. This chapter will give a detailed definition, an overview of measurement and characterisation methods and a discussion of the state of the art and possible future improvements.

2.7.4.1 Fidelity, preference and discrimination

The colour of an object seen by our eyes is the result of a complex interaction between the spectrum that illuminates that object, the material properties of that object and the registration of the stimulus from that object by our visual system. Assuming that we know the response of our visual system and that the object has stable properties, the colour we perceive from the object varies with the illumination spectrum.

The colour rendering properties of a light source can be described by a preference, fidelity or discrimination index. Preference indices are based on the results of a number of psychovisual experiments in which people give an opinion on the rendering of colours by a certain illumination spectrum while a fidelity index compares the colour rendering of objects illuminated by the source-

under-test to the colour rendering of the same object under a reference spectrum. A discrimination based index measures the capability of an illuminant to allow for an observer to distinguish between a variety of colours when viewed simultaneously.

2.7.4.2 The General Colour Rendering Index

After the introduction of gas discharge lamps and other non-thermal radiators in the middle of the 20th century (chapter 3.1), people noticed that although white and grey objects appeared identical, coloured objects changed their appearance depending on the chosen illumination technology. The CIE set up a committee to define a measurement and characterization method for the colour rendering properties of light sources: the *General Colour Rendering Index* (CRI R_a).

The R_a is based on the colorimetric comparison of a number of samples from the Munsell Colour System with a standard reference light source. The detailed test method is explained below.

1. Measure the chromaticity coordinates of the source-under-test using the 2-degree standard observer and CIE 1960 UCS chromaticity diagram. The u, v coordinates are obtained from the XYZ tristimulus values

$$u = \frac{4X}{(X+15Y+3Z)} \quad \text{(Eq. 2.37)}$$

$$v = \frac{6Y}{(X+15Y+3Z)} \quad \text{(Eq. 2.38)}$$

2. Calculate the CCT of the source-under-test. CCT is valid only for white light sources defined by the CIE as having a chromaticity distance (DC) of less than 5.4 x 10^{-3} to the planckian locus.

$$DC = \sqrt{\left(u_{s,r} - u_{s,t}\right)^2 + \left(v_{s,r} - v_{s,t}\right)^2} \quad \text{(Eq. 2.39)}$$

With $u_{s,t}, v_{s,t}$ the chromaticity coordinates of the source-under-test and $u_{s,r}, v_{s,r}$ the chromaticity coordinates of the reference source.

3. Assign a reference source: for source-under-test-CCTs below 5000 K, a black body source has to be used. When the source-under-test has a CCT > 5000 K, a CIE daylight illuminant is used (36).
4. Obtain the chromaticity coordinates U*, V* and W* of the samples defined by the CIE illuminated by the source-under-test, using the 2-degree standard observer method and CIE 1964 UCS colour space.

$$W^* = 25Y^{\frac{1}{3}} - 17 \quad \text{(Eq. 2.40)}$$

$$U^* = 13W^*(u - u_n) \quad \text{(Eq. 2.41)}$$

$$V^* = 13W^*(v - v_n) \quad \text{(Eq. 2.42)}$$

8 samples selected from the Munsell Book of Colors serve as the test samples to evaluate the light source under test (Fig. 29). Their spectral reflectances represent low-saturation colours evenly spread over the hue circle.

5. Usually the chromaticity coordinates of the source-under-test and the reference source are not an exact match. A Von Kries chromatic adaptation that corrects both the chromaticity coordinates of the source-under-test (u_{st}, v_{st}) and the chromaticity coordinates of the samples (u_i, v_i) illuminated by that source aims to solve this.

$$u_{s,t}{}' = u_{s,r} \quad \text{(Eq. 2.43)}$$

$$v_{s,t}{}' = v_{s,r} \quad \text{(Eq. 2.44)}$$

$$u_{i,t}{}' = \frac{10.872 + \frac{0.404 c_{s,r} c_{i,t}}{c_{s,t}} - \frac{(4 d_{s,r} d_{i,t})}{d_{s,t}}}{16.518 + \frac{1.481 c_{s,r} c_{i,t}}{c_{s,t}} - \frac{d_{s,r} d_{i,t}}{d_{s,t}}} \quad \text{(Eq. 2.45)}$$

$$v_{i,t}{}' = \frac{5.520}{16.518 + \frac{1.481 c_{s,r} c_{i,t}}{c_{s,t}} - \frac{d_{s,r} d_{i,t}}{d_{s,t}}} \quad \text{(Eq. 2.46)}$$

With $u_{s,t}{}'$ and $v_{s,t}{}'$the adapted chromaticity coordinates of the source-under-test, $u_{s,r}$ and $v_{s,r}$ the chromaticity coordinates of the reference illuminant and $u_i{}'$ and $v_i{}'$ the adapted chromaticity coordinates of the test samples.

The c and d coefficients are calculated using the formula below

$$c = \frac{4 - u - 10v}{v} \quad \text{(Eq. 2.46)}$$

$$d = \frac{1.708v + 0.404 - 1.481u}{v} \quad \text{(Eq. 2.47)}$$

Substituting the above values in to Eq. 2.40, 2.41 and 2.42 results in the U*, V*, W* coordinates of both the chromatically adapted reference samples and test samples illuminated by, respectively, the chromatically adapted reference light source and light source under test.

$$W_{i,r}{}^* = 25(Y_{i,r})^{\frac{1}{3}} - 17 \quad \text{(Eq. 2.43)}$$

$$U_{i,r}{}^* = 13W_{i,r}{}^*\left(u_{i,r} - u_r\right) \quad \text{(Eq. 2.44)}$$

$$V_{i,r}{}^* = 13W_{i,r}{}^*(v_{i,r} - v_r) \quad \text{(Eq. 2.45)}$$

$$W_{i,t}{}^* = 25(Y_{i,t})^{\frac{1}{3}} - 17 \quad \text{(Eq. 2.46)}$$

$$U_{i,t}{}^{*} = 13W_{i,t}{}^{*}\left(u_{i,t}{}' - u_{t}{}'\right) \quad \text{(Eq. 2.47)}$$

$$V_{i,t}{}^{*} = 13W_{i,t}{}^{*}\left(v_{i,t}{}' - v_{t}{}'\right) \quad \text{(Eq. 2.48)}$$

6. Finally, the individual colour differences in the CIE 1964 UCS are calculated as follows

$$\Delta E_i = \sqrt{\left\{\left(U_{i,r}{}^{*} - U_{i,t}{}^{*}\right)^2 + \left(V_{i,r}{}^{*} - V_{i,t}{}^{*}\right)^2 + \left(W_{i,r}{}^{*} - W_{i,t}{}^{*}\right)^2\right\}} \quad \text{(Eq. 2.49)}$$

With the colour rendering index for each sample R_i equal to

$$R_i = 100 - 4.6\Delta E_i \quad \text{(Eq. 2.50)}$$

And the general colour rendering index R_a

$$\boldsymbol{R_a} = \frac{\sum_{i=1}^{8} \boldsymbol{R_i}}{\boldsymbol{8}} \quad \text{(Eq. 2.51)}$$

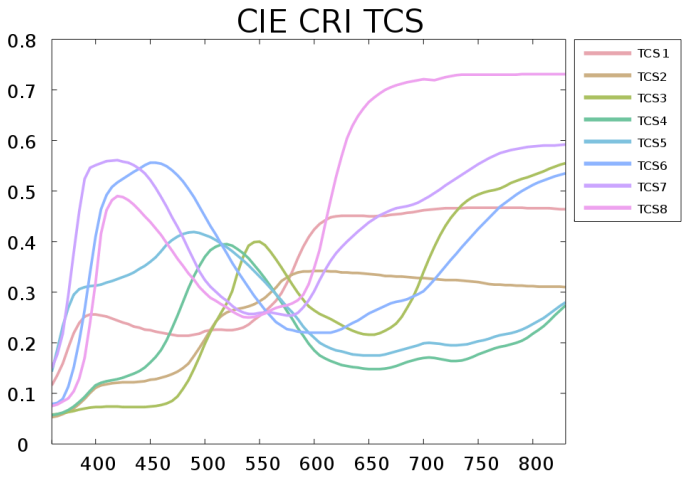

Fig. 2.19. The 8 reflectance spectra used to calculate the General Colour Rendering Index

Besides the 8 reflectance spectra to calculate the general colour rendering index (Fig. 2.19), there are 7 more samples. Test colours 9-12 represent saturated colours with sample 9 being an important indicator of how a light source renders saturated red colours. Sample 14 and 15 represents the skin colour of, respectively, a white Caucasian and a female white Asian person while sample 13 shows the colour of a typical green leaf.

2.7.4.3 Limitations of the CRI-R_a

Although the CIE CRI is a widely used and accepted metric to characterize the colour rendering properties of light sources there are some major deficiencies that spark discussions within working groups of the CIE and lighting companies.

As far back as the early 1980's, just 15 years after the introduction of the CIE CRI-R_a, its meaningfulness was questioned (37). Indeed, the CRI method has a number of shortcomings which are especially pronounced when narrow-band illumination spectra are involved (38).

- The use of an infinite number of reference illuminants: The colour appearance of low and high CCT reference illuminants is different (e.g. CIE standard illuminant D65 and illuminant A) although the present method categorises both illuminants as perfect.
- The use of a limited number of test samples: using different sets of samples that are metameric to each other, one might obtain a different ordering of the sources.
- The use of an outdated colour space: the CIE 1964 UCS is far from equidistant and has been outdated for decades.

Royer et al. outlines a number of other problems (39):

- The CRI – R_a is a fidelity metric only
- All 8 test samples have a low colour saturation
- The results of the individual R_i metrics are averaged to a single number
- The CRI – R_a is applicable only to sources with chromaticities near the black body locus
- The CRI – R_a uses an outdated Von Kries chromatic adaptation formula

In 2006, the CIE set-up a dedicated research group, Technical Committee (TC) 1-69 with the aim to investigate the shortcomings and propose new methods to characterize the colour rendering of light sources. TC 1-69 came to a close in 2012 without any conclusive recommendation for a new colour rendering metric, but the CIE agreed that there was a need to make a clear difference between measuring colour fidelity and colour preference. Two new TCs continue the work started in TC 1-69: TC 1-90 "colour fidelity index" and TC 1-91 "new method for evaluating the colour quality of white light sources" (colour fidelity methods excluded).

2.7.4.4 Alternative colour rendering metrics

Over the years a rather large number of alternative colour rendering metrics have come and gone. Some of them specifically focused on colour fidelity, while other incorporated preference or discrimination metrics. An overview of the most important ones is given below.

- Flattery Index (R_f) – 1967 (40)

The flattery Index is based on the CRI-R_a but uses 10 test samples with shifted chromaticity coordinates. The shift in chromaticity coordinates is based on the results of a psychovisual test on preferred and remembered colours of common items, including complexions, food and foliage (Table 2.1). A weight percentage is given to each of these test samples (Table 2.2).

Table 2.1. Chromaticity coordinates of actual colours of natural objects compared to the preferred or remembered ones.

Natural Object	Chromaticity Coordinates				Differences (Preferred or remembered minus actual)		
	x	y	u	v	Δu	Δv	$[(\Delta u)^2 + (\Delta v)^2]^{1/2}$
Average Caucasian complexion[6]	0.377	0.342	0.237	0.323			
Preferred[2]	.441	.379	.265	.341	+ 0.028	+ 0.018	0.033
Complexion (average of 8 women)							
No cosmetics[6]	.373	.341	.236	.322			
With cosmetics[6]	.395	.345	.249	.326	+ 0.013	+ 0.004	.014
Butter							
Actual[2]	.403	.415	.225	.347			
Preferred[2]	.375	.386	.218	.336	− 0.007	− 0.001	.013
Foliage[7]							
Actual	.325	.369	.192	.327			
Remembered	.266	.368	.155	.321	− 0.037	− 0.006	.037
Green grass							
Actual[7]	.346	.415	.190	.342			
Remembered[7]	.248	.415	.132	.333	− 0.058	− 0.009	.058
Remembered[3]	.305	.438	.160	.344	− 0'030	+ 0.002	.030

Table 2.2. Identification of the 10 test samples used in the definition of the flattery index with their respective weights.

Test Sample	Munsell Notation	Chromaticity Differences			Weight Per Cent,
		Δu	Δv	$[\Delta u^2 + \Delta v^2]^{1/2}$	
1	7.5R 6/4	+ 0.010	+ 0.004	0.011	5
2	5Y 6/4	0.000	0.000	0.000	15
3	5GY 6/8	− 0.010	+ 0.004	0.011	5
4	2.5G 6/6	− 0.010	+ 0.005	0.011	5
5	10BG 6/4	− 0.010	− 0.002	0.010	5
6	5PB 6/8	− 0.006	− 0.010	0.012	5
7	2.5P 6/8	+ 0.004	− 0.010	0.011	5
8	10P 6/8	+ 0.010	− 0.005	0.011	5
13	5YR 8/4	+ 0.020	+ 0.011	0.023	35
14	5GY 4/4	− 0.020	0.000	0.020	15
			Weighted Average	0.01490	

The flattery index was not updated and is not recommended to be used in its current form, although the basic idea led to later developments such as the memory colour rendering index (MCRI).

- Colour Discrimination Index (CDI) – 1972 (41)

The CDI is a gamut based colour discrimination metric which quantifies the gamut area covered by the test samples of the CRI-R_a illuminated by the source-under-test. The CDI is normalized to the gamut area covered when the samples are illuminated with CIE illuminant C.

The CDI combines both colour discrimination and colour rendering in one metric. The idea was later adapted for the Gamut Area Index, which is recommended to be used in conjunction with the CRI-R_a as a combined fidelity – discrimination indicator.

- Colour Rendering Capacity (CRC) – 1984 (42)

The CRC is a metric that shows how many colours a given spectral power distribution can reproduce, presented as a colour solid in the CIE 1960 UCS with an update to the CIELUV colour space in 1993 (Fig. 2.20). The CRC´s only input parameter is the spectrum of the illuminants, no test samples are required. The volume of the colour solid can be regarded as an indicator for how colourful a certain spectrum renders a scene.

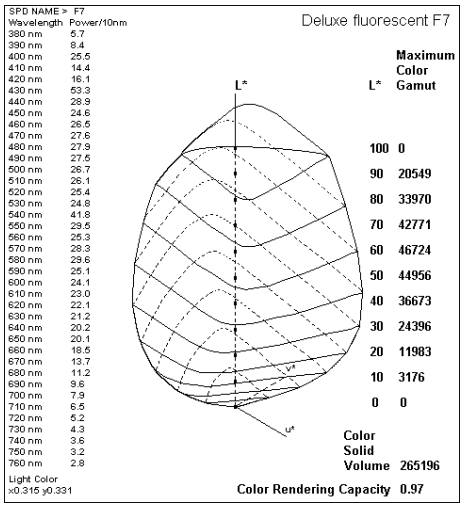

Fig. 2.20. CRC colour solid formed by CIE illuminant F7 (deluxe cool-white fluorescent)

- Full Spectrum Colour Index (FSCI) – 2004 (43)

The FSCI is a purely mathematical metric based on the squared deviations between the cumulative spectral power distributions of the test and reference light source. The reference light source is, in this case, and equal energy spectrum (EES) or “full spectrum” that contains all visible wavelengths at the same radiant power (380 – 730 nm). Any illumination spectrum differing from the ideal EES will have non-ideal colour fidelity. No test samples are used. Interesting to note is that the R_a of an equal energy spectrum is not 100, but just 95.

- Feeling of Contrast Index (FCI) – 2007 (44)

The FCI estimates the “feeling of contrast” between object colours under a certain illuminant using four saturated Munsell samples: red (5R4/12), yellow (5Y8.2/10), green (5.5G5/8) and blue (4.5PB3.2/6). The gamut area of the samples illuminated by the test source and reference source (D65) is then computed in the CIELAB colour space. Chromatic adaptation is done using CIECAT94.

- Rank-Order Colour Rendering Index (RCRI) – 2009 (45)

The RCRI was introduced by Bodrogi et al. to allow non-expert users to assess the equality of colour rendering properties of a test light source or to assess the ranking among different test light sources. Bodrogi used 17 colour samples: 12 from the Macbeth Colour Checker Chart and 5 from the NIST colour set. Visual ranking experiments (1: excellent to 5: very bad) result in a variable *R,* used later in the calculation of the metric. For a given test source, the colour differences between reference and test source are calculated in the CIECAM02 UCS. The index was then derived from the prediction of the ranking category corresponding to a computed colour difference.

- Memory Colour Rendering Index (MCRI) – 2010 (46, 47)

The MCRI takes a different approach on characterizing the colour quality parameters of an illuminant. While most colour rendering metrics compare the test source to a reference, the MCRI references to memory colours: the colour one remembers (in long-term memory) a familiar object to have. A special diffusing tunnel, illuminated by an array of RGB LEDs, was constructed to change the apparent hue of a familiar object, while the back surface of the viewing space was illuminated with an adaptation white having a CCT of 5600 K (Fig. 2.21).

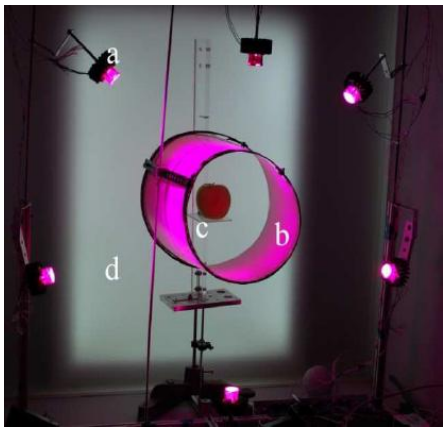

Fig. 2.21. Experimental setup to change apparent hue of objects. (a) RGB LEDs, (b) white background illumination, (c) object, (d) diffusing tunnel.

For each of the 10 selected objects, ranging from green fruits to a blue Smurf figurine and a neutral grey sphere, a colour solid was created by changing the RGB values of the main illuminant. Observers were then asked to rate the similarity of the perceived object to their idea of how the object should look like on a scale from 1: very poor to 5: very good. The pooled ratings were modelled in the IPT uniform colour space with tristimulus values (CIE 10-degree observer) of the objects converted to a D65 white point using CIECAT02 (48). For each object a similarity function compares the objects measured chromaticity coordinates with the associated memory colour. A geometric mean of the ten resulting values describes the general degree of memory colour similarity.

Validation experiments confirmed that the MCRI correlates visually very well in terms of object preference, attractiveness, fidelity and naturalness while the correlation was poor for object vividness.

- Colour Quality Scale (CQS) – 2012 (49)

Developed in the NIST by Ohno et al., the CQS´s primary aim is to alleviate the deficiencies in the CRI-R_a. The set of test samples is different than the set the CRI-R_a uses: instead of 8 samples with low chroma, the CQS uses 15 Munsell samples that span the full hue circle with even spacing and very high chroma. The obsolete 1964 UCS is replaced by the 1976 CIELAB colour space. No change in the CAT has been implemented: the CQS continues to use the Von Kries chromatic adaptation method.

Perhaps the most important difference, when compared to the CRI-R_a, is the way of penalizing colour differences. While the CRI-R_a lowers the score for shifts in hue, chroma and lightness, the CQS does not penalize an increase in chroma of a particular Munsell test sample. Increasing chroma is generally regarded as a positive feature that helps colour discrimination (but of course decreases absolute colour fidelity). CRI-R_a rates all reference sources perfect (100), independent of the CCT. The CQS introduces a multiplication factor that lowers the CQS value when the CCT is lower than 3500 K or higher than 6500K.

The CQS is heavily supported by the NIST and is one of the leading players in the competition to replace the CRI-R_a.

- Colour Rendering Map (CRM) – 2012 (50)

The Colour Rendering Map, developed in the Institute for Energy Research of Catalonia (IREC), aims to alleviate one of the major problems of the CRI-R_a: the representation of a very complex phenomenon in one single number. While the majority of the colour fidelity metrics averages a number of individual colour difference calculations into a single number that aims to express the overall colour fidelity of a light source, the CRM shows, in a graphical representation, the performance of the test light source for each of the test samples. Instead of using only 8 test samples, the CRM uses the reflectance spectra of 1269 matte test samples of the Munsell Book of Colors. The colour differences between the samples illuminated by the chromatically adapted reference and test source (Von Kries CAT), calculated using the same methods as the CRI-R_a, are then plotted in the 1932 CIE x, y colour space. The resulting gamut shows the full collection of colour coded test samples.

- CRI2012 Colour Rendering Index (nCRI) – 2012 (51)

The CIE-R_a has often been criticized for having rather poor correlation with visual perception, especially for narrowband light sources. On the other hand, the industry is reluctant to switch over to a completely new metric. The CRI2012 or nCRI aims to improve the major issues of the CRI-R_a while at the same time leaving the main attributes of the old metric unchanged.

    - The reference illuminant is identical to the one used in the CRI-R_a
    - A new set of test samples: the 8 Munsell samples of the CRI-R_a are replaced with 2 new samples sets. The HL17 set, containing 17 artificially generated reflectance spectra uniformly spread over the spectrum to calculate a general CRI2012 index and the real210 set containing 210 real-life reflectance spectra including 90 low colour constancy, 90 high colour constancy samples and 30 artists colours + skin tones to

provide specific hue information. As an option, the Leeds1000 test colour set can be used as well.

- The XYZ tristimulus values are calculated using the CIE 10-degree observer
- The CAM02 UCS is used with the following CIECAM02 viewing condition parameters:
  - L_A = 100 cd/m^2
  - Y_b = 20
  - F = 1.0
  - D = 1.0
  - C = 0.69
  - N_c = 1.0
- Only the *root mean square* (*RMS)* value of the colour differences of the HL17 set are used to determine the CRI-$R_{a,2012}$, the other test samples are only used to provide extra information or as a basis for special colour rendering indices.
- The average of the $R_{a,2012}$ of the CIE illuminants F1 to F12 is set equal to the standard CRI-R_a.

The nCRI, however, also has a few shortcomings:

- The nCRI results in lower colour fidelity scores than the CRI-R_a for triphosphor fluorescent lamps with a CCT ≤ 4000 K. This particular group of fluorescent lamps is one of the most common light sources and a lower CRI number will not be accepted by lamp manufacturers. The likely cause for this is the deep red test samples of the HL17 set (A. Tsukitani, 2013)
- The test sample set lacks test colours in magenta hues, as magenta does not occur in the pure spectral reflectance spectra generated for the artificial HL17 set.

- Recent developments in TC 1-90

The CIE TC 1-90, successor of TC 1-69, is a study group that focuses on developing a new colour fidelity metric. The last meeting, held in Manchester, UK in July 2015, came to an end with the proposal to support a new colour rendering metric developed by the Illumination Engineering Society of North America (IES) (L. Whitehead).

The *IES metric* builds upon the foundations laid out by the CRI2012, but introduces a number of significant changes (A. David).

- As in the CRI2012, the CAM02 UCS and 1964 10-degree colour matching functions are used.

- An updated sample set consisting of 99 test samples selected from a database of 105 000 samples measured from real-world objects is proposed. The test samples are uniformly distributed in the CAM02 UCS and their reflectance spectra have uniform spectral sensitivities.

- David et al. propose to eliminate the sudden jump from black body to daylight reference illuminant at a CCT of 5000K and introduce a gradual changeover. Doing so will introduce issues

with characterizing known reference illuminant simulators, such as CIE D50, an important standard in the printing industry.

- Several outputs: colour fidelity (R_f), special indices (R_i), a colour distortion map, a colour gamut metric, etc.

While the IES metric has fairly comparable results with CRI-R_a for smooth spectra, discontinues spectra results in significant lower scores. This could be a problem for fluorescent lamps, and will influence the acceptance of the metric by the lighting industry. A scaling factor has been proposed to compensate for these differences.

Opponents of the IES colour rendering index argue that a new fidelity index is not necessarily better than the well-established CRI-R_a and that it might be better to extend the R_a with a colour saturation icon (K. Teunissen).

Comparisons between the CRI-R_a and the IES-R_f show that the selection of test samples is absolutely critical to not introduce any bias. The 99 test samples of the IES CRI, as well as the HL17 set used for CRI2012 has been shown to have excellent correlation with subjective appearance (Tsukitani et al.). This could mean that a reduced version of the IES sample set is equally valid to accurately characterise light sources.

2.8 Summary and conclusions

The visible part of the electromagnetic spectrum spans a wavelength range from 380 to 750 nm and contains all colours, including shades of white that the human visual system can distinguish. Human vision starts with the photoreceptors on the retina where the three different cones determine the eye's spectral response and sensitivity curves. Besides the cones, there are two other photoreceptors: rods enable monochromatic vision in near-dark conditions and ipRGCs play a major role in the regulation of the circadian system. Over the years a large number of colour models tried to mathematically represent the complex interaction between the different parts of the visual system. New CAM models incorporate, besides the central viewing area, also peripheral viewing conditions resulting in a more accurate human vision model. With the increasing popularity of narrow band (LED) light sources, colour rendering is a once again a popular discussion topic. TC 1-90 of the CIE recently came to an agreement to support the EIS metric, a colour fidelity indicator that uses a new reflection sample set, the CAM02 UCS and 1964 10-degree observer functions. The result is a more accurate rating, especially for narrowband white light emitters and PC white LEDs.

3. Light sources

The chapter below gives an overview of the most important past and present lighting technologies, discussing their discovery, uses and main electrical and optical characteristics.

Artificial lighting can be divided in four main categories

- Incandescent sources
- Chemical light sources
- Gas discharge lamps
- Solid state light sources

While solid state lighting is gaining traction, and will without any doubt replace common incandescent and gas discharge lighting in the near future, the current lighting market is very diverse.

3.1 The history of light sources

For billions of years sunlight has been a driving force for life on earth. It provided the necessary energy for plant life to develop and animal life to flourish. Composed mainly of hydrogen and helium, the sun is a giant sphere of hot plasma that is powered by nuclear fusion. With a surface temperature of around 5800 K, it is a perfect black body radiator that provides a very balanced spectrum of electromagnetic radiation.

Sunlight during the day, combined with the occasional lighting storm, forest fire or aurora borealis was the only light source known to men. It was not until circa 500 000 BC that we discovered fire. Homo erectus learned how to generate and control it, not only for safekeeping but also as a light source at night. Open fires, oil candles burning vegetable oils or animal fat and wax candles were the first artificial light sources used by modern day humans.

During coal mining in the 17th century, it was well known that certain gases escaping from the mine were highly flammable, but the benefits and possible uses were ignored until the early 1790s when William Murdoch used gas to light his own house in Cornwall, UK and later a number of public locations nearby (52). Due to its ease of use and clean flame the popularity of gas lighting rose quickly. There was, however, a downside: the amount of light produced by a gas flame was rather limited. Using gaslight to heat another material produced more light than only the flame by itself could. Limelights operated by directing a gas flame towards a piece of calcium oxide, heating it to a temperature of 2500 ºC. Limelight produced white light only by incandescense of lime, which required a relatively high amount of energy. In the mid 19th century gas mantles, made from woven fabric impregnated with a mixture of thorium actinide and cerium oxides, provided a solution. The mantle is heated by a gas flame and emits radiation in the visible part of the spectrum. Gas mantles remained a very important light source until the onset of electric lighting.

At the same time, electricity started to become widespread. One of its first uses was to power the carbon arc lamp, invented by Humphry Davy in the early 1800s. Arc lamps use two carbon electrodes separated by a small air gap. During the ignition phase, the electrodes touch each other and a large current starts to flow. Both electrodes are then slowly separated. The evaporating carbon maintains an electrical arch across the air gap while the ionised carbon vapour and air emits a large amount of broad spectrum light, including high amounts of UV-A, UV-B and UV-C radiation. They were mainly used for lighting large theatres or market places until being faded out with the introduction of the incandescent bulb.

3.2 Incandescent light sources

Incandescence is one of the simplest ways of making light. From burning wood to wax candles: a material is heated to a temperature high enough to emit radiation within the visible spectrum. The same principle is used in incandescent light bulbs where an electric current passes through a resistive filament that rises in temperature until the amount of heat that is radiated away from the filament equals the amount of heat generated by the filament.

- The incandescent light bulb

Around the mid 1850s, several inventors started playing with the idea of passing electricity through a thin filament in order to generate light. Platinum and iridium filaments where heated to incandescence by passing an electric current through them. Joseph Swan and Thomas Edison discovered that carbonised paper or fabric could be used to create a filament that had a considerably longer lifetime than the earlier filaments. Both inventors realised that evacuating the air out of the glass balloon was crucial for the lifetime of the light bulb. Edison, who had access to better vacuum equipment, succeeded in creating the first long-life incandescent light bulb. In 1904, a Hungarian patent was filed for a tungsten filament. Tungsten allowed for a higher filament temperature (resulting in a higher efficacy) and longer lifetimes. Instead of using a vacuum inside the glass bulb, inert gases such as argon or krypton were introduced. Gas-filling increases the lifetime of incandescent light bulbs by preventing evaporative destructing of the filament. This also meant that the filament itself could be operated at higher temperatures, once again increasing its efficacy. The larger the atoms of the gas, the lower the evaporation rate of the filament and the lower the heat conductivity of the gas-fill. Gas-filling does, however, increase heat conduction which slightly lowers the overall efficiency of the lamp.

A typical 100W, 230V incandescent lamp, used extensively until a few years ago, operated its filament at a temperature of 2850 K while generating 1340 lm for 1000 hours[6]. The reason for this relatively poor efficacy is the low operating temperature of the thermal radiator to prevent the tungsten filament from melting (3695 K). Being a true black body radiator, the incandescent lamp has a CRI of 100.

[6] Philips 100W E27 230V A55 CL

More than 15% of the worldwide electricity production is used for artificial lighting. Rising energy costs, depleting resources and environmental concerns have resulted in a controversial near-worldwide phase-out of incandescent bulbs for general lighting purposes. Brazil and Venezuela were the first countries in 2005 to ban incandescent bulbs, followed by the European Union, Switzerland and Australia in 2009. In 2012 Russia started a phase-out plan followed by the USA, Canada and a number of South American and Asian countries in 2014 (53). While new lighting technologies definitely provide higher efficiency values, opponents argue about the high replacement costs, polluting raw materials and poorer light quality of those replacements. Several government initiatives have been put to place with the aim to promote energy saving alternatives, improve manufacturing and (light) quality standards and educate the public (54).

- Halogen lamps

In 1953, Elmer Fridrich of General Electric, discovered that adding trace amounts of a halogen in the gas fill of an incandescent light bulb increased the lifetime dramatically (4000 hours typical). Halogens, such as iodine combine with evaporating tungsten to form WI_2 which dissociates back to tungsten in the high temperature environment of the filament. This called the halogen cycle. Halogen bulbs are usually low voltage devices operated at higher temperatures than normal incandescents, resulting in a higher efficacy of around 17 lm/W[7] and a CT of 3000K. The latest incarnation (and most likely last before halogen lamps will be superseded by superior technologies) is the addition of an infrared thin-film coating on the bulb glass. This coating reflects a large part of the infrared heat radiation back to the filament thereby decreasing losses and increasing the temperature of the filament. Infrared coated (IRC) halogen lamps have a significantly higher efficacy compared to the regular variant: a typical 50W IRC halogen lamp has an efficacy of 24 lm/W[8].

3.3 Gas discharge lamps

A decreasing majority of today´s light sources, from street lighting fixtures to the flash on a photographic camera, are based on gas discharge technologies. Their working principle is based on sending an electrical current through ionised gases. Free electrons, either provided through thermionic emission (hot-cathode lamps) or very high voltage (cold-cathode lamps) are propelled through the plasma by the discharge current and collide with gas atoms. These collisions excite electrons in the gas atoms causing them to jump to a higher energy state. Upon relaxing back to a lower energy state, a photon at a specific wavelength is emitted. Additional elements, such as mercury or rare-earth metals salts can be added to change the lamp´s emission spectrum. A gas discharge has a negative resistance characteristic which means the operating current of the light source is unlimited. An external power supply, also called *ballast* regulates the different operating modes.

[7] Philips Capsuline 50W GY6.35 12V
[8] Osram Halostar Pro 50W 12V GY6.35

Humphry Davy sparked the interest in electric arc lighting after his demonstration of the carbon arc lamp in the early 1800s, but it was Heinrich Geissler, a German glass blower, who invented the first low pressure gas discharge lamp. Geissler constructed glass tubes filled with an inert gas mixture under low pressure that glowed brightly when connected to a high voltage source. The first neon light was born.

3.3.1 Low pressure gas discharge lamps

Low pressure gas discharge lamps consist of a glass tube with a fill gas under low pressure (significantly less than 1 atmosphere). A relatively large distance between the gas molecules results in little interaction. The emitted spectrum consists out of one or more narrow spectral lines associated with the transition of electrons from excited states to ground states in the gas atoms.

3.3.1.1 Neon lamps

The original Geissler tubes were cold-cathode gas discharge or neon lamps. A true neon lamp is a thin glass tube containing a mixture of argon and neon gas, resulting in a typical spectrum rich in red spectral lines. Argon is often added to the gas mixture to reduce the breakdown voltage of the discharge and to increase the operating lifetime of the lamp. Although several gas mixtures can be used to generate different emission spectra, it is common to use a mercury-argon mixture combined with phosphors. The mercury discharge emits a considerable amount of UV light which is converted into visible light by a fluorescent phosphor mix (chapter 3.3.1.3).

Depending on the length of the gas discharge, neon lighting requires very high operating voltages. A special current-limited, high voltage ballast provides 6000 to 15000V at 15 to 60 mA (55). A typical phosphor-based white “neon” lamp achieves a wall-plug efficacy (WPE) of 75 lm/W. Neon lighting is primarily used for decorative signs but a variation, the cold-cathode fluorescent lamp (CCFL) was until 2010 the main light source for backlighting liquid crystal displays (LCD). Nowadays, both the decorative lighting and display industry have switched to LEDs for almost all applications.

3.3.1.2 Low pressure sodium lamps

Low pressure sodium (LPS) lamps were invented in 1920 by Arthur Compton at Westinhouse and commercialised by Philips in the early 1930s. Nowadays they are used as highway illumination in European countries.

The lamp contains a neon-argon gas mixture under very low pressure and solid sodium in sodium-resistant glass discharge tubing containing two tungsten thermionic electrodes. The discharge tube is surrounded by a vacuum and a glass envelope coated with an infrared reflective coating. The vacuum

envelope and heat reflective coating help to maintain the discharge at a temperature high enough to evaporate the metallic sodium, which takes around 5-10 minutes after start-up in normal conditions.

Despite its rather average conversion efficiency (30%), the LPS lamp has one of the highest LERs of any available light source: up to 198 lm/W for a 131 W lamp (56). The reason for this is that the spectral profile consists almost entirely of the yellow 589.0 and 589.6 nm sodium lines located very close to V(λ) cone sensitivity peak. The monochromatic line spectrum also means that the colour rendering properties of LPS lamps are extremely limited. LPS lamps have a rated lifetime of up to 16000 hours.

3.3.1.3 Fluorescent lamps

The invention of the fluorescent lamp was one of the largest breakthroughs in illumination technology. Although the general idea of a gas discharge combined with a wavelength-converter existed since the late 1800s, it was not until 1938 that the first commercial fluorescent lamp was introduced.

The working principle of a fluorescent lamp is identical to that of other low pressure gas discharge lamps. Two thermionic electrodes are preheated to generate a large number of electrons within the tube. A high voltage pulse then ionises the argon gas inside the lamp which in its turn heats up a small amount of mercury (either in liquid state or as an amalgam). The evaporated mercury contributes in the gas discharge and gives of intense amounts of ultraviolet radiation at 253.7 nm. The main difference between pure low pressure discharge devices, such as LPS lamps, is the use of a fluorescent phosphor that converts the invisible, ultraviolet radiation into visible wavelengths. The choice of phosphor in combination with the spectrum of the mercury discharge determines the final lamp spectrum.

A fluorescent lamp, just like any discharge lamp, needs an external device to limit current and provide the correct starting voltage. Due to its immense popularity quite a lot of research and development efforts have been made to improve that ballast. Before the advent of electronic ballasts, the current through the gas discharge was limited by a magnetic or reactive ballast. The inductance of the windings limits the AC current flow through the lamp. When a fluorescent lamp is started, both electrodes are preheated before a high voltage pulse ionises the gas. This can be done manually via a switch or, more commonly, automatically by a *starter.* The starter contains a bimetallic switch inside an argon-filled bulb that, upon switching on the fluorescent lamp, temporarily places both electrodes in series with the supply voltage (Fig. 3.1). This causes the electrodes to heat up and emit electrons. At the same time the bimetallic switch heats up and closes, extinguishing the glow discharge. The lack of a glow discharge in the starter causes the bimetallic switch to open and the current through the filaments is interrupted. This sudden change in current through the filaments and the series connected ballast causes a high voltage peak that starts the lamp. Usually, several cycles are needed for a successful start.

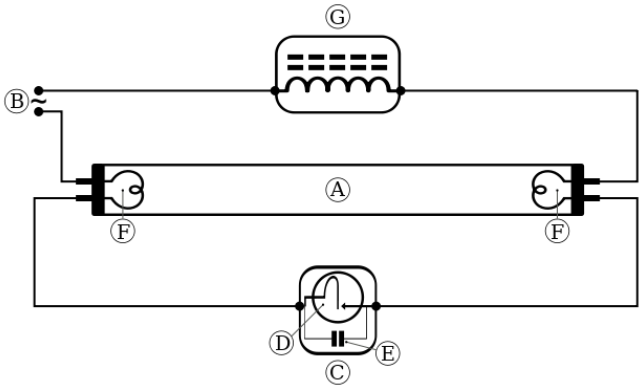

Fig. 3.1. Magnetic ballast and fluorescent preheat circuit showing its different components: fluorescent tube (A), AC supply voltage (B), starter (C), enclosed bimetallic switch (D), filter capacitor (E), lamp electrodes (F), inductive ballast (G)

Nowadays, most magnetic ballasts are replaced by an electronic variant. The size of the inductor within the ballast circuit is directly proportional to the frequency of the AC supply voltage. In Europe, the standard line frequency is 50 Hz which results in a rather large inductor. Electronic ballasts increase the line frequency to 20 KHz or higher so that a much smaller current limiting inductor can be used. The operating modi, including start and ignition sequences are usually controlled by a specialised integrated circuit that changes the oscillation frequency depending on the operating regime of the lamp. Compared to the energy losses in the iron core and windings of a magnetic ballast (between 5 and 25 % of the lamp power), an electronic ballast has an efficiency near 90 %. Furthermore, operating fluorescent lamps at frequencies above 10 KHz results in an additional 9 % increase in efficiency due to a more continues gas ionisation (57). An additional benefit of the high operating frequency is the removal of lamp flicker, a nuisance that is clearly visible when lamps are operated on 50 Hz magnetic ballasts.

Besides the preheat-start method described above, fluorescent lamps can also be started instantaneously by providing a high voltage pulse between the lamp´s electrodes (> 400 V). This starting voltage creates highly energetic ions that, upon impact with the cathode, sputter off emission material which drastically reduces the lifetime of the lamp. Instant-start ballasts, while cheaper than the programmed preheat-start variant are recommended only for near-continuous operating fluorescent lamp luminaires.

Electronic ballasts often have a digital interface, such as DALI, which enables timer and dimmer controls.

The spectral characteristics of fluorescent lamps are determined by the mercury discharge lines (identical for all fluorescent lamps, except quartz-tube germicidal lamps) and the composition of the fluorescent phosphor coating on the inside of the discharge tube. Phosphors are materials that emit light through luminescence caused by inhomogeneities in their crystal structure created by dopants or activators.

Early fluorescent lamps, before the 1940s, used zinc beryllium silicate, a (harmful) phosphor that resulted in white light with reasonable colour rendering properties. Typical 40W fluorescent tubes achieved an efficiency of 35 lm/W. A breakthrough in fluorescent lighting technology (and probably one of the most important lighting related discoveries in history) was the development of the calcium

halophosphate phosphor ($Ca_5(PO_4)_3(F,Cl):Sb^{3+},Mn^{2+}$) by A.H. McKeag et al. in 1942. This phosphor strongly absorbs the ultraviolet mercury line at 253.7 nm and emits a double emission band spectrum peaking in the cyan (Sb^{3+}) and orange (Mn^{2+}) regions of the spectrum (Fig. 3.2). Combined with the mercury lines, the CCT of the fluorescent lamp can be tuned by changing the Sb^{3+} to Mn^{2+} ratio.

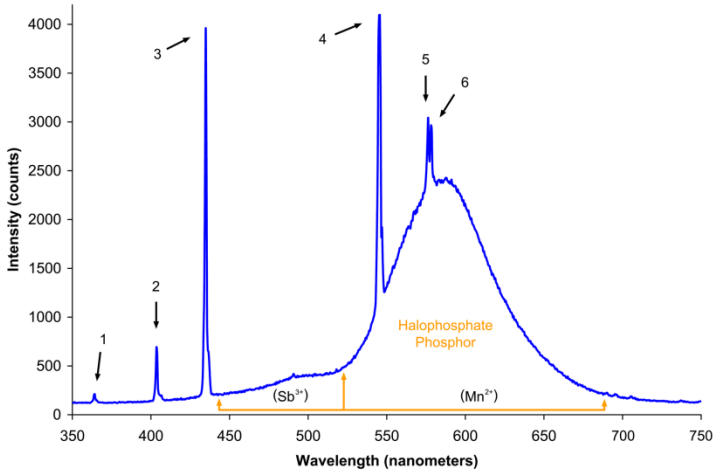

Fig. 3.2. Spectrum of a General Electric halophosphate T12 fluorescent lamp with a CCT of 3000K. The broad-spectrum halophosphate phosphor (yellow arrows) combined with the mercury lines (numbered) results in white light emission.
Source:
https://en.wikipedia.org/wiki/File:Spectrum_of_halophosphate_type_fluorescent_bulb_(f30t12_ww_rs).png#/media/File:Spectrum_of_halophosphate_type_fluorescent_bulb_(f30t12_ww_rs).png

Halophosphate based lamps have a relatively low CRI-R_a (51 for a CCT of 3000K to 76 for a CCT of 6500K) due to the lack of radiated energy in wavelengths longer than 650 nm. The colour rendering properties can be significantly improved by adding a deep-red Sn^{2+} activated strontium orthophosphate phosphor. A typical T-8 halophosphate fluorescent lamp has a lifetime of around 6000 hours, mainly limited by phosphor degradation. During the 1970s a new series of phosphors improved the colour rendering properties, efficiency and operating lifetime of fluorescent lamps dramatically. Eu^{3+} activated Y_2O_3 (611 nm), Tb^{3+} activated $CeMgAl_{11}O_{19}$ (543 nm) and Eu^{2+} activated $BaMgAl_{10}O_{17}$ (450 nm) are three narrowband rare-earth activated phosphors used in today´s triphosphor fluorescent lamps (Fig. 3.3). The emission wavelengths, located near the peak of the tristimulus functions, provide both a high LER and a CRI-R_a between 80 and 85. The subjective appearance is improved as well with especially green and red colours being slightly oversaturated when compared to a black body with an equal colour temperature. Different CCTs (and colours) can be produced by changing the ratio of red, green and blue emitting phosphors. The extraordinary stability and low degradation of rare-earth phosphors results in a lamp life exceeding 20000 hours. Additional phosphors can be added to fill-in gaps in the emission spectrum of the triphosphor mix, increasing the colour rendering (up to CRI-R_a = 98) of multiband lamps at the expense of lamp efficacy.

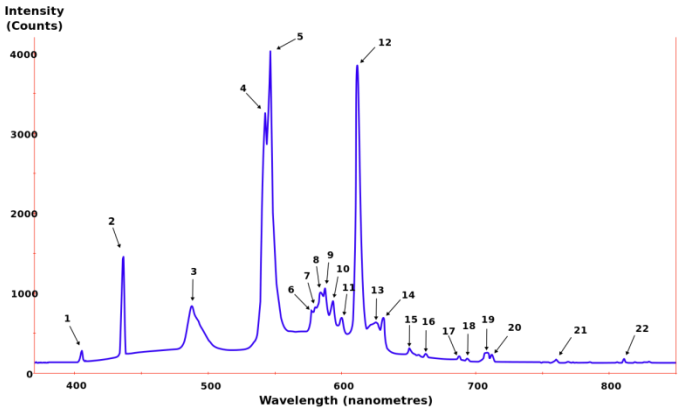

Fig. 3.3: Triphosphor fluorescent lamp showing the main emission peaks.
Source: https://commons.wikimedia.org/wiki/File:Fluorescent_lighting_spectrum_peaks_labelled.svg#/media/File:Fluorescent_lighting_spectrum_peaks_labelled.svg

Because of their stability, higher discharge currents and narrower lamp diameters can be used without any negative side-effects. This led to the development of smaller-diameter lamps such as T-8 (25.8 mm), T-5 (15.9 mm) lamps and narrow diameter compact fluorescent lamps (CFL) where the tube itself is folded or coiled to make a very compact light source. Some compact fluorescent lamps contain miniature electronic ballast and are aimed directly at replacing incandescent lamps. Their wall-plug-efficacy is between 60 and 70 lm/W.

3.3.2 High pressure gas discharge lamps

High pressure gas discharge lamps or high intensity discharge (HID) lamps produce light through a short-arc discharge in a relatively high pressure environment (slightly less than 1 to over 250 times the atmospheric pressure). The emission lines produced when excited electrons fall back to their ground state have a certain spectral width. Low-pressure systems, such as the lamps discussed in the previous chapter, are characterised by narrow spectral emission lines. When the pressure inside the discharge vessel is increased, pressure broadening mechanisms increase the spectral width of the emission lines.

- Collisional broadening

The emission process itself is interrupted by collisions with other particles in a denser gas at higher pressures which increases the uncertainty in the energy emitted.

- Quasistatic pressure broadening

The emitted wavelength is influenced by the presence of other particles causing shifts in the energy levels in the emitting particle.

Because of their intense, short arcs, they are often used for applications where a large amount of precisely controlled light is needed.

3.3.2.1 Mercury vapour lamps

Mercury vapour (MV) lamps ionise a mixture of argon gas and liquid mercury in a quartz tube. The discharge tube is surrounded by an outer envelope to absorb UV radiation and provide thermal insulation. The gas pressure inside the discharge tube depends on the lamp size and lies between 2 and 20 bar.

Upon starting the mercury lamp, the line voltage applied between the 2 outer electrodes is too low to ionise the argon gas. A small auxiliary electrode, connected through a current limiting resistor provides a short discharge path to one of the main electrodes. This initial discharge then generates free electrons to start the main gas discharge. The heat generated by the ionised argon gas evaporates the liquid mercury resulting in a mercury discharge.

The spectrum of a MV lamp consists of the main mercury lines and is rich in ultraviolet wavelengths giving an overall blue-greenish tint to the light. Little pressure broadening means that the colour rendering properties are bad. Later incarnations of mercury vapour lamps had a red phosphor (orthophosphate, halophosphate or yttrium vanadate) coating on the inside of the outer glass bulb which converted the otherwise wasted UV radiation into long wavelengths, greatly improving the colour rendering index. Standard, non-phosphor coated MV lamps have a CRI-R_a of 15 at a CCT of 5700 K while the yttrium vanadate phosphor coated variants can reach a CRI-R_a of 60 at a CCT of 4200 K. The average lamp efficacy of a clear MV lamp reaches 60 lm/W while the phosphor coated variety has a slightly lower efficacy of 50 lm/W. Lamps of lower power typically have lower lamp efficacies as well.

Once very popular and widespread in European cities, the second step of the EU directive 245/2009 (ErP), 347/2010 (ErP) and 2011/64 (RoHS 2) cites that the use of high pressure mercury vapour (and some sodium vapour) lamps is no longer permitted after April 13, 2015. The main reason is the combination of their relatively low efficiency in combination with the high toxicity of metallic mercury (58).

Ultra high pressure mercury lamps (UHP) are manufactured by Philips B.V. These extremely short arc lamps operate at a pressure of 200 atmospheres which results in a broadband spectrum. UHP lamps are used in projection systems where the short arc distance enables an efficient and compact optical system design.

3.3.2.2 High pressure sodium lamps

High pressure sodium (HPS) lamps were developed by General Electric in 1965. The lamp is similar in construction to the high pressure mercury vapour lamp, except for the discharge tube itself. The reason why the development of a high pressure variant of the sodium lamp was a difficult process is the corrosivity of hot sodium. Glass, even quartz, cannot withstand the operating conditions of the lamp. The key was a new translucent ceramic made from polycrystalline aluminium oxide, called Alumina.

HPS lamps use xenon as a starting gas while sodium is the main light emitter. A small amount of mercury is added to stabilize the discharge at higher currents. The spectrum shows broadened sodium lines with a rather high amount of energy in the orange-red part of the spectrum. This gives the HPS lamp its characteristic golden-white colour with a CCT of 2000 K and a CRI-R_a of 25. Typical lamp efficacies exceed 140 lm/W. HPS lamps require an additional pulse-starter to generate a high voltage ignition pulse.

HPS lamps are the most used form of outdoor illumination in the world, mainly because of their excellent balance between efficiency, reasonable colour rendering properties and long lifetime (often more than 25000 hours).

White HPS versions of HPS lamps feature a further increase in pressure and further broadening of the spectrum. These lamps were marketed for retail applications and reached a CRI-R_a of 85 at the expense of slightly reduced efficacies.

3.3.2.3 Metal halide lamps

Metal halide (MH) lamps operate in a similar manner as MV lamps. The difference is the addition of metal halide salts, compounds between metals and halogens, which drastically improve the colour rendering qualities and lamp efficiency. MH lamps where developed in the early 1960s by General Electric.

The spectrum of the lamp is determined mainly by the metal halides evaporated by the mercury discharge. There are three main MH lamp catagories (59)

- Triband lamps emit radiation in distinctive red, green and blue regions of the spectrum, generated by sodium (yellow), indium (blue) and thallium (green). Lithium can be added to increase the red parts of the spectrum. Their CCT lies between 3700 K and 4200 K with a CRI-R_a between 60 and 70. Triband lamps have a relatively high lamp efficacy of nearly 100 lm/W, but a rather short useful lifetime of 6000 hours.
- Multiline lamps use iodides of rare-earth metals such as dysprosium, scandium, thulium and holmium. These iodides generate light spectra with a large number of spectral lines, resulting in good colour rendering properties (CRI-R_a 75-85) and an efficacy around 75 lm/W
- Molecular lamps based on SnI_2 or $SnCl_2$ emit a quasi-continues spectrum with excellent colour rendering properties (CRI-R_a > 95).

In the mid 1990s, the quartz discharge tube was replaced with a polycrystalline alumina vessel, similar to the ones used in HPS lamps. Alumina is more resistant to corrosion a permits higher wall temperatures. This allows for a more efficient operating point, resulting in higher lamp efficiency, better colour rendering and longer lamp life. Ceramic MH lamps are offered in CCTs between 3000 K and 4500 K with a CRI-R_a of 85 for the lower CCT variants to 90 for the 4500 K series. The lamp efficacy reaches 100 lm/W for the 250 W versions with a lifetime exceeding 10000 hours.

3.3.2.4 Xenon lamps

Xenon lamps are short-arc discharge lamps that generate a discharge in a pure quartz envelope filled with xenon gas under very high pressure (up to 30 atmosphere). Ionised pressurised xenon produces a near continues spectrum in the visible wavelengths that closely resembles natural sunlight. Due to the spectral peaks in the infrared range, the LER of a Xenon lamp is rather low, limiting its use to specialised applications such as laboratory solar simulators or high-end projection systems.

Xenon lamps need a very high voltage starting pulse (>20 kV) but are operated at a low voltage, high current DC regime.

3.4 *Solid state light sources*

3.4.1 Semiconductors

Solid state lighting (SSL) refers to lighting technologies where light is emitted by electroluminescence instead of incandescence, gas discharge or other mechanisms. Electroluminescent materials emit light when an electrical current is passed through them, resulting from a radiative recombination of electrons and holes in the material.

In practice this material is a semiconductor. Semiconductors are a class of materials whose conductive properties fall in between those of an insulator and a conductor. Opposite to conductors, the conductivity of a semiconductor increases with increasing temperature: a rising temperature increases the probability of an *electron* leaving is lattice and leaving behind a *hole.* In solid materials, an electron is allowed to have only a certain range of energies, called *bands*. Other ranges, called *band gaps*, are forbidden. The interesting bands are those with energies near the *Fermi level:* the highest occupied molecular orbital at 0 K. The *valence band*, the closest band beneath the Fermi level, is the highest range of electron energies in which electrons are normally present at 0 K. The *conduction band*, the nearest band above the Fermi level, contains electrons that had enough energy to escape the valence band and jump into the conduction band, called negative charge carriers. Positive charge carriers or the lack of an electron are called *holes*. The movement of electrons in the conduction band creates an electron current and the holes formed by that movement create an opposite hole current. The figure below shows the energy bands in insulators, semiconductors and conductors.

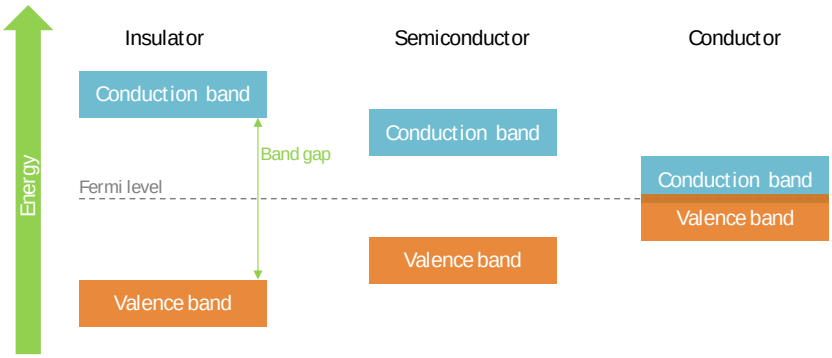

Fig. 3.4. Simplified representation of the band structure in solid insulators, semiconductors and conductors.

The conductivity of a semiconductor can be increased by adding impurities to a very pure or intrinsic material. Doping of a semiconductor increases the amount of holes or electrons within the material. Depending on the dopant used, two different kinds of doped or extrinsic semiconductors are formed: n-type materials that have an excess of electrons or p-type semiconductors that have an excess of holes. The Fermi level shifts down towards the valence band for p-type materials and up towards the conduction band for n-type semiconductors (Fig. 3.5).

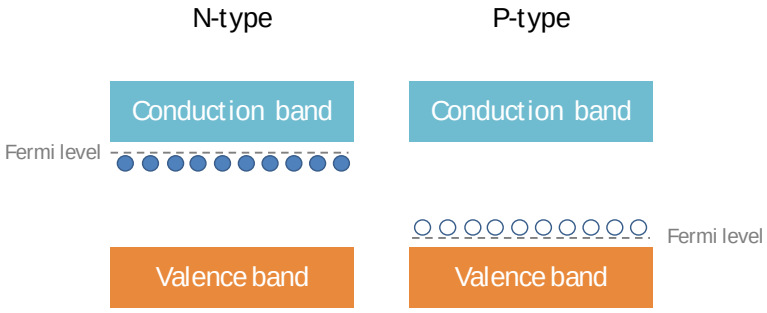

Fig. 3.5. Fermi levels in n- and p-type semiconductors after doping.

When a p-type material and n-type material is placed in contact, a p-n junction is created. At the junction, free electrons from the n-region recombine with holes in the p-region to form negatively charged ions. The donor sites left behind in the n-region create positive ions. The transfer ends in a steady-state when the electric field (E_{sp}) generated by the space charge in both sides of the junction is high enough to block further electron transport. In steady-state, the region around the junction is called the depletion zone (Fig. 3.6).

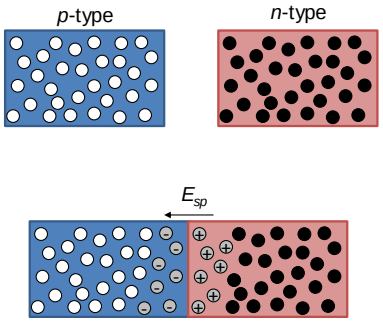

Fig. 3.6. Formation of the depletion zone around a p-n junction.

A positive bias applied to the p-side of the junction (reverse bias) pushes electrons on the n-side and holes on the p-side out of the junction, preventing on electron-flow across it. In contrast, a negative bias (forward bias) higher than the built-up potential, results in an attraction of electrons in the n-side to the p-side where they recombine with holes (Fig. 3.7).

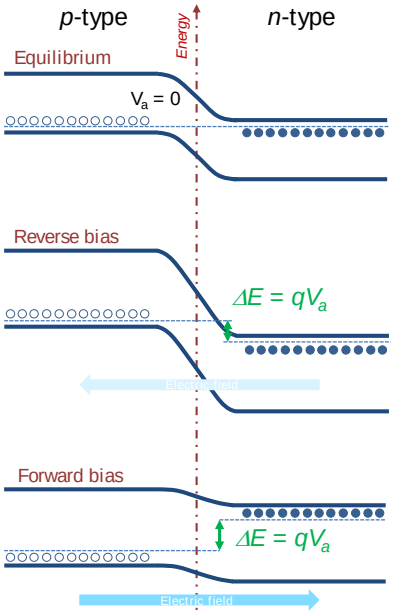

Fig. 3.7. p-n junction under equilibrium, reverse and forward bias

Electron-hole recombination can happen in a non-radiative or radiative way. The latter results in the emission of a photon and is a semiconductor-based light source.

In contrast to the simplified diagram in Fig. 3.4, the actual energy bands are not flat, but consist of a number of relative maxima and minima. The minimum energy difference between the top of the valence band and the bottom of the conduction band defines the actual band gap. When the minimum of the conduction band and the maximum of the valence band occur at the same momentum, the material is called a direct band gap semiconductor. A minimum and maximum that are occurring at a different momentum value are characteristic of an indirect band gap semiconductor (Fig. 3.8). When an electron

decays from the conduction to the valence band in a direct band gap emitter, a photon is emitted. In indirect band gap emitters, radiative decay can only occur if the process involves a change in electron momentum. In this case, light emission is a two-particle process: a phonon and a photon. This very unlikely phenomenon makes direct band gap semiconductors the material of choice for LEDs (60).

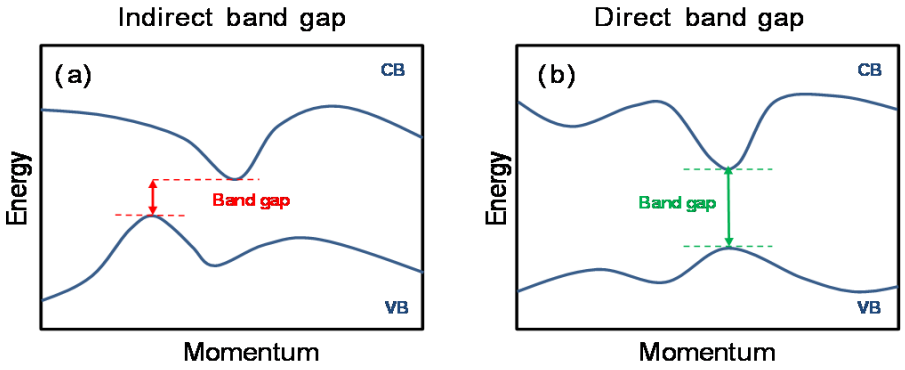

Fig. 3.8. Schematic representation of indirect band gap versus direct band gap emitters.

3.4.2 Light Emitting Diodes

The story of the light emitting diode starts in 1907 when H.J. Round, one of Marconi's assistants in England, discovered electroluminescence (EL) by applying more than 100 V to a crystallite used for sandpaper abrasive. However, Round did not further investigate the phenomenon. The basis of the operation principle of LEDs was established during the 1920s by O. V. Losev. In his studies on ZnO and SiC based structures, he related the LED emission to diode action, established the threshold voltage for the onset of light and measured the current-voltage characteristics of the device in detail. In the 1930s, French physicist G. Destriau discovered the electroluminescence of zinc oxide and is often cited as the true discoverer of the electroluminescent effect. In the early 1950s, the discovery of the transistor and the advances in semiconductor physics that went hand in hand with it made it possible to accurately explain EL light emission. Ten years later, the first commercial red GaAsP LEDs were available on the market. Since then the adoption of LEDs has grown rapidly. Their small source size simplifies the design of optics such as lenses and reflectors, their low voltage requirements, fast switching capabilities and different wavelength options offer new possibilities for compact, intelligent lighting design and their extremely long lifetimes, often in excess of 75000 hours, leave no doubt that LEDs are here to stay and transform the current lighting market.

LEDs are forward biased p-n junctions based on direct band gap trivalent and pentavalent semiconductors (III-V semiconductors). The efficiency at which the LED operates is determined by two main aspects: the light generation at the junction and the light extraction from that junction. Early LEDs showed poor internal quantum efficiency numbers as they were based on a simple p-n junction of the same semiconductive material leading to high leakage current and migration phenomena. Also, since the photon energy is similar to the material gap, photons emitted towards the substrate are mostly

absorbed. By creating a p-n junction with two materials having different band gap energies, a heterojunction device is created. The local variation of the energy band at both sides of the junction increases carrier confinement and results in higher quantum efficiencies. This mechanism is further improved by sandwiching the narrow-gap material between two wide-gap layers, effectively creating a double heterojunction which forms a barrier that restricts the region of electron-hole recombination within the lower bandgap material. A more efficient confinement of the carriers in the active region leads once again to a higher internal efficiency. A breakthrough in quantum-well physics led to the application of quantum-well structures in LEDs. Quantum-well based emitters have a very thin active layer, smaller than the de Broglie wavelength, in which the carriers and photons are confined. Additional carrier confinement and 3D carrier concentration increases the internal quantum efficiency and reduces recombination lifetimes. The thin layer also reduces dislocation to lattice mismatches which allows the use of materials of which matched substrates are not available. In multi-quantum-well structures several quantum-well structures are stacked on top of each other. While this further improves efficiencies, the number of defects associated with the process increases up to a point where they become detrimental.

The heterostructures of LEDs are manufactured by growing layers of different materials on top of each other while dopants are added. There are three main manufacturing techniques

- Molecular beam epitaxy (MBE) is an ultrahigh vacuum evaporation in which atoms or molecules of the material are directed by beams origination from effusion cells. Invented in the late 1960s in Bell laboratories, MBE allows high precision (< 0.01 nm) single crystal growth.

- Metalorganic chemical vapour deposition (MOVCD) is a chemical reaction process where evaporated carbon based compounds combined with metal atoms containing group III elements are mixed with hydrides of group V. In a low pressure atmosphere of hydrogen, these elements react and form a layer of III-V binary or mixed compounds.

- Chemical beam epitaxy (CBE) is a combination of the two methods above where the metalorganic vapours and hydrides are directed to the substrate as beams.

The spectral characteristics and quantum efficiencies of LEDs largely depend on the material systems used to construct the semiconductor. The discovery, application and main specifications of the most important ones are discussed below

- Gallium arsenide

GaAs-based devices were developed during the early 1960s as infrared emitters. Their emission peaks at 950 nm and is completely invisible to the human eye. Efficiencies in the range of 1 % were achieved. This success undoubtedly boosted the research in the field but the practical application of these devices was limited due to the absence of visible light emission.

- Gallium arsenide phosphide and gallium phosphide

Soon after the discovery of GaAs emission, researchers discovered the possibility of shifting the emission wavelength towards the visible range by growing a ternary alloy, a mixture of GaP and GaAs (61). The

exact wavelength of the emission was controlled by accurately monitoring their relative composition. In 1968 the first commercial GaAsP device was introduced in the market. The device, composed of an active layer of GaAsP on a GaAs substrate, exhibited emission in the red range with wall-plug efficiencies of 0.1 to 0.3 %. Shortly thereafter, more efficient devices were introduced based on GaP doped with Zn and O. These devices, fabricated on GaP substrates, emitted in the red region with efficiencies peaking at 2 %. Another interesting alternative for early LEDs was the discovery of isoelectronic impurities such as nitrogen, which can act as efficient emitting centers when incorporated into GaP and GaAsP alloys. These GaAsP:N- and GaP:N-based LEDs emitted in the yellow-green, yellow and orange range and exhibited wall-plug efficiencies ranging from 0.1 to 1 %. This relatively low efficiency was caused by the GaAsP/GaAs lattice mismatch, resulting in a large number of misfit dislocations in the GaAsP epitaxial films. Further development resulted in the discovery of the possibility to alloy GaAs and InP, two compounds with perfect lattice match, to form a quaternary compound: InGaAsP. This material is typically used for fabricating LEDs in the near infrared range, including the optical fibre telecommunication window between 1330 and 1550 nm. The exact emission wavelength is defined by the GaAs to InP ratio.

- Aluminium gallium arsenide

An important breakthrough in LED performance was the development of the AlGaAs/GaAs single heterojunction LED emitting in the red range. These devices introduced a novel concept: local variation of the energy band gap resulting in carrier confinement. The use of semiconductors with different energy band gaps results in carrier confinement and, subsequently, in improved internal quantum efficiencies. This approach was further improved in 1985 with the introduction of the first commercial AlGaAs/GaAs double heterojunction (DH) device, formed by sandwiching a narrow-gap material between two layers of wide-gap semiconductor. This provides more efficient confinement of the carriers in the active region, translating into emission in the red range with an efficiency of around 5%. It should be noted that, despite these noticeable improvements, the AlGaAs/GaAs LEDs presented an obvious disadvantage compared to early GaP based diodes: unlike GaP, the GaAs substrates are not transparent to visible light (absorbing substrate, AS), which led to low output powers. Fortunately, this issue was rapidly solved with the introduction of transparent AlGaAs substrates that contributed to the reduction of optical absorption, enhancing the emission efficiency by a factor of two. The first commercial transparent substrate (TS) LED was introduced in 1987 and showed an efficiency of about 10 % (62).

In the light of the promising results provided by the heterostructures, the parallel advances in quantum-well physics attracted many experts in the field to assess the feasibility of incorporating such structures into LEDs. The subsequent introduction of quantum-well and multi-quantum well heterostructures into semiconductor devices represented a new paradigm in the development of LED technology and boosted the development of high brightness LEDs.

- Aluminium gallium indium phosphide

A common problem observed in all the structures discussed above is the limited tunability of the alloy composition. For low P-fractions, GaAsP has a direct band-gap and is almost lattice matched to GaAs

substrates. As the P concentration is increased to extent the emission to shorter wavelengths, the lattice mismatch and thus the defect density increases appreciably, leading to a rather low efficiency. Furthermore, when the P content is too high the band-gap becomes indirect, which also contributes to the reduction of the emission efficiency. In a similar way, spectral tuneability of AlGaAs-based compounds is restricted to a certain range of Al concentrations. Emission wavelengths shorter than 660 nm cannot be achieved since the compound becomes indirect at high Al fractions. At low concentrations, in contrast, the emission shifts to the infrared range. The problem appears to be solved with the appearance of one of the so-called *high-brightness* alloys: the AlInGaP. With the AlInGaP material, tuneability from the yellow-green range to the red is possible whilst maintaining lattice matching on GaAs. Within this range, the device efficiency increases with the emission wavelength, reaching its maximum value in the red region. Record wall-plug efficiencies of over 60% at 609 nm have been achieved (63).

- Gallium nitride - Indium gallium nitride

In the early 1960s, green and red emission had been already achieved through the usage of GaP:N and GaAsP respectively. All that was needed to obtain white light was an efficient blue-emitter. Until then, only LEDs made of SiC had exhibited blue light emission but with efficiencies of just 0.05 to 0.1 %. From that moment on, much effort was devoted to the research of GaN which at the time was expected to provide bright blue emission. In this process, the first GaN single crystal was fabricated in 1968 and, surprisingly, it seemed to have intrinsic *n*-type behavior. The following aim was to find an efficient *p*-type dopant to enable the creation of a GaN *p*-*n* junction. After several attempts the difficulties in achieving efficient *p*-doping in III-N alloys were solved in 1989 when *p*-conductivity was generated by activating Mg dopants through electron beam irradiation. Finally, Nichia Chemicals developed a more straightforward method for activating these dopants by subjecting the doped nitride films to high temperature annealing. This resulted, in 1994, in the first commercial blue LED on the market. Such a device consisted of a GaN die deposited onto a sapphire substrate, since GaN substrates were not commercially available at the time. Fig. 3.9 shows an example of such a device. One interesting advantage of GaN-based alloys is the possibility of tuning the emission wavelength over a wide range, from 362 nm (3.4 eV) to 615 nm (2 eV), by altering the indium concentration in the InGaN alloy. Alternatively to sapphire substrates, which are electrically insulating and exhibit a sizeable lattice mismatch with GaN, InGaN can also be grown on SiC that is conductive and has a closer lattice match with GaN. This technology was developed by Cree Research and resulted in the GaN/SiC LED chip introduced in 1995. At present, Cree still is at the forefront in this area through its SC^3 Technology Platform with commercially available wall-plug efficiencies over 55% (64).

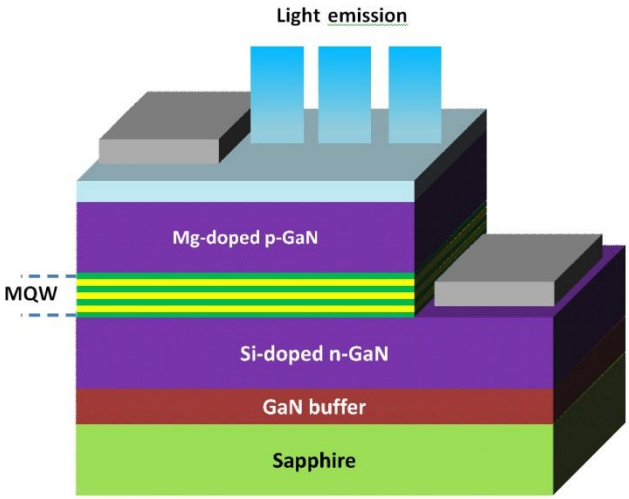

Fig. 3.9. GaN LED device structure.

- Zinc selenide

ZnSe LEDs are white light emitting devices that do not rely on phosphor conversion to generate white light. These diodes, based on II-IV compound materials emit blue-green light from the active P-N junction. A part of this emission is absorbed by the conductive substrate which emits broadband light peaking at 585 nm by photoluminescence. The combination of both emission bands results in white light with a CCT of 3400 K and a CRI-R_a of 68. The efficiency of ZnSe LEDs barely reaches 4 %. This relatively low efficiency combined with lifetimes of less than 1000 hours led to a very low market penetration.

- Aluminium nitride

The fabrication of violet and ultraviolet LEDs (< 400 nm) on sapphire substrates, commonly used for blue and green InGaN LEDs, results in more than 10^8 dislocations per square centimeter. UV InGaN LEDs down to a wavelength of 365 nm are commercially available, but their efficiency and lifetimes are a fraction of those figures for blue LEDs based on the same technology.

Aluminium nitride decreases the number of dislocations to less than $10^4/cm^2$. The result is a significant increase in both efficiency and LED lifetime. Recently developed 280 nm LEDs with external quantum efficiencies of 5 % are now available. Further improvements in efficiency and lifetime will cause an increased adoption of deep UV LEDs in applications to sterilize medical equipment and water purification, a field that is now dominated by mercury discharge lamps (65).

3.4.3 Organic Light Emitting Diodes

Organic LEDs are light emitting diodes made from an organic semiconducting material. Just like in inorganic LEDs, forward biasing the semiconductor injects holes and electrons from the opposite electrodes, forming excitons. Their radiative decay results in the emission of photons. OLEDs have a surface brightness that is several orders of magnitude lower than typical inorganic LEDs. This means that, for an equal amount of radiated power, an OLED needs to have a significantly larger emission area. The resulting emitter is a large area, glare-free light source.

Small molecule OLEDs or SMOLEDs contain an organic compound with a relatively small number of atoms in crystalline form while polymer OLEDs (PLEDs) use long-molecule polymers. Fig. 3.10 shows the layered structure of a standard and stacked OLED device.

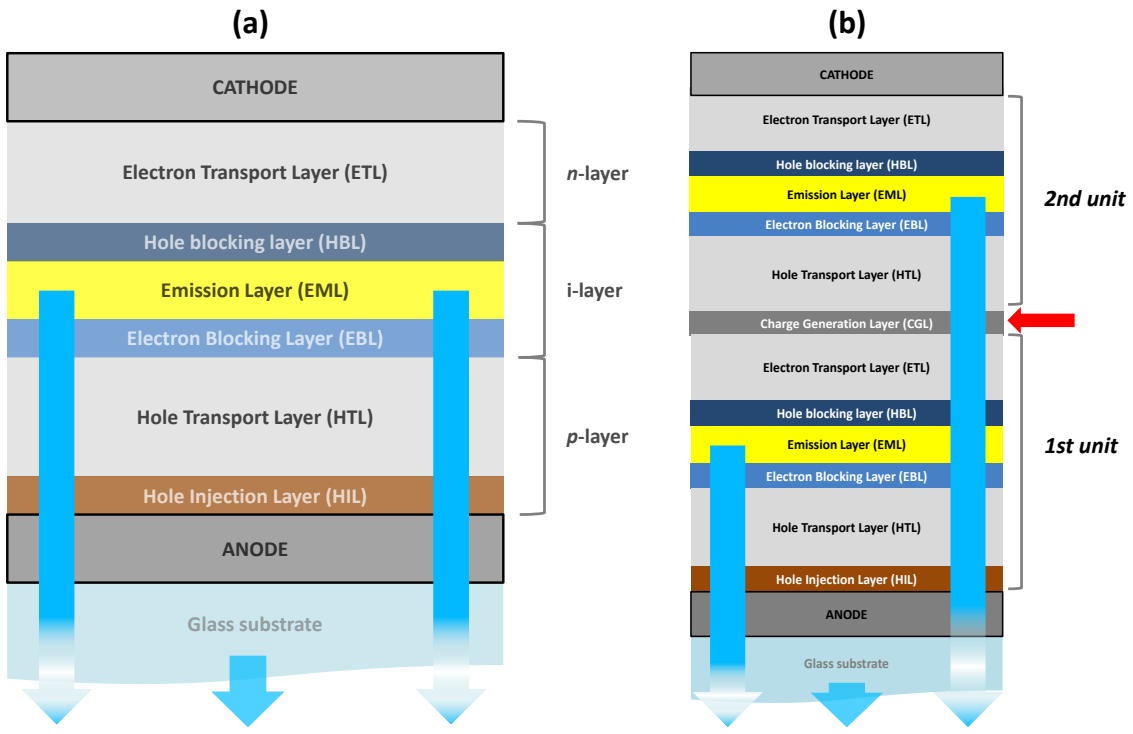

Fig. 3.10. Layout of a standard single unit p-i-n (a) and tandem structure (b) OLED

The first successful SMOLEDs were fabricated in 1987 by Eastman Kodak (66). Organic layers are usually deposited on an ITO, or similar transparent conductive substrate that forms the anodes and cathodes. A vacuum deposition technique, while expensive, guarantees a very homogeneous deposition of the layer structure. The emission layer, sandwiched between a p-type layer for transporting holes and an n-type layer transporting electrons, determines the main spectral characteristics of the OLED, while the hole and electron transport layers have a significant influence on the exact peak wavelength. The emission material can be either fluorescent or, preferably, phosphorescent. Phosphorescent materials have longer lifetimes and are commonly used for all OLED devices except short wavelength blue emitters. The

electron and hole blocking layers improve recombination efficiency by ensuring charge carrier confinement within the emission layer. Several p-i-n units can be combined to form a stacked OLED structure, which enables either higher emission power from the same area or lower current density to improve lifetimes. Stacked OLEDs can also combine emission layers emitting at different wavelengths, enabling colour or spectrally tuneable devices.

PLEDs are based on conjugated polymers that provide highly conductive layers to the device. These layers are deposited on substrates similar to the ones used in SMOLEDs. Since neither transport nor blocking layers are needed, the construction of PLEDs is relatively simple. The first devices were demonstrated in 1990 at Cambridge University.

The majority of today´s OLED devices are SMOLEDs because their efficiency is higher and they offer greater lifetimes than their polymer cousins. The interest in PLEDs, however, is large. A huge amount of R&D efforts are made for PLED devices as they are compatible with roll-to-roll manufacturing techniques. This means that the layers in PLEDs can be deposited by standard deposition techniques such as spin coating, roll-to-roll WEB coating or even screen and inkjet printing. The high flexibility of polymers also enables the use of flexible substrates which allows curved OLED light sources.

Despite their attractiveness and pleasant light distribution, there is still a large performance difference between the state-of-the-art OLED and inorganic LEDs. While typical, commercially available state-of-the-art white LEDs have no trouble reaching 170 lm/W[9], with the possibility to generate over 1000 lumen from device with a 3.45 x 3.45 mm footprint, commercially available OLEDs struggle to reach 50 lm/W[10], resulting in 300 lumens from a 100 x 100 mm device. The LED costs 1.25 euro, leading to a costs of less than 1.25 euro per klumen while the OLED costs more than 450 euro for 1000 lumens of white light. It is clear that the development and use of OLEDs is still in early stages, but despite the rather weak performance the OLED market is forecasted to reach 82 million USD in 2015 with an exponential growth to over 4.7 billion USD in 2020 (67).

3.4.4 White light emission from LEDs

Creating white light using light emitting diodes is not a trivial task. A LED is a highly monochromatic emitter, while white light is by definition polychromatic. Polychromatic light can either be created by combining multiple monochromatic emitters or through the use of wavelength converters.

3.4.4.1 Wavelength converters

Wavelength converters are organic or inorganic materials that absorb radiation in a certain wavelength range and re-emit light in another wavelength range. Wavelength converter materials include

[9] Cree XP-L 6500 K, I_f = 0.5A
[10] Philips Lumiblade FL300

fluorescent dyes, semiconductors and phosphors. Phosphors are widely used in fluorescent lighting systems where they convert ultraviolet light emitted by a mercury discharge into a range of visible wavelengths. Their emission colour and spectral width depends on the phosphorescent materials and dopants, and covers the full visible spectrum plus the near-infrared and near-ultraviolet region.

An important characteristic of a fluorescent or phosphorescent converter is the efficiency, η, given by the following equation:

$$\eta = \eta_{ext} \cdot \left(\frac{\lambda_1}{\lambda_2}\right) \quad \text{(Eq. 3.1)}$$

where

$$\eta_{ext} = \left(\frac{\#photons\ per\ \sec @\lambda_1}{\#photons\ per\ \sec @\lambda_2}\right) \quad \text{(Eq. 3.2)}$$

In LED-based applications, phosphors can be coupled either directly or remotely to an ultraviolet, violet or blue LED, creating a single emitter light source with the possibility of a very high CRI, gamut area or efficiency. Compared to the multi-emitter systems described in the next paragraph, phosphor-converted LEDs have the advantage of being significantly easier and cheaper to manufacture and operate. There is no need for complex electronics to provide a specific current to each LED die and there is no feedback mechanism to keep chromaticity points under control.

Immediately after its invention in the early 1990s, a yellow $Y_3Al_5O_{12}:Ce^{3+}$ (YAG) phosphor was combined with a blue LED to create white LED emission. These dichromatic LEDs still dominate the white LED market today.

YAG phosphors very efficiently absorb blue radiation between 440 and 460 nm, and re-emit a broadband spectrum with a half-width of 130 nm centred at 550 nm. The result is a conversion system with an IQE over 90 % and relatively good colour rendering properties due to the broad emission spectrum of the YAG phosphor. The addition of Ga shifts the spectrum of the phosphor to shorter wavelengths while the addition of Gd shifts the spectrum to longer wavelengths. This spectral tuneability allows manufacturers to create white LEDs with different CCTs down to 3000 K. The thickness of the phosphor layer determines the exact location of the chromaticity coordinates of the white LED. A thicker phosphor layer will absorb more blue light, moving the chromaticity coordinates towards the yellow region of the CIE diagram. Additional materials can be incorporated into the phosphor mix to improve colour rendering qualities or achieve lower CCTs.

Aluminate phosphors provide blue-green to pure green light with a very wide spectral range, allowing the creation of highly efficient white LEDs with colour rendering indices exceeding 95.

Silicate phosphors provide green to orange light with a relatively narrow spectral width, making them ideal for use in display backlighting. The narrow emission spectrum of a silicate phosphor allows the creation of weaker colour filters in LCDs, creating a larger colour gamut and a more efficient display.

Nitride phosphors are red-emitting converters primarily used to create high colour rendering, warm white LED sources.

Not all white LEDs are based on a blue InGaN pump. A different approach uses violet or near-UV LEDs to excite three or more phosphors to create white light. The huge advantage of this method is that the radiation of the pump does not contribute significantly to the final output spectrum. This allows manufacturers to create LEDs with exceptional colour rendering properties and very low unit-to-unit spectral variation. The downside is that the large difference between excitation and emission wavelengths (Stokes shift) results in a relatively low down-conversion efficiency. InGaN UV-based white LEDs have a significantly lower efficiency than InGaN blue/ YAG-based emitters.

The way phosphor particles are distributed inside the LED package influences the colour distribution and efficiency of the output beam.

Early LED packages used the so-called proximate phosphor distribution where the phosphor was mixed with the encapsulating material. The thickness and concentration of the phosphor layer determined the final chromaticity coordinates of the LED. The main problem with this method is that the length of the light path through the phosphor varies over the location of the semiconductor die. This results in an inhomogeneous colour distribution in the output beam pattern.

A conformal coating covers the whole semiconductor wafer with a very evenly-controlled layer of phosphor particles. This allows manufacturers to greatly enhance the beam uniformity of the resulting LED and also reduces phosphor material consumption while reducing manufacturing variation between devices with regard to colour differences and luminous flux.

Very high power devices or luminaires have to fight another problem: as the quantum efficiency of the phosphor is less than 100 percent, part of the absorbed radiation is converted into heat. This heat has a detrimental effect on the efficiency of the phosphor itself and lowers the efficiency of the LED die. Placing the phosphor layer at a relatively large distance from the die (several mm to cm) reduces these effects considerable. A remote phosphor application also reduces reflection losses between the phosphor and the LED die, resulting in an overall increase in system efficiency, colour stability and lifetime (68).

3.4.4.2 The green gap

The Achilles heel of LEDs has always been efficient light emission in yellow-green wavelengths, the band between 530 and 570 nm. While the LER of LEDs emitting near the maximum of the V(λ) curve is very high, their ability of converting electrical power to electromagnetic radiation is rather limited. The reason for this is that there is no ideal material system to work with. The III-N materials used to create UV, violet and blue LEDs are far less efficient at longer wavelengths and III-phosphides that are extremely efficient in the red to far-red range retain only a fraction of their performance in shorter wavelength ranges. When a phosphide system is configured to emit at yellow-green to green

wavelengths, the relatively low band gap leads to insufficient carrier confinement which prevents efficient radiative recombination. Nitride based systems are plagued by a reduction in external quantum efficiency and a decrease in electrical efficiency. The first issue expresses itself as an increase in forward voltage while the second problem causes *droop.* Droop is a phenomenon that plagues mainly blue, cyan and green LEDs, showing a decline in quantum efficiency with rising current density. This leads to low efficiencies at common forward currents. Because the major importance of LEDs emitting near the peak of the eye sensitivity (the efficiency of the green emitting component of a lighting system has the largest impact on the luminous efficacy of a light source), a lot of R&D efforts are being made to find solutions for the green gap problem.

One obvious method is decreasing the current density in current GaN materials. This would mean larger dies for the same amount of radiated power which increases costs and has the downside of increasing the size of the source. Osram reports efficacy figures of 108 lm/W at a forward current of 350 mA in a 1 mm^2 die radiating at a wavelength of 533 nm, an efficiency of only 15 %. Increasing the die size to 2 mm^2 increases the efficacy to 136 lm/W and very large dies show efficacy values up to 300 lm/W. The use of a-plane (semi-polar) GaN instead of conventional c-plane (polar) GaN, whether or not combined with a reduction in number of quantum wells to reduce droop effects, results in a further increase in quantum efficiency.

A second method, instead of focusing on improving the semiconductor itself, is the use of down-converting phosphors. As an example, the LED itself can be a blue emitting GaN device with an efficiency over 50%. The phosphor is a ceramic lutetium aluminium garnet, featuring a peak wavelength of 531 nm. The blue LED – phosphor combination reaches an efficacy of 191 lm/W at a forward current of 350mA, significantly better than the direct emission green LEDs. Note that this is for a relatively short-wavelength green emission. The difference for wavelength near 555 nm will be larger. A side effect of phosphor converted LEDs is the larger spectral width of the emission. Direct-emitting green LEDs have a typical full width at half maximum (FWHM) of 30 nm while phosphor converted variants, depending on the exact phosphor, settle around 100 nm. While this is beneficial for the colour rendering properties of white light sources (better spectral coverage) it is detrimental for their LER (69).

3.4.4.3 Multichromatic LED sources

Multichromatic LED sources use a combination of monochromatic emitters to create a certain spectrum. While this increases, sometimes considerably, the complexity of the electronics and optical system, it offers many advantages regarding colour or spectral tuning. While most phosphor based white LED systems are in fact multichromatic light sources, this paragraph focuses on LED sources using a combination of monochromatic emitters.

- Dichromatic LEDs

Due to their inherent problems with accurate and pleasing colour rendering, very few light emitting diodes made it further than the research laboratory. While the combination of two complementary

wavelengths can provide a chromaticity point close to the black-body locus, the colour rendering of objects is heavily distorted. Narrow spectrum dichromatic light sources are not useable for general illumination

- Trichromatic LEDs

Trichromatic LEDs are widely used in lighting and display applications. Their most famous incarnation, the RGB LED, consists of three emitters packaged together to form a compact semiconductor light source with a tuneable chromaticity point. Usually the peak wavelengths of the three LEDs are chosen to maximize the colour gamut whilst keeping a relatively high efficacy. This results in emission peaks at 455 nm, 530 nm and 610 nm. RGB LEDs are primarily used in the display industry as direct view LED screens for large outdoor events and efficient, wide colour gamut backlights for high-end LCD panels. At the same time the entertainment industry is abandoning electricity-hungry discharge lamps with different colour filter combinations in favour of much more energy friendly RGB LEDs.

In colour-critical applications where a stable white point must not be affected by temperature variations or the aging of semiconductor material, a closed loop feedback system is necessary. A tristimulus sensor tuned to the peak wavelengths of the red, green and blue emitters provides a feedback signal to the LED driver electronics, allowing careful adjustment of the LED drive current when any change in chromaticity is detected.

- Polychromatic LEDs

A new trend in general illumination systems is combining high quality light with an interactive control where the user can select an ideal illumination depending on a specific location, the time of the day or the mood of a person. While RGB-based lighting solutions are very flexible, their spiky spectra rate poorly when rendering subtle hues of daily objects. When combining a sufficient number of narrowband LEDs, a tailored lighting spectrum without significant gaps or valleys can be created. Such polychromatic light engines can have both excellent colour fidelity and high efficiency. The challenge in this kind of sources is finding effective and efficient methods of combining the output of those monochromatic emitters to form a single homogeneous beam of light.

The colour rendering qualities of a white light source created by monochromatic spectra are highly dependent on the reflectance spectra of the object being illuminated.

Trichromatic light sources offer better colour fidelity then *bichromatic* light sources. However, objects with reflection spectra not matching the emission spectrum of the light source will be rendered incorrectly. This does not necessarily mean that the object illuminated by that spectrum will look highly undersaturated or with low colour contrast. Depending on the interaction between the source spectrum and the object's reflection spectrum, a scene can look more saturated with better colour contrast under trichromatic illumination compared to a broadband illumination source with high colour fidelity.

Polychromatic light sources can have very high colour fidelity values. Depending on the number of monochromatic emitters in the source, CRI-R_a values of 95 to 100 are achievable. In extreme cases, even a complete spectral match to a reference spectrum is possible.

In the case of a monochromatic light source emitting at 555 nm, the LER is maximized at 683lm/W. Of course, this pure green light can hardly be called a white light source since its colour rendering properties are non-existent. LED light sources containing individual emitters can be carefully optimized to provide a balance between LER, gamut area coverage and colour rendering. Depending on the application, one of these criteria might be more important than another. By choosing the LED peak wavelengths closer to the 555 nm emission wavelength, the LER is maximized. LEDs with a narrow emission spectrum located near the edges of the chromaticity diagram favour a very wide colour gamut, a useful feature in certain display applications. The design and application of spectrally tuneable, polychromatic LED light sources is described in extensive detail in chapter 4.

3.5 Summary and conclusions

Artificial light sources have evolved from candles made from natural oils, to mass produced electric lamps. The introduction of the incandescent light bulb, fluorescent lamp and, more recently, the LED all resulted from giant leaps forward in illumination technology. LEDs, especially, will allow us to enjoy an energy efficient, nearly infinitely long lasting light source that offers a tremendous amount of possibilities. Their small size and monochromatic behaviour allows them to be integrated into compact multi-emitter light sources that can generate illumination spectra on-demand. The same monochromatic behaviour makes it impossible for LEDs to emit white light from a single source. The solution is a combination of a short wavelength LED with a down-converting phosphor or scintillator. A critical wavelength region for LEDs is the green-gap between 530 and 570 nm where both InGaN and AlInGaP materials have rather low quantum efficiencies.

4. Designing a spectrally tuneable LED light source

A spectrally tuneable light source has the unique ability of changing its emission spectrum to accommodate certain parameters such as LER, CCT or CRI. Limited forms of spectral tuning have been performed since the invention discharge lamps where their rather spikey spectrum was combined with the black body spectrum of an incandescent or with other discharge lamps in the attempt to improve the colour rendering properties of the light source. The invention of efficient narrowband emitters, such as LEDs, opened up a new world of possibilities.

Building an arbitrary spectrum can be done in two different ways: downconverting a narrowband light source using a special phosphor mixture or building a spectrum using many narrowband emitters covering a certain spectral range (70). The former method is widely used in fluorescent and white LED lighting. One or more phosphors convert either ultraviolet or blue light into longer wavelength light. By adjusting the weight of each individual phosphor a tailored spectrum can be created. This technique is fairly cheap but once the light source is designed and manufactured the spectrum is, as in any other normal lamp, not adjustable. When combining multiple narrowband emitters not only an arbitrary spectrum can be created, but this spectrum does not have to be fixed. By changing the radiated power of each emitter the spectral properties of the light source can be changed on demand.

The latter method, while creating a very flexible light source, creates a number of difficulties. Each individual wavelength consists of one or more unique LEDs. Each of these LEDs has specific requirement regarding forward current and forward. This means that each wavelength “channel” requires electronics to control these parameters. LEDs, being less than 100% efficient, generate heat that deteriorates their efficacy and limits operating lifetimes. It is crucial that this heat is moved away from the junction and dissipated into the environment. Furthermore, the output characteristics of each LED will differ significantly, resulting in a very inhomogeneous radiation pattern. An optical system has to be designed to combine the radiation patterns of each of the individual emitters and efficiently bundle them in a uniform beam. Lastly, a software-based user interface has to be designed to control each of the wavelength channels and generate illumination spectra with desirable spectral shape, flux, CCT and CRI.

The chapter below presents a breakdown of the components used in the design of a spectrally tuneable solid state light source followed by a detailed discussion of the full design process, from the first proof-of-concept to a finalized light engine.

4.1 LED selection

A first important aspect when designing a tuneable light source is the selection of individual emitters: besides the fact that the LEDs should emit a flux as high as possible (low current devices are not useable), the spectral range that has to be covered is ideally divided into equal bands, each of those bands containing a number of LEDs having a bandwidth equal to the width of that spectral band and an output power equal to the other emitters. The number of bands eventually determines the accuracy of the system when reproducing a certain spectrum. Ideally, an infinite number of infinitesimal narrow

spectral bands spanning the whole visible spectrum would allow for perfect tuneability. In reality, this is unfortunately not possible. Manufacturers aim to produce LEDs in key regions of this visible spectrum: blue (460 nm), cyan (500 nm), green (525 nm), yellow (590 nm), orange (610 nm) and red (635 nm). Some manufacturers offer application specific LEDs at other wavelengths, for example at 660 nm to promote plant photosynthesis. During production, however, it is impossible to know the exact amount of dopants that diffuse in each location on the semiconductor wafer. These small concentration differences results in variation in forward voltage, efficacy and peak wavelength. For this reason, LEDs are sorted in so called *bins*. When placing an order, the customer can then specify his or her preferred forward voltage, luminous flux and wavelength bin. This disadvantage for manufacturers is here used as an advantage in creating the spectrally tuneable *light engine* as it will enable the use of a larger number of discrete wavelength channels.

4.1.1 Covering the green gap

Binning LEDs, however, does not solve the green-gap issue discussed in 3.4.4.2. Efficient material systems emitting in the 550 nm range simply do not exist, and measures to overcome this efficiency gap are very costly. A viable solution is the use of wavelength converters that convert short wavelength radiation to a spectrum in the green-gap region.

During this doctoral research, two different approaches were explored: one direct emitting OLED approach and two phosphor converted solutions. The results are presented below.

4.1.1.1. Green OLED emitters

One of the main objectives of the EU FP7 HI-LED project was the integration of organic and inorganic LEDs in a spectrally tuneable light source. The OLEDs, developed in collaboration with Fraunhofer COMEDD, supplement the inorganic LEDs at wavelengths within the green-gap region (chapter 3.4.4.2) were LEDs lack efficiency.

The emission spectrum of OLEDs is defined by the emission layer material and the general architecture of the device that influences the light-outcoupling from the emission layer to the surrounding environment. There are three basic OLED structures:

- Standard bottom emission: the emission layer is sandwiched between the semiconductor layer. The top of the stack is covered by a glass substrate with an aluminium or silver cathode metallisation while the bottom glass cover contains a transparent ITO anode (Fig. 4.1 (a)).
- Adding a semi-transparent silver metallisation between the bottom semiconductor layer and ITO anode creates a resonant cavity within the OLED stack (Fig. 4.1 (b)).
- If instead of an ITO based anode and aluminium or silver metallisation is used and the cathode is constructed from a semi-transparent metal, the device turns into a top-emitting OLED (Fig. 4.1 (c)).

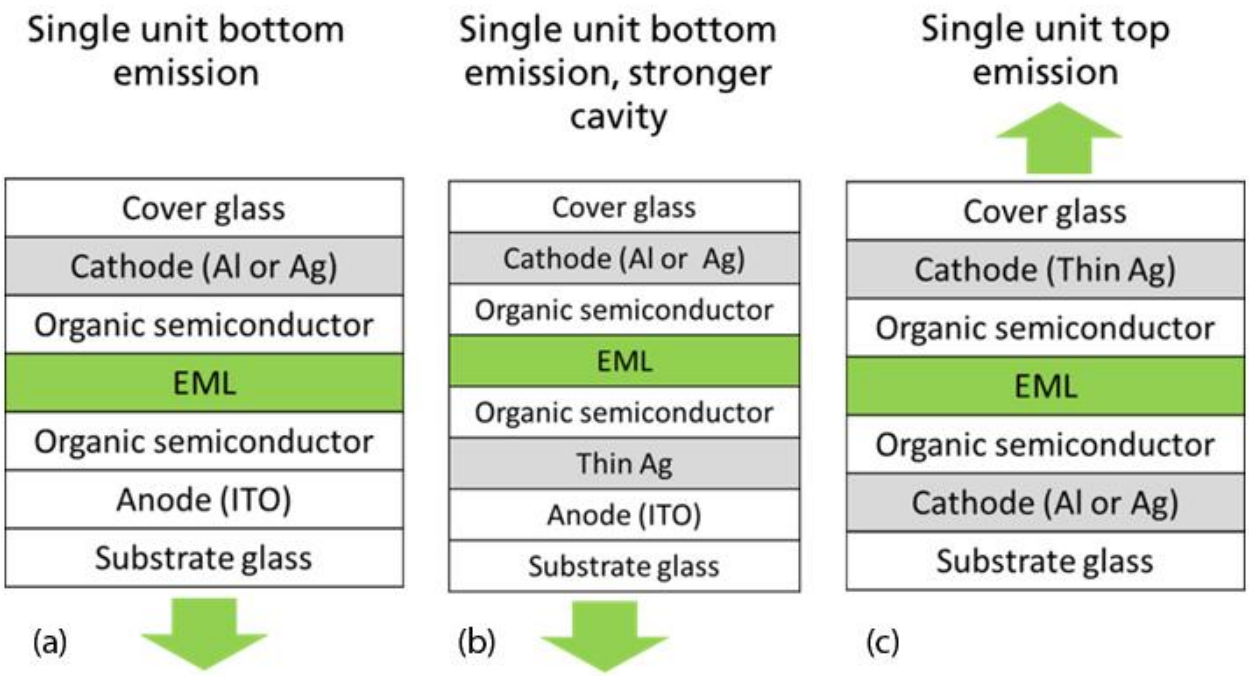

Fig. 4.1. Different OLED architectures: (a) bottom emission, (b) resonant cavity bottom emission and (c) top emission.
Source: Fraunhofer COMEDD

As mentioned before, the main spectral characteristics are determined by the emission material in the emission layer (EML) and the architecture of the device. By varying the thickness of the electron and hole transport layers within the semiconductor, slight variations in peak emission wavelength can be accomplished. Spectral emission profile simulations were done for all three stacks using EM2-1 as a phosphorescent emission material emitting in the green region of the spectrum. The aimed-for emission peak is centred on 545 nm. Fig. 4.2 shows a simulation of the emission spectra of a bottom emission, resonant cavity and top emission OLED with a peak emission of 540 nm. Note that the bottom emission OLED, having no resonant cavity structure, has by far the broadest emission profile. Adding a resonant structure reduces the width of the emission spectrum significantly which is a desirable feature in a spectrally tuneable light source. Based on the spectral simulations, a top emission layout was selected.

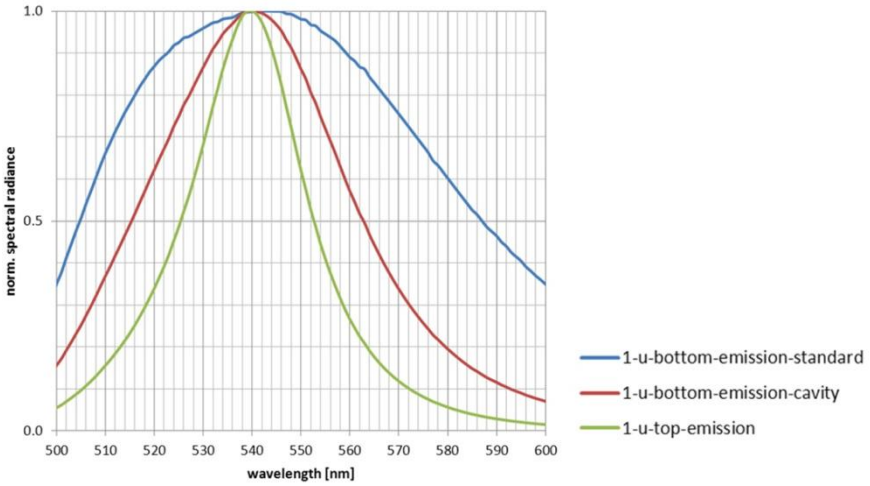

Fig. 4.2. Simulation of the emission spectrum of a bottom emission (blue), bottom emission with resonant cavity (red) and top emission OLED (green). All three OLED structures use identical emission layers and hole – electron transport layer thicknesses.
Source: Fraunhofer COMEDD

The figures below show the effect of the electron and hole transport layer thickness on the peak wavelength (Fig. 4.3), spectral width (Fig. 4.4) and emission efficiency (Fig. 4.5).

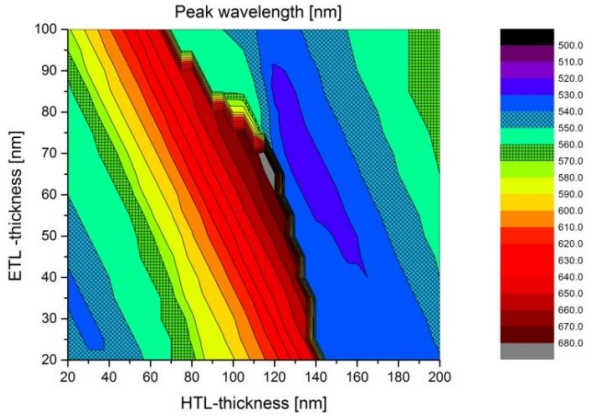

Fig. 4.3. Top emission device – electron and hole transport layer thickness versus peak wavelength.
Source: Fraunhofer COMEDD

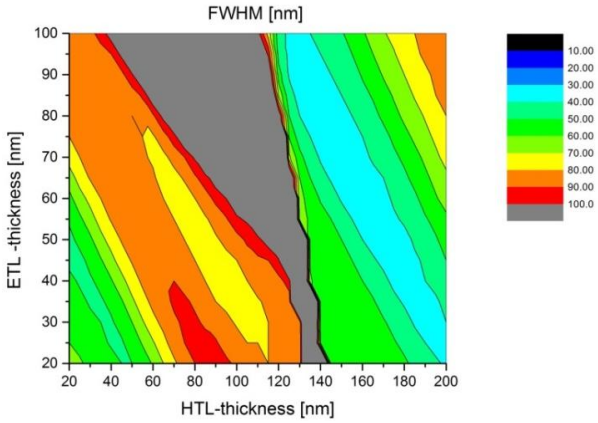

Fig. 4.4. Top emission device – electron and hole transport layer thickness versus spectral width.
Source: Fraunhofer COMEDD

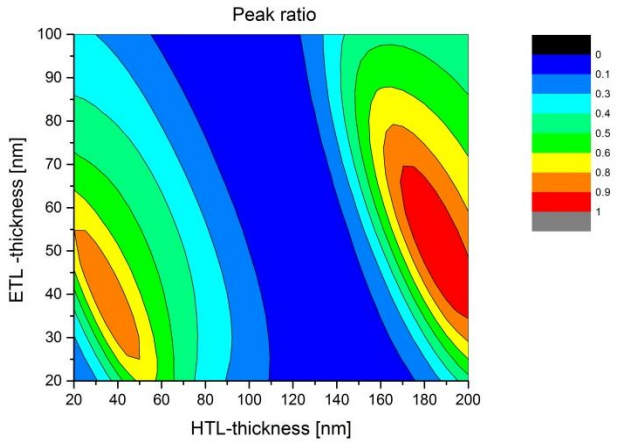

Fig. 4.5. Top emission device – electron and hole transport layer thickness versus emission efficiency.
Source: Fraunhofer COMEDD

With the simulations finished, prototype devices where manufactured in a hexagonal shape (for ease of integration) and with an active surface area of 7 cm^2. Although larger devices would emit a higher flux, thin-film process yield and stability (emission spectrum variation within one device) would cause problems. Fig. 4.6 shows a schematic diagram and cross-section of the prototype green OLED.

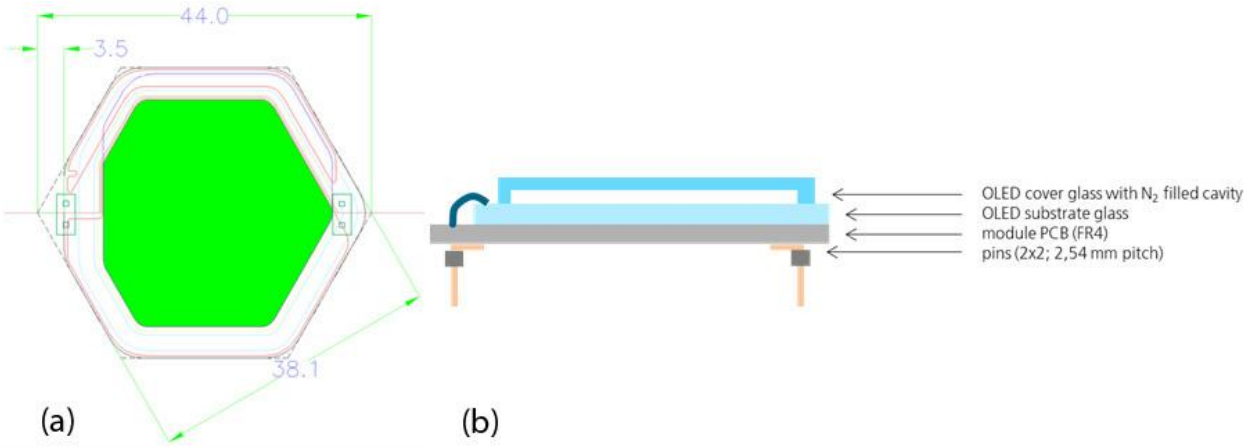

Fig. 4.6. Schematical representation of the OLED prototype. (a) Top view, active area in green and (b) cross-section showing the different components.
Source: Fraunhofer COMEDD

Fig. 4.7 shows the spectrum of the finalised sample emitting green light, indicating a peak wavelength of 547.01 nm and a FWHM of 34.44 nm. Driven with a forward current of 34.0 mA, the OLED has a forward voltage of 4.22 V and emits 4.95 lumen of green light with an efficiency of 34.50 lumen per Watt. The relatively narrow bandwidth results in a chromaticity point located close to the edge of the 1931 x,y chromaticity diagram (71-73).

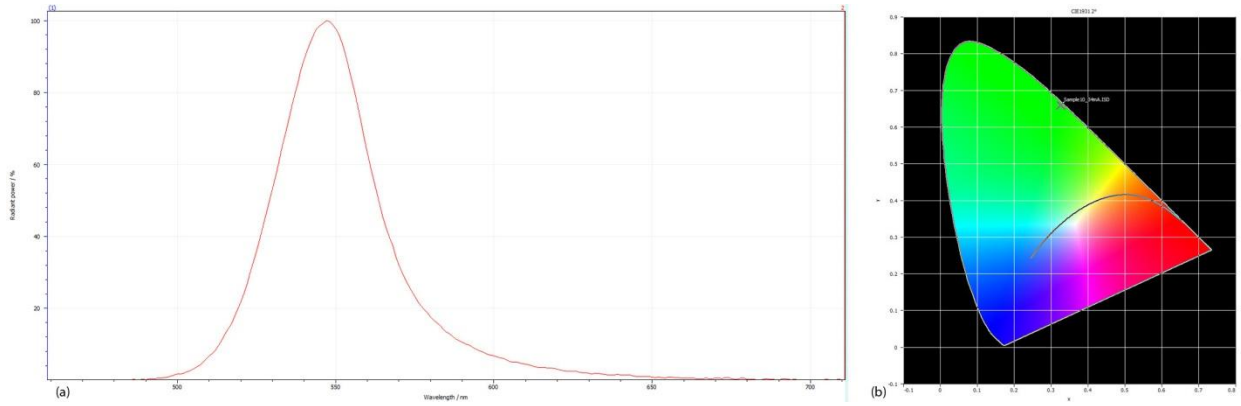

Fig. 4.7. (a) Spectral power distribution of the green top emission OLED prototype (I_f = 34.0 mA) and corresponding chromaticity coordinates x= 0.3148, y=0.6675 (b).

4.1.1.1.2 Cyclometallated PtII complexes with N-Heterocyclic carbene ligands: a new generation of wavelength converters

Phosphors for LEDs are typically inorganic materials doped with rare-earth activators such as europium and cerium ions. The high cost associated with rare-earth elements has sparked interest in the development of new wavelength conversion materials. Platinum(II)-based phosphorescent complexes, in particular CN-cyclometallated derivatives, are considered as a possible alternative dopant. To determine whether these compounds are suitable for developing both LEDs that cover the green-gap area and white LEDs, a novel LED phosphor was synthesised by the University of Zaragoza and a new remote-proximate hybrid deposition technique was used to deposit the phosphor on a blue LED device.

The strong ligand field induced by the carbon σ-bond and the aromatic fragment characteristics of the CN-ligands enhance the splitting of the d-orbitals and raise the energy of the non-radiative excited states of the metal center. This effectively reduces thermal quenching, the rapid loss of quantum efficiency when the temperature of the compound is raised. Cyclometallated N-heterocyclic carbenes (NHC) may surpass the high ligand field splitting capacity of the CN-ligands, which implies an even greater heightening of the d-d energy levels. The resulting enlargement of the energy gap with the emissive excited states improves quantum yields. Tuning of the emission wavelength of the phosphor is achieved by modification of the cyclometallated and/or ancillary ligands. Seven different compounds where fabricated using the synthesis method shown below (Fig. 4.8)

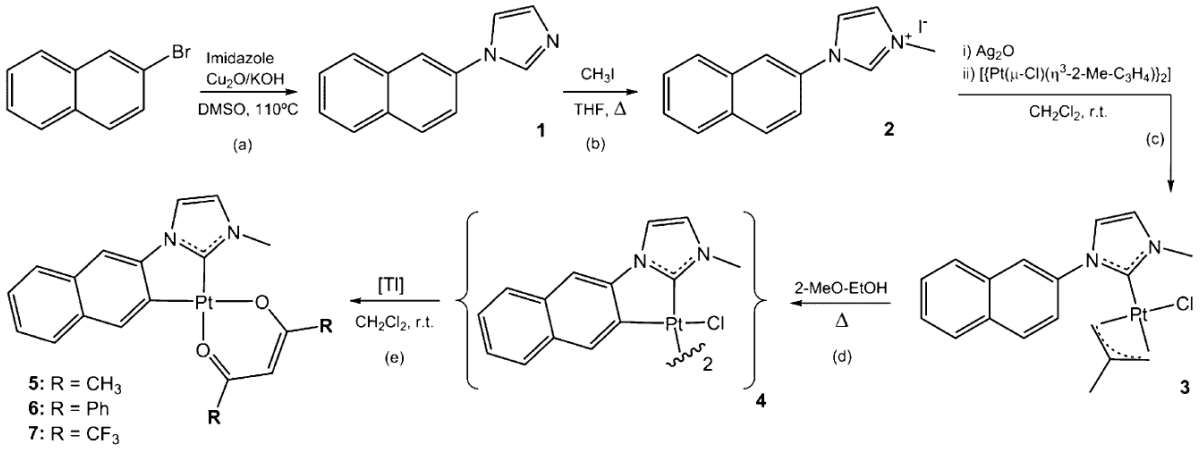

Fig. 4.8. Synthesis of compounds 1-7.

After quantum yield and emission-absorption spectra testing sample 5, ($\left[Pt\left(\widehat{CC}^*\right)(L-O,O')\right]$ ($L = acac$ 5)), was selected as the candidate for LED deposition. Compound 5 has an absorption band in the UV to blue range of the spectrum which is highly compatible with InGaN LEDs having a peak wavelength around 450nm. The emission spectrum shows efficient broadband radiation peaking in the yellow-green between 500 and 700 nm (Fig. 4.9), making the material attractive as a down-converting phosphor for LEDs.

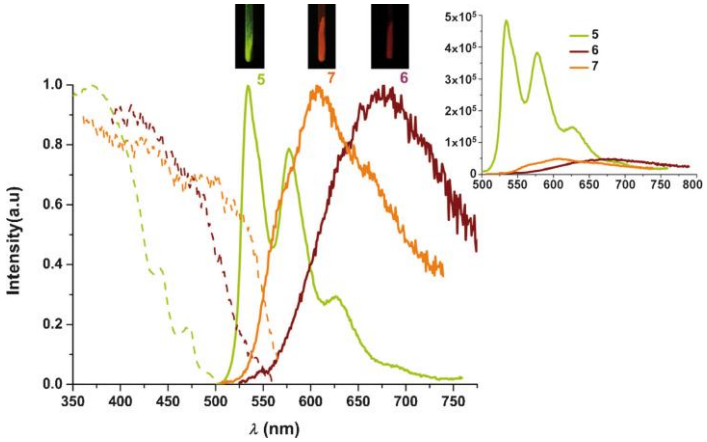

Fig. 4.9. Normalized absorption (dotted line) and emission (solid line) spectra of compounds 5, 6 and 7. Inset: Non-normalized emission spectra, showing the superior quantum yield of compound 5.

The quantum efficiency of sample 5, although the highest in the series of 7 compounds, measured a rather average 50%. Commercial YAG: Ce phosphors used in white LEDs have a typical quantum yield of 97% (74). To investigate the behaviour in a real LED system, the phosphor was deposited on specially prepared Lumileds LXML-PR01 LEDs. The Luxeon Rebel series consist of a ceramic substrate containing a 1 mm^2 die and a protection diode. The assembly is covered by a silicone coating which includes a moulded silicone lens element. To prepare the LEDs for phosphor deposition, the silicone coating was shaved down to a thickness of approximately 0.2 mm. A mixture of phosphor sample 5 and Dow Corning encapsulant OE 6531 with 2 different concentrations, 9.5% and 17.3% was applied on top of the silicone layer covering the LED using a constant-weight drop coating technique. After heat-curing the encapsulant, this results in layered structure containing the LED die, a silicone protection layer of 0.2

mm and a layer of the encapsulant – phosphor mix. The structure provides a heat-barrier between the LED die and the phosphor, resembling a remote phosphor.

Emission spectra of the two LEDs, driven at a forward current of 50mA, are presented in Fig. 4.10. A few interesting observation can be made:

- The difference in phosphor concentration translates directly to a difference in absorption of the pump energy and strength of the emission spectrum. The higher the phosphor concentration, the higher the absorption of the blue pump and the higher the contribution of the yellow phosphor emission.
- A higher phosphor concentration also results in a slight (3 nm) red-shift of the peak wavelength of the blue pump LED. This is the direct result of an increase in junction temperature and subsequent reduction of the energy band gap due to the relatively low quantum efficiency of the phosphor. According to Lumileds, a 3 nm shift represents an increase of the junction temperature of 100 ºC.

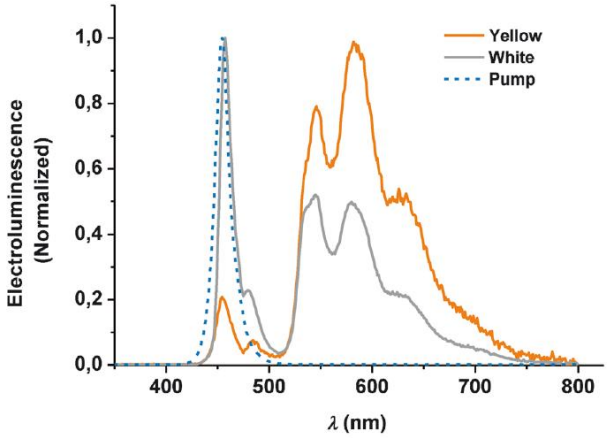

Fig. 4.10. Emission spectra of two LEDs containing phosphor sample 5 at concentrations of 17.3% (yellow) and 9.5% (white) and the emission spectrum of the Lumileds LXML-PR01.

The resulting chromaticity coordinates and prepared LEDs are shown in Fig. 4.11. The near-monochromatic blue pump (chromaticity coordinates: x = 0.1507, y = 0.0263) shifts to a white light emitter by adding a 9.5% phosphor mixture (chromaticity coordinates: x = 0.3456, y = 0.3585) and changes to yellow (chromaticity coordinates: x = 0.4690, y = 0.4681) when the concentration is increased to 17.3% (75).

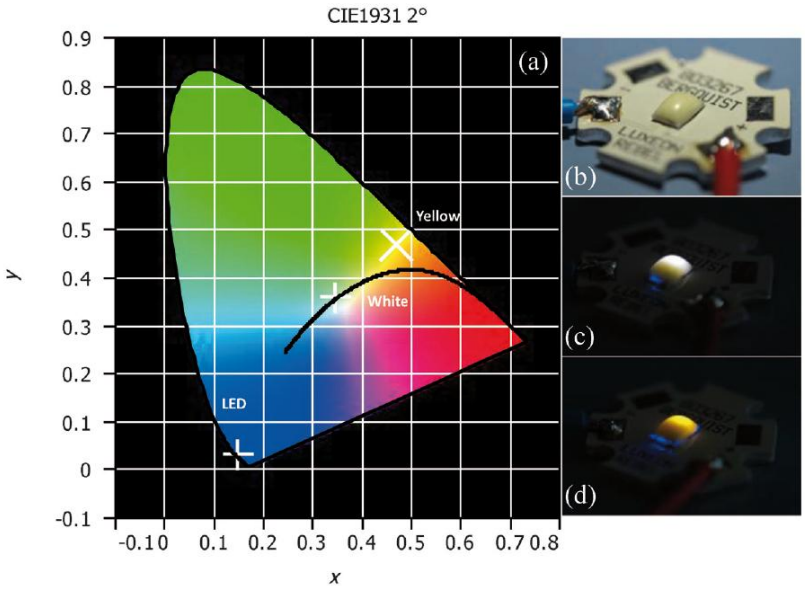

Fig. 4.11. Chromaticity coordinates of the blue pump, white emitting LED and yellow emitter (a), prepared LED with remote-proximate phosphor deposition in off-state (b), lit LED showing white light emission (c), lit LED showing yellow light emission (d).

4.1.1.1.3 Towards an efficient yellow-green LED

During the design-phase of the polychromatic spectrally tuneable LED sources described in chapters 4.5.6 and 4.5.7, it became clear that sourcing a suitable yellow-green emitting LED was going to be very difficult. Direct emitting GaN or AlInGaP emitters with the desired output power simply did not exist and using a broad-band white LED instead proved to limit the spectral tuneability. The cyclometallated PtII complexes discussed in the previous section result in a desirable spectral shape, but their quantum efficiency is simply too low for high power applications. Commercial phosphos, based on rare-earth materials proved to be an efficient solution.

Three phosphors from the Intematix Corporation with a peak wavelength centred near 555 nm were selected:

- GAL550: A yellow-green aluminate-based phosphor. Aluminate materials offer higher thermal stability than other LED phosphors in high power applications (less thermal quenching). GAL phosphors have a very broad excitation (200 to 480 nm) and emission spectrum (FWHM = 120 nm).
- EY4156: A narrow-band silicate-based phosphor. Silicates offer quantum yield higher than 96%, but are sensitive to heat (high amount of thermal quenching). Because of their narrow emission bandwidth of just 75 nm they offer high colour purity. The EY4156 material has an excitation range between 200 and 490 nm and emission peak centred around 550 nm.
- NYAG4156: A YAG-based material with extremely high quantum yield (>95 %), stability and high heat resistance. The medium broadband emission spectrum, centred around 545 nm, has a

relatively large extension in the medium to long wavelength range and contains little energy in shorter wavelengths. YAG phosphors can be excited very efficiently by GaN blue LEDs (excitation range: 430 nm to 490 nm), but are not suitable for shorter violet or UV LEDs.

The three phosphors where characterized, in conjunction with a blue Luxeon Rebel (λ_p = 451 nm), at concentrations ranging from 10 to 50 % phosphor-to-encapsulant weight in steps of 5 %. The selected encapsulant, Dow Corning 6531, is a 2-component clear silicone formulated for optical encapsulation and prototyping. The phosphor and both components were combined and manually mixed during 1 minute, followed by a 5 minute automated roll-mixing period. Using the remote-proximate hybrid deposition method described in chapter 3.4.4.1.1, a 10 µl drop was deposited on each Luxeon Rebel LED package. The finished LEDs were cured at 150 ºC for 3 hours before characterization (Fig. 4.12).

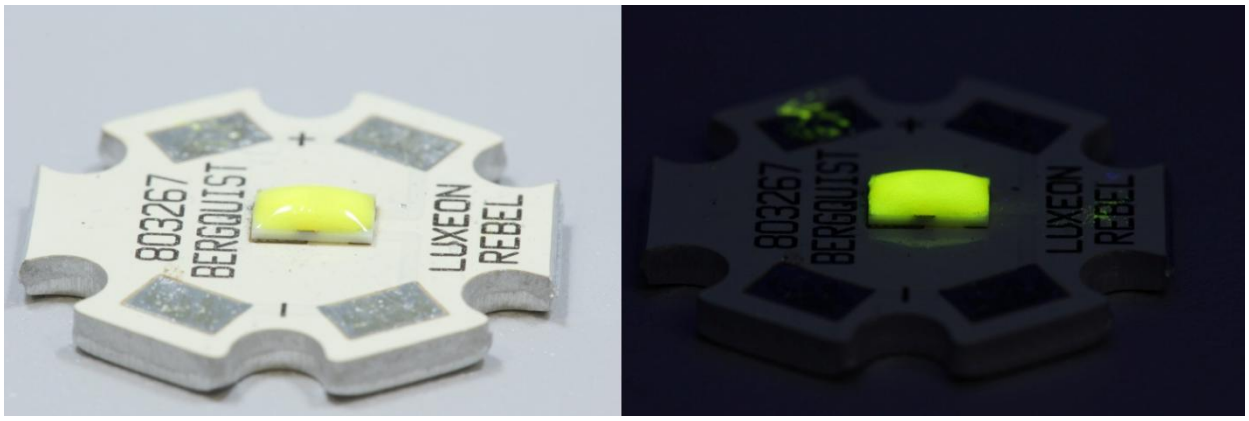

Fig. 4.12. Final LED with NYAG phosphor deposition mounted on a MCPCB. Off-state (left) and polarized with a forward current of 1 mA (right)

Each phosphor-converted (PC) green LED was mounted a metal-core printed circuit board (MCPCB) made by Henkel Bergquist and measured at a forward current of 350 mA and 700 mA. The temperature of the MCPCB was held at a constant 25 ºC.

The results of the measurements, grouped per each of the three phosphor classes, are shown below in a spectral graph showing the emission spectrum of the LEDs, the corresponding chromaticity coordinates and a table with the respective radiometric and photometric powers.

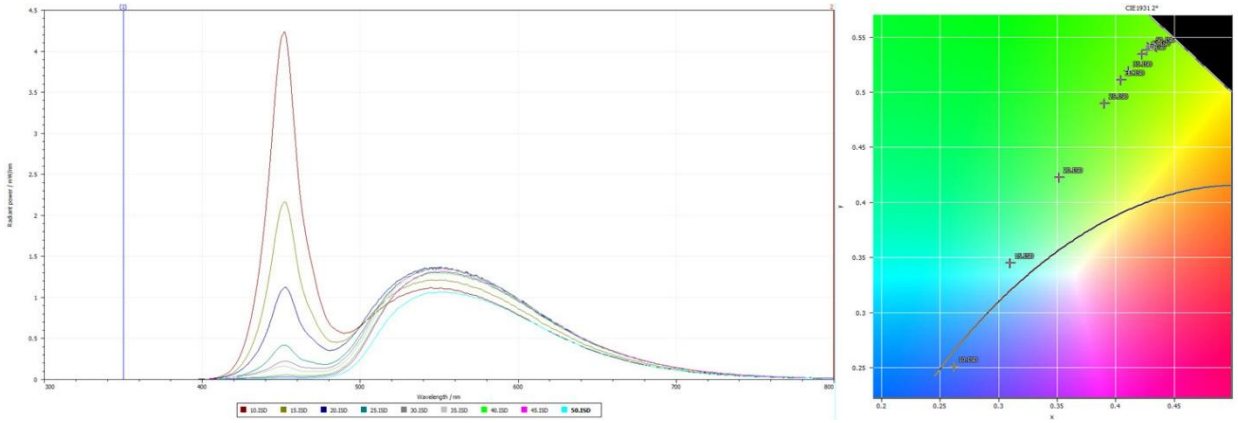

Fig. 4.13. Intematix GAL550 phosphor converted LED – SPD and chromaticity coordinates. Green aluminate phosphors are characterized by a relative broad emission spectrum, extending deep into the red –orange range of the visible spectrum. Forward current = 350 mA.

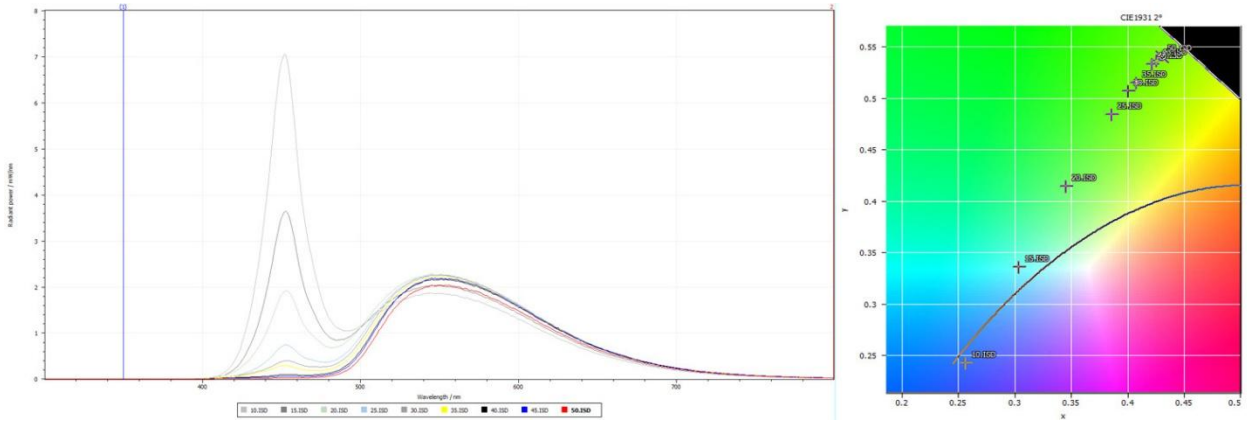

Fig. 4.14. Intematix GAL550 phosphor converted LED – Forward current = 700mA. In comparison with the lower drive current of 350 mA, a slight blue-shift of the colour coordinates can be noticed, especially when the phosphor concentration exceeds 25 %.

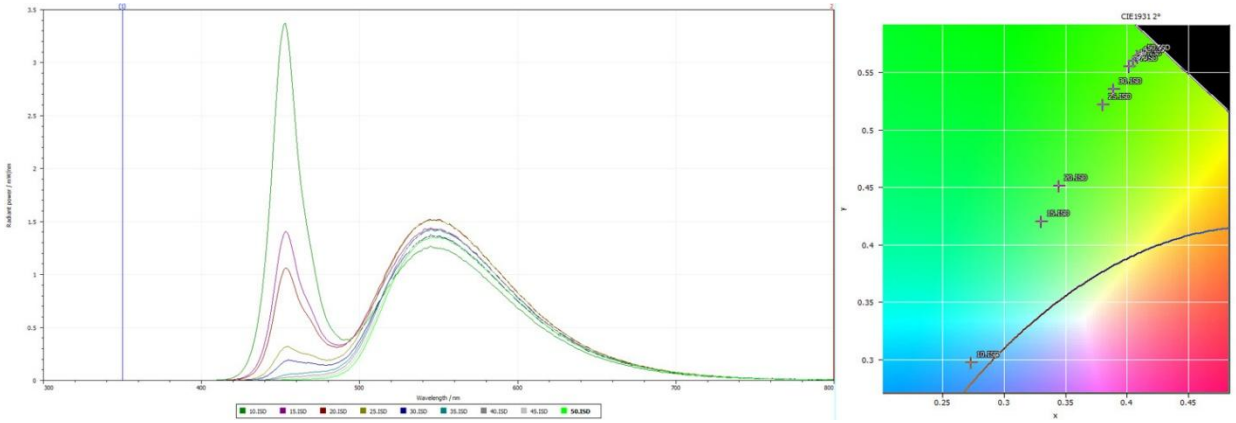

Fig. 4.15. Intematix EY4156 phosphor converted LED – SPD and chromaticity coordinates. The narrower emission spectrum of the silicate phosphor is seen in the SPD and translates directly to a more saturated green emission, especially for lower phosphor concentrations (15 – 25 %). Forward current = 350 mA.

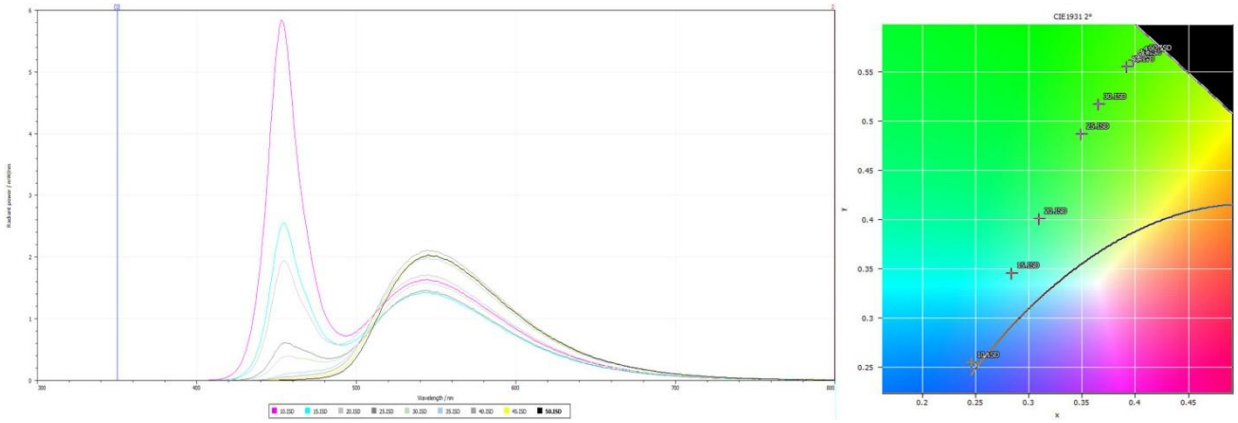

Fig. 4.16. Intematix EY4156 - forward current = 700 mA. A strong blue shift of the lower concentrations indicates severe thermal quenching problems. The phosphor is operating beyond its thermal limits.

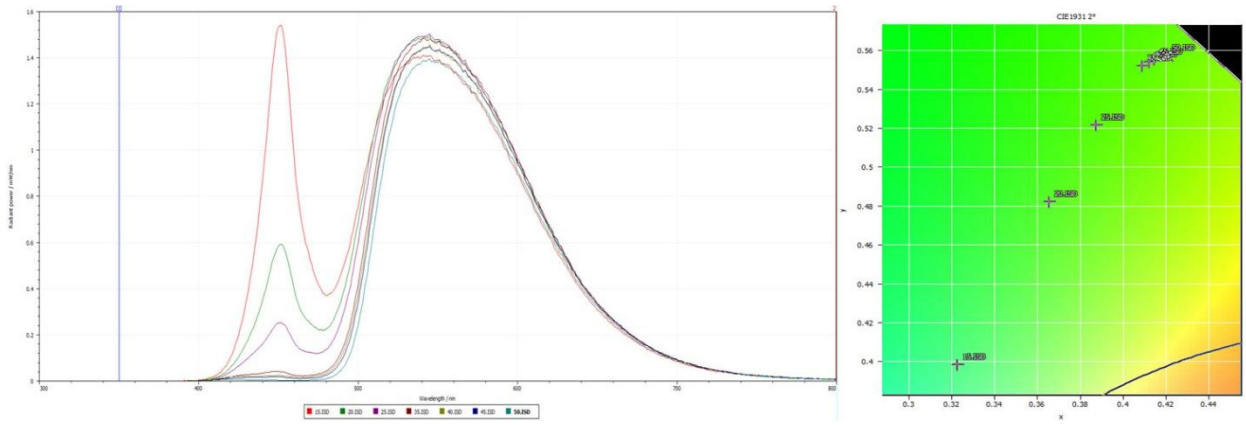

Fig. 4.17. Intematix NYAG4156 – SPD and chromaticity coordinates. The YAG phosphor converted LED provides a relatively narrow-band green emission resulting in saturated chromaticity points. Forward current = 350 mA.

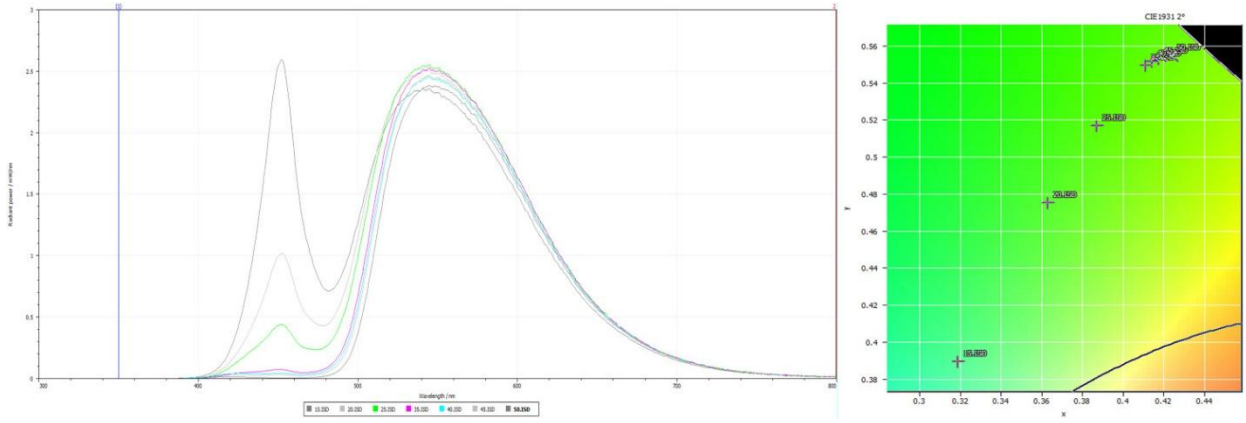

Fig. 4.18. Intematix NYAG4156 – forward current = 700 mA. A slight blue shift shows the effect of higher temperature on the quantum efficiency of the phosphor. Thermal quenching effects are clearly less severe than in the silicate phosphor and slightly better than in the aluminate material.

Table 4.1 summarises the measured radiometric power and luminous flux of each of the phosphor converted LEDs at a forward current of 350 mA and 700 mA. The purity gives a percentual indication of the saturation of the emitted light compared to the maximum attainable saturation for that dominant wavelength.

Table 4.1. Summary of all phosphor converted LED measurements.

Phosphor	Concentration (weight %)	Forward current (mA)	Purity	Radiometric power (W)	Luminous flux (lm)	Rating
GAL550	10	350	0.324	0.266	68.24	2.87
	15	350	0.073	0.224	71.81	1.85
	20	350	0.336	0.214	79.25	2.53
	25	350	0.644	0.188	76.87	3.22
	30	350	0.75	0.183	77	3.48
	35	350	0.794	0.179	75.96	3.58
	40	350	0.875	0.167	72.68	3.72
	45	350	0.896	0.167	72.99	3.78
	50	350	0.919	0.133	58.93	3.60
	10	700	0.352	0.463	115	1.49
	15	700	0.099	0.382	120.4	0.96
	20	700	0.282	0.363	132.2	1.18
	25	700	0.614	0.318	128.6	1.56
	30	700	0.726	0.305	127.3	1.69
	35	700	0.773	0.294	124.4	1.73
	40	700	0.867	0.277	120.5	1.83
	45	700	0.891	0.277	121.1	1.87
	50	700	0.916	0.254	111.9	1.85
EY4156	10	350	0.234	0.220	67.12	2.28
	15	350	0.255	0.190	74.36	2.12
	20	350	0.391	0.190	78.1	2.50
	25	350	0.711	0.169	76.79	3.27
	30	350	0.776	0.149	68.85	3.31
	35	350	0.874	0.149	71.18	3.59
	40	350	0.901	0.148	71.09	3.66
	45	350	0.919	0.140	67.96	3.65
	50	350	0.934	0.137	66.67	3.67
	10	700	0.368	0.333	89.45	1.24
	15	700	0.161	0.224	72.22	0.71
	20	700	0.146	0.238	88.95	0.72
	25	700	0.513	0.173	73.96	1.10
	30	700	0.653	0.179	79.92	1.32
	35	700	0.847	0.209	98.97	1.66
	40	700	0.885	0.218	104.6	1.73
	45	700	0.909	0.207	100	1.74
	50	700	0.929	0.205	99.5	1.77
NYAG4156	15	350	0.168	0.218	80.02	2.08
	20	350	0.547	0.199	83.12	3.02
	25	350	0.731	0.187	82.59	3.46
	30	350	0.888	0.172	80.22	3.80
	40	350	0.902	0.167	77.98	3.80
	45	350	0.914	0.166	77.87	3.83
	50	350	0.937	0.156	74.14	3.82
	15	700	0.131	0.373	133.7	0.99
	20	700	0.518	0.338	139.4	1.46
	25	700	0.714	0.319	139.8	1.70
	35	700	0.886	0.293	135.5	1.89
	40	700	0.901	0.283	131.4	1.89
	45	700	0.915	0.281	131.4	1.91
	50	700	0.940	0.267	125.9	1.91

The table gives a rating to each LED calculated as follows

$$Rating = \frac{p+\frac{P_{opc}}{P_{opp}}}{I_f} \quad \text{(Eq. 4.1)}$$

With

p = purity of the phosphor-converted LED spectrum

P_{opc} = radiometric power of the phosphor-converted LED

P_{opp} = radiometric power of the blue pump before phosphor conversion

Red highlighted numbers are resulting from dominant wavelengths other than those located in the yellow-green area of the chromaticity diagram and should be disregarded. Rating numbers above 3.70 are highlighted green and represent the top choices. Lower drive currents clearly result in higher efficiencies represented by higher rating scores. Due to the relatively strong thermal quenching of the silicate material, rating scores are lower, especially at higher forward currents and phosphor concentrations. The best performing phosphor is the YAG-based NYAG4156 at a concentration of 45 % phosphor to encapsulant weight (rating score = 3.83). A prototype spectrally tuneable light engine was designed and built using 10 Luxeon Rebel Royal blue LEDs combined with an Intematix NYAG4156 phosphor deposition. Full details can be found in chapter 4.5.4.

Shortly after finishing the prototype light engine, Lumileds introduced the Luxeon Z portfolio of LEDs, including a "lime green" variant that uses violet pump emitting at 425 nm combined with a ceramic phosphor plate (first mentioned in LEDs Magazine, December 2012). The LED has a peak wavelength of 545 nm and an average efficacy of 120 lm/W (76, 77).

A LED market report, presented below, lists the major manufacturers and gives a detailed list of their high-power LED ($I_f \geq 350$ mA) inventory as of 2014. This report, together with the result from the green-gap experiments described above, will serve as the basis to select the LEDs to be used in the design of the spectrally tuneable light engines.

Table 4.2. Top-ten LED manufacturers (2012) (78)

Rank #	Company	Growth in 2012
1.	Nichia	+5%
2.	Samsung	+22%
3.	Osram Opto	+5%
4.	LG Innotek	-1%
5.	Seoul Semi	+14%
6.	Philips Lumileds	+21%
7.	Cree	+18%
8.	Toyoda Gosei	+37%
9.	Sharp	+14%
10.	Everlight	-1%

From the top-ten companies listed in Table 4.2, only four (in red) have a product portfolio including high power devices (input power ≥ 1 W) spread over more than four monochromatic wavelengths. Other manufactures focus mainly on phosphor-converted white LEDs while offering a selected number of discrete wavelengths, usually in the blue, green, red and amber regions of the spectrum.

Table 4.3. Osram Opto coloured LED product range (2014)

Model	Peak Wavelength	Max. Current	(Luminous) flux @ 350mA	Footprint
LR W5SM	632nm	1000mA	50lm	6x11x1.8mm
LA W5SM	624nm	1000mA	60lm	6x11x1.8mm
LY W5SM	597nm	1000mA	40lm	6x11x1.8mm
LCY W5SM	615nm (PC)	500mA	56lm	6x11x1.8mm
LT W5SM	520nm	1000mA	81lm	6x11x1.8mm
LD W5SM	449nm	1000mA	412mW	6x11x1.8mm
LB W5SM	465nm	1000mA	25lm	6x11x1.8mm
LA H9GP	624nm	1000mA	75lm	3.85x3.85x2.3mm
LY H9GP	597nm	1000mA	60lm	3.85x3.85x2.3mm
LR H9GP	632nm	1000mA	60lm	3.85x3.85x2.3mm
LT H9GP	520nm	1000mA	87lm	3.85x3.85x2.3mm
LD H9GP	449nm	1000mA	635mW	3.85x3.85x2.3mm
LB H9GP	465nm	1000mA	27lm	3.85x3.85x2.3mm
LCY H9PP	615nm	700mA	65lm	3.75x3.75x0.7mm
LA H9PP	624nm	1000mA	64lm	3.75x3.75x0.7mm
LR H9PP	632nm	1000mA	55lm	3.75x3.75x0.7mm
LS H9PP	645nm	1000mA	47lm	3.75x3.75x0.7mm
LY H9PP	597nm	1000mA	55lm	3.75x3.75x0.7mm
LH CP7P	660nm	1000mA	365mW	
LA CP7P	624nm	1000mA	64lm	3.0x3.0x2.23mm
LY CP7P	597nm	1000mA	55lm	3.0x3.0x2.23mm
LCY CLBP	585nm (PC)	1000mA	92lm	3.0x3.0x2.23mm
LB CP7P	450nm (PC)	1000mA	55lm	3.0x3.0x2.23mm
LV CP7P	503nm	1000mA	82lm	3.0x3.0x2.23mm
LCY CEUP	585nm (PC)	1000mA	75lm	1.90x1.50x0.75mm
LUW CQAR	550nm (PC)	1500mA	189lm	3.0x3.0x1.88mm
LE A Q9WN	624nm	1000mA	48lm	3.48x3.48x1.20
LCG H9RN	515nm (PC)	1000mA	180lm	3.75x3.75x0.5mm
LE B Q9WN	455nm	1000mA	420mW	3.48x3.48x1.20
LR W5SN	632nm	1000mA	41lm	6.0x6.0x1.8mm
LA W5SN	624nm	1000mA	48lm	6.0x6.0x1.8mm
LY W5SN	597nm	1000mA	65lm	6.0x6.0x1.8mm
LD W5SN	449nm	1000mA	405mW	6.0x6.0x1.8mm
LB W5SN	465nm	1000mA	22lm	6.0x6.0x1.8mm
LT W5SN	520nm	1000mA	70lm	6.0x6.0x1.8mm
LV W5SN	503nm	1000mA	60lm	6.0x6.0x1.8mm

Table 4.4. Lumileds coloured LED product range (2014)

Model	Dominant Wavelength	Max. Current	(Luminous) flux @ 350mA	Footprint
LXML-PR01	447.5nm	1000mA	520mW	4.50x3.50x2.0mm
LXML-PR02	447.5nm	1000mA	616mW	4.50x3.50x2.0mm
LXML-PB01	470nm	1000mA	41lm	4.50x3.50x2.0mm
LXML-PB02	470nm	1000mA	46lm	4.50x3.50x2.0mm
LXML-PE01	505nm	1000mA	83lm	4.50x3.50x2.0mm
LXML-PM01	530nm	1000mA	102lm	4.50x3.50x2.0mm
LXML-PX02	567.5nm (PC)	1000mA	148lm	4.50x3.50x2.0mm
LXM2-PL01	591nm (PC)	700mA	112lm	4.50x3.50x2.0mm
LXML-PL01	590nm	700mA	61lm	4.50x3.50x2.0mm
LXM2-PH01	617nm	700mA	72lm	4.50x3.50x2.0mm
LXM2-PD01	627nm	700mA	62lm	4.50x3.50x2.0mm
LXM3-PD01	655nm	700mA	360mW	4.50x3.50x2.0mm
LXZ1-PR01	447.5nm	1000mA	487mW	1.30x1.70x0.7mm
LXZ1-PB01	470nm	1000mA	33lm	1.30x1.70x0.7mm
LXZ1-PE01	505nm	1000mA	56lm	1.30x1.70x0.7mm
LXZ1-PM01	530nm	1000mA	85lm	1.30x1.70x0.7mm
LXZ1-PX01	567.5nm (PC)	1000mA	147lm	1.30x1.70x0.7mm
LXZ1-PL02	591nm (PC)	700mA	69lm	1.30x1.70x0.7mm
LXZ1-PL01	590nm	700mA	50lm	1.30x1.70x0.95mm
LXZ1-PH01	617nm	700mA	55lm	1.30x1.70x0.95mm
LXZ1-PD01	627nm	700mA	43lm	1.30x1.70x0.95mm
LXZ1-PA01	655nm	700mA	255mW	1.30x1.70x0.95mm
LHUV-0425	425nm	1000mA	500mW	1.30x1.70x0.7mm
LHUV-0420	420nm	1000mA	500mW	1.30x1.70x0.7mm
LHUV-0415	415nm	1000mA	500mW	1.30x1.70x0.7mm
LHUV-0410	410nm	1000mA	500mW	1.30x1.70x0.7mm
LHUV-0405	405nm	1000mA	500mW	1.30x1.70x0.7mm
LHUV-0400	400nm	1000mA	393mW	1.30x1.70x0.7mm
LHUV-0395	395nm	1000mA	393mW	1.30x1.70x0.7mm
LHUV-0390	390nm	1000mA	353mW	1.30x1.70x0.7mm
LHUV-0385	385nm	1000mA	206mW	1.30x1.70x0.7mm
LHUV-0380	380nm	1000mA	169mW	1.30x1.70x0.7mm

Table 4.5. Cree Inc. coloured LED product range (2014)

Model	Dominant Wavelength	Max. Current	(Luminous) Flux @ 350mA	Footprint
Xlamp XP-E	450nm	1000mA	475mW	3.45 x 3.45 x 2mm
Xlamp XP-E	470nm	1000mA	35lm	3.45 x 3.45 x 2mm
Xlamp XP-E	525nm	1000mA	96lm	3.45 x 3.45 x 2mm
Xlamp XP-E	590nm	500mA	68lm	3.45 x 3.45 x 2mm
Xlamp XP-E	615nm	700mA	72lm	3.45 x 3.45 x 2mm
Xlamp XP-E	625nm	700mA	60lm	3.45 x 3.45 x 2mm
Xlamp XP-E2	450nm	1000mA	512mW	3.45 x 3.45 x 2.26mm
Xlamp XP-E3	470nm	1000mA	39lm	3.45 x 3.45 x 2.26mm
Xlamp XP-E4	525nm	1000mA	105lm	3.45 x 3.45 x 2.26mm
Xlamp XP-E5	590nm	1000mA	47lm	3.45 x 3.45 x 2.26mm
Xlamp XP-E6	590nm (PC)	1000mA	94lm	3.45 x 3.45 x 2.26mm
Xlamp XP-E7	615nm	1000mA	81lm	3.45 x 3.45 x 2.26mm
Xlamp XP-E8	625nm	1000mA	65lm	3.45 x 3.45 x 2.26mm
Xlamp XQ-E	470nm	1000mA	38lm	1.60 x 1.60 x 1.44mm
Xlamp XQ-E	525nm	1000mA	104lm	1.60 x 1.60 x 1.44mm
Xlamp XQ-E	590nm (PC)	1000mA	77lm	1.60 x 1.60 x 1.44mm
Xlamp XQ-E	615nm	1000mA	77lm	1.60 x 1.60 x 1.44mm
Xlamp XQ-E	625nm	1000mA	65lm	1.60 x 1.60 x 1.44mm
Xlamp XR-E	450nm	1000mA	475mW	9 x 7 x 4.4mm
Xlamp XR-E	470nm	1000mA	35lm	10 x 7 x 4.4mm
Xlamp XR-E	525nm	700mA	96lm	11 x 7 x 4.4mm

Xlamp XT-E	450nm	1000mA	538mW	3.45 x 3.45 x 2.35mm
Xlamp XB-D	450nm	1000mA	500mW	2.45 x 2.45 x 1.84mm
Xlamp XB-D	470nm	1000mA	35lm	2.45 x 2.45 x 1.84mm
Xlamp XB-D	525nm	1000mA	97lm	2.45 x 2.45 x 1.84mm
Xlamp XB-D	590nm	1000mA	65lm	2.45 x 2.45 x 1.84mm
Xlamp XB-D	615nm	1000mA	87lm	2.45 x 2.45 x 1.84mm
Xlamp XB-D	625nm	1000mA	62lm	2.45 x 2.45 x 1.84mm
Xlamp XP-C	450nm	500mA	300mW	3.45 x 3.45 x 2mm
Xlamp XP-C	470nm	500mA	27lm	3.45 x 3.45 x 2mm
Xlamp XP-C	525nm	500mA	65lm	3.45 x 3.45 x 2mm
Xlamp XP-C	590nm	350mA	48lm	3.45 x 3.45 x 2mm
Xlamp XP-C	615nm	350mA	59lm	3.45 x 3.45 x 2mm
Xlamp XP-C	625nm	350mA	48lm	3.45 x 3.45 x 2mm
Xlamp XR-C	450nm	500mA	275mW	9 x 7 x 4.4mm
Xlamp XR-C	470nm	500mA	16lm	10 x 7 x 4.4mm
Xlamp XR-C	525nm	500mA	46lm	11 x 7 x 4.4mm
Xlamp XR-C	590nm	350mA	32lm	12 x 7 x 4.4mm
Xlamp XR-C	615nm	700mA	35lm	13 x 7 x 4.4mm
Xlamp XR-C	625nm	700mA	32lm	14 x 7 x 4.4mm

Osram Opto, Lumileds Lighting and Cree inc. all offer a wide selection of efficient, high power LEDs in a small footprint. In the critical yellow and yellow-green area (540-600 nm) all three manufacturers have their solution to overcome the green-gap problem. Cree, Osram and Lumileds have a phosphor converted Amber LED (Osram LCY CLBP and LCY CEUP, Cree Xlamp XP-E6 and Xlamp XQ-E, Philips Lumileds LXM2-PL01 and LXZ1-PL02), drastically improving the thermal droop issues associated with AlInGaP LEDs in that wavelength range. Only Osram and Lumileds provide a solution in the 540-570 nm range (Osram LUW CQAR, Philips Lumileds LXML-PX02 and LXZ1-PX01). The Osram LUW CQAR series, however, is intended to be the provider of both blue and green wavelengths which, combined with red LEDs, results in a novel warm-white light engine. The high amount of blue light in its spectrum, and thus low colour saturation, makes it a poor yellow-green light candidate. The Lime-Green Luxeon LXZ1 series

developed by Lumileds is a fully converted LED light source and provides a very saturated yellow-green light with a spectral peak at 540 nm, completely lacking any radiation in the blue wavelengths. Both Osram and Lumileds manufacture LEDs in the deep-red wavelengths near 700 nm while the short wavelength range is covered only by Lumiled's Luxeon LHUV UV series.

Osram fails to deliver its range of wavelengths in one singe LED package size. This poses a rather complicated issue when integrating the LEDs in the optical and thermal system, as an LED with a different footprint will have different optical and thermal characteristics. Lumileds delivers a wide range of wavelengths in compact footprints. Osram, Cree and Lumileds´s high power LEDs are all based on ceramic packaging technology. The alumina substrate has a low thermal resistance which helps to provide a low-resistance thermal path from the LED junction to the heatsink. Philips is the sole manufacturer using *flip-chip technology* for its InGaN based devices. Instead of wire-bonding the electrical contacts to the top surface of the semiconductor *die,* it is flipped upside-down and soldered directly to the current-supply contact points on the LED package. The advantage is a thermal path of lower resistance and a higher efficacy due to the absence of light-blocking bonding wires.

4.2 LED drivers

LEDs, like all diodes, conduct current only when the p-type material is at a higher potential than the n-type semiconductor. In this so called *forward bias* regime, electrons pass from the n-region to the p-region and an opposite current flows from the anode of the diode (positive terminal) towards the cathode (negative terminal). The diffusing carriers eventually recombine and emit photons.

The current-voltage characteristic of an (ideal) diode is given by the Shockley ideal diode equation

$$I = I_S\left(e^{\frac{V_D}{nV_T}} - 1\right) \qquad \text{(Eq. 4.2)}$$

With

I the diode current

I_S the reverse bias saturation current

V_D the voltage across the junction

V_T the thermal voltage

n the ideality factor which depends on the semiconductor material and the manufacturing process.

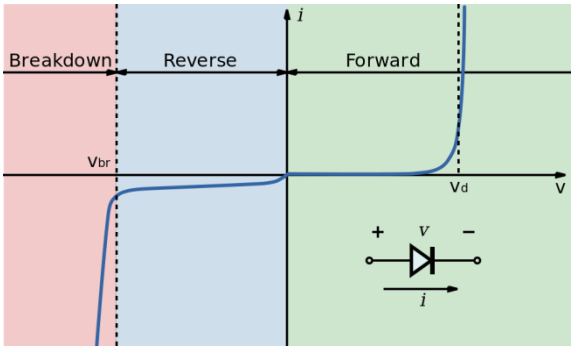

Fig. 4.19. Diode I, V plot showing the current through the junction in function of the voltage across it.

The above I, V plot illustrates that once the threshold voltage is reached, the current through the junction rises exponentially (Fig. 4.19). The threshold voltage depends on the bandgap energy of the semiconductor (typically 0.7 V for Si, 1.4 V for GaAs and 2.9 V for InGaN). This clearly shows that diodes, and therefore LEDs, are *current driven devices*: a small change in forward voltage results in a very large change in current through the junction.

In practice, this means that the current through the LED has to be limited. If not, a small change in forward voltage, introduced by fluctuations in the power source or through temperature effects, will have large effects on the light output. A small decrease in supply voltage will have an exponential effect on the current-flow, possibly extinguishing the LED completely. On the other hand, a small increase in supply voltage will cause an abnormally large current flow through the die, probably damaging the junction.

4.2.1 Resistor based current limiting

The easiest method to control the current flow through an LED is a series resistor (Fig. 4.20)

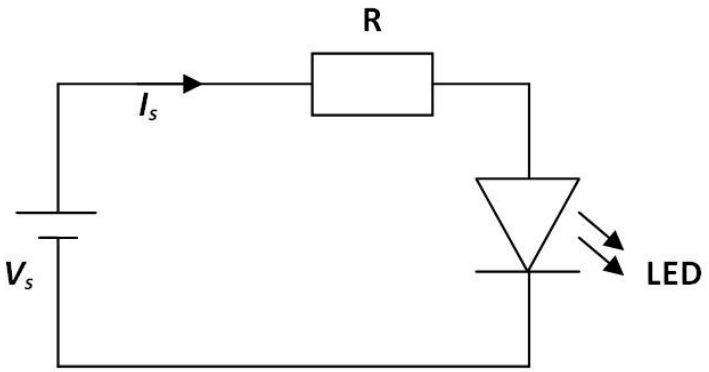

Fig. 4.20. Resistor-based LED driver.

Ohms law states that current in a series circuit equals a voltage V divided by a resistance R. In the above schematic this translates to

$$I_s = \frac{V_s - V_{fLED}}{R} \qquad \text{(Eq. 4.3)}$$

With

$I_s = I_{LED}$, the current flowing through the circuit

V_s the voltage provided by the source

V_{fLED} the forward voltage of the LED at a certain forward current

R the resistance of the current limiting resistor

Fig. 4.21 shows the current flow in function of the supply voltage for a typical high-power LED with a forward voltage of 3.2 V at 350 mA (red). A resistor value of 5.14 Ohm is chosen to limit the current to 350 mA at a supply voltage of 5 V. While it is clear that a series resistor results in a linear I, V characteristic, the LED current (I_{LED}) is still dependant on the supply voltage (V_s).

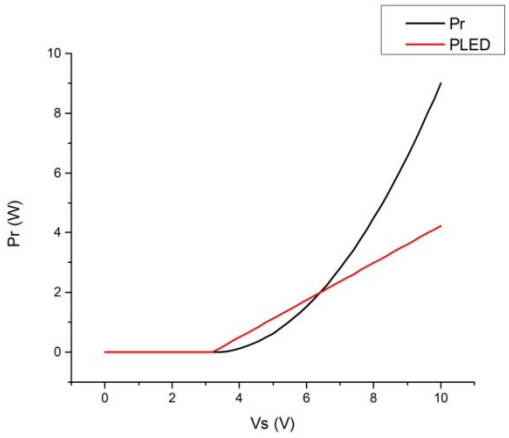

Fig. 4.21. Power dissipated by the LED (black) and in the resistor (red) in function of the supply voltage in a resistor-based current-limited LED circuit (V_{fLED} = 3.2V) .

The efficiency of the circuit is in direct relation with the difference between the supply voltage and the LED´s forward voltage. The larger this difference, the more power has to be dissipated by the current-limiting resistor and the lower the efficiency (Fig. 4.21, black). Note that a resistor-based LED driver needs a supply voltage equal or higher than the forward voltage of the LED. The voltage dependency and variable efficiency of the circuit means its primary application is limited to low-power, low-cost designs.

4.2.2 Linear current regulators

Linear regulators act as a smart, variable resistor and provide a constant current independent of the supply voltage. They operate by using a voltage-controlled current source that gets feedback from a sense resistor located in series with the load (in this case, an LED).

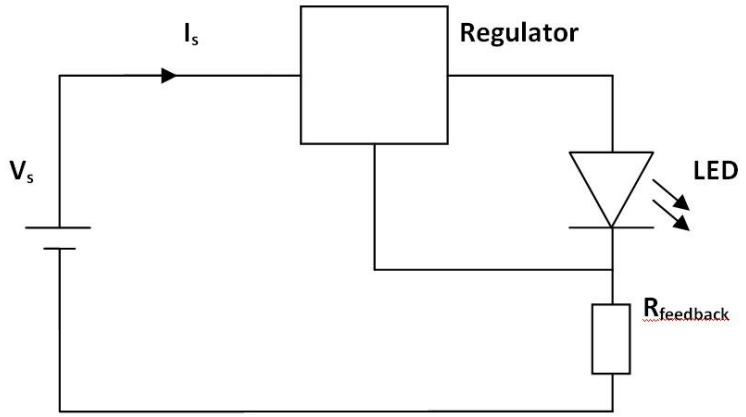

Fig. 4.22. Linear constant-current LED driver.

Fig. 4.22 shows the principal components of a linear constant-current LED driver. An error amplifier inside the current source receives feedback from the series connected resistor (R_f) to set the current. The amplifier in its turn is connected to the base of a PNP transistor driving a NPN darlington configuration. The error amplifier ensures a constant voltage across the feedback resistor which guarantees a constant current through the series connected LED. Similar to a resistor-based current source, the efficiency of a linear regulator depends on the difference between the source voltage and the forward voltage of the LED. Any voltage higher than the forward voltage of the LED will cause heat generation within the regulator.

On top of that, a small overhead voltage has to be provided to ensure correct output regulation. The standard Darlington regulator described above needs a minimum drop-out voltage of 1.5 to 2.2 V. Low drop-out versions have a slightly different topology and require as little as 0.7 V of overhead voltage to work correctly. It is important to note that a sudden change in supply voltage will cause spikes in the LED current as the regulator has a transient response: the feedback loop needs a certain time to correct the output when the input conditions change.

Low drop-out linear regulators are an excellent choice in low to medium power circuits where the supply voltage is slightly higher (but never lower) than the forward voltage of the LED. Usually, only the regulator itself and a small capacitor to ensure stable behaviour is all that is needed to provide a voltage independent current to an LED light source (79).

4.2.3 Switching regulators

Switching regulators are widely used to provide a constant current to LED light sources. To understand the working principle of a switching regulator, one has to keep two characteristics that directly follow the law of inductance in mind:

- A current flowing through an inductor that changes with time induces a voltage across that inductor.
- The rate of change of the current flowing through the inductor determines the size of the induced voltage difference.

$$v(t) = L\frac{di}{dt} \quad \text{(Eq. 4.4)}$$

With

$v(t)$ the induced voltage

L the inductance of the inductor

$i(t)$ the current flowing through the inductor

While linear regulators provide a desired current to the LED by dissipating excess power as heat, a switching regulator stores energy in the magnetic field of an inductor and then discharges this energy into the load. This is a reversible, energy loss-free process. The switching process itself is handled by a transistor or FET operating outside its active region to ensure extremely low losses. The current is regulated by controlling either the switching frequency or the on to off-time ratio (PWM or Pulse Width Modulation).

Although there is a large number of switching regulator topologies, they can be divided in 3 classes:

- Buck regulators provide a lower output voltage, but higher output current than the source supplies to the input of the regulator
- Boost converters provide a higher output voltage at a lower output current than presented at the input of the regulator
- Buck-boost regulators can work in either buck or boost regime

All three are non-isolated systems, meaning that there is no electrical barrier between the input and output of the regulator. This can possess a serious safety risk when using high input voltages.

4.2.3.1 Buck regulators

Buck regulators are commonly used when high-power LEDs with a forward voltage significantly lower than the supply voltage have to be powered. A basic buck-regulator based LED driver (Fig. 4.23) consists of a FET-based switch (S), an inductor (L), a capacitor (C) , a diode (D) and a feedback resistor (R_f).

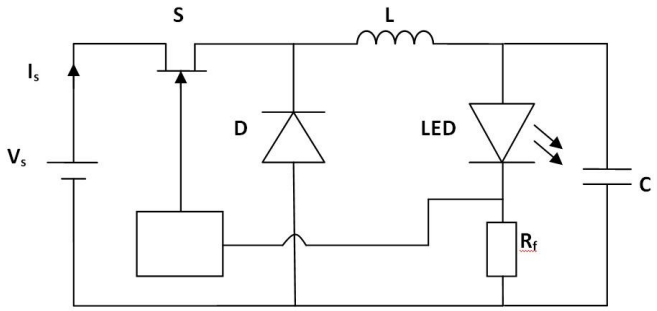

Fig. 4.23. Buck regulator schematic diagram.

When the switch closes, current flows into the inductor. The diode is reverse-biased and thus does not conduct. The current in the inductor increases according to Equation 46 and additional energy is stored in its magnetic field. After a certain time, the switch is opened. When the voltage across the inductor is higher than the forward voltage of the diode, it conducts the current stored in the magnetic field of the inductor. The feedback resistor provides a reference voltage that controls the frequency of PWM controller driving the FET. When that voltage, and thus the current flowing through the LED, drops below the set point, the switch closes and the cycle starts over. While the input current pulsates with the on and off periods of the FET, the output current is near constant. The capacitor plays only a minor role in providing a smooth DC waveform with a low amount of *ripple.*

4.2.3.2 Boost regulators

The boost regulator, pictured below in Fig. 4.24, consists of an inductor (L), FET (S), diode (D), capacitor (C) and a feedback resistor (R_f).

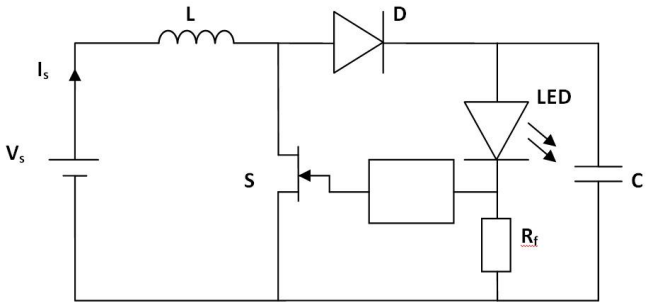

Fig. 4.24. Boost regulator diagram.

When the FET closes, the diode is reverse-biased by the output voltage stored in the capacitor. The current in the inductor increases and energy is stored in its magnetic field. Upon opening the FET, the sudden change in current induces a voltage in the inductor. The diode is forward biased and places the inductor in series with the source voltage which charges the capacitor with a voltage higher than the input voltage of the regulator. When the FET is not conducting, the current through the LED is provided both by the source and capacitor while during its conductive state the LED current is provided solely by the output capacitor. A boost regulator has a continuous input current, but discontinues output current. The feedback resistor once again generates a voltage that is used by external circuitry to set the frequency or duty cycle of the FET controller.

Most buck and boost converters operate in a so called *continuous mode* which implies that the current in the inductor never drops to zero. In low-power applications one can downsize the inductor size and operate the converter in discontinuous mode.

4.2.3.3 Buck-boost regulators

A buck-boost converter generates a negative output current (polarity opposite to the polarity of the input) that can be either higher or lower than the input current. The basic components are identical to the ones used in the buck and boost regulators with a FET (S), inductor (L), diode (D), capacitor (C) and feedback resistor (R_f) (Fig. 4.25).

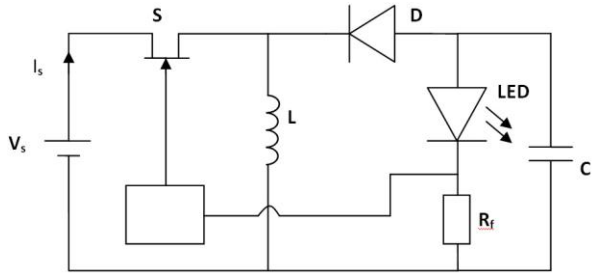

Fig. 4.25. Buck-boost regulator schematic diagram.

When the FET conducts, the input voltage causes an increasing current flow through the inductor. At this moment, the current through the LED is supplied by the capacitor. When the FET opens, the diode is forward-biased and sudden change in voltage over the inductor causes current to flow from the inductor into the capacitor and parallel connected LED. As the supply is never directly connected to the LED, all the energy comes from the magnetic field of the inductor. The output voltage is a direct function of the duty cycle or frequency of the FET driver.

Typical switching frequencies range from 20 kHz to several MHz. The rapidly changing magnetic field in the inductor generates a large amount of electromagnetic noise directly in the cables and components of the illumination system, but also noise that is being radiated in the surroundings. This is one of the main drawbacks of switching regulators. Proper filtering of the input and output stages combined with

radiation shielding prevents most of the problems regarding electromagnetic interference and compatibility.

The LED drivers discussed in the chapter above are for use in low-voltage DC applications. Many LED applications, however, are connected directly to the AC line voltage. Isolated AC to DC off-line converters can generate a DC current directly from the mains voltage. Instead of using a simple inductor, they use a high-frequency transformer. The *flyback regulator*, one of the most common and efficient topologies for low to mid-power applications, uses a single FET to switch a DC voltage or rectified AC voltage over the primary side of a transformer. When the FET is switched off, the induced magnetic field in the primary collapses and transfers energy to the secondary windings of the transformer. Because of the high switching frequency, the size of the transformer is many times smaller than a conventional 50 Hz iron core version. The ratio of primary to secondary windings and switching timings determine the output current. Higher power applications (> 500W) typically use a *half-bridge* or *full-bridge* FET configuration to drive a high-frequency transformer. Because of their isolated designs, feedback is often performed by opto-couplers instead of directly sensing the voltage of a feedback resistor.

Off-line based LED drivers have to comply with strict norms regarding electromagnetic pollution and consumer safety (voltages over 325 V DC are present when fed by a 230 V AC mains signal), which makes the design rather complicated. External circuitry ensures effective filtering and power factor correction.

4.2.4 Driving LED arrays

In most applications, a single LED will not provide enough flux. In LED-based light bulbs or luminaires, a number of LEDs may be combined to increase the total power output. For reasons of cost reduction, a large number of low-power LEDs can substitute a smaller number of high-power variants and driving each LED with a separate driver would both increase the cost and size of the product dramatically.

LEDs are current controlled devices. This means that a series connection of LEDs is the only layout that guarantees that the same current flows through each of the devices in the array (Fig. 4.26). The total forward voltage of the array is the sum of the forward voltages of each individual emitter. In practice, LEDs can be added until their combined forward voltage reaches the maximum output voltage of the constant-current driver. Forward voltage fluctuations of the LEDs, caused by temperature or semiconductor aging, have no effect on the current through the array. A large light engine, containing many LEDs, requires either a high output voltage of the driver or a large amount of drivers powering smaller sections of the light source. High circuit voltages (> 60 V) pose a significant electrical shock hazard and should be properly shielded while a large number of drivers increase the cost and size of the luminaire.

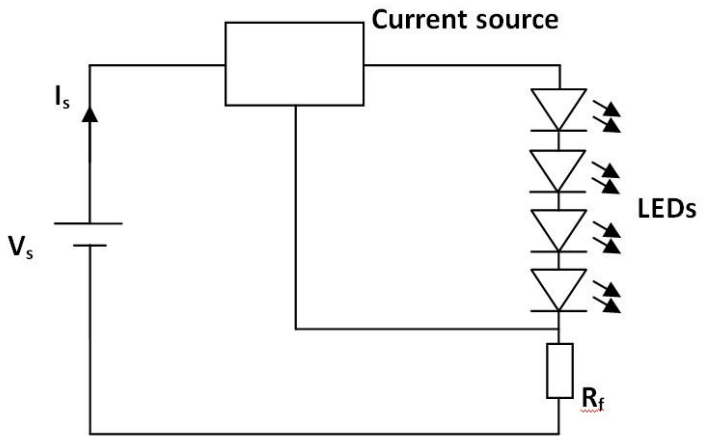

Fig. 4.26. Series connected LED array consisting of a current source, LED series string and feedback resistor (R_f). The total number of LEDs that can be connected in series is limited by the maximum output voltage of the current source.

A solution chosen by many designers is to use one single driver that shares its output current between several parallel connected strings of LEDs. A small number of series connected LEDs per string guarantees a low forward voltage and the output current of the driver is shared between each of the parallel connections (Fig. 4.27). This method lowers the circuit voltage and reduces component cost, but introduces a significant problem. Due to inherent differences in forward voltages between each of the LEDs, caused by manufacturing tolerances and local temperature variations, the current supplied by the single LED driver will be unequally divided over each parallel connection of LEDs. The string with the lowest total forward voltage will receive the highest current and vice versa. This will cause extra heating in the junctions of the LEDs of that strings causing a further drop in forward voltage resulting in a thermal runaway condition that can negatively impact the lifetime of the array or result in LED failures due to overheating. While these problems can be helped to some degree by choosing LEDs with matched forward voltages, a single-driver series-parallel circuit layout is considered bad design practice.

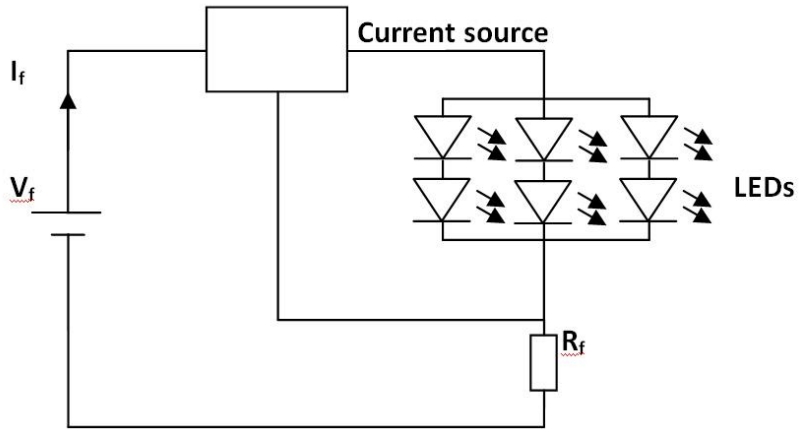

Fig. 4.27. Series – parallel connected LED-array consisting of a current source, a number of series connected LEDs connected in parallel strings and a feedback resistor (R_f). The current supplied by the current source is divided among the three parallel strings of LEDs.

An in-between solution involves placing a *ballast resistor* in series with each series connection of LEDs (Fig. 4.28). The ballast resistor should be calculated to have a voltage drop identical to the maximal summed voltage variation of all the LEDs in that series connection at the forward current of the string. This ensures that slight variations in forward voltage of individual LEDs have negligible effect on the total forward voltage and thus received current of that particular string. The clear disadvantage is the reduced efficiency as, depending on the amount of LEDs in each series string and the number of parallel circuits, a large amount of power is wasted as heat in the ballast resistors.

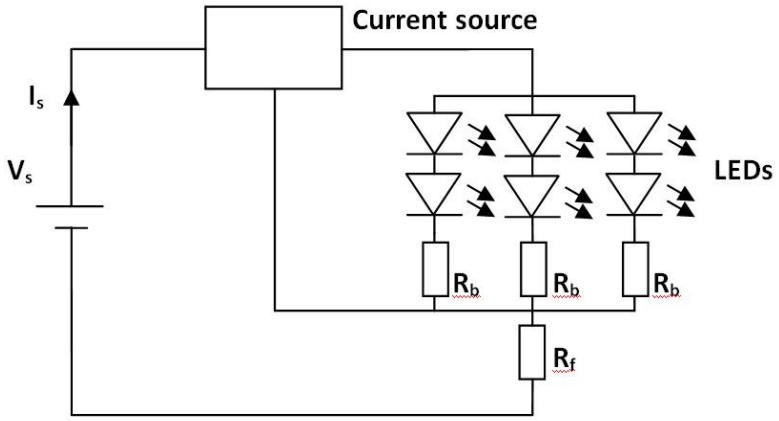

Fig. 4.28. Series – parallel connected LED array consisting of a current source, a number of series-parallel connected LEDs with individual ballast resistors (R_b) and a feedback resistor (R_f). The current supplied by the current source is divided among the three parallel strings of LEDs while the influence of forward voltage fluctuations of individual LEDs is minimized by the ballast resistors.

4.2.5 Dimming LEDs

Dimming a light source can reduce energy consumption or enhance the atmosphere. While incandescent bulbs can be dimmed from off-state to 100 % by altering their supply voltage or modifying the AC waveform (phase control dimming), other illumination technologies, such as gas discharge lamps, need more elaborate driving schemes to be dimmed below 20 to 10 %. On top of that, dimming gas discharge lamps often has a negative impact on their lifetime and efficiency.

LEDs are current controlled devices. While they cannot be dimmed using simple voltage control schemes such as the ones used to control incandescent lamps, LEDs do possess the ability to reliably emit anywhere between 0 and 100 % of their rated output power. To dim an LED, the current flowing through the junction needs to be adjusted. Changing the forward current has a number of implications on the behaviour of the device:

- Output flux does not linearly decrease with decreasing current. Although theoretically light output rises linearly with the recombination of excess charges, droop, especially in longer wavelength InGaN-based LEDs results in lower efficacy values with increasing current. As an example, Fig. 63 shows the relative flux versus the forward current for royal blue, blue, cyan and green InGaN-based Lumileds Luxeon Z LEDs at a constant junction temperature of 25 ºC. While

AlInGaP amber, red-orange, red and deep red LEDs have a fairly linear relationship, droop causes issues in longer wavelength cyan and green InGaN emitters (Fig. 4.29).

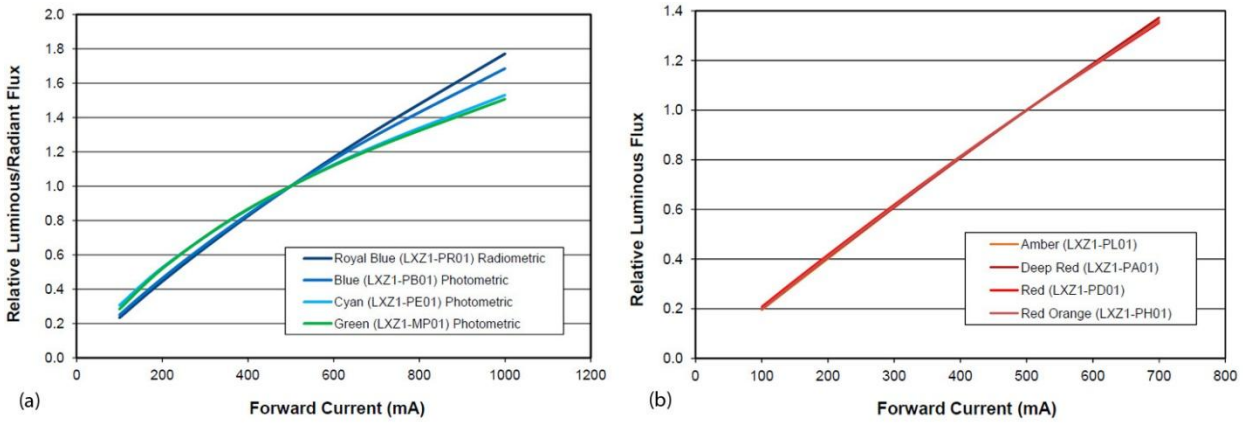

Fig. 4.29. Relative flux versus forward current for InGaN-based LEDs (a) and AlInGaP-based devices (b).

Source: http://www.lumileds.com/uploads/415/DS105-pdf

- The peak emission wavelength of an LED is dependent on the forward current. InGaN emitters exhibit a shift towards shorter wavelengths with increasing currents due to band filling and the quantum-confined Stark effect caused by indium concentration fluctuations and the thickness of the InGaN active layer . InGaN LEDs with higher indium content, necessary to fabricate green LEDs, show an increase in peak wavelength of 9 nm at 5 % of their nominal forward current (534 versus 525 nm). At a constant junction temperature, AlInGaP based LEDs show a negligible shift in peak wavelength (80).

Based on the above observation, a decision regarding the dimming method can be made. Either the LED light source can be dimmed using a constant current reduction scheme (CCR) which supplies a constant current with reduced amplitude or pulse-width modulation (PWM) which pulses the LED with constant current pulses with varying duty cycle.

CCR LED drivers have a slightly modified feedback circuit as compared to the circuits shown in sections 4.2.2 and 4.2.3. Either a variable resistor is introduced in series with the feedback resistor R_f or an external input to the PWM controller of the FET allows the injection of a dimming voltage to set the desired LED current (Fig. 4.30).

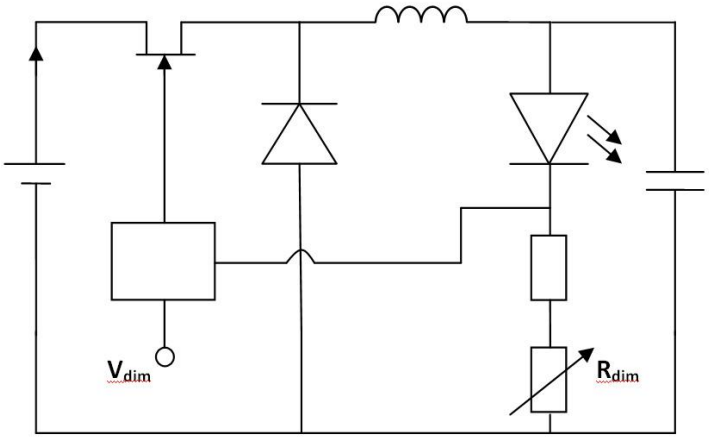

Fig. 4.30: CCR dimmable LED buck regulator, offering dimming by potentiometer (R_{dim}) or by supplying an external dimming voltage to the V_{dim} pin.

PWM is a modulation technique where the average current is controlled by switching the current supply on and off at a fast rate. The on the off ratio determines the average LED current, while the actual current during each on period is equal to the forward current and during each off period equal to zero (Fig. 4.31).

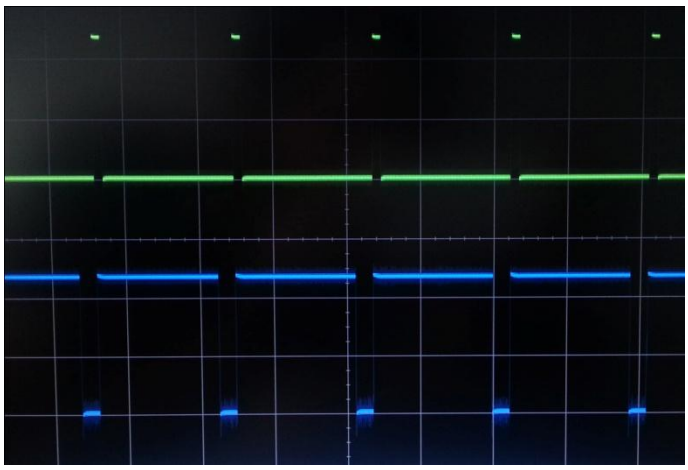

Fig. 4.31: PWM output of 2 channels of the constant current driver used in the spectrally tuneable spotlight (chapter 4.5.7). The green signal shows a current of 350 mA at a duty cycle of 10 % ($I_{average}$ = 35 mA) while the blue line shows a current of 350 mA at a duty cycle of 75 % ($I_{average}$ = 262.5 mA).

PWM dimmable LED drivers usually have an external PWM pin that switches the FET controller on or off (Fig. 4.32)

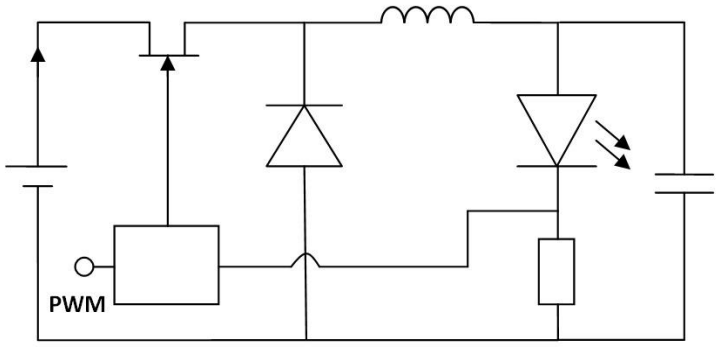

Fig. 4.32. PWM dimmable buck regulator featuring an external PWM-pin

PWM dimming results in different LED and driver behaviour when compared to CCR methods:

- Efficacy gains, especially in longer wavelength InGaN devices, due to lower forward currents are lost as PWM drivers either supply the full nominal forward current or no current at all. This also means that there is a linear relationship between the emitted flux and PWM level.
- Shifts in peak emission wavelength due to changes in forward current are nonexistent. While this might seem a relatively unimportant issue for general illumination purposes, it is absolutely crucial when multiple monochromatic LEDs are combined. Tuneable LED light sources, RGB LED-based display backlights and direct LED displays are very sensitive to slight changes in the emission characteristics of individual emitters. Any unpredictable change in either flux or peak wavelength can have a large effect on the chromaticity point of the desired illumination spectrum.
- PWM dimmable drivers cause significantly more EMI and audible noise than CCR-based LED drivers.

An important parameter in PWM dimmable LED drivers is the PWM frequency. As opposed to CCR drivers, PWM regulators do not provide a constant light output. To avoid visible flicker and eye-fatigue, the on-off frequency has to be higher than the flicker-fusion threshold of the visual system which reaches a plateau of around 60 Hz for the cones (81). However, in many cases it is possible to detect significantly higher flicker rates via the *phantom array* effect where fast moving objects, either caused by rapidly moving eyes or by object motion itself, can cause a dotted appearance at frequencies of up to 500 Hz (82). This is especially the case with high-contrast images such as a light source against a dark background and at low PWM duty cycles. For near point sources, the PWM frequency needs to be even higher. They eye can saccade more than 500 º per second. Combined with a resolution of 2 arcminutes, the theoretical maximum frequency is 15 KHz.

4.3 Thermal management

Non-perfect internal and external quantum efficiencies generate considerable amounts of heat inside the LED junction. A high-power device with a die of 1 mm^2, driven at a current of 350 mA, has a power

density near 70 W/cm^2. The generated heat, when not dissipated, will increase the junction termperature which has several consequences:

- The flux emitted by the LED drops with increasing junction temperature. Fig. 4.33 shows the relative flux of Lumileds Luxeon Z LEDs in function of the thermal pad (a section of the LED package near the die) temperature.

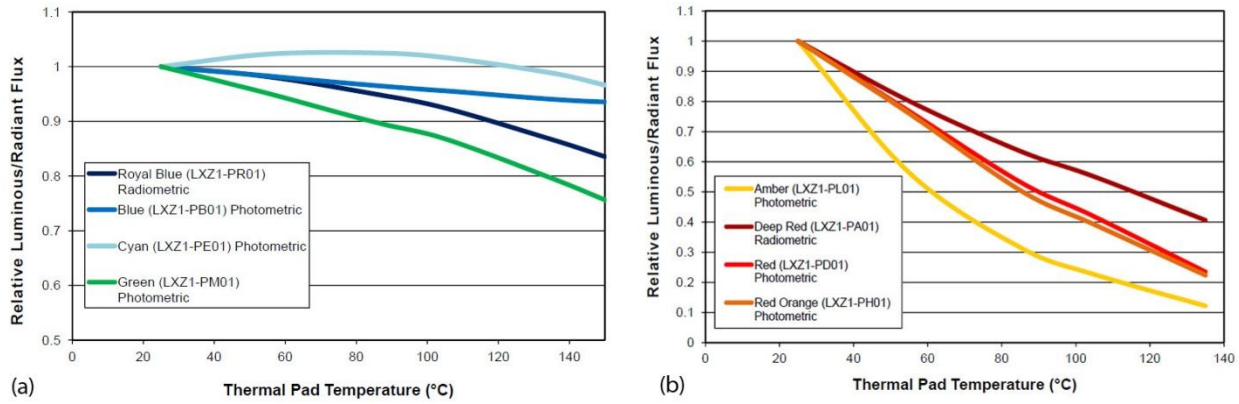

Fig. 4.33. Relative flux in function of thermal pad temperature of InGaN-based Lumileds LEDs (a) and AlInGaP-based Lumileds devices (b). Source: http://www.lumileds.com/uploads/415/DS105-pdf

The figures above clearly show a decreasing flux with increasing junction temperature. While the efficacy decrease is relatively low for InGaN based structures (18 % for a 100 º increase in thermal pad temperature in Luxeon Z green LEDs), AlInGaP-based LEDs perform much worse (83 % for the same temperature increase).

- The peak emission wavelength shifts towards longer wavelengths with increasing junction temperature. Lumileds states a typical temperature coefficient of 0.03 nm/degree for their InGaN LEDs to 0.1 nm/degree for amber emitting AlInGaP devices (Fig. 4.34).

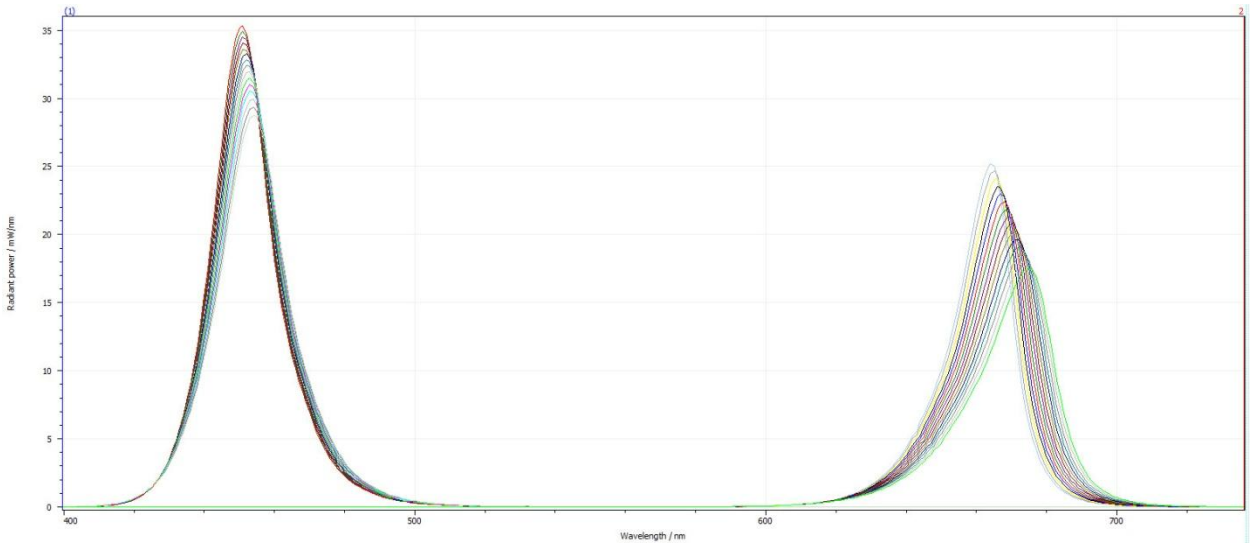

Fig. 4.34. Temperature effects on the performance of blue InGaN and red AlInGaP Lumileds Luxeon Rebel LEDs (10 ºC ≤ T_{case} ≤ 80 ºC). The comparatively large flux decrease and wavelength shift of the red LED is clearly demonstrated.

In light sources where LEDs of different wavelengths are combined to create a specific emission spectrum, this spectral shift causes noticeable changes in chromaticity coordinates. Applications that require a stable emission spectrum need, besides excellent thermal management, an active way to compensate for any spectral drift. RGB backlights for LCDs and high-end LED illumination products use colour or spectral sensors that feed real-time information to a feedback circuit that controls the current supplied to each group of LEDs.

Since a low operating current is important not only for the spectral stability and efficacy of a light source, but also to prevent catastrophic failure of the LED by delamination or cracks in the semiconductor structure, correct thermal management is required for all LED based light sources.

Heat transfer takes place by radiation, convection and conduction when there is a temperature difference between two bodies. Proper thermal management maximizes the transfer of heat between those bodies. LEDs, having a relatively low temperature, rely mainly on conduction and subsequent convection based heat transfer modes. Traditional 5 mm LEDs are limited to a few 100 mW of input power because of the high thermal resistivity of the metal wireframe holding the LED die. All the heat generated in the junction has to be dissipated in the anode and cathode legs of the LED. Modern high power LED systems are highly optimized to minimize the thermal resistance between different components and provide a solid, low resistance thermal contact point from the LED junction to the case. Thermal resistance is defined by the equation below

$$R_{th} = \frac{\Delta T}{Q} \qquad \text{(Eq. 4.5)}$$

With

ΔT the temperature difference between two components in the system and Q the thermal flux in the components in steady state.

A drawing of a typical high power LED (InGaN-based Lumileds Luxeon Z) shows how a minimalistic approach leads to a low thermal resistance from LED die to heatsink (Fig. 4.35). The semiconductor die is directly soldered to a metalized Al_2O_3 ceramic base using the flip-chip principle. There are no further layers, such as isolating dielectrics needed. This very short thermal path, combined with the excellent thermal conductivity of alumina results in a junction to case thermal resistance of only 5 º/W. Identical Lumileds AlInGaP-based devices use a traditional wire bonding technique which results in an increased junction to case thermal resistance of 8 º/W.

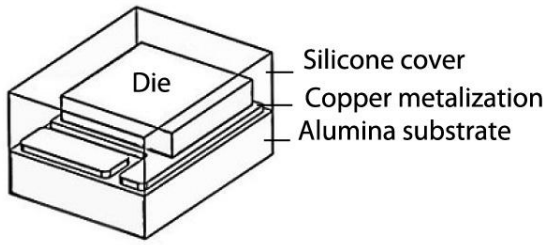

Fig. 4.35. Overview of the main heat generating and conducting components in a Lumileds Luxeon Z InGaN LED. The silicone cover adds environmental protection to the die while the underside of the Al_2O_3 substrate is metalized and can be soldered directly to a carrier PCB.

Lower thermal resistances translate directly in lower junction temperatures for an equal forward current or the possibility to drive the LED at higher power levels without overheating the semiconductor structures. Miniaturization and the demand for higher power density push the LED industry towards more compact light engines. Instead of combining separate LED packages on a single circuit board, multiple LED dies can be grouped together to form a large *chip on board* (COB) device. COB devices can contain hundreds of individual dies, spaced less than 0.2 mm from each other. With such extreme power densities, thermal management becomes crucial. High power COB LEDs use dies directly soldered to a highly conductive copper substrate for ultimate thermal conductivity.

The second step in keeping LED sources cool is providing an effective thermal path from the package to the environment. This function is performed by a heatsink that transfers heat to the environment by means of convection. Similar to a heating radiator, heatsink are devices made out of a thermally conductive material, usually a metal such as aluminium, with a number of fins to increase the contact area between the heatsink and surrounding air. Heat dissipation to the environment can be divided into active and passive cooling. Passive devices rely on natural convection processes to supply fresh cooling medium to the heat exchange area while active cooling always involves external input power to a fan or a pump. For low to medium power illumination devices, extruded aluminium heatsinks are the most common way of keeping the system thermally stable. Wide-spaced ribbed fins ensure a good convection-based airflow. Heat transfer can be significantly improved by using heat pipes to extract heat from the LED case. A heat pipe contains a liquid in a low-pressure atmosphere that is evaporated by the heat of the LEDs. The gas flows through the pipe, condenses in its colder spots and the liquid returns to the hot region by capillary action. Since there is a phase transition from liquid to gas inside the heat pipe, a large amount of heat can be transported even with a very small temperature difference between

the hot and cold side of the pipe. The cold side of the heat pipe is connected to a traditional aluminium heatsink.

Active cooling solutions use either a fan or a pump to provide a flow of cooling medium to the heat exchanger. Fan-based solutions can drastically reduce the size and weight of the illumination device by using lightweight heatsinks with dense fin population. An increased airflow increases the heat transfer coefficient, which results in a smaller and lighter heatsink for an equal thermal resistance value ($R_{th(heatsink-air)}$). Synthetic jet (synjet) technology provides a more efficient solution than fan-based systems. Synjets are produced by a periodic suction and expulsion of air through a narrow channel. The resulting flow can be directed accurately towards hotspots on the heatsink or LED module. When forced air cooling cannot provide the heat transfer needed to keep the LEDs within safe operating temperatures, liquid cooling is used. Very high package density combined with high input powers, such as in UV LEDs deployed in large format printers using UV-cureable inks, use a silicon heatsink with a microchannel structure. Water, pressurized by a pump, is forced through these microchannels. The high heat transfer capability of water removes the heat from the LEDs and transports it to a radiator located elsewhere in the cooling loop. Once the heat has been dissipated to the environment, cooled water is pumped once again towards the heatsink. While active cooling solutions enable higher package densities (and thus higher light output and higher optical efficiency, they come with a number of disadvantages

- Noise: Fans, and in a lesser degree pumps and synjets, generate acoustic noise. While this might be tolerable in large outdoor luminaires, it would be disturbing in a quiet living room environment.
- Reliability: Rotating or vibrating mechanical devices are subject to wear. Besides the catastrophic effects of failure of fans or pumps (insufficient cooling), the performance of the thermal solution over the lifetime of the illumination device has to be guaranteed.
- Efficiency: electrical fans and pumps use a certain amount of energy. A fan with a consumption of 5 W is negligible for an illumination system consuming 100 W, but represents 50 % of the energy consumption for a light engine consuming only 5 W.

When combining different heat conducting elements (LEDs, PCB, heatsink) an excellent thermal connection between each element has to be ensured. Small surface inconsistencies create air gaps between the mating surfaces. Air, being an excellent thermal insulator, hinders the conduction of heat. To prevent this, a thermal interface material (TIM) is inserted between each component in the thermal chain of the light engine. Typical gap-filling materials are silicone pastes, usually mixed with alumina or silver particles to improve thermal conductivity or soft silicone pads for less demanding applications that require a fast and clean assembly workflow.

The total thermal resistance of the device can be seen as a series-parallel circuit of individual thermal resistances of LEDs, the PCB, TIM and heatsink. The figure below shows a typical surface mount LED light engine design together with its equivalent thermal circuit.

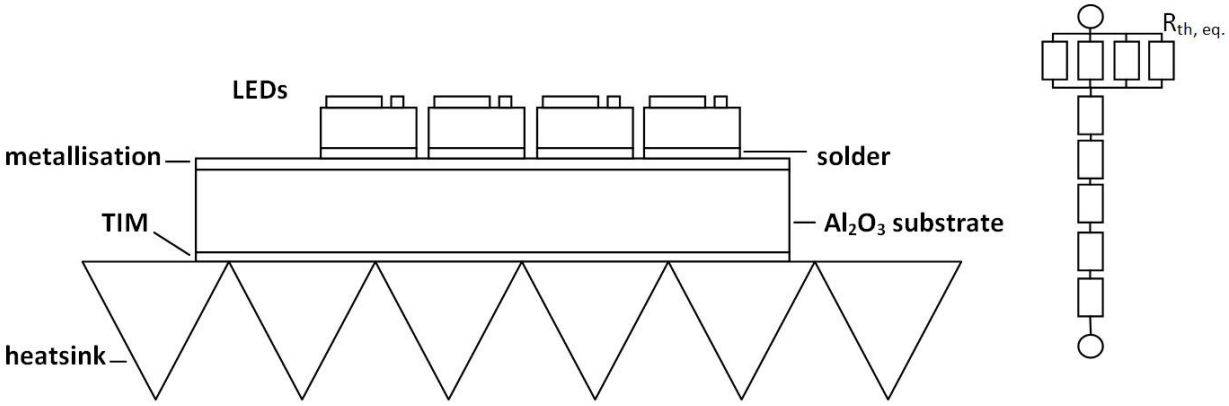

Fig. 4.36. Simplified thermal model of an LED light engine.

The combined thermal resistance of the light engine is equal to the resistance of the equivalent circuit:

$$R_{th,\,total} = R_{th,\,LED\text{-}solder}/4 + R_{th,\,solder\text{-}metalisation} + R_{th,\,metalisation\text{-}alumina} + R_{th,\,alumina\text{-}TIM} + R_{th,\,TIM\text{-}heatsink} + R_{th,\,heatsink\text{-}air} \quad \text{(Eq. 4.6)}$$

The increase in temperature from the environment can then be calculated as follows:

$$\Delta_T = R_{th,total} * P_d \quad \text{(Eq. 4.7)}$$

With P_d being the total dissipated power by the LEDs

While temperatures within an LED system can be calculated building such an equivalent circuit, a more thorough approach is preferred. Modern simulation software uses computational fluid dynamics (CFD) to simulate the interaction of gases and liquids with surfaces. Starting from an accurate computer aided design (CAD) drawing of the light engine or luminaire model, the different materials of the model are defined and boundary conditions such as air temperatures and flow rates are set. The CFD software then calculates the flow of the cooling medium through the different components and builds a model that shows in each point of the CAD drawing the evolution of temperature over time. Such computer models help to pinpoint problematic areas and improve thermal design, allowing high performance and further miniaturization (83).

4.4 Optics

While many optics, such vision-correcting lenses or camera objectives, are designed to project an accurate image of an object, most optical systems used for illumination purposes are of the nonimaging variant. Nonimaging optics simply transfer energy from a light source to a receiver where a prescribed radiation distribution pattern is produced (84).

4.4.1 Primary optics

In LED light sources, nonimaging optics provide a number of important functions. At device level, a primary function of the LEDs optics is to enhance light extraction from the semiconductor die. The refractive index of a typical InGaN material is around 2.4, which limits the escaping cone to only 23 º when the outer surface of the die is in direct contact with air. An InGaN die with smooth top surface couples only around 15 % of the light generated at the junction to the outside environment. Roughening the top layer of the semiconductor, a technique commonly used in high-power, high-efficiency LEDs, increases the extraction efficiency to 30 – 50 %. Adding an encapsulant with a refractive index of 1.6 can add another 10 to 15 % to the total light extraction.

A second function of the primary optics is to determine the radiation pattern of the LED. Most LEDs are designed to emit a lambertian radiation pattern, but batwing designs are often used in backlighting application where light has to be injected in a light guide. Modern LED packages strive towards miniaturization. Instead of using different layers of index matching silicones followed by a polycarbonate lens, the silicone protection layer on top of the LED package is shaped in the correct form to function as a primary LED optic. Very compact LED designs, such as the Lumileds Luxeon Z, omit the primary optic. While this results in a slight decrease in LED efficacy due to lower extraction efficiencies, the smaller size enables a more compact light engine design which, in its turn, enables more compact and more efficient secondary optics.

Fig. 4.37 compares the polar radiation pattern of an InGaN-based Luxeon Rebel LED with a hemispherical silicone moulded primary lens to equivalent Luxeon Z devices that lack any primary optics.

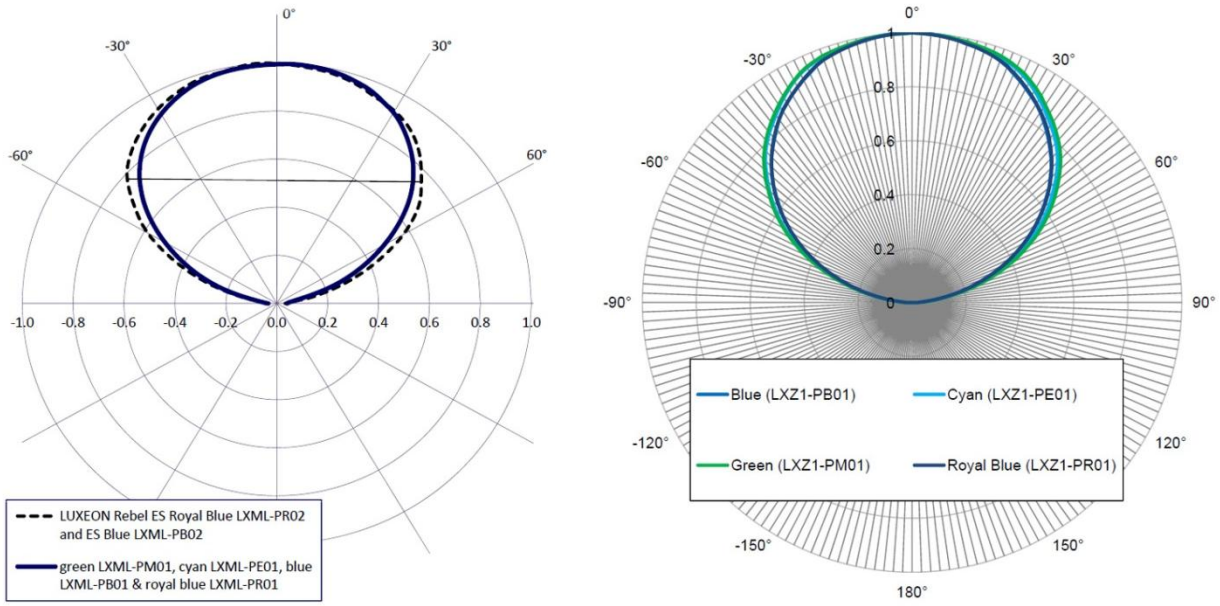

Fig. 4.37. Polar radiation pattern of InGaN Luxeon Rebel LEDs (left) versus Luxeon Z devices (right). The Z series have a near-lambertian radiation pattern while the moulded silicone lens on top of the Rebel devices results in better light extraction.

4.4.2 Secondary optics

Secondary optics collect light from the LED and form a specific illumination pattern. These optics can be either reflectors that use highly reflective surfaces, lenses that rely on total internal reflection (TIR) or hybrid systems that utilize a combination of both.

For individual LEDs, optics based on the TIR principle are very popular. They rely on the difference in refractive index between two materials (here air and PMMA or PC plastics) to confine and reflect light that hits the wall of the optic at an angle greater than the *critical angle*. The lens can be formed in such a way that the majority of the light emitted by the LED is captured, reflected off the walls and shaped into a specific beam before emerging from its front surface. The small source size of LEDs makes it possible to design compact optics that project beams ranging from simple circular distributions to freeform optics that project a complex pattern for road illumination or automotive applications. The optic is often combined with surface patterning or a diffuser on the exit aperture. The main collimator creates a semi-wide circular spot while the patterning contains microlenses that finetune the beam profiles and create smooth light fall-off at the edges of the light beam. A diffusive surface hides slight colour and luminance variations due to lens or LED imperfections and creates a smoother beam profile (Fig. 4.38). TIR optics have efficiencies between 85 and 93 %, depending on the complexity of the beam profile and the diffusing grade of the exit surface of the lens.

Fig. 4.38. LED optics showing a basic TIR lens with surface patterning to create the final beam profile: Real Spot (1), Smooth Spot (2), Diffused Spot (3), Medium (4), Oval (5) and Wide (6).

Source: http://www.ledil.com/sites/default/files/tir_lens_guide-web.pdf

Reflectors rely on specular metalised or diffuse plastic surfaces to reflect incident light rays. Contrary to TIR lenses, the reflection on such a surface is not 100 % efficient. While parabolic reflectors, projecting a

circular beam pattern, are often used, different geometries result in different beam patterns. The surface of the reflector can be patterned to smooth out the beam edges. Large changes in beam profiles are not possible by just changing the pattern or reflective material. Reflectors are used in conjunction with larger source sizes, such as LED arrays or COB devices, where a TIR optic is large, hard to design and expensive.

TIR collimators produce spots with a faster transition between light and dark at the beam edge than reflectors do. The figure below shows a schematic diagram of TIR optic and reflector with their resulting beam patterns.

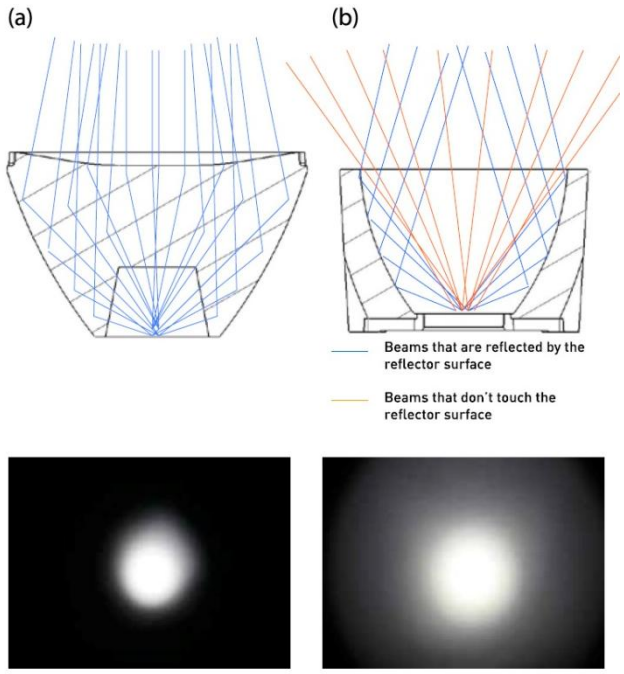

Fig. 4.39. Schematic view with ray-traces representing light beams in a TIR optic (a) and reflector (b). The lower figures are a representation of the resulting radiation patterns. Note that the reflector provides a lot more spill-light compared to the TIR lens.

Source: http://www.ledil.com/sites/default/files/tir_lens_guide-web.pdf

Certain applications that require a very narrow beam angle or a variable beam combine reflectors and TIR optics with other optics, such as condenser lenses. The TIR lens or reflector directs most of the light emitted by the LED towards the accepting surface of the condenser where it is bundled and projected on the receiver.

4.4.3 Beam homogenising

LED arrays, especially in system where LEDs of different wavelengths or CCTs are used, often require a solution to provide a homogeneous output beam, free from colour variations. Colour mixing and beam homogenising can be done either at source level or in the far field.

Far field mixing relies on carefully calculated and positioned optics to project perfectly overlapping beams from different sources. The lenses are often bundled in a single combined optic consisting out of 3 to 7 collimators. Although highly efficient (each collimator has an efficiency > 90 %), this method has a number of drawbacks

- Each collimator has to be exactly matched to the type of LED used. Different primary optics, changes in die size and even die shape of the LED will result in a difference in the projected beam pattern. This means the optic has to be redesigned when a different type of LED is used.
- When the beam from the light source crosses an object, coloured shadows will form and the colour mixing is disrupted. This effect becomes more pronounced with larger distances between individual collimators.
- The light source itself is not mixed and shows individually coloured sources when viewed directly.
- Small misalignments between the LED and collimator result in a change of the projected beam and in non-perfect colour mixing at the receiver end.
- The final source size becomes physically large when a large number of emitters are used.

The above drawbacks limit the use of far field colour and homogenising optics to applications where efficiency is the number one priority, such as architectural and stage lighting.

Source level mixing and homogenising involves a series of optics placed in between the primary optics of the LED and secondary, beam shaping reflectors or collimators. These optics act as a scatter mechanism, randomly directing light rays that pass their surface in various directions. Scattering can be done through the TIR mechanism in special structures called *mixing rods*, by normal diffuse reflection in a *mixing chamber* or by using *diffusing structures*.

The homogenisation capability of a diffuser depends on the random distribution of its scattering centres. This distribution classifies two different families of diffusers

- Volumetric diffusers consist of a large number of scattering centres throughout the whole material. The number of scattering centres and the length the light path has to follow (= thickness of the diffuser) determine the diffusive properties. Typical opal glass, PMMA or PC acts as an excellent lambertian diffuser, with the downside of transmitting only 20 to 60 % of the incident light rays. The thinner the diffuser and the less scattering centres, the more translucent the material appears and the weaker its diffusing properties are.
- Surface diffusers are transparent materials with one of the surfaces treated in such a way that incident light rays are scattered. Grounding glass creates random surface imperfections that scatter light, resulting in a Gaussian beam profile. Holographic and engineered diffusers have carefully designed microstructures on the material´s surface to direct the light in specific directions. This makes it possible to do additional beam shaping besides simply diffusing and homogenising light. Engineered diffusers that create asymmetric beam profiles are often used in LC-displays to increase the brightness in a certain direction without having to increase the flux of the backlight system. Diffusers using microstructures have typical transmission values exceeding 90 % (85).

The figure below shows the difference in light propagation between a volumetric diffuser and a surface diffuser.

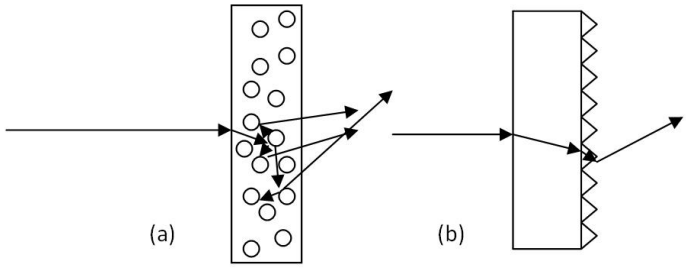

Fig. 4.40. Propagation of a light ray through a volumetric diffuser (a) and a surface diffuser (b).

Scattering of light also happens when rays hit a non-specular reflective surface, such as high reflective PTFE (Teflon®). When a diffuser cannot provide the amount of scattering necessary to provide proper beam homogenising, a different approach is necessary. Creating a highly reflective cavity can greatly improve the random scattering of light rays, which in turn improves colour mixing and removes beam artefacts.

Such a cavity, also called a mixing chamber, contains the LED circuit board on the bottom and is covered by a diffuser on top. The rest of the walls and any other non-radiating surface needs to be covered by highly reflective, non-specular materials such as microfoamed PET which offers diffuse reflectivity percentages over 97 %. The mixing chamber should be dimensioned in such a way that the diffuser is fully lit by the direct emission from the LED. If the sidewalls are too low (under filled aperture), the mixing performance will suffer and hot spots on the diffuser will show up. An over filled aperture (sidewalls too high) will results in better colour mixing, but worse efficiency due to the higher number of interactions between the light rays and reflecting material (86). A large aperture (68 mm) mixing chamber is shown in Fig. 4.41.

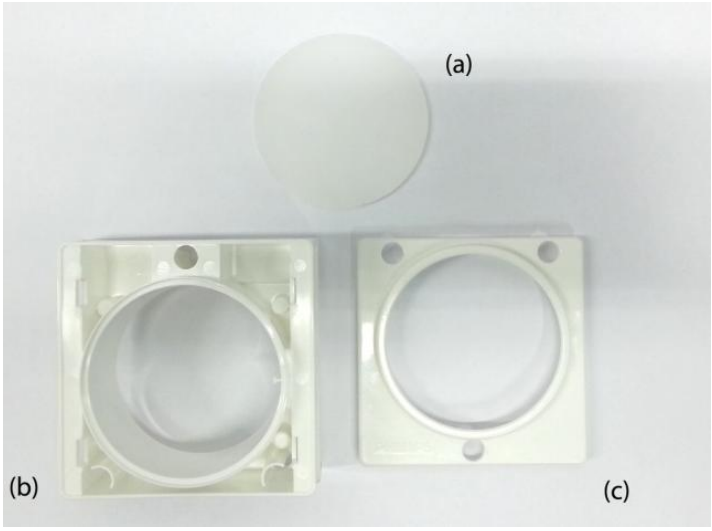

Fig. 4.41. Philips Fortimo mixing chamber. (a) top diffuser, (b) main mixing chamber lined with foamed PET, (c) top cover.

While mixing chambers are often used in combination with a remote phosphor to create white light, they can be excellent colour mixing tools. A number of secondary optics manufacturers combine compact mixing chambers with secondary TIR lenses to provide a homogeneous beam of light from RGB(W) LED sources (87). Mixing chamber achieve optical efficiencies between 60 and 85 %, depending on the dimensions of the chamber, the reflectivity of the diffuse reflector, the area of non-reflective surfaces such as LEDs and the efficiency of the top diffuser.

A more advanced version of a mixing chamber is the integrator rod. This type of optical integrator uses the TIR principle to conduct light in a light guide, providing an effective means to homogenise light sources. When light from the (LED) sources is injected in the light guide made from a higher refractive index than the surroundings, such as PMMA, it is confined within the light guide until it reaches the exit surface where the acute angle forces the light to exit the rod. The exit surface is once again topped with a diffuser that provides a lambertian radiation pattern. Integrator rods can have a circular, square or multi-angled shapes. Longer rods provide more opportunities for a light ray to reflect from one the sidewalls and thus provide better beam homogenisation. A circular cross section has worse homogenisation properties than a multi-angled or square cross sectioned integrators. Besides the cross section, the material of the rod and its length influence the optical efficiency. As TIR is a 100 percent efficient process, losses within the integrator rod are limited to absorption losses in the material used to construct the integrator, making high transparency glass or PMMA preferred choices. The efficiency of the integrator system can be further increased by improving the incoupling efficiency of the sources through the application of antireflective coatings or optical structures on the accepting surface of the integrator rod. The same measures can increase the outcoupling efficiency at the other side of the rod as well. Further details, including optical simulations, will be discussed in the next section as part of the design process of a spectrally tuneable light source.

4.5 The design of a LED light engine and spectrally tuneable luminaire

The knowledge gathered from studying the behaviour of light, the workings of the visual system and the characteristics of LEDs, control electronics and optics is combined into the design of a lighting module, and later a luminaire that aims to improve both lighting quality and energy efficiency while at the same time provide a spectrally tuneable output within the visible part of the electromagnetic spectrum. Five different light engine designs, consisting of a circuit board containing a number of carefully selected LEDs and electronics to control the LEDs and light output, were designed and analysed.

4.5.1 Light engine prototype I

A first prototype light engine, constructed mid 2011, was designed as a proof-of-concept. A TLC5940NT IC, manufactured by Texas Instruments, provides a PWM modulated constant current of 30 mA to each of the 16 channels. One channel contains 3 series-connected, monochromatic 5 mm LEDs. The LED

driver is controlled by an STM32 discovery board, manufactured by STMicroelectronics, containing a STM32F100 microcontroller that sends signals through a serial interface to control the PWM generation within the TLC5940NT which, in its turn, controls the average current through the LEDs. The board is fed by a 12V DC laboratory power supply.

Table 9 shows the chosen peak wavelengths for each channel, the radiometric power and luminous flux per LED.

Table 4.6. LED selection for prototype I.

Channel	Peak wavelength (nm)	Flux per LED (mW)	Flux per LED (lm)
1	375.0	20.27	0.015
2	404.3	35.95	0.064
3	415.1	26.05	0.104
4	447.4	27.46	0.843
5	466.1	20.30	1.532
6	484.3	9.39	1.524
7	500.1	15.47	4.584
8	521.8	10.76	5.480
9	536.5	6.88	4.081
10	535.45	3.3	1.907
11	594.2	6.69	3.289
12	609.6	2.40	0.885
13	630.8	15.42	3.137
14	652.4	6.80	0.543
15	691.4	11.05	0.105
16	748.2	12.29	0.007

Even in these early stages of development, a clear choice was made for a PWM controlled constant current source: PWM allows precise near-linear control over the flux over the LEDs, simplifies driver circuits and results in less electrical losses within the LED driver.

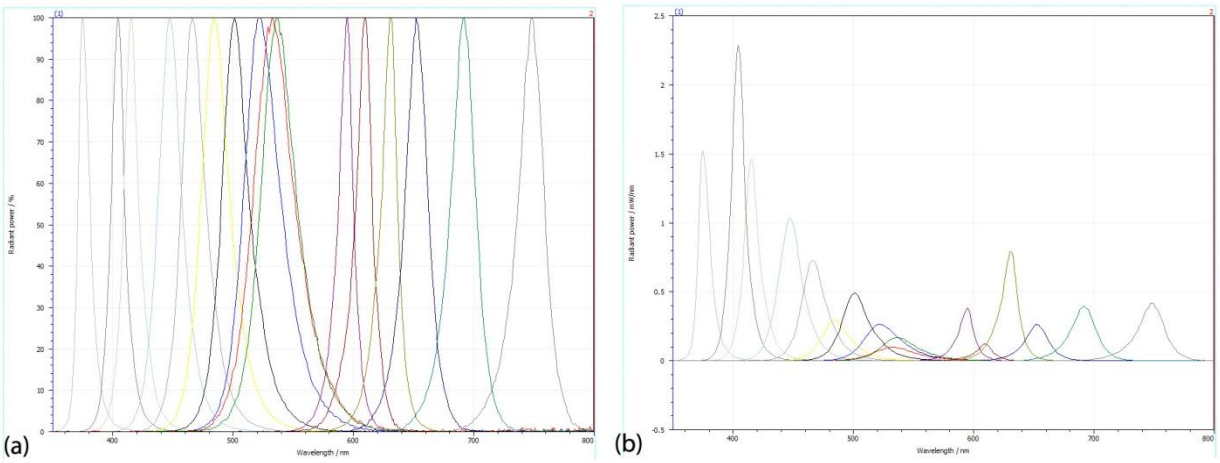

Fig. 4.42. Spectra of the 16 LEDs used in prototype 1. Normalised (a) and absolute radiometric values (b).

The spectra shown in Fig. 4.42 raise a number of questions:

- What should be the shape of the “base spectrum” (spectrum when all LEDs are driven at equal current)? Is an equal radiometric flux for each channel ideal?
- Different LEDs have varying fluxes. Depending on the base spectrum, this should be compensated.
- What is the ideal spectral range for the light engine?
- Output in the 550-570 nm range is almost non-existant. What is the solution?

Besides the issues mentioned above, the light engine is not suitable for general illumination. With a photometric flux of less than 85 lumens at a power consumption of 5.8 W (an efficacy of less than 15 lm/W) the efficiency and total flux is too low.

The light engine pictured in Fig. 4.43 was built completely within the facilities of IREC using a LPKF PCB prototyping machine.

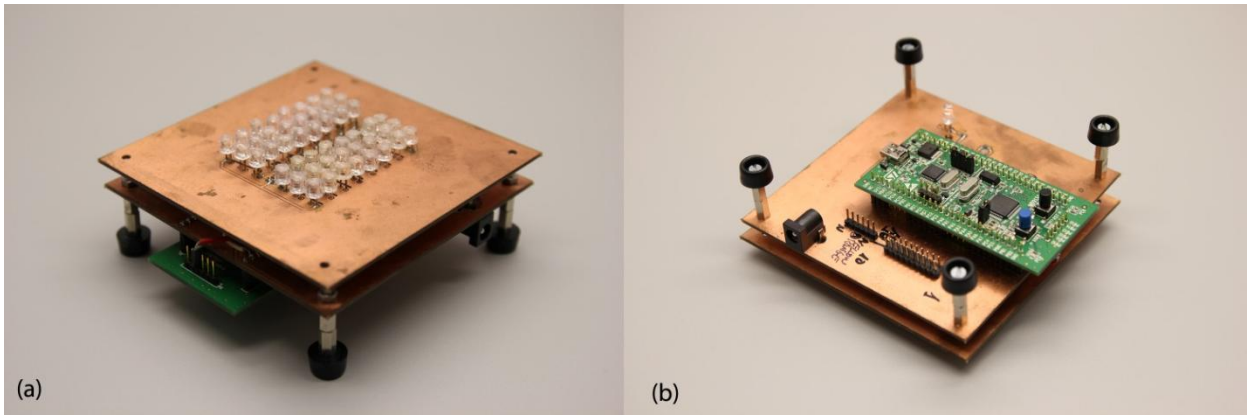

Fig. 4.43. Prototype I double-decker PCB with the LEDs and driver on top and control board on the bottom. (a) top view and (b) bottom view.

4.5.2 Prototype II

While the first prototype demonstrated the feasibility of the idea, there was a clear need for higher output powers. 39 LEDs spanning 13 individual wavelength channels were selected and driven with a forward current of 350, 500, 700 or 1000 mA, depending on the LED series string. A first attempt was made to address the green-gap issue by combining a phosphor down-converter with a near-UV LED pump to generate light in the yellow-green region of the spectrum. Table 10 shows the LED channels with their corresponding peak wavelengths and fluxes.

Table 4.7. LED selection for prototype II

Channel	Number of LEDs	I_f (mA)	Peak wavelength (nm)	Flux per LED (W)	Flux per LED (lm)
1	2	1000	400.4	0.346	1.034
2	3	350	416.0	0.232	1.072
3	1	700	453.0	0.713	29.26
4	1	700	462.8	0.707	46.32
5	1	700	473.0	0.590	60.64
6	3	700	495.3	0.388	92.73
7	3	700	518.8	0.300	136.8
8	5	1000	557.4	0.133	54.66
9	4	700	600.6	0.169	74.93
10	2	700	626.5	0.430	100.4
11	2	700	635.0	0.455	80.8
12	2	700	661.3	0.361	22.32
13	5	500	694.8	0.107	0.896
14	5	500	744.8	0.131	0.076

At full power, the light engine generates 1815 lumens at a power consumption of 81.3 W. Fig. 4.44 shows the emission spectrum of the second prototype. Channel 8 contains 5 LEDs emitting at a peak wavelength of 400 nm combined with a nitride based phosphor supplied by Phosphortech Corporation (HTG540). Although the emission characteristics perfectly cover the green gap, its relatively low quantum efficiency combined with the rudimentary deposition method result in a rather weak light emission (54.7 lm, 13.67 lm/W). The phosphors where mixed with a 2 component epoxy glue at a concentration of 50 %. The resulting mixture was then used to coat the primary optic of the pump LEDs. Besides the relatively low efficiency, inconsistencies in the coating resulted in leakage of the pump spectrum, as seen in the figure below.

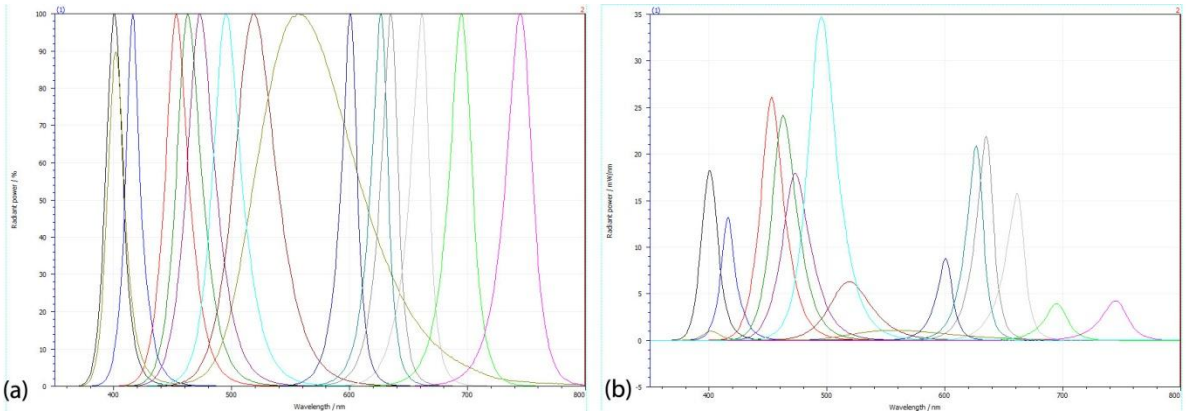

Fig. 4.44. Emission spectrum of the LEDs in Prototype II. (a) Normalised and (b) absolute radiometric values

Each series string is powered by an individual buck converter designed by LEDdynamics. The Lux-drive buckpucks are sealed units that provide a constant current of 350, 500, 750 or 1000 mA and have a control input for PWM signals. A TLC5940NT acts a primary driver, generating 14 individual PWM signals based on serial instructions received from the STM32F100 microcontroller.

The high power dissipation of prototype II (>80 W) needs a well designed means to dissipate the generated heat. The metal core substrates on which the emitters are soldered ("stars") have a relatively high thermal resistance of 10 ºC/W ($R_{th,\ junction\text{-}ambient}$). Assuming similar LED efficiencies, the emitter driven at the highest forward current combined with the highest forward voltage, in this case channel 8, generates the largest amount of heat. The LEDs in channel 8 need to dissipate nearly 4 W of heat. A junction to ambient thermal resistance of 10 ºC/W combined with a thermal resistance of 1 ºC/W added by the thermal epoxy used in the assembly process raises the junction temperature by 44 ºC in the case of an ideal, infinitely large heatsink. The maximum allowable junction temperature for this particular LED is a rather low 120 ºC. This means the heatsink temperature cannot exceed 76 ºC, at a room temperature of 25 ºC, without damaging the LED. The minimum thermal resistance needed for the heatsink can be calculated by dividing the maximum allowable temperature of the heatsink (in this case 76 ºC) minus the ambient temperature, by the combined dissipated power of all the LEDs.

$$R_{th,heatsink} \leq \frac{T_{max} - T_{ambient}}{P_{D,LEDs}} \qquad \text{(Eq. 4.8)}$$

$$R_{th,heatsink} \leq 0.63\ ^{o}C/W$$

The selected heatsink, shown in Fig. 4.45 has a thermal resistance of just 0.5 ºC. Thermal measurements indicate a maximum heatsink temperature of 59.4 ºC, well below the limit to guarantee safe operation of the LEDs.

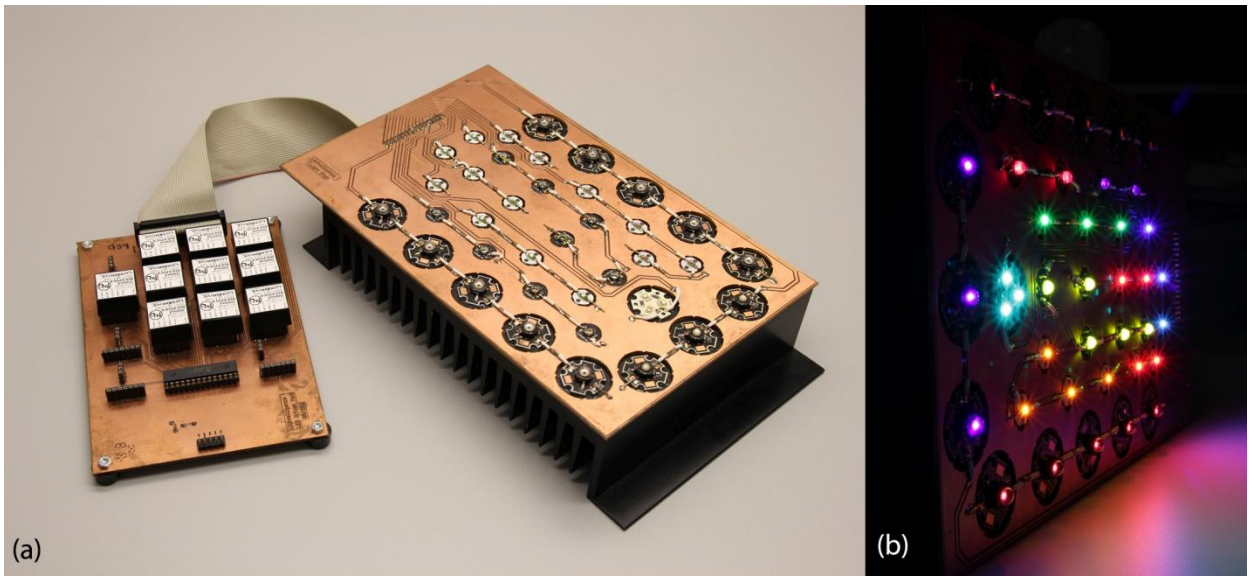

Fig. 4.45. Prototype II LED board and driver circuits, produced within the IREC facilities. Unpowered (a) and powered (b).

Prototype II accomplishes its goal by delivering an output flux exceeding a typical 100 W incandescent light bulb. Its low efficiency and, more importantly, bulky size prevent applications in general lighting. The size of the light engine creates a second problem: the large light emitting area makes it extremely difficult to design secondary optics that can efficiently homogenise and redirect the light generated by the LEDs. A second issue with the wide spreading of the LEDs is coloured shadows and obvious beam inhomogeneities in the far-field.

4.5.3 Light engine prototype III

Prototype III focuses on miniaturisation and efficiency improvements through the selection of a new set of LEDs and the design of a new driver module. At the same time, light mixing optics create a homogeneous light output. A selection of Lumileds Luxeon Rebel LEDs, shown in the table below, enables a drastic miniaturisation of the LED PCB. The flux values, measured at module level, are the combined values of all LEDs of that particular channel, including losses within the mixing chamber and diffuser.

Table 4.8. LED selection for prototype III

Channel	Number of LEDs	Peak wavelength (nm)	Flux (W)	Flux (lm)
1	1	446.3	0.45	15.62
2	1	451.4	0.46	19.18
3	1	468.5	0.36	30.11
4	1	475.3	0.36	39.17
5	2	497.0	0.46	116.6
6	1	517.5	0.19	87.57
7	2	528.3	0.33	175.0
8	6	PC white: 2814 K	1.24	383.0
9	3	597.6	0.52	180.4
10	3	PC white: 2794 K	0.62	191.6
11	1	636.7	0.28	46.2
12	1	657.1	0.34	25.12
13	1	663.5	0.35	20.10

The 24 LEDs are divided into 12 different channels. The Lumileds Luxeon Rebel series is a compact footprint, ceramic based surface mount device. Unfortunately, at the time of construction there was no option that emitted in the green-gap. The phosphor deposition method used in the previous prototype resulted in a relatively low efficiency. Prototype III uses warm-white PC LEDs to provide energy in the yellow-green area of the visible spectrum. The phosphor has a fairly broadband emission spectrum and the low CCT results in a relatively small amount of energy in the shorter wavelengths. While this solution does increase both the colour rendering properties and efficacy of the light engine, the broadband emission of the phosphor with extensions in the blue region and yellow to red region of the spectrum results in restrictions regarding tuneability (a spectrum containing energy only on the 530-600 nm region is not possible). Fig. 4.46 shows the spectral distribution of the 13 LED channels of the third prototype.

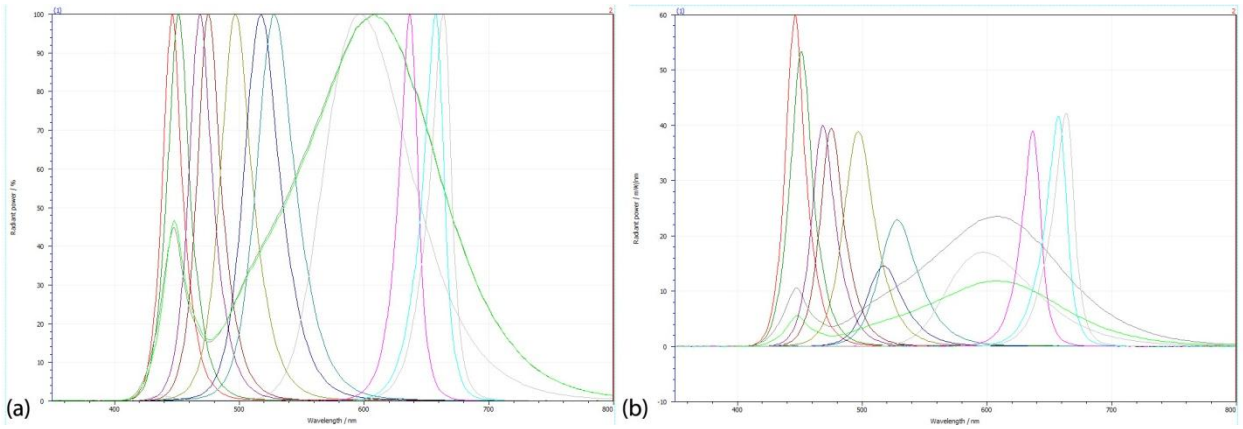

Fig. 4.46. Emission spectrum of the 13 LED channels of prototype III. Normalised (a) and absolute radiometric flux (b).

The LEDs are arranged in a circular pattern on a standard FR4 PCB. Multiple copper vias, connecting the thermal pad around the LEDs with the copper bottom layer provide a thermal path from the case of the

LED to the base below the PCB. The PCB is pressure-glued to the aluminium heatspreader with a thermal compound, separated only by a thin Kapton layer to provide electrical isolation (Fig. 4.47). The LED PCB also contains 4 Microchip MCP98242 digital temperature sensors to provide temperature feedback to the main control unit. Spectral data of each channel, measured at full power at temperatures between 10 and 80 ºC, is stored inside a flash database within the microcontroller. During operation of the light engine, the average temperature of the 4 sensors is then used to access the correct spectral correction file.

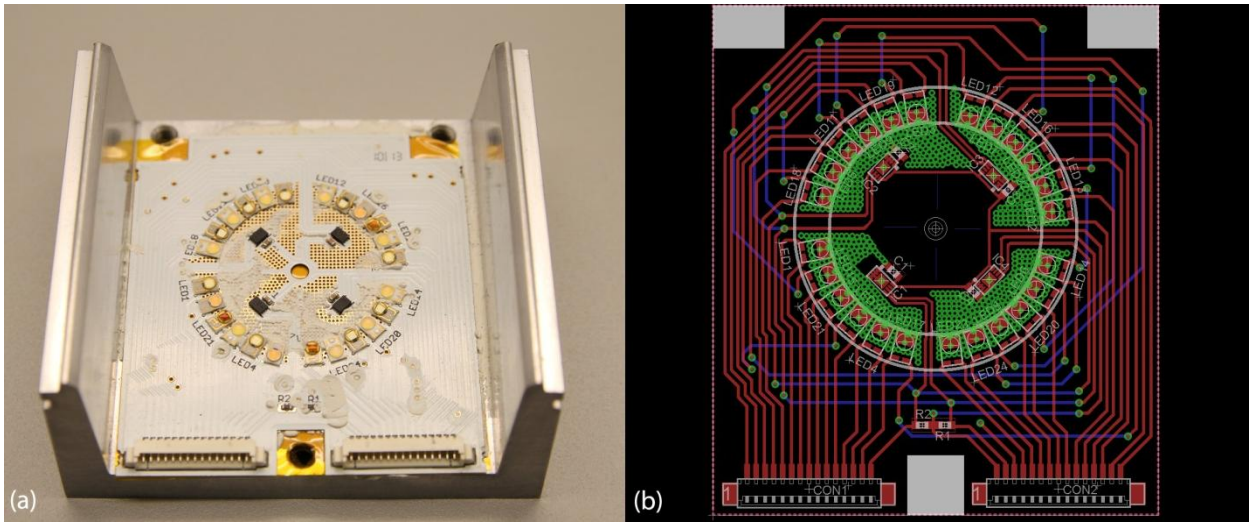

Fig. 4.47. LED PCB. (a) Finished board mounted on an aluminium heatspreader with isolating Kapton foil (yellow) and (b) PCB design with top layer in red, bottom layer in blue and (thermal) vias in green. Note the 4 black temperature sensors in (a).

The colour mixing and homogenisation is performed by a mixing chamber adapted from a Philips Fortimo DLM module (1st generation). The chamber measures 58 x 32 mm (d x h) and is lined with a microfoamed diffuse reflective foil. A 2 mm thick volumetric PC diffuser generates a homogeneous lambertian beam pattern.

The light engine is controlled by a custom designed LED driver solution. The STM32 discovery board controls, through a serial data interface, a Linear Technology LT8500 PWM generator generating a PWM signal with a resolution of 12-bits. The IC, in its turn, drives the PWM input of each of the 13 Texas Instruments LM3406 constant current buck regulators configured to supply each LED string with a constant current of 700 mA.

The result is a spectrally tuneable light engine capable of delivering 1377 lumen (radiometric flux = 6.17 W) at a power consumption of 59.8W, including losses in the LEDdriver. The maximum achievable R_a is 95 at CCTs between 2600 and 7000 K. The large amount of heat generated by the LEDs has its effect on the light output (chapter 4.3). Four temperature sensors on the LED board constantly monitor the board temperature. This information is then used to access a database containing thermal degradation values to compensate per channel flux losses. While this approach does help thermal spectral stability, it does not correct thermally induced peak wavelength shifts.

Prototype III shows distinct improvements over the previous model:

- Surface mount, highly efficient Lumileds Luxeon Rebel LEDs reduce the source size, resulting in a compact light engine that provides better beam homogenisation and allows the use of secondary optics
- A better wavelength selection, focusing more energy in the V(λ) peak region, increases the luminous efficacy of the module
- A new LED driver offers more precise control over the LED flux and increases the electrical efficiency of the module

The finished light engine, shown in Fig. 4.48, was used in the construction of a spectrally tuneable downlight luminaire, described in detail in 4.5.6.

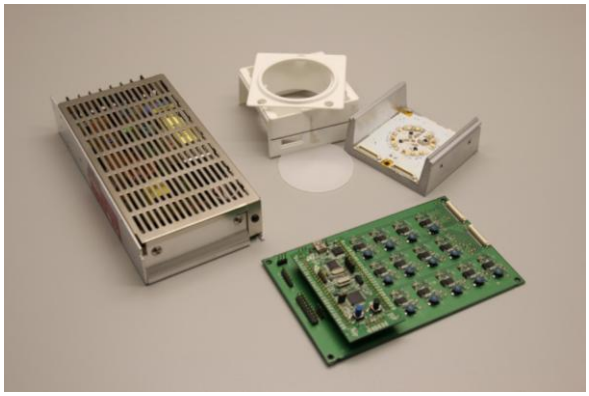

Fig. 4.48. Prototype III: LED PCB, heatsink and mixing chamber, LED driver with STM32 discovery board and buck regulators and a 24V, 100 W power supply.

4.5.4 Light engine prototype IV

The fourth prototype accomplishes four important goals

- Further downsizing of the light emitting area, LED driver and power supply
- Wireless communication interface
- Improved thermal characteristics
- Improved spectral fidelity in the green-gap region

One of the major downsides of the third prototype was the dependence on the Philips Fortimo mixing chamber. Prototype IV was designed to be used in conjunction with a more compact homogenisation solution. To accomplish this, the LED layout was drastically changed from a circular to a square grid pattern. The much higher packaging density of the Luxeon Rebel LEDs made the use of a traditional FR4 based solution impossible. A highly conductive Al_2O_3 ceramic based PCB material, provided by CeramTec GmbH, proved to be an ideal base for the light engine. Traditional FR4 has a typical thermal conductivity of 0.25 W/m.K, an aluminium based metal-core board offers an improved conductivity value of up to 2 W/m.K while ceramic alumina provides top performance with values up to 25 W/m.K, 100 times the

conductivity of a standard FR4 PCB. Important to note is that while bare metal substrates such as aluminium offer much superior thermal conductivity values (205 W/m.K), an electrically isolating dielectric has to be used to separate the current carrying traces on top of the PCB from the electrically conducting metal beneath them. This thin dielectric dramatically decreases the thermal conductivity of the whole structure.

The final PCB, shown in Fig. 4.49 (a), consists of a 0.63 mm thick alumina base combined with a 35 micron silver plated metallisation layer. Five holes provide a screw-mount option to firmly attach the PCB to its heatsink. Because of space restrictions, the 4 temperature sensors used in prototype III have been replaced by one sensor of the same type, located in the upper right hand corner of the LED matrix. The source size was reduced from 33 mm to 27.8 mm while the LED count was increased from 24 to 40 LEDs.

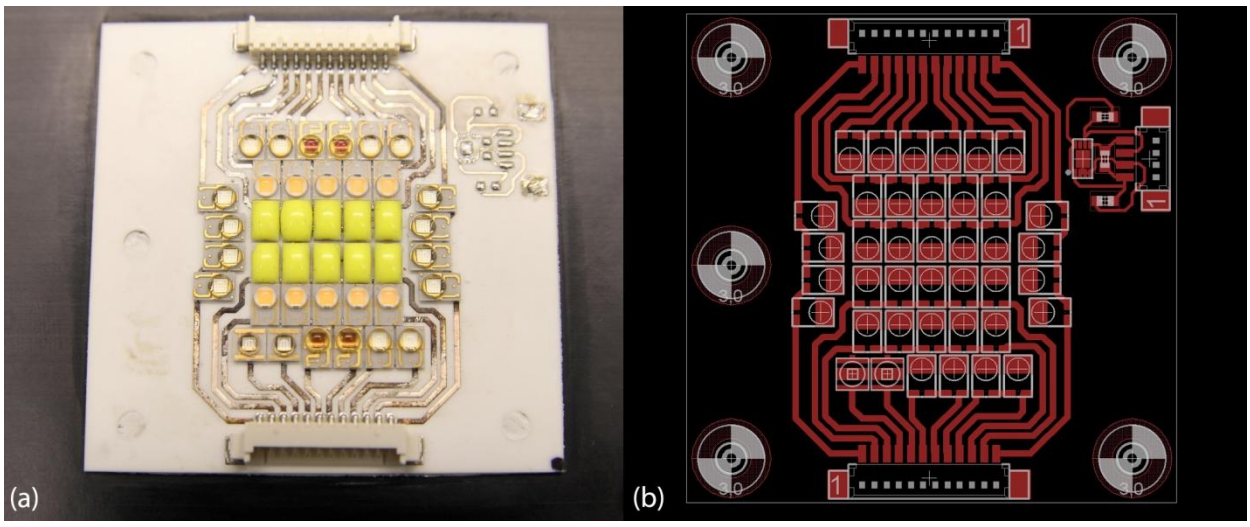

Fig. 4.49. Prototype IV PCB. Finished alumina-based board (a) and PCB design (b).

Besides the physical location of the LEDs, the properties of each channel have been optimised as well. A phosphor converted yellow-green channel has been added, using the technique described in detail in chapter 3.4.4.2: The green gap. On top of that, a new violet channel has been added using custom-binned surface mount LEDs manufactured by the Zhuhai Tianhui Electronic Co., LTD. The addition of shorter wavelength LEDs increases the maximum achievable general colour rendering index to over 99 between a CCT of 2500 and 8000 K. Channel 1 (λ_p = 446 nm), channel 6 (518 nm) and channel 12 (657 nm) were removed because the disadvantages caused by the increase in source size (larger and more difficult to design secondary optics and increased LED driver size) did not outweigh the advantages provided by these LEDs (marginally better spectral tuneability, no increase in R_a). Table 12 shows the LED selection for prototype IV while Fig. 4.50 shows the spectral distribution of the 12 LED channels, measured at the exit aperture of the mixing chamber.

Table 4.9. Distribution, peak wavelength and flux of the LEDs used in prototype IV

Channel	Number of LEDs	Peak wavelength (nm)	Flux (W)	Flux (lm)
1	2	426.4	0.27	9.70
2	2	453.0	0.65	43.8
3	2	468.7	0.32	32.5
4	2	475.1	0.31	39.7
5	4	498.4	0.45	124.4
6	4	527.8	0.29	284.5
7	5	551.3	0.32	151.7
8	5	551.4	0.29	137.3
9	5	598.0	0.48	165.6
10	5	597.7	0.47	163.6
11	2	638.9	0.52	79.6
12	2	664.2	0.30	16.0

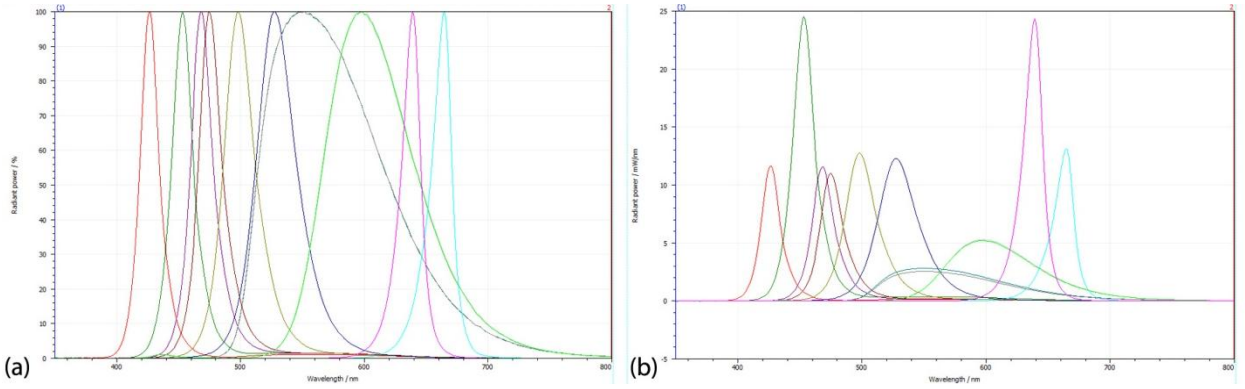

Fig. 4.50. Spectral distribution of the 12 channels of prototype IV measured after the mixing chamber and diffuser. (a) normalised and (b) absolute radiometric values.

The LED distribution was chosen with the aim to provide an equal amount of energy in each of the wavelength bands. To ensure sufficient flux for white light spectra consisting of only a few channels (channel 2 (453 nm), channel 6 (527 nm) and channel 7 (639 nm)) are driven at a forward current of 700 mA while the other channels receive a current of 350 mA. Fig. 4.51 compares the emission spectrum of the bare LEDs with the emission spectrum of the light engine including losses within the secondary optics. These secondary optics include a mixing chamber measuring 30 x 50 mm and a volumetric diffuser measuring 30 mm in diameter with a thickness of 3 mm. The lambertian radiation pattern generated by the diffuser matches the requirements for using a highly efficient reflector from the Britney series, developed by LEDiL Oy (Fig. 4.52 (b)).

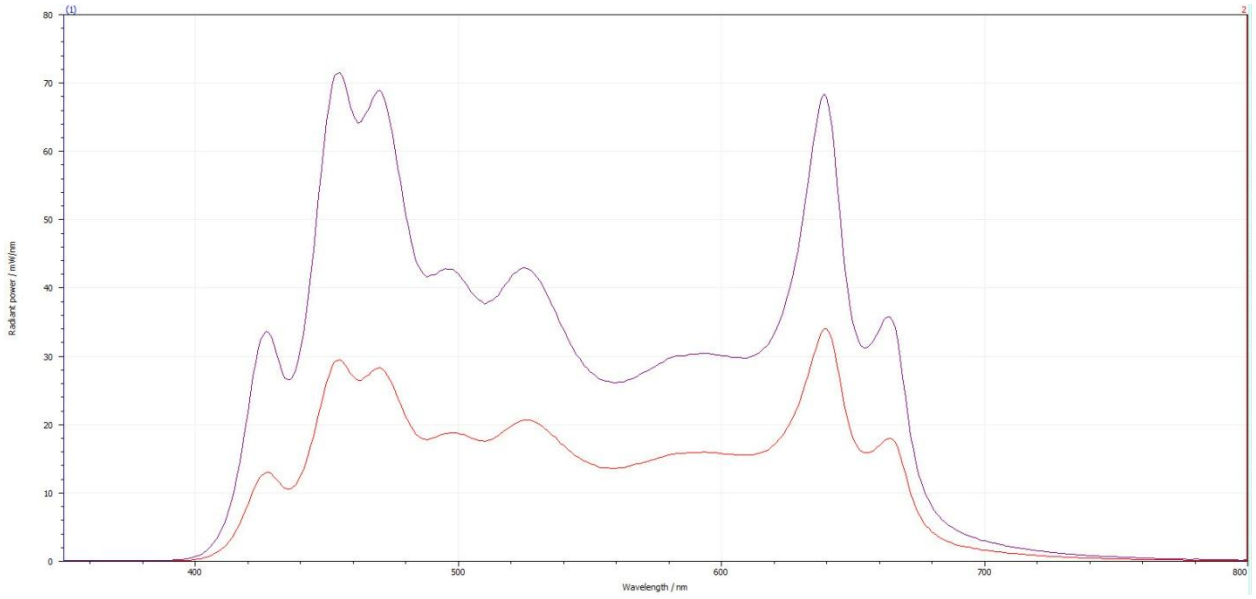

Fig. 4.51. Full power SPD of prototype IV (Flux = 4.90 W, 1242 lm at a CCT of 6056 K (ΔE = -0.009) and R_a of 79.2) compared to the spectrum of the LEDs only (Flux = 10.44 W, 2501 lm at a CCT of 7774 K (ΔE = -0.011) and R_a of 74.4).

The board size of the driver size was reduced by incorporating the microcontroller onto the same PCB with the LED drivers, thereby eliminating the STM32 discovery board. The STMicroelectronics STM32F437 is a cortex-M4 based microcontroller running at 180 MHz. It provides 4 UARTs, 6 SP interfaces and 3 I^2C lines, up to 17 timers and 3 12-bit analog to digital converters.

Furthermore, a Roving Networks (now Microchip) WiFly 802.15.4 wireless communication module was added to enable full wireless control of the light engine. The module interfaces with one of the UART modules of the microcontroller. The board dimensions of the LED driver were reduced to 132 x 67 mm from the original size of 160 x 100 mm in prototype III.

A last step in system miniaturization is the introduction of a compact, efficient power supply from Mean Well Enterprises Co., Ltd. The PLP 60-24 series, measuring only 101.6 x 50.8 x 29.6 mm, provides a regulated 24 V with maximum current of 2.5 A at a maximum efficiency of 88 %.

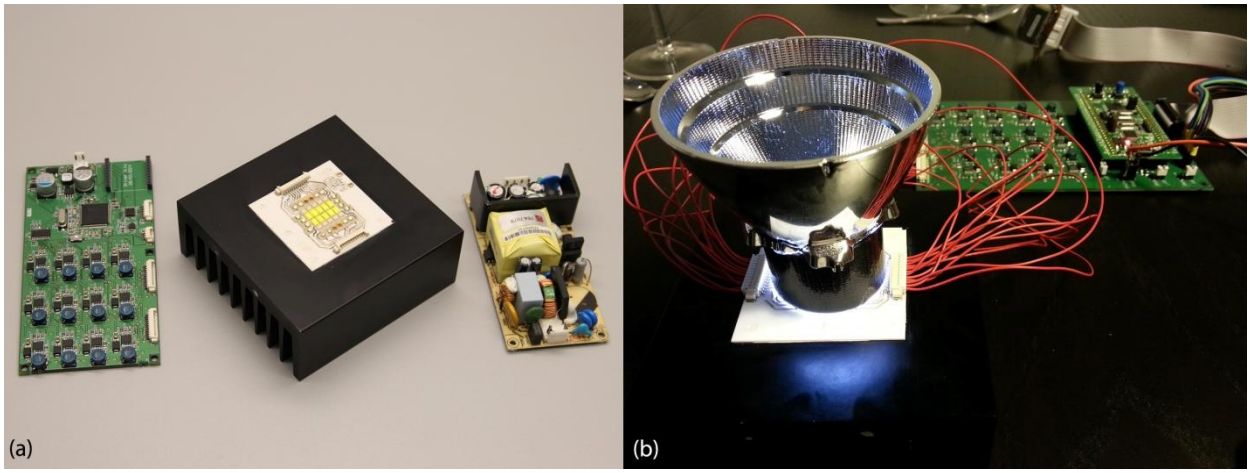

Fig. 4.52. Prototype IV. (a)compact LED driver (Wi-Fi module not shown), ceramic LED board on heatsink and power supply unit and (b) test of the light engine and secondary optics using the LED driver of prototype III. The black tube contains a hollow cylinder lined with microfoamed PET supplied by Furukawa Co. Ltd. and acts as a colour mixing chamber.

4.5.5 Final design of the light engine

The final version, version V, of the LED light engine series continues the miniaturisation trend started with the 3rd prototype and includes a novel concept of colour mixing and beam homogenisation.

With the release of a new, more compact line of Luxeon Z LEDs by Lumileds that includes a phosphor converted yellow-green emitter (Luxeon Z "lime") the light engine could be designed using a single footprint type for all wavelength channels. A LED distribution identical to the one used in prototype IV was used for the final light engine design, but the physical placement of the LEDs was optimised with proper heat management and secondary optics design in mind. The table below summarizes the LED distribution and performance of the final light engine design, measured including the secondary beam homogenisation optics.

Table 4.10. Distribution, peak wavelength and flux of the LEDs used in the final light engine design

Channel	Number of LEDs	Peak wavelength (nm)	Flux (W)	Flux (lm)
1	2	427.1	0.40	5.93
2	2	449.4	0.73	25.4
3	2	470.7	0.31	27.3
4	2	472.8	0.28	27.1
5	4	496.0	0.41	101.7
6	4	522.2	0.41	202.0
7	5	546.2	0.77	360.7
8	5	546.0	0.77	361.3
9	5	599.6	0.59	191.8
10	5	599.7	0.57	189.7
11	2	637.6	0.38	61.5
12	2	661.0	0.24	14.9

The flux provided by the LED light engine depends on the chosen spectrum. This means a design choice has to be made with regards to the number of LEDs per channel. While an equal radiometric flux per channel maximises tuneability, general illumination apllications have different needs. Black body spectra provide high quality, natural illumination properties. An optimal trade-off point to ensure sufficient light output at both extremes of the CCT range used for illumination purposes (2000 – 10 000 K) is an optimization for an equal-energy spectrum. This spectrum provides a near-black body spectral shape and a white point around 5500 K with chromaticity coordinates near the black body locus. As in the previous prototype, only channel 2 (453 nm), channel 6 (527 nm) and channel 7 (639 nm) are driven at a forward current of 700 mA while the other channels receive a current of 350 mA. Fig. 4.53 shows the design layout of the LED PCB (a) and the finished alumina-based circuit board measuring 40.1 x 40.1 mm. The metallisation consists of a gold-flashed copper layer with a thickness of 35 micron. As in prototype IV, a single MCP98242 digital temperature sensor provides critical temperature feedback.

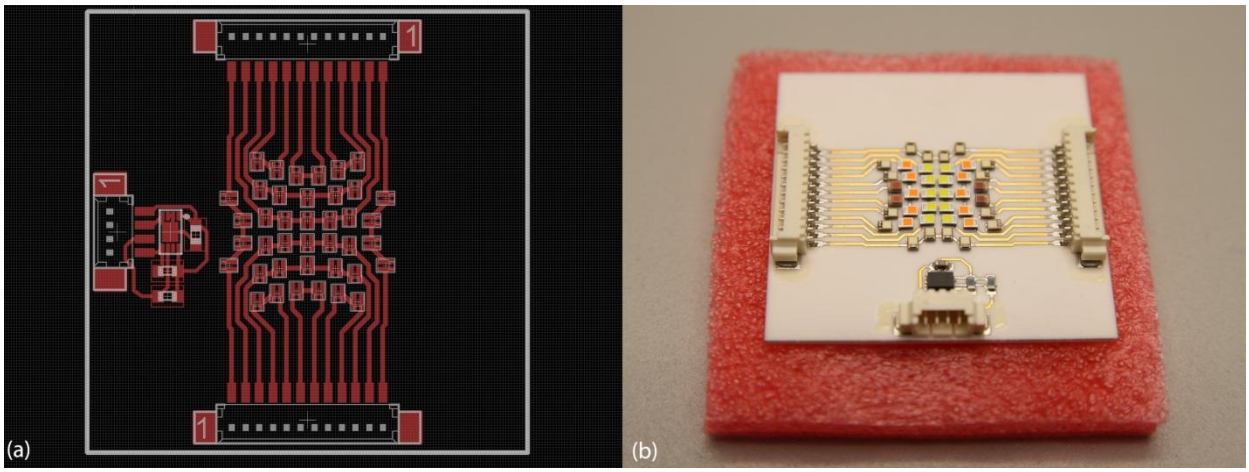

Fig. 4.53. Final LED board design. Layout (a) and completed ceramic PCB (b). Note the “spider” layout of the LEDs to optimize the distance between each emitter and to improve the thermal characteristics and beam homogenisation properties. The source diameter has been further reduced from 27.8 mm (prototype IV) to 16.5 mm.

The rather low efficiency (< 47 %) of the mixing chamber and volumetric diffuser led to a redesign of the secondary optics. The large number of LEDs concentrated in a small area needs a more robust mixing solution than the mixing chamber proposed in prototype IV, especially when a small homogenised source size is the final goal.

Devices that need efficient and near-perfect beam homogenisation, such as video projectors, often use optical integrating rods instead of simple diffusers or mixing chambers. Starting from this idea, Lambda Research´s TracePro optical design software was used to simulate and optimise the secondary colour mixing optics.

The homogenization characteristics of an optical integrator depend on a number of factors:

- The material of the integrator
- Its length and diameter
- The cross-sectional shape of the mixing rod

Due to manufacturing constraints, the options were limited to only 1 material for the integrator: PMMA. PMMA is a near ideal choice, as it has excellent transmission characteristics in the visible spectrum and is very resistant to short wavelength radiation.

The diameter of the rod is fixed as well. The light engine will be used in conjunction with the Britney reflector series, manufactured by LEDiL Oy of Finland. These particular series of parabolic reflectors expects a lambertian radiation pattern at its entrance aperture that has a diameter of 30.5 mm. For this reason, the maximum diagonal size of the mixing rod is limited to 30 mm.

This leaves two design parameters to optimise: the shape of the mixing rod, which can be circular, square or multi-angled and the length of the integrator. Chapter 4.4.3: beam homogenising already mentions that integrators with a square cross-section provide better beam homogenization while the shorter the length of the mixing rod is, the less effective its colour mixing will be.

The main simulation model is shown below. Depending on the optimisation routines, different parts of the full model were excluded or modified.

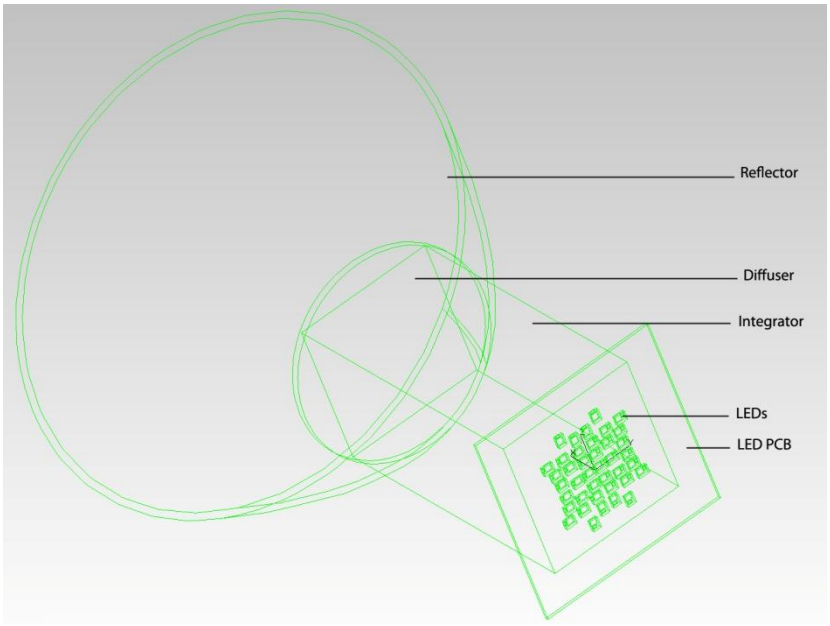

Fig. 4.54. Main simulation model including a LEDiL Britney reflector, optical integration rod with diffusing surface, the LED array used in the final light engine and the alumina LED PCB.

A set of simulations was performed to characterise the effects of the cross-sectional shape of the integrating rod on the optical efficiency and homogenisation properties. Three different models were prepared (Fig. 89). To ensure proper homogenisation even when only a small number of channels were used, all simulations were done using three channels only (channel 3 – 2 LEDs, 6 – 4 LEDs and 11 – 2 LEDs of the final light engine design) which emit a total luminous flux of 786 lumen. Simulations were performed with 100 000 rays per source.

1. The first model consists of an integrator measuring 40 mm high with a circular cross-section of 25 mm. A square surface, placed 2 mm above the exit aperture of the integrator is used to visualise the exiting rays. No diffuser was used (Fig. 4.55).

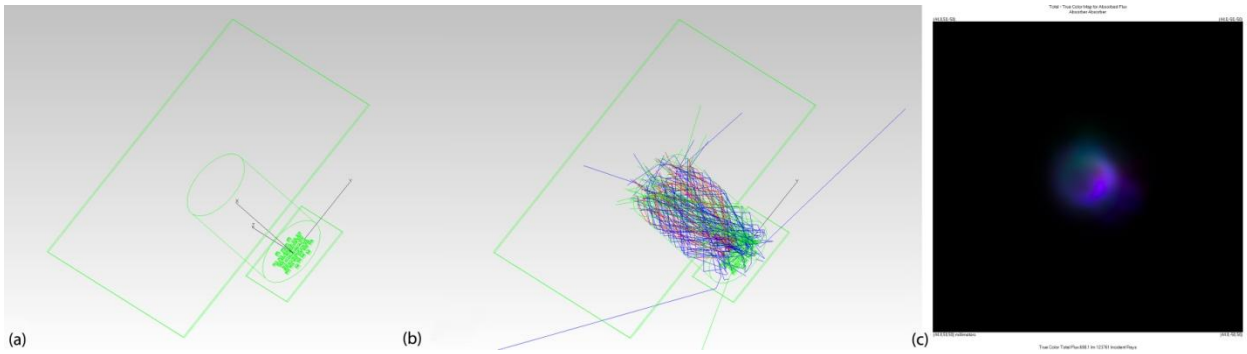

Fig. 4.55. Simulation of a circular cross-section integrator. (a) Simulation model, (b) 0.01 % of the rays exiting the LEDs and (c) real colour image projected on the square absorber.

The simulation results indicate that, although the integrator manages to efficiently capture and confine the light emitted by the LEDs, the colour mixing is not ideal. 698.1 lm from the 786 lumen generated by the LEDs leaves the exit aperture of the mixing rod, resulting in an optical efficiency of over 88 %.

2. The second model is identical to the first, with the exception of the cross section of the diffuser. Instead of a circular aperture, an octagonal shape was introduced (Fig. 4.56)

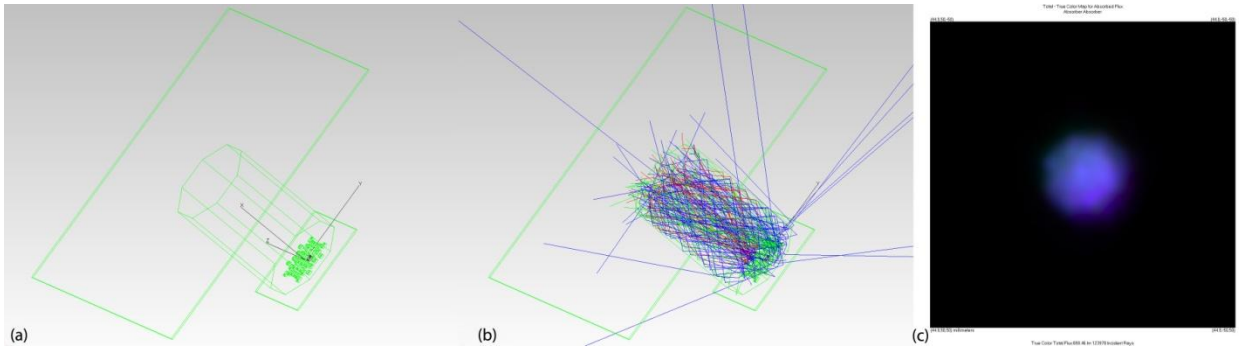

Fig. 4.56. Simulation of an octagonal integrator. (a) Simulation model, (b) 0.01 % of the rays exiting the LEDs and (c) real colour image projected on the square absorber.

An octagonal integrator results in clearly superior beam homogenisation. The optical efficiency is similar to the circular integrator with a flux 698.46 lm measured at the exit of the rod, indicating an efficiency of almost 89 %.

3. Changing the integrator to a square cross-section visibly improves colour mixing without lowering the optical efficiency. The simulated output flux is 699.1 lm, indicating efficiency values near 89 % (Fig. 4.57).

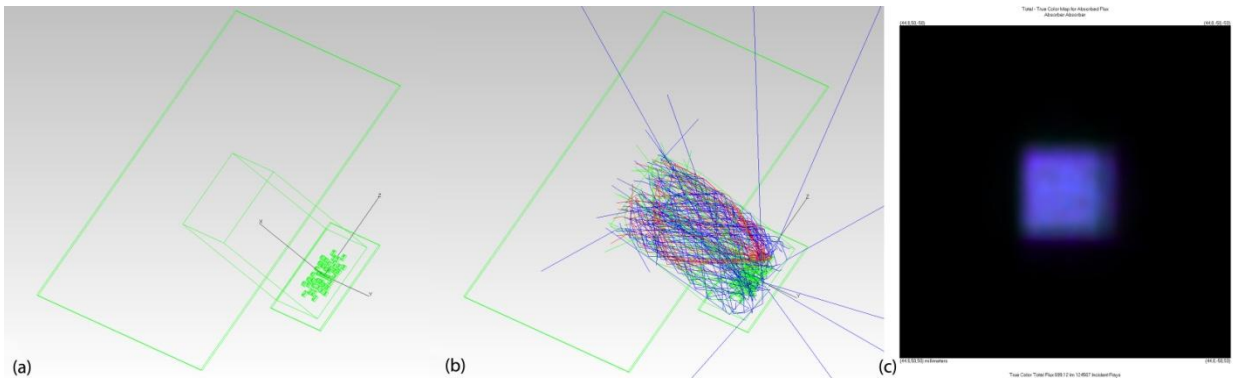

Fig. 4.57. Simulation of a square integrator. (a) Simulation model, (b) 0.01 % of the rays exiting the LEDs and (c) real colour image projected on the square absorber.

The above simulations demonstrate that a square cross section provides not only better homogenisation features but slightly increases the optical efficiency as well.

The effects of the length of the integrator on its homogenising capabilities is characterised in the simulations pictured below in Fig. 4.58.

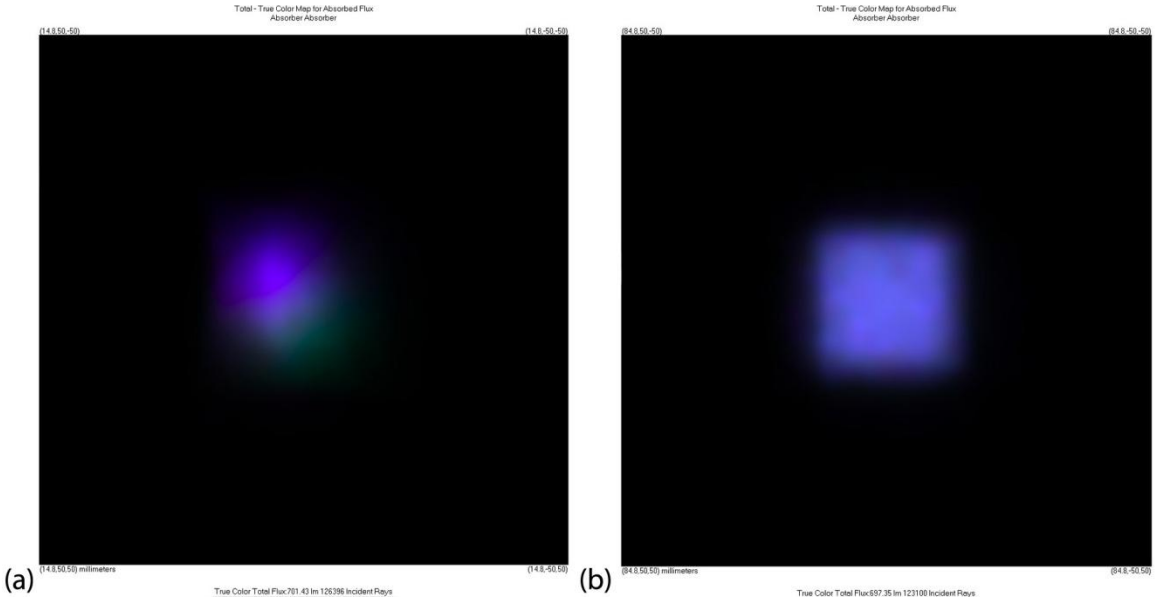

Fig. 4.58. Difference in beam homogenisation between a square mixing rod with a diameter of 25 mm and length of 10 mm (a) and 80 mm (b).

A longer integration path results clearly in better colour mixing. The optical efficiency is largely unharmed (89.2 % for the 10 mm high rod versus 88.7 % for the 80 mm rod). The length of the mixing used in the light engine is a trade-off between a perfectly homogeneous beam and a compact module.

The simulation below shows the finalised optical design of the light engine, including a square optical integrator measuring 50 x 21 x 21 mm (l x w x d). A volumetric diffuser, measuring 15 mm in diameter and 2 mm thick, made from PC (transmittance = 85 %), transforms the output of the integrator in a lambertian radiation pattern. The LEDiL reflector model is finished with a highly reflective MIRO 4

coating (reflectivity = 95 %), manufactured by ALANOD GmbH. A smooth specular surface, such as MIRO 4, will clearly show any artifacts present in the beam pattern at source level (here the diffuser).

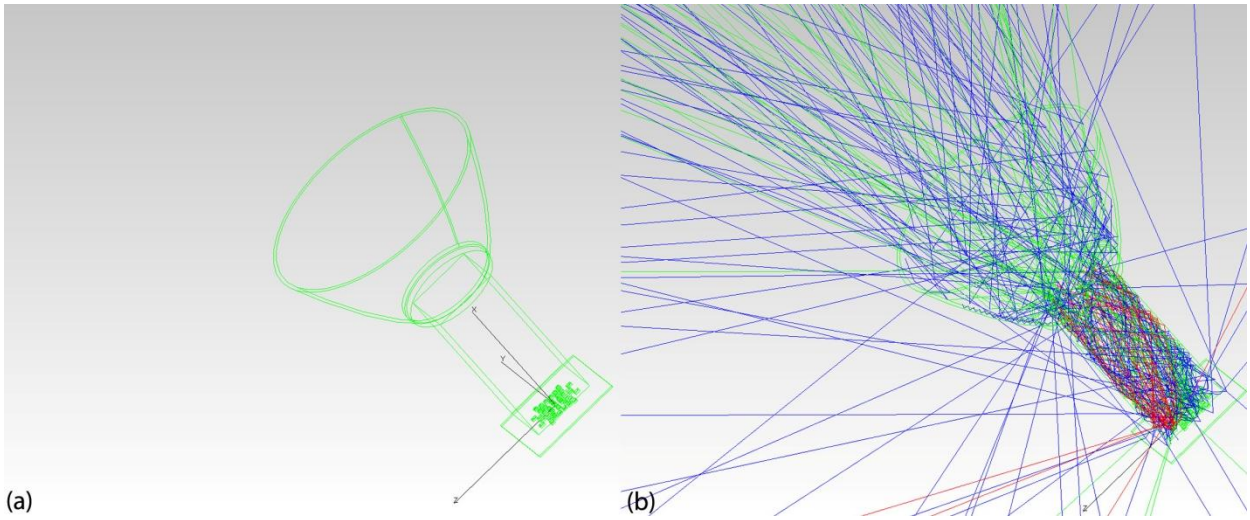

Fig. 4.59. Simulation model of the finished module (a). (b) shows the ray propagation through the optics, including light losses at the air-material bounderies.

The simulations below, performed using 250 000 rays per source, give an accurate representation of the performance of the light engine. Beam shape and colour analysis were done in the far field through a projection on an absorbing surface measuring 2 x 2 m at a distance of 1 m from the source.

Fig. 4.60 shows the results of the homogeneity analysis. The combination of a 50 mm long integration rod with a 2 mm thick PC volumetric diffuser and a specular parabolic reflector results in a near-perfect beam without any obvious colour or luminance artifacts. Unfortunately, the strength of the diffuser needed to generate a lambertian radiation pattern has its impact on the efficiency of the optical system. While the losses in the integrating rod are rather limited, the total optical efficiency of the integrator – diffuser – reflector stack drops to 52.5 %. Further experimentation showed that this number is highly dependent on the properties of the diffuser. Weaker diffusers allowed a much higher light transmittance and raised the efficiency to as high as 75 %, but at the same time resulted in noticeable colour artifacts within the projected beam. A possible solution would be to increase the length of the mixing rod and weaken the lambertian diffuser. An obvious drawback of this method is the increase in size of the assembled light engine. Fig. 4.60 (b) shows the chroma information present in the projected beam. y represents the point in the beam with the highest colour difference compared to point x, located in the center of the projected beam. This colour difference, $\Delta uv = 0.00361$, is an order of magnitude less than the maximum allowable variation in chromaticity for white light sources (according to the CIE: $0.05 \geq \Delta uv \geq -0.05$).

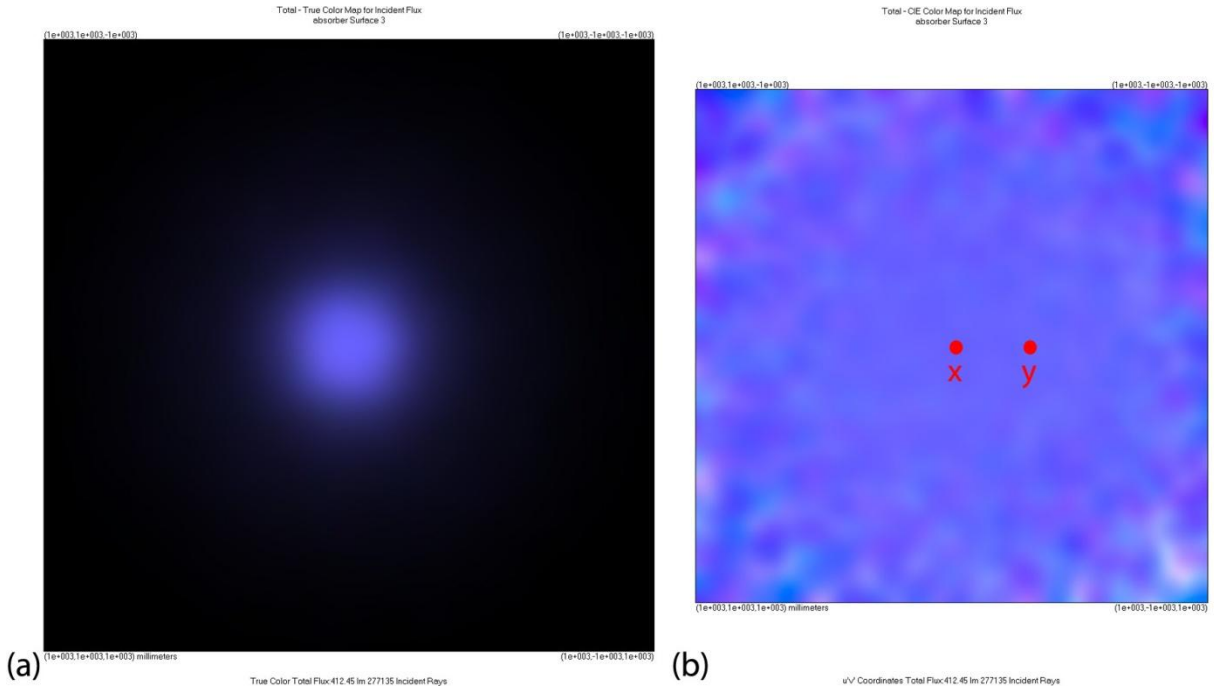

Fig. 4.60. Beam homogeneity analyses of the finalised light engine design. (a) True colour map analysing the beam characteristics in the far-field and (b) colour difference analysis.

Fig. 4.61 pictures the polar candela plot of the light engine, showing a symmetrical, artefact-free beam with a FWHM of 24 º. Although the dimensions and shape of the simulated reflector and the offer by LEDiL are identical, there is a difference in beam width due to the absence of surface patterning on the simulated reflector.

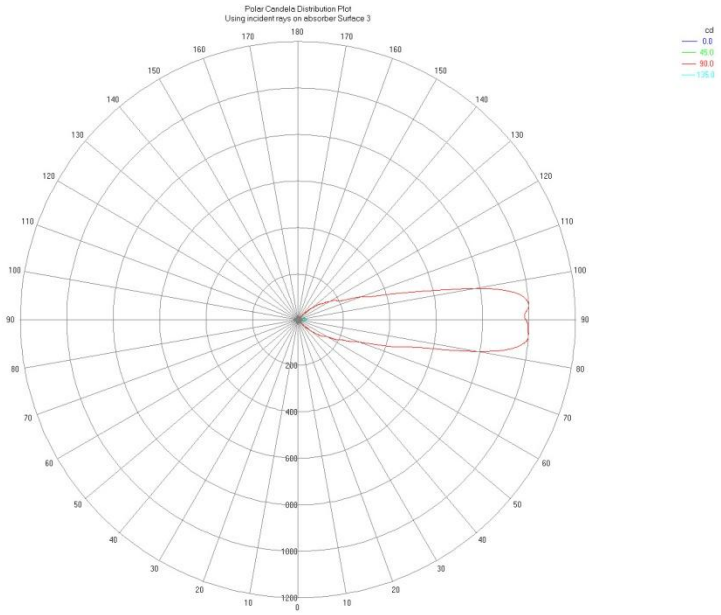

Fig. 4.61. Polar candela distribution of the light engine, including secondary optics.

Based on promising simulation results, a 3D-printed mechanical structure for the secondary optics and CNC-machined aluminium heat spreader for the LEDs was manufactured. Both the diffuser and optical integrator were custom made by Gilbert Curry Industrial Plastics Co, Ltd (Fig. 4.62).

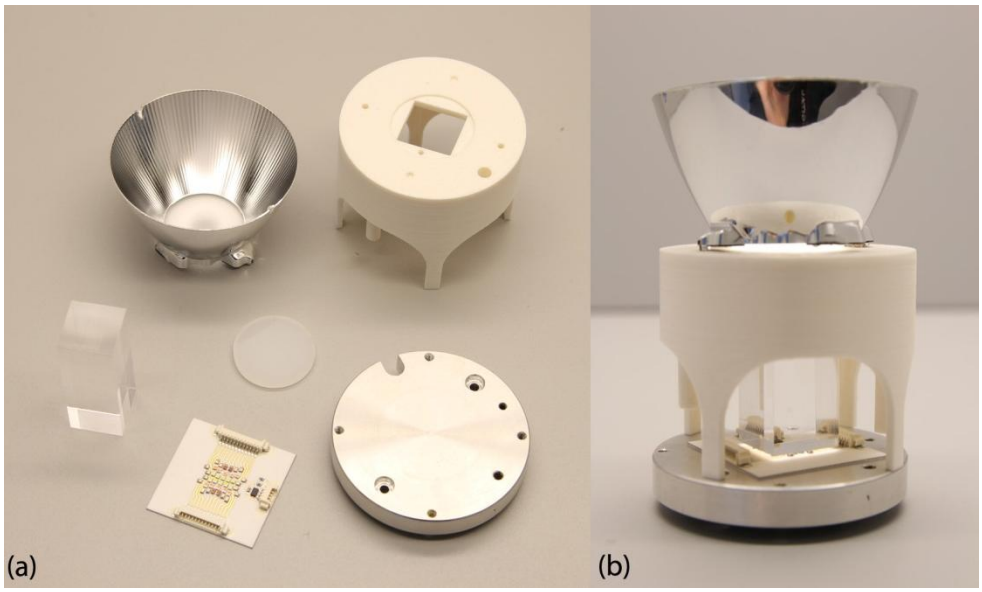

Fig. 4.62. Finalised spectrally tuneable LED light engine. (a) components, including a 3D-printed optics holder and CNC-machined aluminium heat spreader and assembled light engine with LEDiL reflector (b).

The emission spectrum of the light engine, including secondary optics is shown in the figure below. The distribution of the peak wavelengths of the different LED channels is arranged in such a way that each LED, driven at a current of 350 mA results in a summed response approximating an equal energy white spectrum. The peaks of the red, green and blue LEDs corresponding with channels 11, 6 and 2, driven at a forward current of 700 mA, are clearly visible in the output spectrum (Fig. 4.63 (b)).

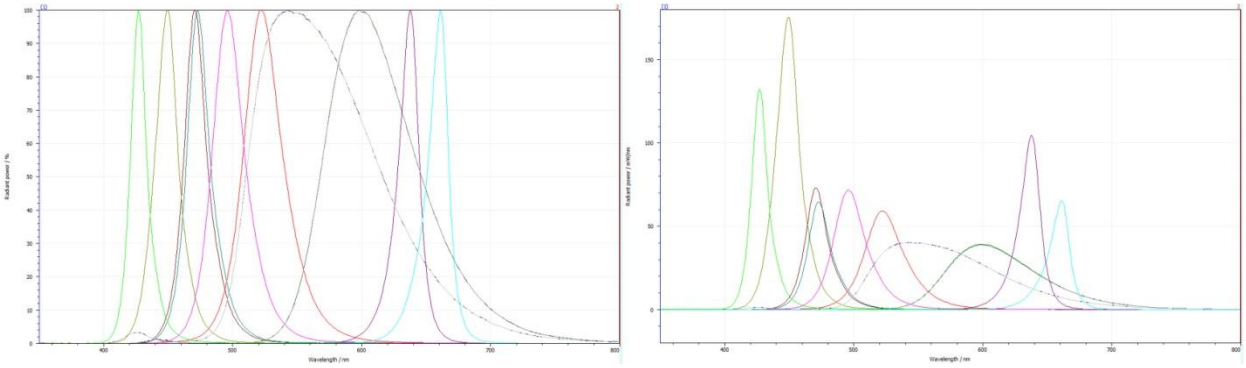

Fig. 4.63. Spectral distribution of the 12 channels of the final light engine design. (a) Normalised and (b) absolute radiometric values.

The LED driver and microcontroller board is identical to the design used in prototype IV.

4.5.6 Luminaire 1: human-centric lighting

Light engine prototype III, built around the Philips fortimo DLM module, was used in the construction of a spectrally tuneable lighting system.

The aim was to illuminate an enclosed laboratory having a floor space of 15 m^2 (5 x 3 m) at a minimum illuminance of 250 lux, measured at a height of 75 cm. The light engines were combined with Troll Lighting 393 Downlight luminaires, consisting of a reflector, heatsink and a means fix the structure to the ceiling (Fig. 4.64).

Fig. 4.64. Spectrally tuneable downlight: host luminaire.

The result is a spectrally tuneable light source capable of delivering 1329 lumen (radiometric flux = 5.96 W) at a power consumption of 59.8 W, including losses in the driver, power supply, reflector and cover glass of the luminaire. The maximum achievable R_a is 95 at CCTs between 2600 and 7000 K. The emission spectrum is rather weak in the green to orange wavelengths due to the lack of a dedicated yellow-green emitter (Fig. 4.65).

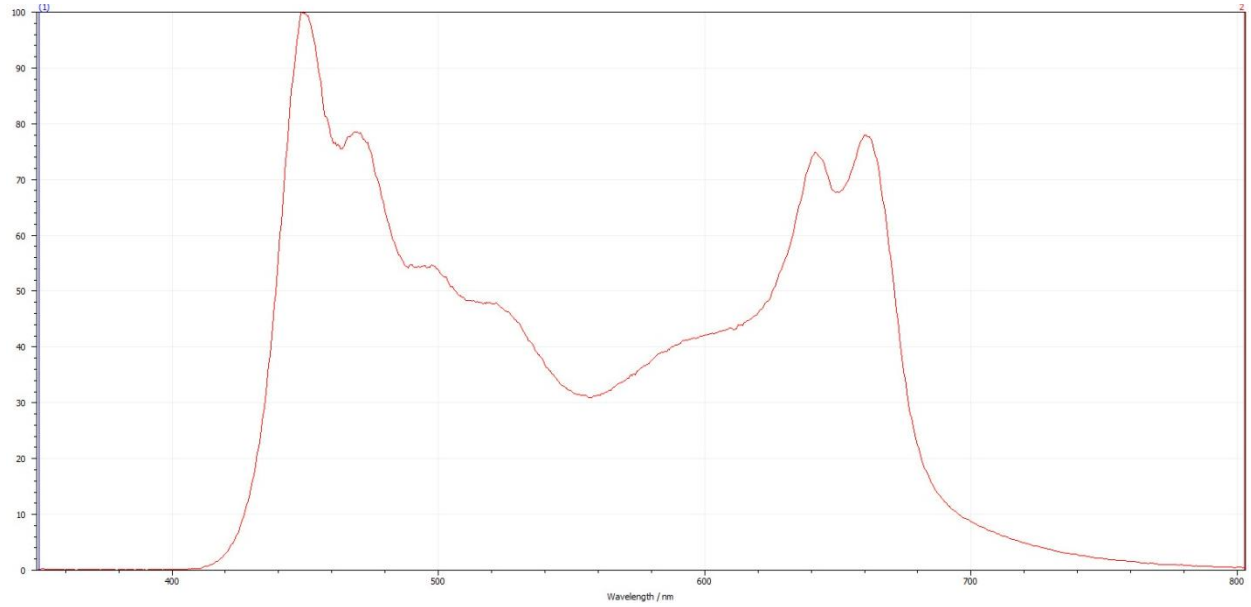

Fig. 4.65. Full power emission spectrum of the spectrally tuneable downlight.

While the illumination requirements for the spectrally tuneable room in IREC were relatively easy to accomplish, a second application of the downlight required extensive simulation. Three downlights were used in the construction of a small spectrally tuneable experimentation space built in the laboratories of the neuroscience department of the University of Newcastle, UK.

The room, measuring 2 x 2 x 2.1 m (l x w x h), required to be illuminated at an illuminance of 500 lux (D65 spectrum), measured at a specific point, located slightly off-center and at a height of 0.85 m. All surfaces, including ceiling and floor, were painted flat white. Measured photogoniometric data was used as input parameters for a Dialux simulation (Fig. 4.66).

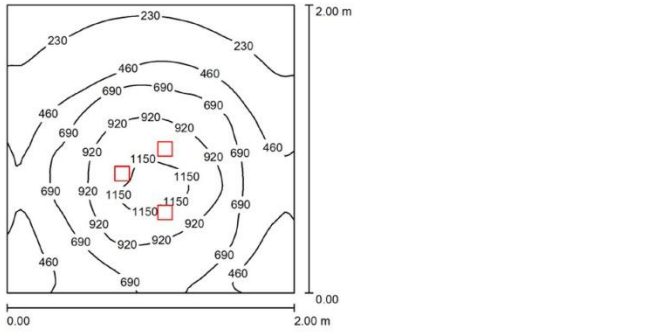

Height of Room: 2.100 m, Mounting Height: 2.100 m, Maintenance factor: 1.00 — Values in Lux, Scale 1:26

Surface	ρ [%]	E_{av} [lx]	E_{min} [lx]	E_{max} [lx]	u0
Workplane	/	586	79	1190	0.134
Floor	75	456	216	592	0.474
Ceiling	85	172	111	206	0.649
Walls (4)	64	246	97	448	/

(a)

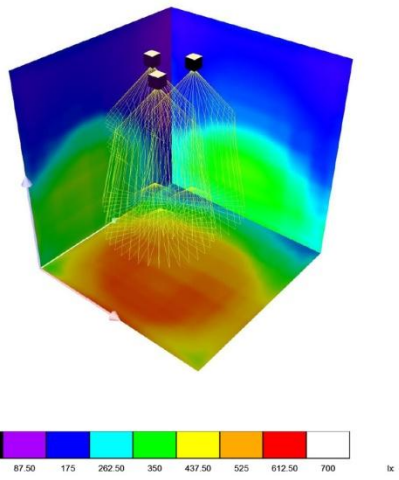

(b)

Fig. 4.66. Dialux simulations of the spectrally tuneable room constructed in the University of Newcastle.

In the light of the HI-LED project, the University of Newcastle (UK) used this spectrally tuneable room to investigate the effects of specific light spectra on the visual and non-visual pathways.

The aim of the experiment was to compare the effects on mood, alertness, cognitive performance and melatonin secretion of two metameric (spectra with the same visual appearance, but different spectral composition), but melanopically modulated spectra. A first (pilot) study exposed three participants to three different lighting conditions (dim, low-melanopic and high-melanopic) during three 3.5-hour sessions (Fig. 4.67). Previous reports suggested that a melanopic-rich light spectrum would result in a more positive mood, higher alertness, better cognitive performance and a low melatonin level (88).

Two experiments were carried out: a pilot test to determine optimal conditions and a main experiment.

Pilot experiment - setup

After screening (Pittsburgh Sleep Quality Index (PSQI), State-Trait Anxiety inventory (STAI), Morningness-Eveningness Questionnaire (MEQ), Beck Depression Inventory (BDI-II) and Ishihara Colour Plates Test) the participants were admitted to continue to the test phase. Provided saliva samples were genotyped for the period 3 clock gene. After screening, each participant was given a wrist actigraph to log activity during the entire duration of the experiment, beginning with a two-week baseline phase prior to the start of the experiment itself. Each participant was asked to refrain from any alcohol or caffeine intake from 3 days prior up to the moment of the experiment.

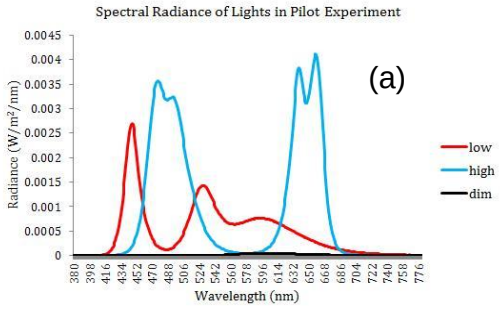

Fig. 4.67. Spectra of the three lighting conditions during the pilot experiment.
Source: University of Newcastle, UK.

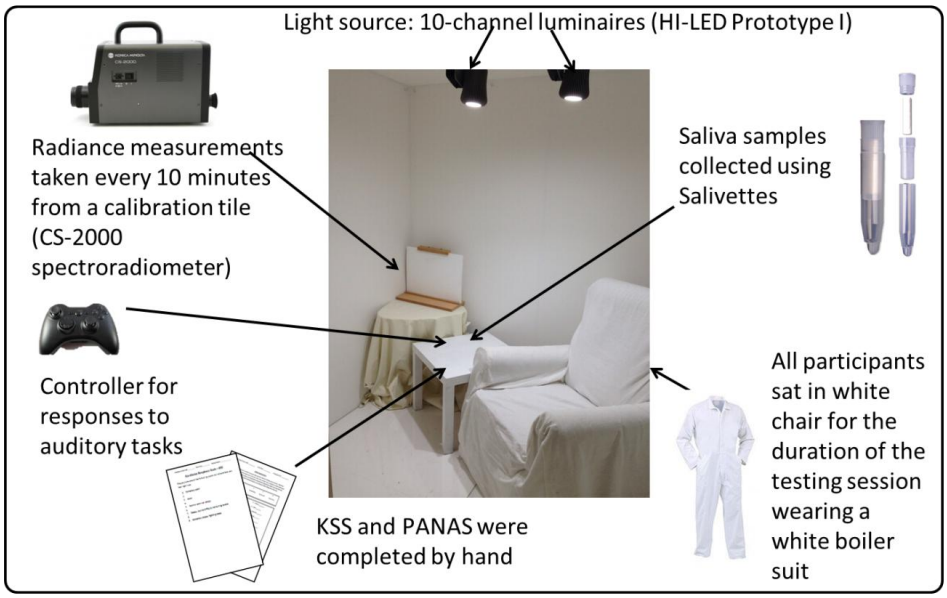

Fig. 4.68. The interior of the experimental lightroom and accessories used during the experiment.
Source: University of Newcastle, UK.

One week after the screening session the participants returned to the laboratory during two consecutive weeks for two more sessions, each of them identical apart from the lighting conditions. The photograph in Fig. 4.68 illustrates the experimental room. For the pilot experiment, each participant started at 20.05 with an 80 minute dark adaptation phase, followed by 120 minutes of light exposure with tasks to be carried out at regular intervals (Fig. 4.69).

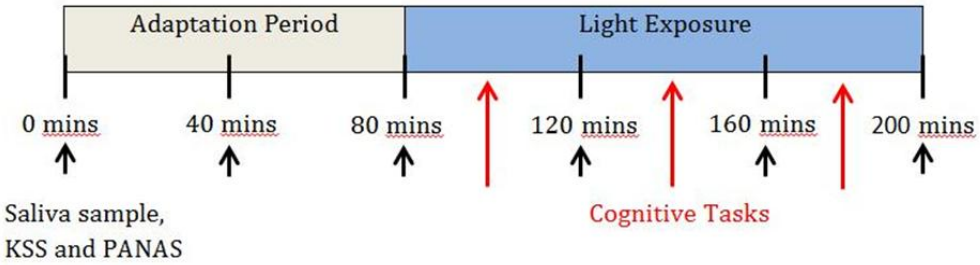

Fig. 4.69. Experimental timeline (pilot experiment).
Source: University of Newcastle, UK.

Three auditory tasks had to be carried out: a psychomotor vigilance task where a button had to be pressed after hearing a tone, a Go/No-Go task where a certain pitch of tone was a “Go” while a different pitch was a “No-Go” and a two-back task where the participant had to press a button when the current letter matched the one that was spoken two letters back. During the session participants were asked to provide a saliva sample, complete a copy of the Karolinska Sleepiness Scale (KSS) and the Positive and Negative Affect Scale (PANAS).

Pilot experiment - results

Contrary to the expectations, both the high and low melanoptic spectrum showed a decrease in melatonin levels when compared with the dim light conditions. Fig. 4.70 shows that the low melanoptic light condition attenuates sleepiness *more* than the high melanoptic spectrum while positive scores decreased during all light exposures. The reaction times were similar between all three lighting conditions (Fig. 4.71).

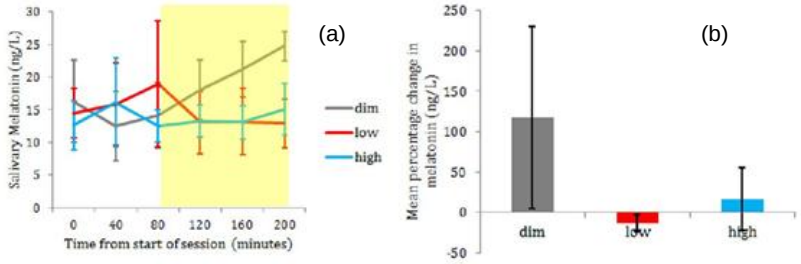

Fig. 4.70. Mean melatonin content in saliva for the dim lighting, high melanoptic and low melanoptic lighting conditions (a). Mean percentage change in melatonin from the start of the light exposure until the end (b). The yellow overlay indicates light exposure.

Source: University of Newcastle, UK.

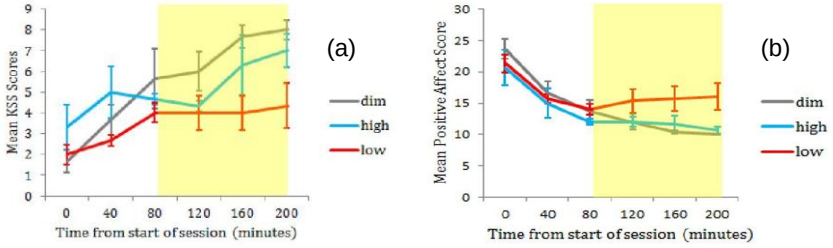

Fig. 4.71. Mean KSS (a) and PANAS (b) scores for the pilot experiment. The yellow overlay indicates light exposure.
Source: University of Newcastle, UK.

Main experiment – setup

The main experiment was carried out following a slightly modified protocol. The luminance of the lighting conditions was lowered significantly and different high and low melanopic spectra (Fig. 4.72) were chosen. Additionally, the cognitive tasks where changed with the intention to increase the difficulty level, a cognitive testing during the adaptation period was included, a recovery period after the light exposure period and an additional cortisol level measurement was added (Fig. 4.73).

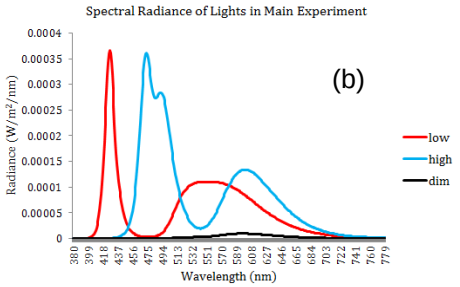

Fig. 4.72. Spectra of the three lighting conditions during the main experiment.
Source: University of Newcastle, UK.

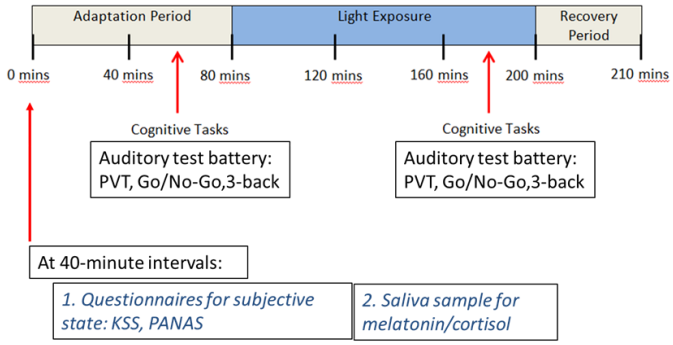

Fig. 4.73. Experimental protocol (main experiment).
Source: University of Newcastle, UK.

Main experiment - preliminary results

Fig. 4.74 shows the mean change in melatonin levels for the three lighting conditions for all 6 participants. There was no significant effect of the lighting condition on the melatonin levels. The same conclusion can be taken for the sleepiness rating, although the rating did differ between morning and evening test sessions (Fig. 4.75).

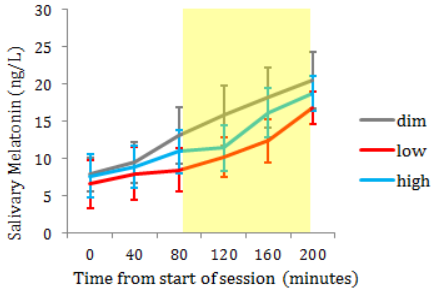

Fig. 4.74. Mean cortisol levels across all 6 participants in the three lighting conditions (evening session only).
Source: University of Newcastle, UK.

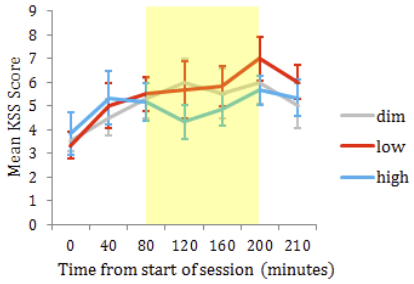

Fig. 4.75. Mean KSS scores across all 6 participants in the three lighting conditions (evening session only).
Source: University of Newcastle, UK.

Conclusions

Spectrally tuneable light sources offer possibilities that no researcher had before: the spectrum is not connected to the type of light source. Previous studies, such as the ones conducted by Chellappa et all. carefully controlled luminance levels but had only rough spectral approximation. Modulation of the melanopic pathway was done using warm white and cold white fluorescent light source. While they do provide different stimuli for the ipRGCs, they are hardly metameric. The stimuli used in the above experiment have identical cone receptor activations while at the same time they provide a very different activation of the non-visual pathway. The table below gives an overview of the chromaticity coordinates, illuminance values and “melanopic illuminance” for the three lighting conditions used in the pilot and main experiment compared to the available data for the experiments carried out by Chellappa et al. (25). The fact that results of previous studies are in disagreement with the results obtained in this experiment might be explained by the difference in chromaticity of the light sources used in those experiments.

Table 4.11. Spectral characteristics of the lighting conditions during the pilot and main experiment compared to the experiments of Chellappa et al.
Source: University of Newcastle, UK.

		Pilot	Main experiment		Chellappa et al. (2011; 2013)	
Light			Position 1	Position 2		
Dim	*CIE (x,y)*	(0.58, 0.42)	(0.526,0.443)	(0.526, 0.441)	**Dim**	--
	Illuminance (lux)	~4.7	1.468	1.754		<8
	Melanopic "illuminance"	~0.22	0.250	0.301		--
Low melanopic	*CIE (x,y)*	(0.30, 0.31)	(0.333,0.348)	(0.329,0.341)	**2500 K (*warm-white*)**	(0.465,0.432)
	Illuminance (lux)	~204	16.707	19.113		29.8
	Melanopic "illuminance"	~150	7.583	8.888		10.06**
High melanopic	*CIE (x,y)*	(0.30, 0.31)	(0.326,0.333)	(0.325,0.332)	**6500 K (*cold - white*)**	(0.298,0.307)
	Illuminance (lux)	~204	17.524	20.439		27.6
	Melanopic "illuminance"	~376	23.715	27.898		29.7**
Melanopic contrast (hi-lo)		**43%**	**51%**	**52%**		**50%**
Colour difference (ΔE) (hi-lo)		**0**	**11**	**7**		**133**

The downlight luminaires installed in the IREC laboratories served during two experiments resulting in publications described below:

- *Energy efficiency and color quality limits in artifical light sources emulating natural illumination*, discusses in detail the effects of *spectral reduction* on the colour rendering and efficacy properties of illumination spectra. While an increase in colour fidelity does have negative effects on the LER, it is proven that a joint optimization can result in a light source that has both excellent colour fidelity and a very high efficacy. Finally, the theoretical spectra resulting from the optimization process are fed to a spectrally tuneable LED light source to demonstrate its practical use. The results show that by reducing the extension of the short and long wavelength range of the visible spectrum, an illumination spectrum with both high colour fidelity properties and high efficacy can be realised.

As a starting point, a blackbody spectrum is used. Limiting the left and right outermost wavelength extension (λ_{left} and λ_{right}), concentrates more energy near the peak of our visual system and, consequently, increases the LER. The disadvantages are twofold: depending on how much of the visible wavelength range is cut, the colour rendering properties of the reduced visible spectrum suffer and the chromaticity coordinates start to deviate from the desired white point. To find a reasonable reduced visible spectrum range, a lower bound on CRI and LER, and an upper bound on Δ_{uv} is selected. These restrictions, combined with a score function, S, given by

$$S = \frac{1}{\sqrt{2}}\sqrt{\left(\frac{R_a}{R_a^*}\right)^2 + \left(\frac{Eff}{Eff^*}\right)^2} \qquad \text{(Eq. 4.9)}$$

Where R_a^* = 100 and Eff^* is the maximal LER for a particular target CCT.

Setting an upper bound on the Δ_{uv} gives results in a region of spectra of interest with the highest score spectra being selected for implementation in the spectrally tuneable downlight. The table below shows the parameters of the highest efficacy, highest R_a and highest combined score spectra at a CCT of, respectively, 3000 K and 5500 K.

Table 4.12. Spectral parameters of the highest efficacy (HE), highest R_a (HRa) and highest score spectra emulating natural illumination at a CCT of 3000 K and 5500 K.

Highest Efficacy (HE)	**Highest Ra (HRa)**	**Highest Score (HS)**
Emulation at **3,000K**. Target Efficacy = **364.41 lm/W**		
$E_{ff} = 363\,lm/W$ $Ra = 90.0$ $S = 0.950$ $\Delta_{uv} = 0.0053$ $\Delta\lambda = [421, 648]$ $CCT = 3,280K$ $R_{9-12} = 75.0$	$E_{ff} = 250\,lm/W$ $Ra = 99.7$ $S = 0.856$ $\Delta_{uv} = 0.0002$ $\Delta\lambda = [403, 703]$ $CCT = 3,010K$ $R_{9-12} = 99.2$	$E_{ff} = 363\,lm/W$ $Ra = 90.5$ $S = 0.951$ $\Delta_{uv} = 0.0054$ $\Delta\lambda = [424, 649]$ $CCT = 3,260K$ $R_{9-12} = 76.0$
Emulation at **5,500K**. Target Efficacy = **314.92 lm/W**		
$E_{ff} = 315\,lm/W$ $Ra = 94.4$ $S = 0.972$ $\Delta_{uv} = 0.0054$ $\Delta\lambda = [421, 653]$ $CCT = 5,620K$ $R_{9-12} = 85.7$	$E_{ff} = 262\,lm/W$ $Ra = 99.2$ $S = 0.916$ $\Delta_{uv} = 0.0021$ $\Delta\lambda = [421, 709]$ $CCT = 5,370K$ $R_{9-12} = 98.4$	$E_{ff} = 313\,lm/W$ $Ra = 95.4$ $S = 0.975$ $\Delta_{uv} = 0.0053$ $\Delta\lambda = [424, 658]$ $CCT = 5,490K$ $R_{9-12} = 88.6$

The implementation of the highest score spectra in the spectrally tuneable downlight luminaires resulted in both excellent LER and CRI-R_a values, approaching closely the theoretical limits calculated earlier. Table 3 presents a summary of the results.

Table 4.13. Comparison of the main spectral parameters of the highest score spectra with measured data from the implementation of those spectra in the spectrally tuneable downlight system.

Parameter assessment	3,000K	5,500K
LER (theoretical, lm/W)	363	313
LER (engine, lm/W)	329	295
$\mathbf{R}_a$ (theoretical)	90.5	95.4
$\mathbf{R}_a$ (engine)	94	92.1
Δ_{uv} (theoretical)	0.0054	0.0053
Δ_{uv} (engine)	0.0054	0.0053
CCT (theoretical, K)	3,260	5,490
CCT (engine, K)	3,256	5,494
$\mathbf{R}_9$ (theoretical)	39.1	66.3
$\mathbf{R}_9$ (engine)	62.5	88.2
$\mathbf{R}_{9-12}$ (theoretical)	76.0	88.6
$\mathbf{R}_{9-12}$ (engine)	85.2	87.1

The experimental data shows that not only the theoretical calculated values are in excellent agreement with the measured data from the luminaire implementation, they also show the benefits of a reduced black-body spectra and a joint optimisation of LER and CRI-R_a on efficacy and colour rendering properties of an illumination spectrum emulating natural illumination (annex I: Hertog, W, Llenas, A., Quintero, J.M., Hunt, C.E., Carreras, J., *Energy efficiency and color quality limits in artifical light sources emulating natural illumination*, Optics Express 22 (S7) (2014)).

- *Optimizing indoor illumination quality and energy efficiency using a spectrally tunable lighting system to augment natural daylight* demonstrates the benefits of complementing a daylight-lit environment with a spectrally-aware illumination system. The system consists of a skylight-equipped room (15 m^2), a roof-mounted miniature spectrophotometer and 6 spectrally tuneable luminaires of the type discussed earlier in this chapter. A number of optimisation algorithms calculate the spectra needed to either supplement the daylight already present in the room, creating a dynamically changing spectrum equal to the daylight conditions outside but at a preset illuminance or to compensate the daylight entering the room, bringing the final illumination conditions to a preset CCT and illuminance value.

  Three different spectral optimisation strategies were selected:

  - Providing an exact spectral match to the daylight spectrum measured by the spectrophotometer, minimising the square error between the input and target spectrum.

  The figure below shows a morning snapshot during the operating of the spectral matching algorithm. The daylight entering the room is measured and carefully reproduced, resulting

in an illumination spectrum that is nearly a copy of the original daylight input, albeit at an illuminance near 400 lx.

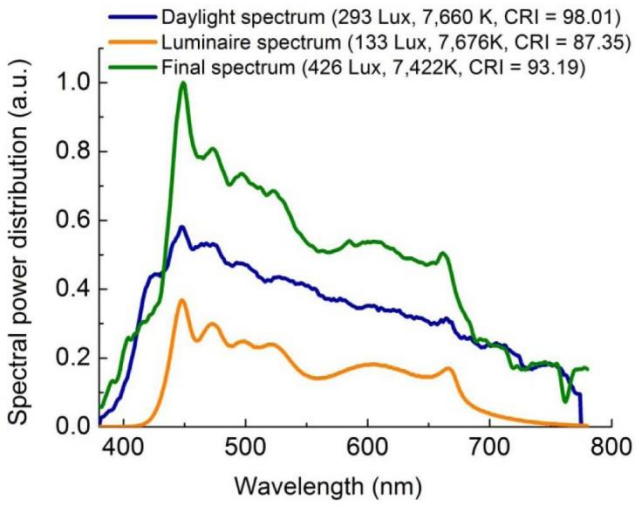

Fig. 4.76. Measured daylight spectrum (blue), spectrum reproduced by the spectrally tuneable luminaires (orange) and final illumination spectrum (green).

The result is a dynamic illumination experience that carefully copies the variations occurring in natural daylight without changing the illuminance. Conclusions made from analysing the energy consumption over a timeframe of one week show that savings over 1600 Whr per day were obtained when compared to an identical system unaware of daylight, emitting a D65 spectrum. Extrapolating these numbers would result in a total savings of 612.1 kWhr year for a space of 15 m^2 or 40.8 kWhr/m^2. These results assume, of course, that the atmospherical conditions and sun position present during the test-phase can be extrapolated to the rest of the year. In reality, this is not the case.

- Minimisation of energy consumption while preserving the measured chromaticity coordinates. By reducing the amplitude of as many channels as possible, the energy consumption of the light engine is minimized. Colour fidelity, of course, is harmed as well.

While keeping a constant CCT target of 4000 K at 400 lx at the workplane, the output of the luminaires can be dynamically adjusted to compensate for any changes caused by the introduction of daylight through the skylight. There are, however, an infinite number of spectra that fulfil these conditions. The number of spectra can be reduced by setting certain constraints. Maximising the LER is one of them. This approach results in a final illumination spectrum with a CCT close to 4000 K and an average CRI-R_a > 86.

- Maximising the colour fidelity while preserving the measured chromaticity coordinates. A genetic algorithm optimises the CRI-R_a while preserving the chromaticity coordinates

measured by the spectrophotometer. While this maximises the colour fidelity, there is a negative impact on power consumption.

An optimisation for colour quality increases the CRI-R_a value to over 98, while consuming around 25 % more power than the optimisation for en energy efficiency. The figure below shows spectra measured during both optimisation methods. It is clear that the energy optimisation algorithm strives to minimise energy consumption by reducing the amplitudes of most of the LED channels, resulting in a near-RGB emission spectrum of the luminaires.

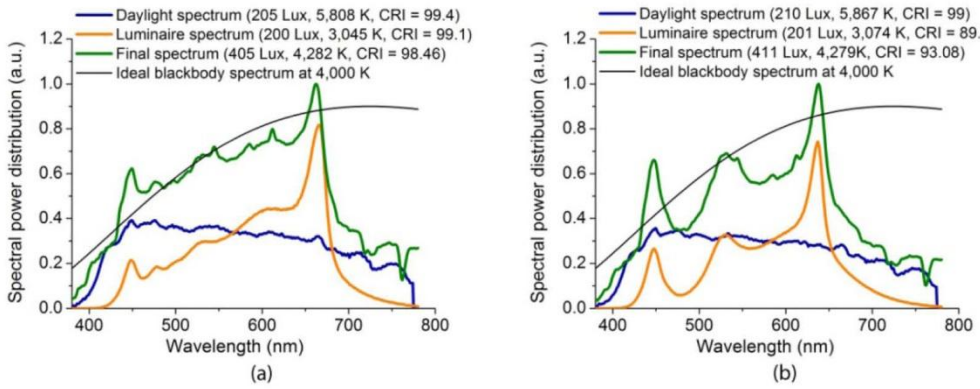

Fig. 4.77. Daylight compensation at a CCT of 4000 K comparing the daylight entering the test room (blue), the compensation spectrum emitted by the luminaires (orange) and the summed illumination spectrum (green), optimised for colour quality (a) and energy efficacy (b).

The colour rendering properties of both approaches are depicted in the colour rendering maps below. Despite similar, high CRI-R_a values, the colour fidelity of the illumination spectrum optimised for colour quality is clearly superior.

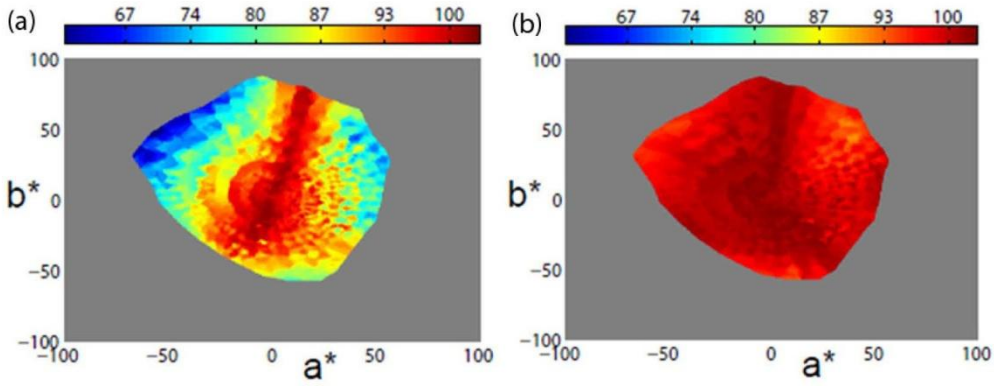

Fig. 4.78. CRMs showing the difference in colour fidelity between the optimisation for energy efficacy (a) and colour fidelity (b). The optimisation for energy efficacy results in severe colour fidelity differences, especially for yellow-green and red coloured objects. The colour-fidelity optimisation results in excellent performance over the full Munsell gamut.

Both rooms in the laboratories of IREC and UoN were controlled through a wirelessly connected Matlab interface. The Matlab code includes four computational functions to generate lighting spectra on demand:

- Function 1: spectral database
  The first function aims to match the output spectrum of the spectrally tuneable light engine to an example spectrum stored in a database. Users can edit the database and add new spectra, either artificially created or measured by a spectrophotometer. Slight differences between the input spectra and the matched spectral output of the light engine result in differences in chromaticity coordinates. A strict constraint ensures that a chromaticity coordinate match between input and output is guaranteed.
- Function 2: colour coordinates
  A second function creates a spectrum based on the user input of a set of chromaticity coordinates. The user can select an optimization routine that either prioritizes wall-plug efficiency, colour quality or computational speed. The genetic algorithm that optimizes the colour quality of the output spectrum finds the spectrum with the general colour rendering index value set by the user.
- Function 3: correlated colour temperature
  The third function creates a spectrum based on the correlated colour temperature value given by the user. The chromaticity coordinates are fixed on the black body locus while the efficiency and colour quality of the output spectrum can be optimized in the same way as in Function 2.
- Function 4: manual
  A last function gives the user full control of each of the 10 individual monochromatic LED channels. The output power of each set of LEDs, represented by a slider, can be changed with a resolution of 4096 steps.

For each of the 4 functions the user can select the output flux between a value of 0 and 100%. This ensures a constant luminous flux, independent of the spectrum generated by the light engine. Fig. 4.79 shows the graphical user interface with the different functions developed in Matlab.

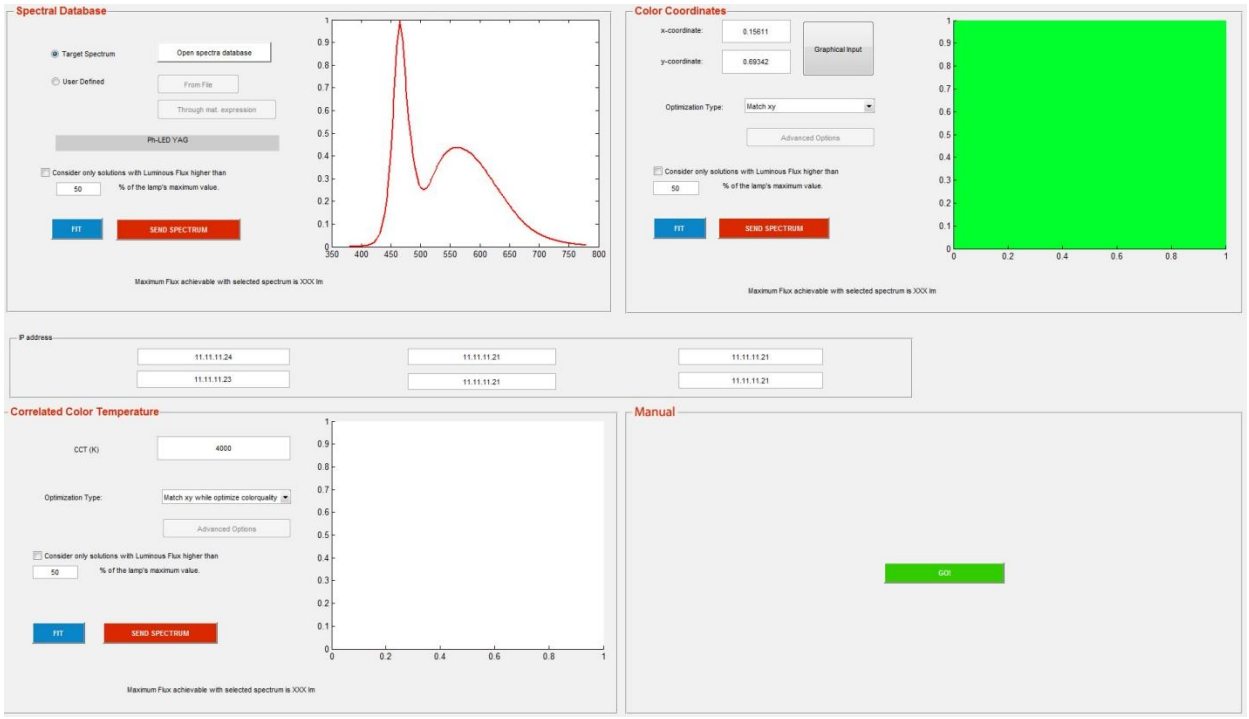

Fig. 4.79. Matlab graphical user interface. Each quadrant performs one of the four spectrum-generating functions.

4.5.7 Luminaire 2: museum lighting

Light engine V was specifically designed to provide a small source aperture, ready to be integrated in a compact spectrally tuneable spotlight to be used for the illumination or artworks. The spotlight, designed completely in-house, consists out of two major parts.

- The lamp housing containing the light engine and a Hamamatsu C12666MA microspectrophotometer
- The driver housing containing the LED driver electronics and Mean Well PLP 60-24 SMPS

The casing of an LED luminaire provides two important functions. Besides being a container for all the electrical and optical components, it also provides the necessary surface area to dissipate heat generated by both the LED themselves and the LED driver electronics. A compact LED array such as the one used in the fifth iteration of the light engine needs careful thermal management. During the design phase of the spotlight, the decision for a passive cooling solution was made. This would not only minimize noise and maximize electrical efficiency, but also improve the reliability of the luminaire. A first mock-up, designed in Autodesk AutoCAD, was fabricated in engineering plastics by means of a 3D printer (Fig. 4.80, 4.81).

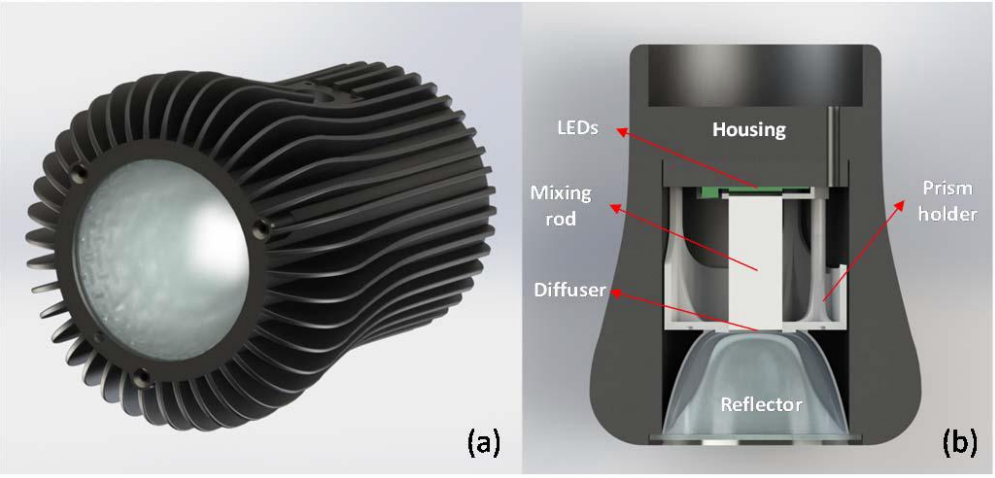

Fig. 4.80. Render of the mechanical design of the lamp housing for the spotlight luminaire. (a) Fully assembled and (b) cross-section with main components.

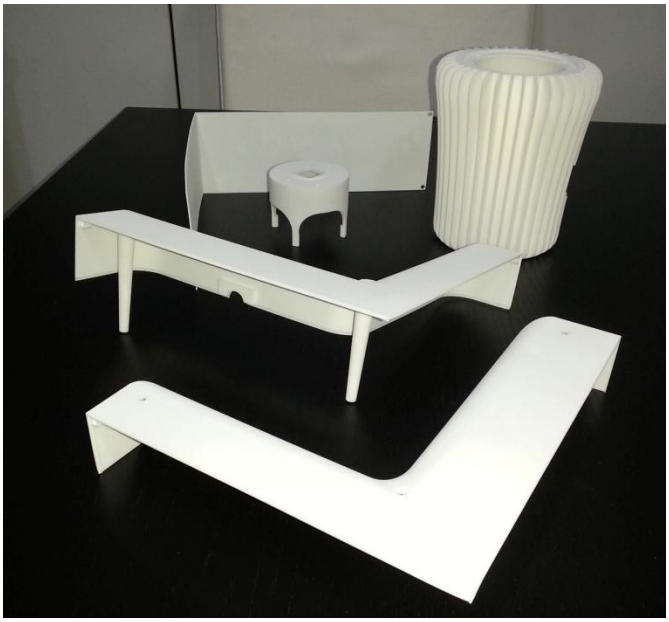

Fig. 4.81. 3D-printed mock-ups of the main components in the spectrally tuneable spotlight.

A second simulation round revealed several shortcomings in the design. First and foremost, heat generated by the LED driver and PSU was trapped inside the L-shaped housing. The thin metal plate on the back did not provide enough thermal mass and surface area. Secondly, the structural strength of the plastic parts was insufficient to carry the heavy aluminium lamp housing.

A second design was made and subjected to a series of CFD thermal simulations, carried out imposing the following conditions:

1. PCB made in ceramic, MCPCB or FR-4
2. 40 luxeon Z LEDs with thermal resistances of 5 °C/W and 8 °C/W distributed as shown in Fig. 4.82

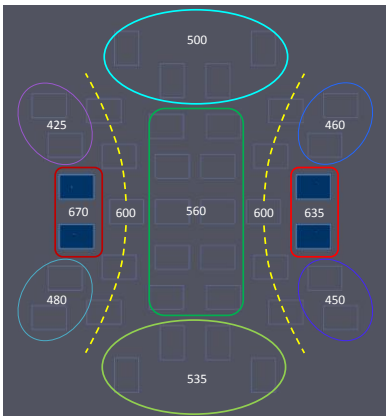

Fig. 4.82. LED array layout. The channels are grouped, indicating the emission peak in nm. The LEDs in blue indicate a thermal resistance of 8 °C/W.

3. Thermal loads of the LEDs are shown in Table 4.14:

Table 4.14. Parameters of the different channels

Channel (nm)	Operation current (mA)	N# LEDs per channel	Power consumption per LED (W)
427	350	2	0.633
449	700	2	1.445
471	350	2	0.800
473	350	2	0.810
496	350	4	0.831
522	700	4	1.780
546	350	10	0.757
600	350	10	0.826
638	700	2	1.232
661	350	2	0.512
		40	**37.14**

4. A 50-micron thick TIM with a thermal conductivity of 8.7 W/m·K (Artic Silver).
5. The lamp housing and heat spreader for the LED PCB were fabricated from $AlSi_7Mg$, an Al-alloy which is cheaper than standard aluminum and has a thermal conductivity of 167 W/m·K as opposed to 210 W/m·K.

6. The housing is anodised black with an emissivity coefficient of 0.8.
7. The calculations have been carried out considering a static outside flux (only convection from the LEDs).
8. The room temperature is fixed at 25 °C.
9. The output surface of the luminaire is facing down.
10. Four different cases have been simulated:
    a. Compact LED array with ceramic PCB
    b. Spread LED array with ceramic PCB (relative distances between the LEDs have been increased by a factor of 3)
    c. Compact LED array constructed on a FR4-based PCB, 0.25 W/m·K
    d. Compact LED array on a MCPCB, 2.4 W/m·K
11. The parameters to be monitored:
    a. Maximum junction temperatures
    b. Junction temperature at channel 638, especially sensitive to temperature variations (AlInGaP).
    c. Housing temperature.
    d. Maximum temperature at the mini-spectrometer.

The results of the different simulations are schematically summarized in Fig. 4.83:

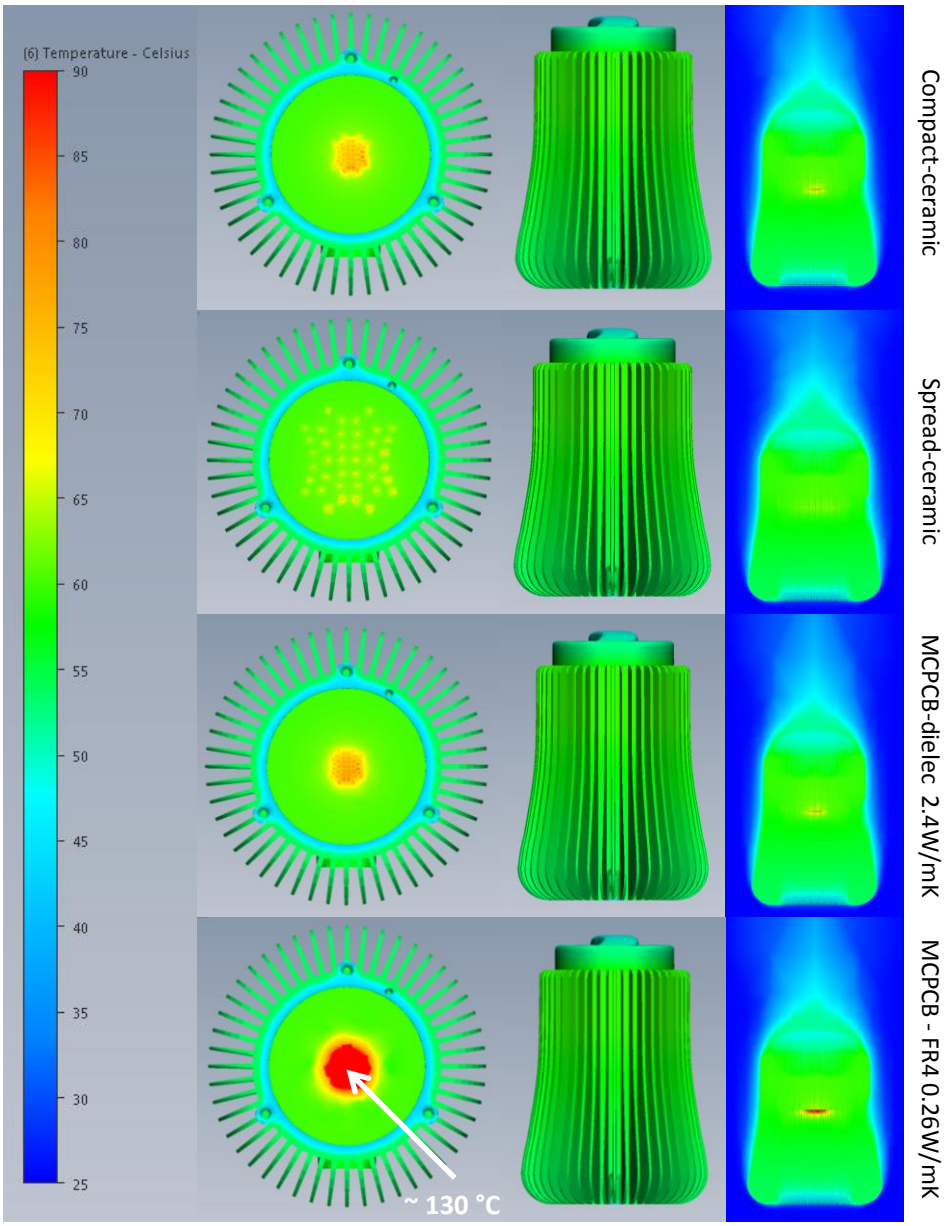

Fig. 4.83. Comparison of the temperature maps. The temperature scale has been adapted to clearly show temperature differences. In the case of the FR4 material, junctions can reach a maximum temperature of 130 ºC.

The ceramic PCB was indeed a good choice and results in lower temperatures than a standard metal core solution ($T_{j,\,max}$ = 83.7 ºC versus 84.5 ºC for the MCPCB). FR4 material, used in prototype light engine III, is clearly not suitable for compact, high power density applications ($T_{j,\,max}$ = 132.2 ºC). The simulation results indicate favourable, albeit slightly high temperatures for the LED junctions and lamp housing. Considering a maximum allowable junction temperature of 135 ºC for AlInGaP and PC emitters, a maximum simulated temperature below 84 ºC places the luminaire in a safe operating zone. To further lower the junction temperature would mean a significant increase in surface area of the housing and a change to a material with higher thermal conductivity (for example, pure aluminium).

The driver housing was changed from an L-shaped plastic enclosure to a rounded rectangular design. This creates both a mechanically strong surface to support the mass of the lamp housing and provides a large area to dissipate any heat generated by the LED drivers and PSU.

The lamp and driver housing are attached through a hollow aluminium tube that allows rotation of the lamp head and provides a passageway for the LED and spectrophotometer supply and data wires.

A series of fully functional track mountable spotlights was manufactured by a combined process of 3D printing and liquid $AlSi_7Mg$ moulding. Fig. 4.84 shows the finished luminaires.

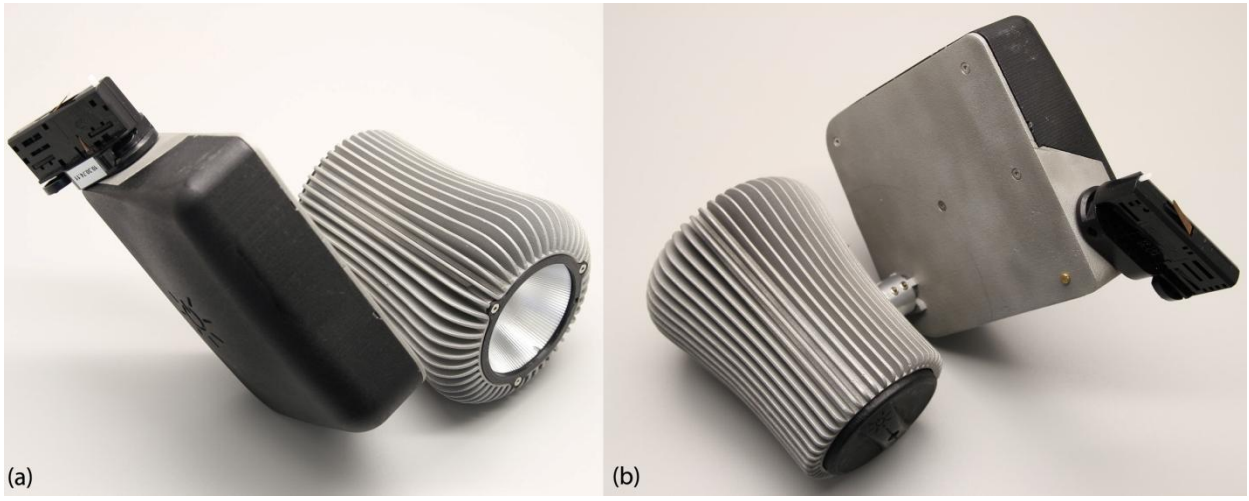

Fig. 4.84. Track mountable spectrally tuneable spotlight. (a) front and (b) back view.

The power consumption of the light engine, including a Mean Well PLP 60-24 power supply is 62.93 W. This equates to an overall full power efficiency of just over 8.85 % and a luminous efficacy of 23.8 lm/W, including losses within the power supply, optics and cover glass. Fig. 4.85 shows the full power spectrum of the luminaire.

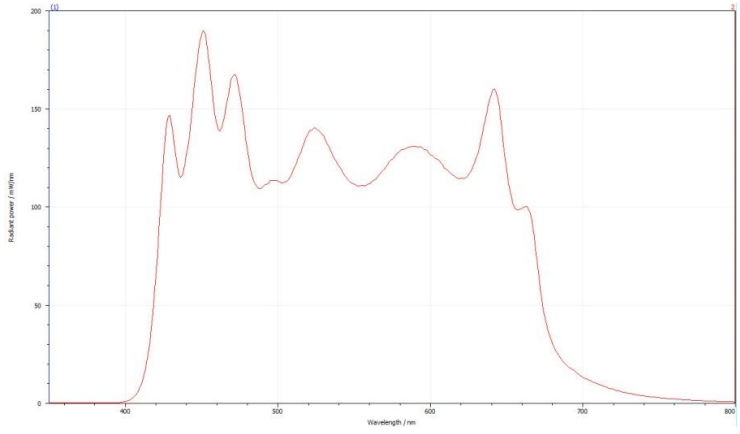

Fig. 4.85. Full power SPD of the spotlight (flux = 5.57 W, 1498 lm at a CCT of 5949 K (ΔE = -0.007) and R_a of 93.8), including beam homogenisation optics, reflector and a cover glass.

The spotlight has a unique feature: the integration of a miniature spectrophotometer combined with a set of plastic fibre optics (POF) to provide spectral information about the performance of the light engine itself and the surroundings of the luminaire (Fig. 4.86). The CMOS-based Hamamatsu microspectrometer gives, first and foremost, accurate spectral feedback on the output of the light engine. After wavelength and intensity calibrations of the spectrophotometer, its measurements are used as input parameters in a closed-loop correction function consisting out of two parts:

- A function that compares the difference in the spectral data that was sent to the light engine with the measured data from the spectrophotometer. A least square error function searches for a proper fit using the existing LED channels and the new spectrum is be added to the existing one.
- The spectrum that was measured by the spectrophotometer with the addition of the amplitude corrections is evaluated for its chromaticity coordinates. When the new x, y coordinates differ from the ones that were derived from the original spectrum sent to the light engine, a correction is applied after which the new amplitudes are sent to the light engine, resulting in a spectrum that is corrected in amplitude and chromaticity.

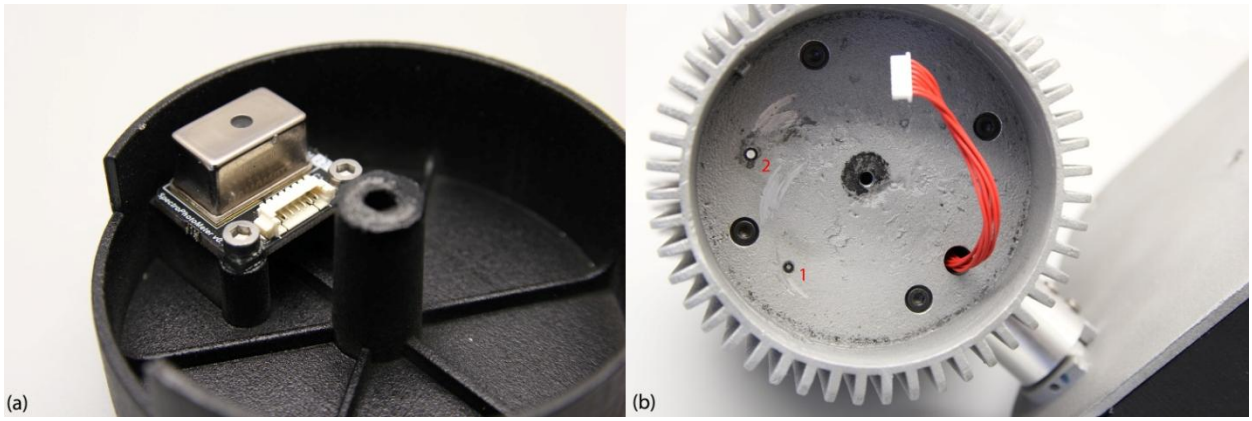

Fig. 4.86. Hamamatsu C12666MA microspectrometer, integrated at the back of the lamp housing (a). POF 1 collects light from the environment while POF 2 provides feedback from behind the light engine´s diffuser (b).

6 spotlights (4 in use, two spares) were used during the prestigious “Making Colour” exhibition that ran from the 18th of June to the 7th of September 2014 in the National Gallery of London, UK.

‘Making Colour’, the first exhibition of its kind in the UK, invites you on an artistic and scientific voyage of discovery. From sparkling minerals to crushed insects, learn about the surprising materials used to create pigments and the incredible journeys made by artists in their pursuit of new hues.

Span hundreds of years from the early Renaissance to the Impressionist movement as you take in displays of paintings, mineral specimens, textiles, ceramics and glass.

Journey from lapis lazuli to cobalt blue, ancient vermilion to bright cadmium red, through yellow, orange, purple and verdigris to deep green viridian – in a series of colour-themed rooms. Finally, enter a dazzling central room devoted to gold and silver.

'Making Colour' is complemented by an interactive display that introduces a new world of contemporary scientific thought on colour. Designed to demonstrate how we perceive and register colour, the experiment will reveal how the eye and brain respond to colour in unexpected ways.'

- *http://www.nationalgallery.org.uk/making-colour*

The luminaires were used to illuminate 2 works of art:

- A copy of Paul Gauguin's Bowl of Fruit and Tankard before a Window, painted with the pigments used by Gauguin in the late 19th century.
- A 12-ink inkjet reproduction

Both reproductions where exhibited as part of an interactive exhibition that demonstrated, through a psychovisual experiment, the influence of different light spectra on the perception of the colour in both paintings.

In order to ensure a very homogeneous illumination on the exhibition surface, a detailed light study was performed. Based on photogoniometric characterisations, a number of simulations were done in Dialux, resulting in the design shown in the figure below.

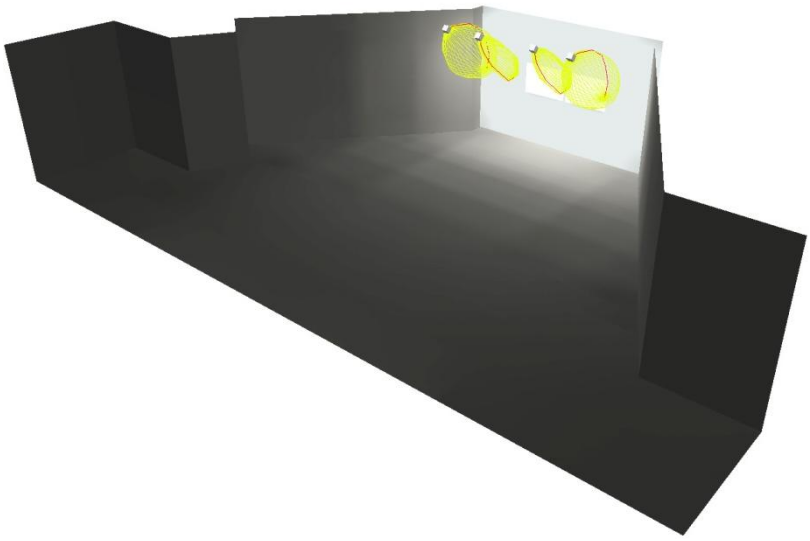

Fig. 4.87. Accurate colour and luminance render of the illumination system designed to illuminate two art reproductions in the National Gallery, London.

The illumination homogeneity of the illuminated wall surface was maximised by using two different versions of the spectrally tuneable spotlight. The two innermost luminaires are equipped with a narrow-beam reflector (FWHM = 28 º) while the two outermost luminaires have a wide-angle reflector (FWHM = 74 º), resulting a very smooth transition in illuminance from the central area to the edges of the viewing wall (Fig. 4.88)

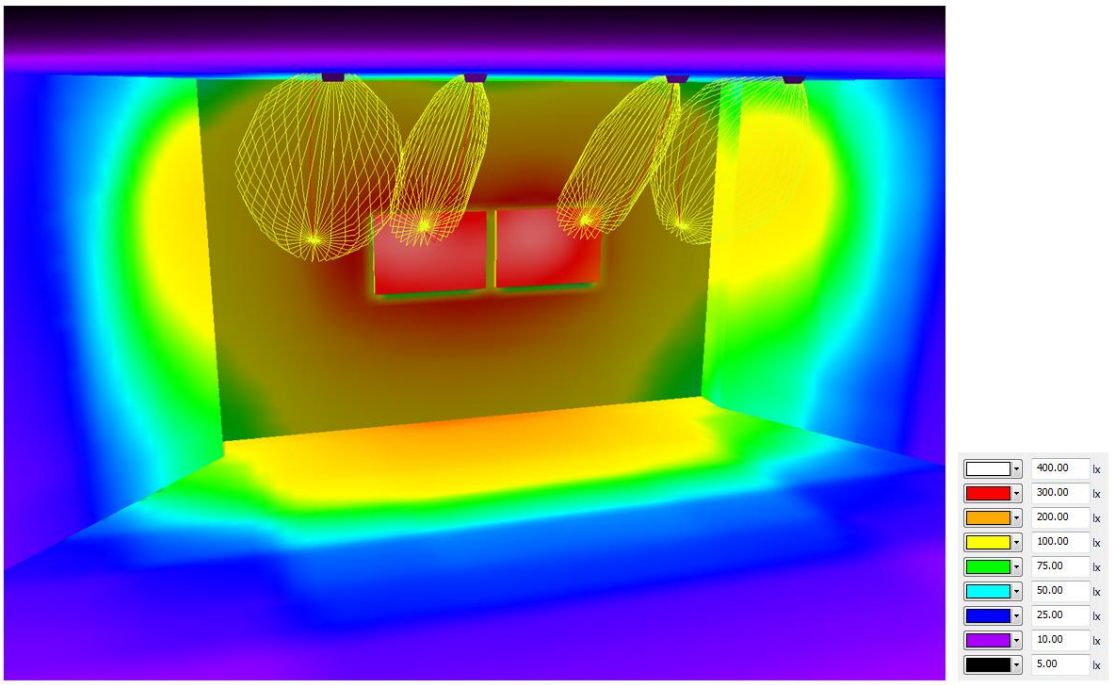

Fig. 4.88. Illuminance distribution on the reproductions and surrounding surfaces. The luminaires have a carefully chosen radiation pattern that, in conjunction with their position, provides a peak illuminance of 350 lux on the painting and print and a soft transition to the dark surroundings.

Fig. 4.89. Lamp housings ready to be attached to their matching drivers. Note the difference between the spot and flood reflectors.

4 wirelessly controllable luminaires (Fig. 4.89) were installed in the National Gallery room and performed flawlessly over the course of the exhibition (Fig. 4.90).

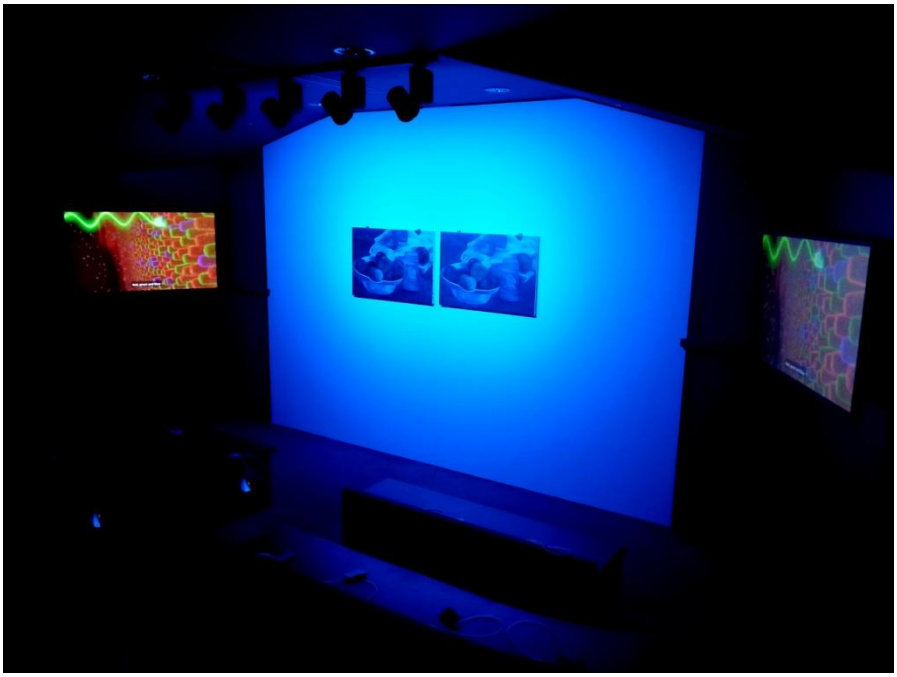

Fig. 4.90. Demonstration of the psychovisual experiment in the finished exhibition space of the National Gallery, London.

4.5.8 Luminaire 3: horticulture lighting

A third luminaire, conceived as part of the FP7 HI-LED project, was designed with the aim to investigate the influence of different illumination spectra on the production of anti-oxidants and other value enhancing substances not directly related to the biomass production of plants (tomatoes, in particular) such as vitamin C and lycopene. While a number of studies have been done surrounding this topic, none of them simulated the dynamic behaviour of sunlight while at the same time altering certain parts of the photosynthetically active radiation (PAR) spectrum.

One of the main requirements, besides the spectral tuneability of the light source, was that the irradiance received by the plants illuminated by the horticulture luminaire had to be equal to the irradiance received by plants grown inside a Spanish greenhouse during a clear summer day, which is 1000 micromoles/m2.s or, converted to radiometric units, 216 W/m^2 of radiation between 400 and 700 nm.

Besides the irradiance and spectral requirements discussed above, a number of guidelines had to be followed for the implementation of the luminaires inside the laboratories of IRTA in Cabrils, Spain.

- Illumination should be provided to the top surfaces of the crops
- Besides spectral tuneability within the PAR region of the spectrum, far-red radiation peaking around 740 nm should be available to modulate certain growth aspects of the plants
- 4 modules have to cover a grow area of 2 x 1.2 x 2 m (l x w x h).

The TracePro raytrace simulations below show the results of a light engine containing 920 Luxeon Z LEDs covering a wavelength range from 430 to 750 nm. Each of the four luminaires has a calculated radiometric output of 194 W, resulting in an injection of over 775 W of light in a 4.8 m^3 space. Four tomato plants are modelled through cylindrical structures with a reflectivity of 25 %, while the other surfaces have a reflectivity of 70 % (Fig. 4.91).

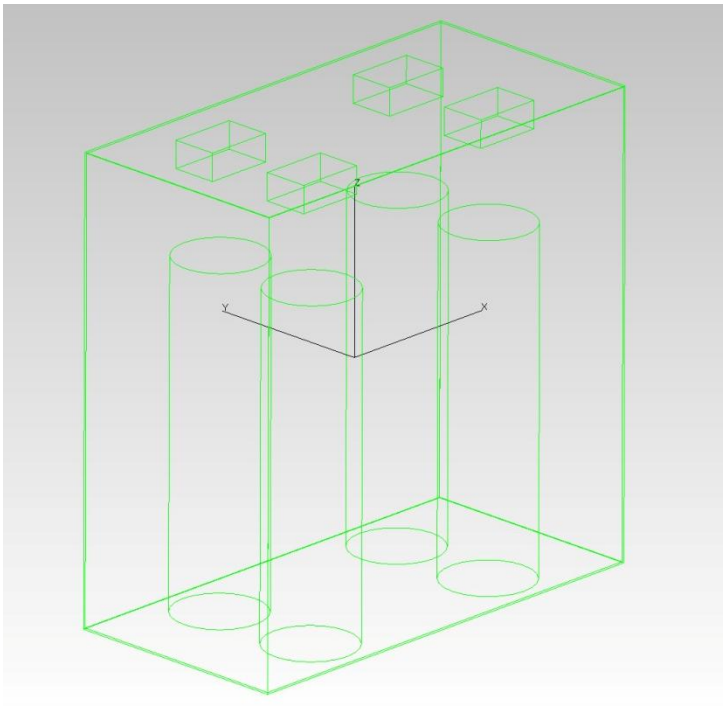

Fig. 4.91. Simulation model of the IRTA grow room containing 4 luminaires and 4 tomato plants. Each luminaire is placed 50 cm above the top surface of the corresponding tomato plant.

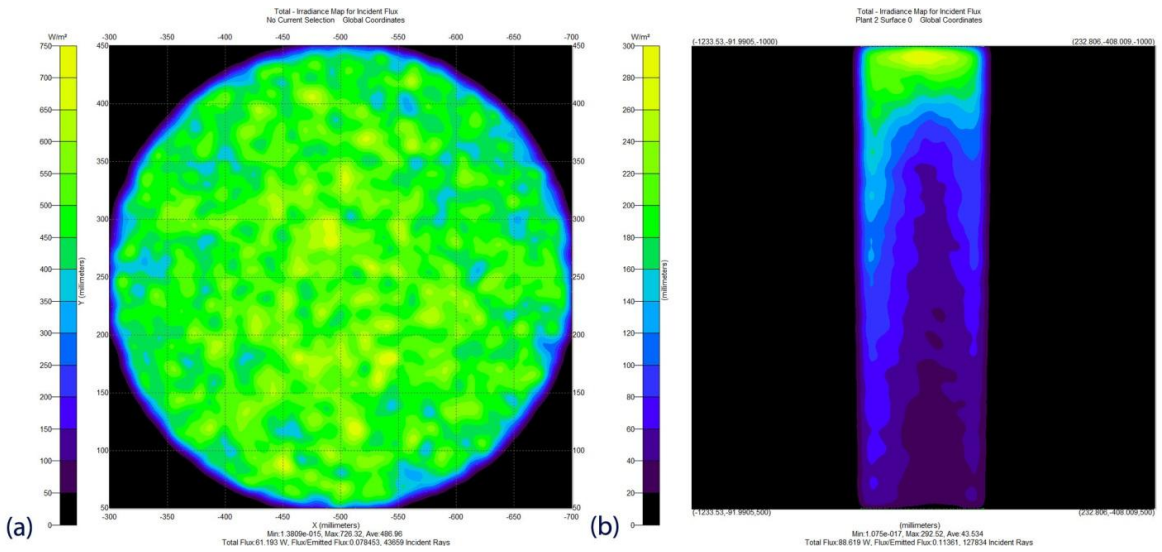

Fig. 4.92. TracePro raytrace simulation showing an average irradiance of 487 W/m^2 on top of the tomato plant (a) and a markedly lower value of only 43.5 W on the lateral sides of the plants (b) (channel 1-9 = 100 %)

The raytrace simulations show a very high average irradiance on top of the plants at maximum power output of the luminaire. On the contrary, the lateral irradiance values are low (Fig. 4.92). Due to the high flux requirements, the decision was made to exclude any efficiency reducing optics. This implies that the modules need to be placed close to the top surfaces of the plants to maximise the delivered flux density.

Based on the simulation results, a large metal core PCB was designed containing 20 identical, circular LED arrays, measuring 36 mm in diameter. Each array consists of 46 LEDs spread over 9 individual wavelength channels. Table 15 summarizes the main characteristics of the light engine while Fig. 4.93 shows the spectrum of each monochromatic LED channel. Note that while channel 9 (λ_p = 735 nm) does not contribute to the luminous flux of the light engine, the radiometric flux is used by plants to regulate their elongation.

Table 4.15. Main optical characteristics of the horticulture light engine.

Channel	Number of LEDs	Peak wavelength (nm)	Flux (W)	Flux (lm)
1	60	450.0	20.54	653.8
2	80	476.3	17.38	1897
3	100	497.0	16.94	4316
4	80	528.3	7.58	4060
5	240	546.8	55.3	25960
6	160	599.3	21.0	7066
7	40	638.3	6.7	1044
8	80	663.4	15.9	906.3
9	80	735.3	12.8	12.6

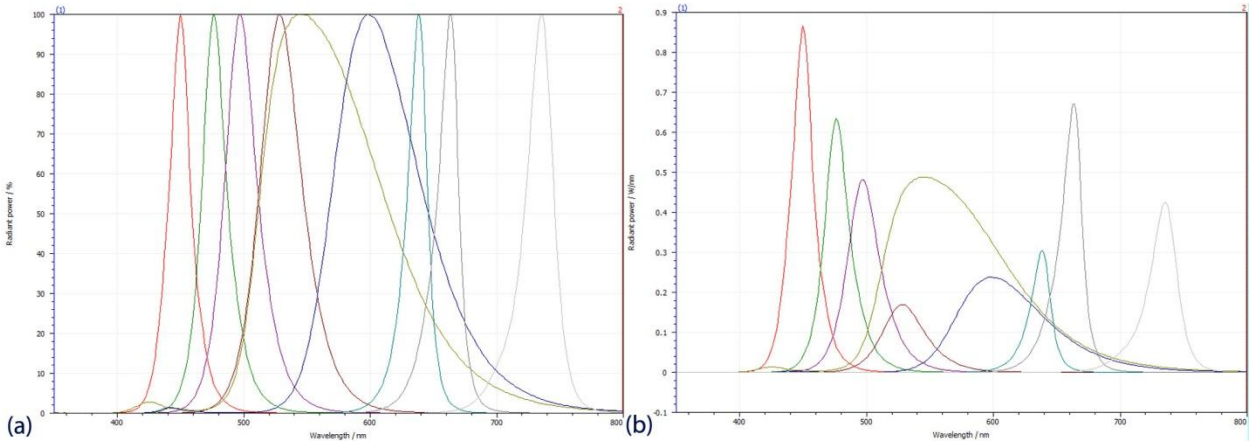

Fig. 4.93. Emission spectra of the 9 individual channels of the horticulture module. (a) Normalised and (b) absolute radiometric values.

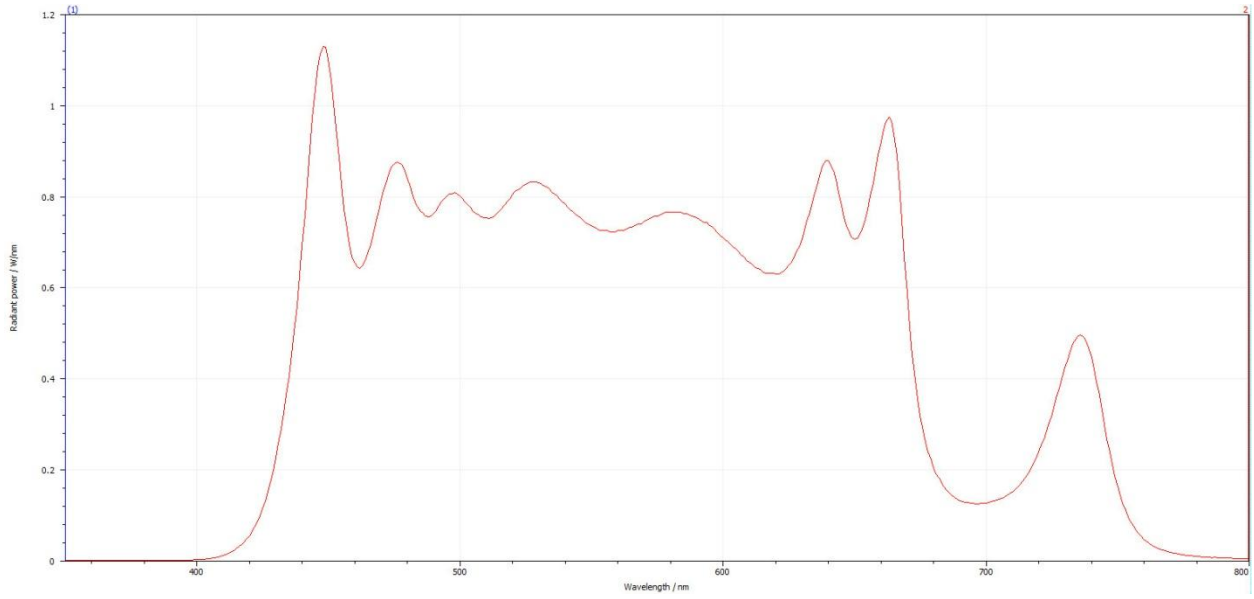

Fig. 4.94. Full power SPD of the horticulture module (flux = 199.9 W, 53270 lm at a CCT of 5615 K (Δuv = 0.0079) and a R_a of 96).

Fig. 4.94 shows the daylight-like spectrum of the light engine at full power, with peaks around the absorption peaks of chlorophyll a-c and energy in the critical far-red region that regulates morphological properties in plants.

The 20 Luxeon Z-based LED clusters where mounted on a 300 x 300 mm MCPCB substrate, as seen in Fig. 4.95.

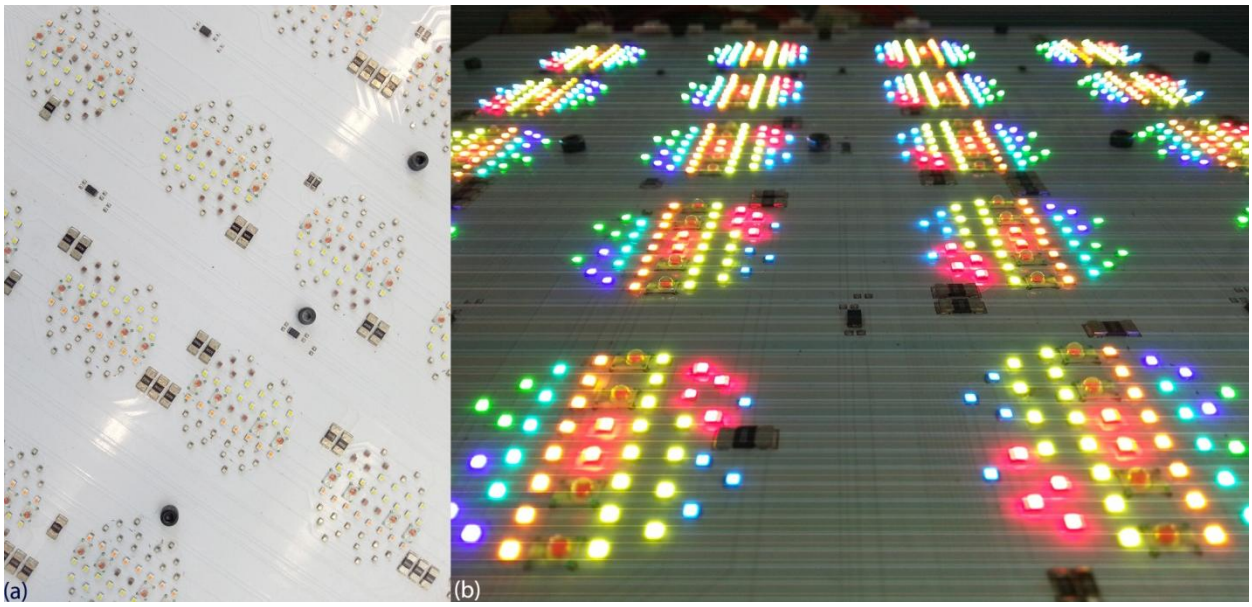

Fig. 4.95. Close-up of the horticulture LED PCB. (a) Unlit and (b) lit at low power.

The enormous quantity of LEDs used in the light engine calls for a specialised power supply. The initial idea of using a high-voltage (> 350 V) DC-DC constant current boost regulator was dismissed after a first

trial. Although such an LED driver would enable a compact and efficient design (the higher the output voltage, the lower the amount of individual LED drivers are needed), it proved to be extremely difficult to guarantee safe operation in a damp environment such as inside a greenhouse. A safer, but more complicated option was to use the buck converter design that was used from prototype III through the final light engine. A total of 63 individual Texas Instruments LM3406 LED drivers were used, delivering 350 mA at a maximum forward voltage of 60 V to the LED strings. A STM32F43x microcontroller, a version with more I/O ports than the one used in the previous designs, manages the PWM ICs that control the LED drivers. A number of extra peripherals were added to facilitate the stand-alone operation of the luminaires:

- A USB communication interface provides the main communication link between the PC and luminaire
- And RS-232 serial interface to link multiple luminaires together
- An SD-card bus for firmware upgrades
- 16 MB SDRAM and 16 MB NOR flash for the storage of calibration files

The LED driver design and finished PCB is shown below in Figs. 4.96 and 4.97.

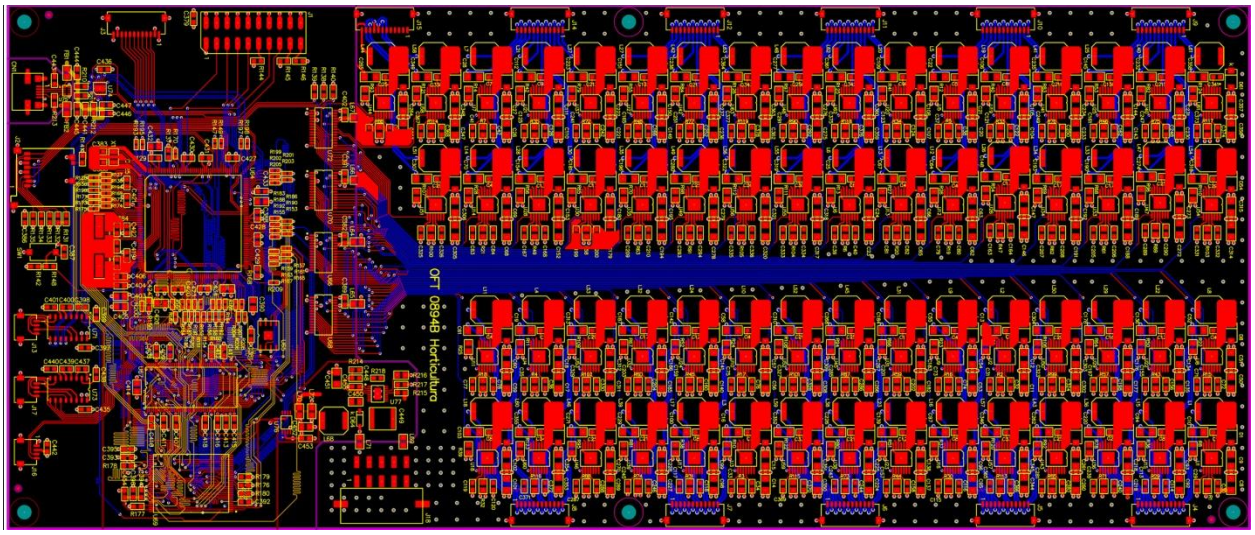

Fig. 4.96. 6-layer PCB design for the horticulture light engine, including 63 buck converters and a myriad of connection possibilities.

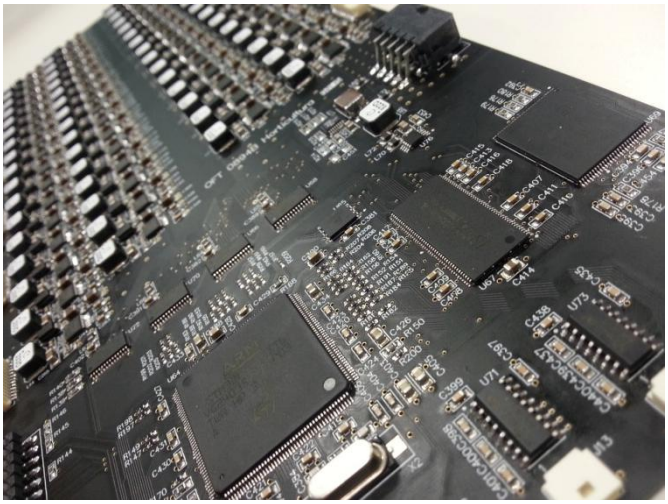

Fig. 4.97. Close-up of the horticulture driver PCB.

The enormous amount of power delivered by the driver (> 850 W) results in a large amount of heat generated within the LED junctions. While simple thermal calculations suffice for low-power applications where there is room for over dimensioning heatsinks and other heat dissipating components, in a high power application like this horticulture module, a 20 % margin of error would results in an unacceptable increase in heatsink capacity. Based on earlier CFD results, a number of LED substrate and heatsink combinations were simulated. Fig. 4.98 shows the simulation results of the chosen combination: a massive 300 x 300 x 260 mm (l x w x h) extruded Fischer Electronik heatsink with a thermal resistance of 0.014 K/W combined with two side mounted 230 VAC 4E-02 cooling fans, each creating a laminar air flow of 2.99 m^3 per minute.

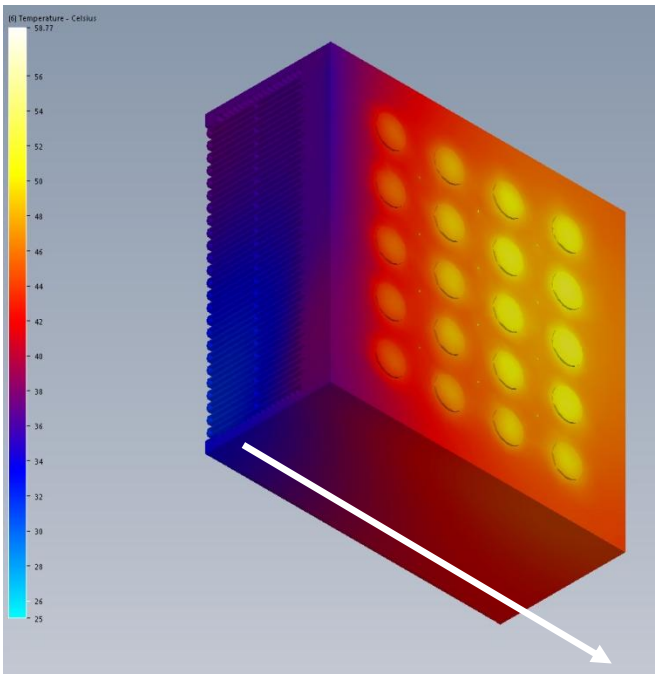

Fig. 4.98. Thermal simulation of the horticulture light engine. The white arrow indicates the direction of the airflow.

The finished luminaire, shown in Fig. 4.99, was thermally characterised using an FLIR SC5000 thermal imaging camera to compare the simulation results with real world performance.

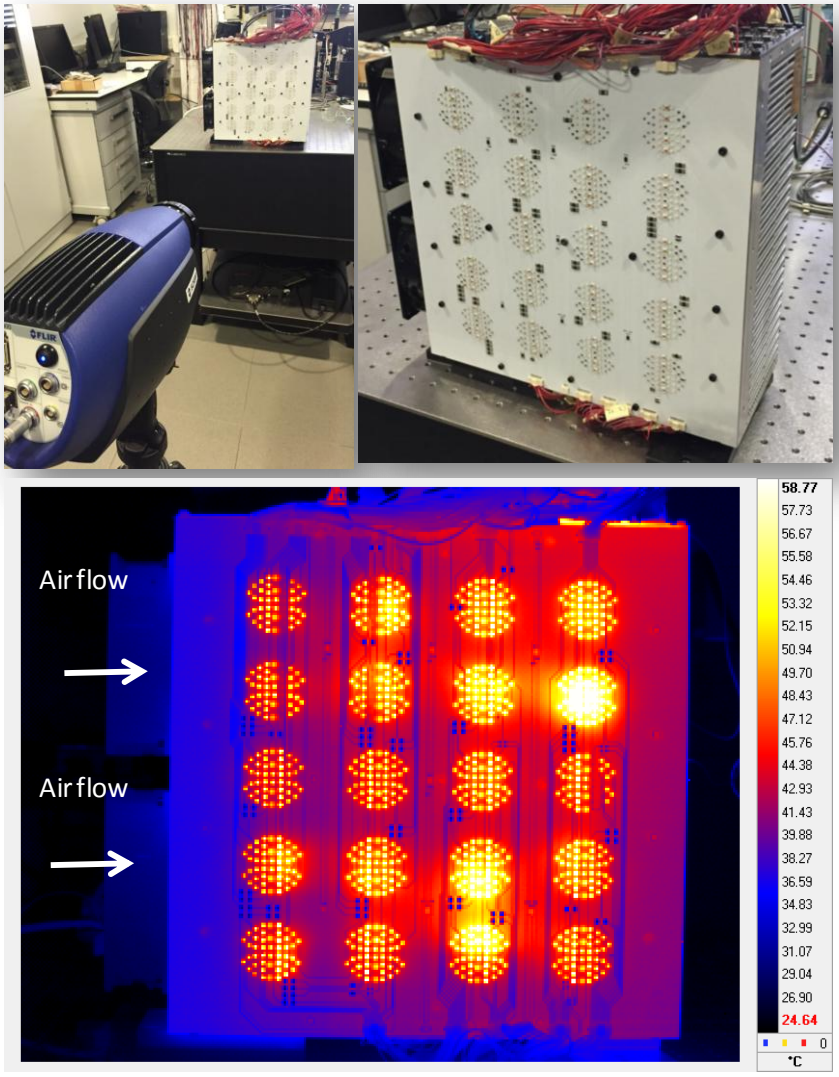

Fig. 4.99. Thermal testing of the horticulture luminaire. Notice the hot-spots on the bottom image.

The results of the CFD analysis correlate exceptionally well with the thermal imaging data, with one exception. The infrared images reveal a number of hot spots on the PCB where the temperature is several degrees hotter than in surrounding clusters. This is most likely the result of soldering voids underneath the LEDs or air bubbles inside the thermal interface layer between the PCB and aluminium heatsink. This problem was solved by adjusting the soldering process and the TIM application method.

Both the simulation and the thermal measurements above do not indicate individual LED junction temperatures. Fig. 4.100 shows the maximum junction temperatures encountered when the horticulture module was driven at full power.

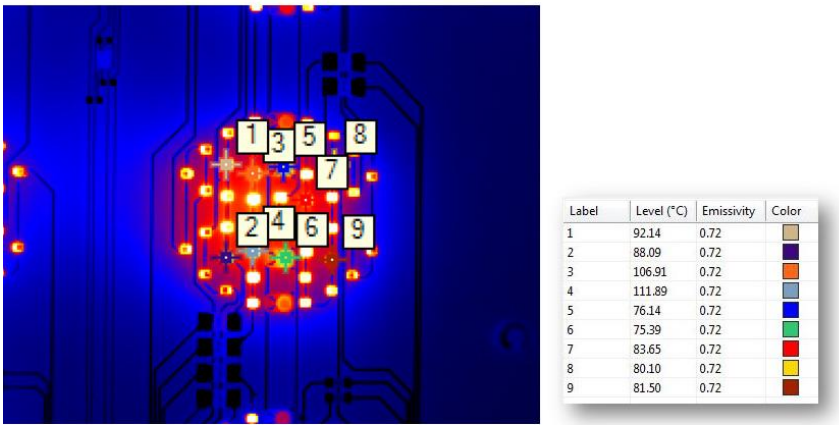

Fig. 4.100. Junction temperatures within one LED cluster of the horticulture luminaire. A maximum temperature of 111.9 ºC was measured in channel 5 (PC green).

The first two luminaires were delivered and installed late October 2015. IRTA has the possibility to create a through Python generated playlist with different illumination spectra, taken from a database or created manually within the control program, creating a spectrally variable growing environment for tomato plants (Fig. 4.101).

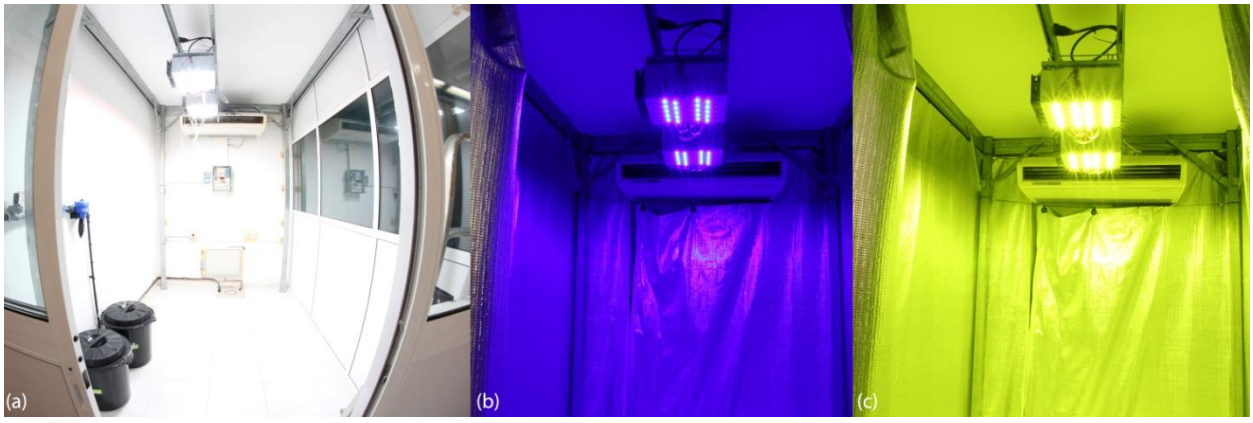

Fig. 4.101. Installation of two luminaires in one of the two grow rooms in IRTA, Cabrils. A USB connection links the luminaires with a control program to create a dynamically changing environment. (a) channels at full power, (b) channel one at 100% and (c) channel 5 at 100%.

4.6 Summary and conclusions

Designing a spectrally tuneable light source starts with the creation of a conceptual idea. Besides combining a number of LEDs, the light engine incorporates control and driving electronics, secondary optics and a system to dissipate heat generated by the LEDs. LEDs, like all diodes, conduct current in one direction only. Their steep I, V characteristic means that a simple voltage source does not allow stable behaviour. Large-die LEDs used for general illumination purposes are generally driven at a forward

current higher than 300 mA. This means that a simple resistor-based LED driver or, depending on the voltage difference between the LEDs and the power source, a linear constant current regulator, results in large heat losses and thus low driver efficiencies. A preferred solution is the use of a switching regulator. To be able to create a particular spectrum, the current through each LED channel (a combination of LEDs with the same spectral characteristics) needs to be independently controlled. Dimming LEDs can be accomplished by changing their forward current, either through the use of a constant current reduction method or through PWM. CCR-drivers inject a non-modulated variable current in the LEDs string, resulting in two very important consequences: the output flux does not linearly change with changing forward current and the peak emission wavelength of the LEDs depends on the forward current. These two, non-linear phenomena make CCR dimming a less desirable option. In PWM-based drivers, the average current through the LED is variable while the peak amplitude of the current is either equal to the nominal forward current or 0. The result is a linear dimming behaviour with minimal spectral shifts. Not only the dimming method, but also the temperature of the semiconductor junction has its influence on the emission characteristics. Proper thermal management starts with the selection of the LED PCB base material. The thermal resistance is further minimized through the use of a properly designed heatsink solution that dissipates heat generated in the LEDs through convection. The last design step is situated in the field of optics. Each LED generates a specific radiation pattern, determined by the shape of its die and primary optics. A light engine, however, needs to deliver a properly homogenised output, free of large variations in flux and chromaticity. Secondary optics can accomplish this either in the near-field or in the far-field. A number of prototype light engines and three fully functional spectrally tuneable luminaires were designed, built and characterised.

5. Conclusions

Since the introduction of the first electrical light bulbs in the 1850s, we have strived for better light quality and higher efficiencies. After the invention of the incandescent light bulb, several gas discharge technologies have drastically improved the amount of light available from a single light source. At the same time, they offered the option to have different illumination spectra, producing light with different CCTs and even different colours. None of them, however, had an impact as large as the introduction of the light emitting diode.

Through steady advances in both quantum efficiency and wavelength range, LEDs evolved from dim red indicator lights to an efficient, robust light source with an unforeseen range of applications. For the first time in illumination technology history, we have the opportunity to create a compact light source that offers the possibility to generate lighting spectra on demand.

Over the course of this doctoral thesis, a number of smart spectrally tuneable LED light engines were simulated, designed, prototyped and integrated into a final production-ready product. Two of those light engines were incorporated in fully functional luminaires that were installed in a laboratory at the IREC facilities in Barcelona, Spain and the University of Newcastle, UK. They were subsequently used during a temporary exhibition in the National Gallery in London, UK where they were the key hardware component to complete valuable psychovisual experiments.

The main developments and achievements accomplished over the course of this PhD research are summarised and discussed below.

5.1 LED selection

Three different approaches to overcome the green gap problem in LEDs were investigated.

- A green OLED, developed in close collaboration with Fraunhofer COMEDD, proved to possess a desirable, narrow emission spectrum peaking at 547.0 nm. The relatively low unit flux, low flux density and associated large source size make the implementation of a hybrid LED-OLED light engine extremely difficult.
- Novel wavelength converters, developed by the University of Zaragoza, were considered as potential candidates for a green gap solution. The cyclometallated PtII complexes were deposited on a blue Lumileds Luxeon Rebel LEDs (450 nm) using a newly developed remote phosphor deposition technique, resulting in a thermally isolated phosphor layer. A fully converted LED resulted in an emission spectrum with chromaticity coordinates x = 0.4690, y = 0.4681. While the spectral shape is relatively favourable for use as a green gap bridge, the quantum efficiency of even the most efficient material is too low, resulting in both high heat generation within the phosphor itself and a low LED flux.
- Three commercially available, rare-earth wavelength converters peaking near 550 nm were evaluated.

- An aluminate-based emitting a broadband spectrum (FWHM = 120 nm). Aluminate phosphors have relatively high thermal quenching limits, with the downside of having a broad emission spectrum.
- A silicate-based material with narrow emission spectrum, but low thermal quenching limit.
- A YAG-based phosphor with high quantum efficiency and excellent thermal stability.

Each phosphor was tested at concentrations ranging from 10 to 50 weight percent and at two different LED forward currents. A rating scale was proposed and the best rated combination, in this case the YAG phosphor at 45 % phosphor to encapsulant weight, was selected. The blue LED-YAG phosphor combination proved to be an excellent solution to cover the green gap area, providing energy at a peak wavelength near the eye sensitivity maximum with an efficacy surpassing 70 lm/W at an ambient temperature of 25ºC.

5.2 Light engine prototypes

- Prototype I and II served as proof-of-concept builds that raised a few important questions:
  - What is the ideal base spectrum to optimise both the resolution of spectral tuneability and the maximum flux?
  - How to minimize the source size to integrate secondary colour mixing optics?
  - How the handle thermal issues when working with high power densities?
  - How to integrate a green gap solution?

- Prototype III focuses on miniaturisation with the aim to provide a fully functional spectrally tuneable light engine that can be integrated in a lighting system.
  - Surface mount Luxeon rebel LEDs significantly decrease the source size and increase thermal conductivity
  - White LEDs are used as a stop-gap solution to cover the green gap. This results in a high luminous flux (1377 lm), but reduced spectral tuneability due to their broadband emission. A CRI-R_a of 95 at CCTs between 2700 and 7000 K was achieved.
  - A Philips Fortimo module provides both a thermal solution and a mixing chamber that homogenises the output of the LEDs.

  The LED module is controlled by a newly developed switch-mode LED driver. 13 individual buck converters provide 700 mA to each LED channel. Powered by a 24V DC source, the LED driver achieves an efficiency between 72 and 93 %. The LED board has 4 temperature sensors to provide thermal feedback. A look-up table-based correction can adjust the individual channel currents based on measured temperature degradation curves.

- Prototype IV accomplishes four important goals:
  - Further miniaturisation of the light emitting area, LED and power supply by optimising component placement.

- Improved thermal characteristics of the LED board by switching from an FR4 based PCB to an alumina substrate.
- The introduction of a phosphor converted LED that emits in the green-gap area
- The addition of a wireless communications interface

The closer spacing of the LEDs in prototype IV, while reducing the source size, causes a large increase in concentrated heat generation. The high thermal resistivity of the FR4 material used in earlier prototypes would result in an increase in junction temperature above the allowed limit. Alumium oxide provides a thermal path with a significantly lower thermal resistance, allowing much higher package and power densities. The introduction of a violet LED channel (425 nm) and a PC yellow-green channel with high colour purity (551 nm) resulted in a light engine capable of generating 2501 lm with a maximum CRI-R_a of 99 between 2500 and 8000 K. The LED driver was updated to include a Wi-Fi wireless communications module and further miniaturised with closer component spacing.

- The final design of the light engine switches to a new series of Lumileds Luxeon Z LEDs, allowing an extremely high package density of 40 LEDs in an area measuring less than 214 mm^2. The Luxeon Z series includes the world´s first commercially available phosphor converted LED that was especially designed to cover the green gap. While the spectral shape is nearly identical to the LEDs developed during this PhD research, the commercial samples have clearly better efficiencies. Further improvement include:
    - Optimised LED selection to improve the spectral resolution (427 – 661 nm)
    - Optimised current delivery to provide an EEW baseline spectrum at a maximum flux of just under 1500 lm, including all optical losses.
    - CRI-R_a > 99 for CCTs between 2500 and 8000 K.

The purpose of the light engine, being incorporated in a compact spectrally tuneable spotlight, demands an efficient set of secondary optics. TracePro raytrace simulations guided the design of an optical integrator that effectively captures the lambertian emission of the LEDs into a PMMA light guide with square cross-section and provides a homogeneously mixed lambertian beam pattern at its exit aperture. Several integrator designs where simulated and compared

- A 40 mm long integrator rod with a 25 mm circular cross section resulted in an optical efficiency (integrator only) of 88 %. The colour mixing properties were not satisfactory.
- A octagonal rod with the same dimensions showed markedly improved homogenisation properties without any additional losses
- A square cross-section delivered the best performance with minimal colour differences ($\Delta uv = 0.00361$) and an optical efficiency exceeding 89 %.

The efficiency of the complete optical stack equates to 52.5 %. While this number is rather low, one has to keep in mind the excellent homogenisation performance. A weaker exit diffuser would increase the optical efficiency considerably, at the expense of worse colour mixing.

5.3 Spectrally tuneable luminaires

- Light engine prototype III was used as the main building block for a spectrally tuneable downlight. The luminaire, delivering a flux of 1329 lm (5.96 W), was installed in the laboratories of IREC in Spain and the University of Newcastle in the UK.
    - The spectrally tuneable room in Newcastle served as a basis for an experiment that aimed to compare the effects on mood, alertness, cognitive performance and melatonin secretion of two metameric, but melanopically modulated spectra. The conclusion of the first series of experiments show that there are no significant differences between the low and high melanopic spectra, a very surprising result that is in disagreement with earlier studies done using conventional light sources.
- A second luminaire was designed specifically for museum lighting purposes. The final light engine design was integrated into a custom designed luminaire, thereby creating the world´s first spectrally tuneable spotlight. The spotlight has a number of notable features:
    - A fibre-coupled miniature CMOS spectrophotometer provides real-time spectral feedback used for closed loop spectral calibration.
    - The optical system provides an extremely well homogenised beam that combined with Ledil´s Britney reflector series, results in three different beam profiles (spot, medium, flood).
    - Passive cooling, no fans or other rotating components.
    - Wireless control through Wi-Fi.

  The housing design results from a series of CFD simulations that optimise the thermal performance of the heatsink for both the LEDs and the LED driver. The final design guarantees a junction temperature below 84 ºC at an ambient temperature of 25 ºC. Further improvements in thermal conductivity are possible by switching from the Al-Mg alloy used in the prototypes to pure aluminium. 4 spotlights were installed in the National Gallery in London for the prestigious "Making Colour" exhibition. Dialux simulations, based on photogoniometric measurements, provided data to ensure a perfectly even illumination of the artworks using two narrow-beam (FWHM = 28 º) and two flood-beam units (FWHM = 74 º).
- A third luminaire was designed to provide a tuneable illumination spectrum inside a greenhouse. The main specifications of the horticulture module are:
    - Flux > 216 W/m^2 on top of the crops
    - Full spectral tuneability in the PAR region
    - Additional radiation at 740 nm
    - 4 modules should cover an area of 2 x 1.2 x 2 m (l x w x h)

  The design incorporates 920 Luxeon Z LEDs covering a wavelength range from 430 to 750 nm, resulting in a theoretical flux of 194 W per luminaire or an injection of over 775 W of light in the grow room. TracePro simulations indicate an average irradiance of 487 W/m^2 on top of the plants, located 50 cm below the luminaire. The MCPCB contains 20 clusters of 46 LEDs powered by a newly designed, 63-channel LED driver that supplies 350 mA to each LED string. The massive 6-layer driver board has additional RS-232, SD-card and USB buses to provide improved

connectivity and the possibility to store calibration data. The enormous amount of heat generated in the LED junctions is dissipated through a fan-cooled aluminium heatsink. Thermal measurements indicate maximum junction temperatures of 112 ºC, well below the allowed maximum.

5.4 Journal publications

- *Energy efficiency and color quality limits in artificial light sources emulating natural illumination* explains the trade off between colour quality and efficacy. Starting from a black body spectrum at a certain CT, both the long and short wavelength extension is reduced towards 555 nm. It is clear that removing any radiation outside of the visible spectrum does not harm the colour fidelity properties of the resulting illumination spectrum (as it is indistinguishable from the non-reduced black body spectrum) but does increase the LER dramatically. When the spectrum is a single peak located at 555 nm, the LER reaches its maximum value of 683 lm/W while, at the same time, colour fidelity reaches a minimum. All other combinations result in intermediate values of LER and CRI-R_a. By placing a lower bound on the colour fidelity and LER and an upper bound on the Δuv, a range of spectra is isolated. This optimisation was done for two CTs: 3000 and 5500 K. The efficacy of a full black body spectrum results in an LER of, respectively, 21 and 89 lm/W. Reducing their spectra to include visible wavelengths only increases the LER to 250 and 262 lm/W, respectively. Further reducing the quasi-black body spectra, imposing a minimum CRI-R_a of 90 and a Δuv less than 0.0054 increases both theoretical LER values to 363 and 313 lm/W (CRI-R_a of 90.5 and 95.4, respectively). To demonstrate the practical advantages of reduced black body spectra, these theoretical results were fed to a fitting algorithm that translated the RV spectrum to the 12 wavelength channels of the downlight luminaires used in the laboratories of IREC. The resulting illumination spectra had a LER of 329 lm/W at a CRI-R_a of 94 (3000 K) and 295 lm/W at a CRI-R_a of 92.1 (5500 K). Colour rendering maps, evaluating the colour fidelity of both spectra over a very large set of reflection samples, show that these high levels of colour fidelity are maintained uniformly over a wide range of colours, proving that a spectrally tuneable illumination system enables a joint optimisation of colour fidelity and efficacy.

- *Optimizing indoor illumination quality and energy efficiency using a spectrally tunable lighting system to augment natural daylight* combines daylight with a spectrally tuneable indoor illumination system. Introducing daylight in a living or working environment can have significant benefits. Not only does it reduce energy consumption, natural daylight has a positive influence on our wellbeing. Previous hybrid systems combined incandescent or fluorescent lighting technologies to supplement daylight at certain times of the day. The obvious disadvantage is the large difference between the daylight spectrum and the spectrum supplied by the illumination system. The introduction of a spectrally tuneable lighting system offers a number of interesting

benefits. Light entering through a skylight is captured by a miniature spectrophotometer. The data is then fed to a computer system that, depending on the chosen optimisation regime, selects a set of fitting algorithms. Two different optimisation schemes were explored. A first algorithm copies, in real-time, the spectrum registered by the roof-mounted spectrophotometer resulting in an illumination that closely resembles the spectral characteristics of the outside environment. The illuminance level of the combined illumination spectrum, however, was fixed at 400 lx. Besides the extremely high light quality (average CRI-R_a >98) and obvious circadian benefits, analysing the power consumption of the system during a period of one week revealed the possibility to save over 40 kWhr/m^2 per year in comparison with an identical illumination system not aware of daylight (static D65 spectrum at 400 lx). A second approach aimed to provide a constant CCT and illuminance in the room, despite changing daylight conditions. There are, however, an infinite number of spectra that can provide the target CCT of 4000 K at an illuminance of 400 lx. Two cases are of particular interest: an optimisation for colour fidelity and an optimisation for efficacy. The efficacy optimisation strives to minimise the channel amplitudes while fulfilling conditions regarding the chromaticity coordinates. This results in an RGB-like supplementary spectrum. When optimising for colour fidelity, as many channel amplitudes as possible are maximised resulting in a smooth, continues spectral shape. While both algorithms show excellent stability, despite large spectral changes in the daylight entering the room, the CRI-R_a optimisation has outstanding colour rendering properties (average CRI-R_a > 97) while the optimisation for efficacy results in a 25% reduction in power consumption in comparison with the optimisation for colour fidelity.

Light emitting diodes are here to stay and they will most likely evolve to become the dominant lighting technology of the coming decennia. Even in this early stage of development, the possibilities offered by LEDs far surpass any other lighting technology. Spectrally tuneable LED light sources are the next logical step towards the never-ending quest towards more efficient and smarter light sources that offer better light quality.

Bibliography

1. Beech, M., *A Story of Light and Deception,* Springer (2012)
2. Baets, R., *Photonics,* Universiteit Gent (2008)
3. Ohta, N., Robertson, A.R., *Colorimetry Fundamentals and Applications,* Wiley (2005)
4. Rodríguez, A.C., Acosta, J.C., Latorre, M.M., *El Libro Blanco de la Illuminación,* Comité Español de Illuminación (2014)
5. Huygens, C., *Traité de la Lumière,* Gauthier-Villars (1690)
6. Maxwell, J.C., *A Dynamical Model of the Electromagnectic Field, Philosophical Transaction of the Royal Society of London 155: 459-512 (1864)*
7. Einstein, A., *Concerning* an *Heuristic Point of View towards the Emission and Transformation,* American Journal of Physics 33: 5 (1965)
8. Lynch, D. K., Livingston, W. C., *Color and Light in Nature* (2nd ed.), Cambridge, UK: Cambridge University Press. p. 231
9. Wagner, C., Harned, N., *EUV lithography: Lithography gets extreme*, Nature Photonics 4, 24-26 (2010)
10. Camara, C. G., Escobar, J. V., Hird, J. R., Putterman, S. J., *Correlation between nanosecond X-ray flashes and stick-slip friction in peeling tape*, Nature 455, 1089–1092 (2008)
11. Smith, D.M., Heckmann, S., *A terrestrial gamma ray flash observed from an aircraft,* Journal of Geophysical Research 116 – D20 (2011)
12. Dwyer, J. R., Smith, D. M., Uman, M. A., Saleh, Z., Grefenstette, B., Hazelton, B., Rassoul, H. K., *Estimation of the fluence of high-energy electron bursts produced by thunderclouds and the resulting radiation doses received in aircraft,* Journal of Geophysical Research 115 – D9 (2010)
13. Ranganath, G.S., *Black-Body Radiation,* Resonance 13 – 2, 115-133 (2008)
14. Boyce, P.R., *Human Factors in Lighting,* Taylor and Francis Group (2003)
15. Purves D, Augustine GJ, Fitzpatrick D, et al., *Neuroscience. 2nd Edition,* Sinauer Associates (2001)
16. Briscoe, A.D., Chittka, L., *The Evolution of Color Vision in Insects,* Annual Review of Entomology 46: 475-510 (2001)
17. Thoen, H. H., How, M. J., Chiou, T.-H. & Marshall, J. , *A Different Form of Color Vision in Mantis Shrimp*, Science 343, 411–413 (2014)
18. Radonjic, A., Alfred, S.R., Gilchrist, A.L., Brainard, D.H., *The Dynamic Range of Human Lightness Perception,* Current Biology 21, issue 22, 1931 – 1936 (2011)
19. Foster, D.H., *Color Constancy,* Vision Research 51-7, 674-700 (2011)
20. Gao, S., Yang, K., Li, C., Li, Y., *A Color Constancy Model With Double-Opponent Mechanisms,* proceedings of the IEEE International Conference on Computer Vision, 929-936 (2013)
21. Bünning, E., *Die endogene Tagesperiodik als Grundlage der photoperiodischen Reaktion,* Berichte der Deutschen Botanischen Gesellschaft 54, 590-607 (1936)
22. Provencio, I., Jiang, G., De Grip, W.J., Hayes, W.D., Rolag, M.D., *Melanopsin: An opsin in melanophores, brain, and eye,* Proceedings of the National Academy of Sciences of the United States of America 95 (1998)
23. Berson, D.M., Dunn, F.A., Takao, M., *Photoransduction by retinal ganglion cells that set the circadian clock,* Science 295 (2002)

24. Freedman, M.S., Lucas, R.J., Soni, B., von Schantz, M., Muñoz, M., David-Gray, Z., *Regulation of mammalian circadian behavior by non-rod, non-cone ocular photoreceptors,* Science 284 (1999)
25. Chellappa, S.L, Steiner, R., Blattner, P., Oelhafen, P., Götz, T., Cajochen, C., *Non-visual Effects of Light on Melatonin, Alertness and Cognitive Performance: Can Blue-Enriched Light Keep Us Alert?,* PLoS One (2011)
26. Hech, S., Shlaer, S., Intermittent Stimulation by Light: V. The Relation Between Intensity and Critical Frequency for Different Parts of the Spectrum, Journal of General Physiology 19 (6): 965-977 (1936)
27. Goodman, T., *The relevance of mesopic photometry for LED street lighting,* NPL Meeting on Best Practice in Street Lighting (2012)
28. Ball, P., *Colour: Natural History*, Natural History magazine 111 (2), 64 (2002)
29. Wright, W. D., *A re-determination of the trichromatic coefficients of the spectral colours,* Transactions of the Optical Society 30 (4): 141–164 (1928)
30. Guild, J., *The colorimetric properties of the spectrum,* Philosophical Transactions of the Royal Society of London. Series A, Containing Papers of a Mathematical or Physical Character 230: 149–187 (1932)
31. Stiles, W. S., Birch, J. M. , N.P.L. *Colour-matching Investigation: Final Report*, Optica Acta 6 (1): 1–26 (1958)
32. MacAdam, D.L., *Visual sensitivities to color differences in daylight,* JOSA 32 (5): 247–274 (1942)
33. Fairchild, M. D., Luo, M. R., Hunt, R. W. G., *A Revision of CIECAM97s for Practical Applications*, Color Research & Applications 25 (4): 260–266 (2000)
34. Moroney, N., Fairchild, M.D., Hunt, R.W.G., Li, C., Luo, R.l., Newman, T., *The CIECAM02 Color Appearance Model,* RIT Scholar Works (2002)
35. Kruithof, A.A., *Tubular Luminescence Lamps for General Illumination,* Philips Technical Review 6 (3): 65–96 (1941)
36. Rea, M.S., Freysssinier, J.P., *White Lighting,* Color Research and Application, 38 2: 82-92 (2013)
37. Judd, D.B.., MacAdam, D.L., Wyszecki, G, *Spectral Distribution of Typical Daylight as a Function of Correlated Color Temperature, JOSA* **54** (8): 1031–1040 (1964)
38. Walter, W., *How meaningful is the CIE color rendering index?,* Light Design Application 11(2), 13–15 (1981)
39. Schanda, J., Madár, G., *Light Source Quality Assessment,* Proceedings of 26th Session of the CIE, Beijing (2007)
40. Royer, M., *Color Rendition Metrics: An Overview of Ongoing Work,* Lightfair (2014)
41. Judd, D.B., *A flattery index for artificial illuminants,* IES Transactions, pp. 593-598 (1967)
42. Thornton, W.A., *Color-discrimination index*, J. Opt. Soc. Am. 62, pp 191-194 (1972)
43. Xu, H., *Colour rendering capacity of illumination,* J. Illum. Eng. Soc. 13, pp. 270-276 (1984)
44. Rea, M., Deng, L., Wolsey, R., *Full Spectrum Light Sources,* http://www.lrc.rpi.edu/programs/NLPIP/lightinganswers/pdf/PRINT/fullSpectrum.pdf (2005)
45. Hashimoto, K., Yano, T., Shimizu, M., Nayatani, Y., *New method for specifying color-rendering properties of light sources based on feeling of contrast*, Col. Res. and Appl. 32, 361-371 (2007)
46. Bodrogi, P., Brückner, P., Khanh, T.Q., *Written report and proposal for a new assessment procedure,* written for the CIE TC 1-69: Colour rendering of white light sources (2009)

47. Smet, K., Ryckaert, W.R., Forment, S., Hertog, W., Deconinck, G., Hanselaer, P., *Colour rendering: an object based approach,* proceedings of the CIE light and lighting conference with special emphasis on LEDs and solid state lighting, 34 (2009)
48. Smet, K.A.G, Ryckaert, W.P., Pointer, M.P., Deconinck, G., Hanselaer, P*., Memory colours and colour quality evaluation of conventional an solid-state lamps,* Optics Express vol.18, 25 (2010)
49. Ebner, F., Fairchild, M.D., *Development and testing of a color space (IPT) with improved hue uniformity*, IS&T 6th Color Imaging Conference (1998)
50. Davis, W., Ohno, Y., *Color Quality Scale,* Optical Engineering 49, no. 3(2010)
51. Quintero, J., Sudría, A., Hunt, C.E. and Carreras, J., *The color rendering map: a graphical metric for assessment of illumination,* Optics Express 20, 4939–4956 (2012)
52. Khan, T.Q., Bodrogi, P., Vinh, Q.T., Winkler, H., LED Lighting: Technology and Perception, Wiley, ISBN 978-3-527-41212-9 (2014)
53. Thomson, J., *The Scot Who Lit The World, The Story Of William Murdoch Inventor Of Gas Lighting* (2003), ISBN 0-9530013-2-6
54. Jäggi, W., *Grosses Lichterlösen für die Glühbirnen*, Tages-Anzieger (2014)
55. Trenev, G, Bertoldi, P., *The 2012 European GreenLight Programme*, JRC technical reports (2014), ISBN: 978-92-79-35419-9
56. Goldwasser, S.M., Klipstein, D.L., *Sam´s and Don´s D-Lamp FAQ: Gas Discharge Lamps, Ballasts and Fixtures,* http://donklipstein.com/dschlamp.html (1999)
57. Comité Español de Iluminación, El Libro Blanco de la Iluminación: Tecnología de la Luz, ISBN 978-84-940273-1-II (2014)
58. Kaufman, J.E., *EIS Lighting Handbook*, Electrical Engineering Society of North America (1984)
59. Osram - Siteco, Light is foresightful: Mercury vapour lamps phase-out from 13th April 2015, OSRAM GmBH (2015)
60. Osram, *Metal Halide Lamps: Instructions for use and application,* OSRAM AG (2012)
61. Perálvarez, M., Higuera, J., Hertog, W., Motto, O. and Carreras, J., *Solid state lighting: an approach to energy efficient lighting,* Materials for sustainable Energy applications, Pan Stanford Publishing (in press)
62. Craford, G., *LEDs Challenge the Incandescents,* IEEE Circuits and Devices vol 8, pp24-29 (1992)
63. Dakin, J.P., Brown, R., *Handbook of Electronics Volume 1,* CRC Press Taylor & Francis Group (2006)
64. Laboratory record: red LED breaks through the 200 lm/W barrier, Optik & Photonik vol. 6, pp 16 (2011).
65. Cree Inc., *Cree news: Cree first to break 300 lm/W barrier,* www.cree.com/News-and-Events/Cree-News/Press-Releases/2014/March/300LPW-LED-barrier (2014)
66. Schubert, F.E., Light-Emitting Diodes – Second edition, Cambridge University Press, ISBN 978 -0-521-86538-8 (2010)
67. Tang, C. W., Vanslyke, S. A., *Organic electroluminescent diodes,* Applied Physics Letters **51** (1987)
68. UBI Research, *OLED Lighting Annual Report* (2015)
69. Törker, M, Peralvarez, M., Higuera, J., Hertog, W., *D3.3.3 Finalization of the simulation work and setup of the best suiting OLED stacks,* FP7-ICT-2013-11 HI-LED deliverable (2014)
70. Törker, M, Peralvarez, M., Higuera, J., Hertog, W., *D3.3.4 Definition of the driver parameters suiting the use of both LEDs and OLEDs,* FP7-ICT-2013-11 HI-LED deliverable (2015)

71. Törker, M, Peralvarez, M., Higuera, J., Hertog, W., *D3.3.5 Final results of the OLED test are available and their usability is verified,* FP7-ICT-2013-11 HI-LED deliverable (2015)
72. Yen, W.M., Shionoya, S., Yamamoto, H., The Phosphor Handbook, CRC Press Taylor & Francis Group, ISBN: 0-8493-3564-7 (2007)
73. Gorrotxategi, P., Consonni, M., Gasse, A., *Optical Efficiency Characterization of LED Phosphors Using a Double Integrating Sphere System*, Journal of Solid State Lighting, Vol. 2:1 (2015)
74. Fuertes, S., Garcia, H., Peralvarez, M., Hertog, W., Carreras, J., Sicilia, V., *Stepwise Strategy to Cyclometallated PtII Complexes with N-Heterocyclic Carbene Ligands: A Luminescence Study on New β-Diketonate Complexes,* Chemistry – a European Journal 21 (04) (2014)
75. Löffler, A., Binder, M., *Cranking up the efficacy of Green LEDs*, Compound Semiconductor, vol. 19 (7), pp. 32-36 (2013)
76. Wright, M., *Philips Lumileds announces worhorse Luxeon T LED family (Updated),* LEDs Magazine http://www.ledsmagazine.com/articles/2012/12/philips-lumileds-announces-workhorse-luxeon-t-led-family-updated.html (December 2012)
77. Lumileds Holding B.V., *DS105 Luxeon Z Color Product Datasheet*, http://www.lumileds.com/uploads/415/DS105-pdf (2015)
78. Mueller, G. O., Mueller-Mach, R., *White Light from LEDs,* CIE Expert Symposium on LED Light Sources: Physical Measurement and Visual and Photobiological Assessment (2004)
79. Shum, E., *Overview of worldwide LED industry*, Strategies in Light (2013)
80. Simpson, C., Linear and Switching Voltage Regulator Fundamental Part 1, Texas Instruments: Power Management Applications (http://www.ti.com/lit/an/snva558/snva558.pdf)
81. Gu, Y., Narendran, N., Dong, T., Wu, H., *Spectral and Luminous Efficacy Change of High-power LEDs under Different Dimming Methods,* Proceedings of the Sixth International Conference on Solid State Lighting of SPIE (2006)
82. Hecht, S., Shlaer, S., *Intermittent Stimulation by Light: V. The Relation Between Intensity and Critical Frequency for Different Parts of the Spectrum,* Journal of General Physiology, 19(06), PP. 965-977 (1936)
83. Hershberger, W.A., *The Phantom Array: a Perisaccadic Illusion of Visual Direction,* The Psychological Record 48, PP. 21-32 (1998)
84. Liu, S., Luo, X., *LED packaging for Lighting Applications,* The Chemical Industry Press, ISBN 978-0-470-82783-3 (2011)
85. Chaves, J., *Introduction to nonimaging optics*, CRC Press Taylor and Francis Group (2008)
86. Morris, M.G., Sales, R.M.T., Chakmakjian, S., Schertler, D.J., Engineered diffusers for display and illuminations systems: design, fabrication and applications, RPC Photonics Inc. (2003)
87. Mixing Chamber Design Considerations for ChromLit Remote Phosphor Light Sources, Intematix corporation
88. LEDiL Rebecca series, http://www.ledil.com/sites/default/files/press_releases/rebecca_pr_web.pdf

Annex

A. Journal publication I. Hertog, W, Llenas, A., Quintero, J.M., Hunt, C.E., Carreras, J., *Energy efficiency and color quality limits in artifical light sources emulating natural illumination*, Optics Express 22 (S7) (2014)

Energy efficiency and color quality limits in artificial light sources emulating natural illumination

Wim Hertog,[1] Aleix Llenas,[1] Jesús M. Quintero,[2] Charles E. Hunt[3] and Josep Carreras[1,*]

[1] *IREC, Catalonia Institute for Energy Research, Jardins de les dones de negre 1. PL2, 08930 Sant Adrià de Besòs, Barcelona, Spain*

[2] *Department of Electrical and Electronics Engineering, Universidad Nacional de Colombia, Bogotá, Colombia*

[3] *California Lighting Technology Center, University of California 633 Faria Ave, Davis California, 95618, USA*

[*] *jcarreras@irec.cat*

Abstract: We present in this work a calculation of the theoretical limits attainable for natural light emulation with regard to the joint optimization of the Luminous Efficacy of Radiation and color fidelity by using multiple reflectance spectra datasets, along with an implementation of a physical device that approaches these limits. A reduced visible spectrum of blackbody radiators is introduced and demonstrated which allows lamps designed to emulate natural light to operate with excellent color fidelity and higher efficiency as compared to full visible spectrum sources. It is shown that even though 3,000K and 5,500K blackbody sources have maximum efficacies of 21 lm/W and 89 lm/W, respectively, reduced-spectrum artificial light sources can exceed those values up to 363 lm/W and 313 lm/W, respectively, while retaining excellent color fidelity. Experimental demonstration approaching these values is accomplished through the design and implementation of a 12-channel light engine which emits arbitrarily-tunable spectra. The color fidelity of the designed spectra is assessed through Color Rendering Maps, showing that color fidelity is preserved uniformly over a large spectral reflectance dataset, unlike other approaches to generate white light.

OCIS codes: (330.1710) Color, measurement; (330.1715) Color, rendering and metamerism; (330.1730) Colorimetry; (230.3670) Light-emitting diodes.

References and links

1. P. Waide and S. Tanishima , *Light's Labour's Lost: Policies for Energy-efficient Lighting* (International Energy Agency, 2006).
2. E. F. Schubert and J. K. Kim, "Solid-state light sources getting smart," Science **308** (5726), 1274–1278 (2005).
3. A. Zukauskas, R. Vaicekauskas, and M. S. Shur, "Colour-rendition properties of solid-state lamps," J. Phys. D: Appl. Phys. **43**, 354006 (2010).
4. J. Y. Tsao, M. E. Coltrin, M. H. Crawford, and J. A. Simmons, "Solid-state lighting: an integrated human factors, technology, and economic perspective," In proceedings of the IEEE, **98**, 1162–1179 (2010).
5. W. Davis and Y. Ohno, "Toward and improved color rendering metric," Proc. SPIE, **5941**, 59411G (2005).
6. W. Davis and Y. Ohno, "Color quality scale," Opt. Eng. **49**, 033602–033616 (2010).
7. M. R. Luo, "A review of chromatic adaptation transforms," Rev. Prog. Color. **30**, 77–92 (2000).

#214288 - $15.00 USD Received 25 Jun 2014; revised 25 Aug 2014; accepted 6 Oct 2014; published 23 Oct 2014

ATTENTION ¡

Pages 173 to 181 of the thesis, containing the article mentioned above are availables at the editor's web https://www.osapublishing.org/oe/abstract.cfm?uri=oe-22-107-A1659

B. Journal publication II. Hertog, W., Llenas, A., Carreras, J., *Optimizing indoor illumination quality and energy efficiency using a spectrally tunable lighting system to augment natural daylight*, Optics Express 23 (24) (2015)

Optimizing indoor illumination quality and energy efficiency using a spectrally tunable lighting system to augment natural daylight

W. Hertog, A. Llenas, and J. Carreras*

Institut de Recerca en Energia de Catalunya (IREC), Jardins de les Dones de Negre, 1, 08930 Sant Adrià de Besòs, Spain

*jcarreras@irec.cat

Abstract: This article demonstrates the benefits of complementing a daylight-lit environment with a spectrally tunable illumination system. The spectral components of daylight present in the room are measured by a low-cost miniature spectrophotometer and processed through a number of optimization algorithms, carefully trading color fidelity for energy efficiency. Spectrally-tunable luminaires provide only those wavelengths that ensure that either the final illumination spectrum inside the room is kept constant or carefully follows the dynamic spectral pattern of natural daylight. Analyzing the measured data proves that such a hybrid illumination system brings both unprecendented illumination quality and significant energy savings.

OCIS codes: (330.1710) Color, measurement; (230.3670) Light-emitting diodes; (350.6050) Solar energy.

References and links

1. Global Efficient Lighting Forum, "Policy options to accelerate the global transition to advanced lighting", http://www.enlighten-initiative.org/Portals/0/documents/global-forum/Green_Paper_FINAL%20reduced.pdf (2014)
2. S. Veeramas and C. Chuntamara, "The evaluation of lighting energy saving in open-plan office building with Daylight-linked system in Bangkok: an experimental study," in *2nd Chulalongkorn University Architectural Design Symposium* (CU:ADS, 2011), pp. 1-19
3. C. Yavuz, E. Yanikoglu, and O. Guler, "Determination of real energy saving potential of daylight responsive systems: a case study from Turkey," Light Eng. **18**(2), 99–105 (2010).
4. D. M. Berson, F. A. Dunn, and M. Takao, "Phototransduction by retinal ganglion cells that set the circadian clock," Science **295**(5557), 1070–1073 (2002).
5. F. A. J. L. Scheer, L. J. P. van Doornen, and R. M. Buijs, "Light and diurnal cycle affect human heart rate: possible role for the circadian pacemaker," J. Biol. Rhythms **14**(3), 202–212 (1999).
6. P. Badia, B. Myers, M. Boecker, J. Culpepper, and J. R. Harsh, "Bright light effects on body temperature, alertness, EEG and behavior," Physiol. Behav. **50**(3), 583–588 (1991).
7. G. Vandewalle, E. Balteau, C. Phillips, C. Degueldre, V. Moreau, V. Sterpenich, G. Albouy, A. Darsaud, M. Desseilles, T. T. Dang-Vu, P. Peigneux, A. Luxen, D. J. Dijk, and P. Maquet, "Daytime light exposure dynamically enhances brain responses," Curr. Biol. **16**(16), 1616–1621 (2006).
8. A. J. Lewy, T. A. Wehr, F. K. Goodwin, D. A. Newsome, and S. P. Markey, "Light suppresses melatonin secretion in humans," Science **210**(4475), 1267–1269 (1980).
9. C. Cajochen, "Alerting effects of light," Sleep Med. Rev. **11**(6), 453–464 (2007).
10. C. M. Gropp, "Regulation of melanopsin and PACAP mRNA by light, circadian and sleep homeostatic processes," Medizinischen Fakultät Charité – Universitätsmedizin Berlin, PhD dissertation (2014)
11. W. Hertog, A. Llenas, J. M. Quintero, C. E. Hunt, and J. Carreras, "Energy efficiency and color quality limits in artificial light sources emulating natural illumination," Opt. Express **22**(S7 Suppl 7), A1659–A1668 (2014).
12. D. Caicedo, A. Pandharipande, and F. M. J. Willems, "Daylight adaptive lighting control using light sensor calibration prior information," Energy Build. **73**, 105–114 (2014).
13. B. Tralau and C. Schierz, "The preference of colour temperature depending on daylight and weather," in *CIE Proceedings Lighting Quality and Energy Efficiency* (CIE, 2014), paper x039.
14. M. Aldrich, N. Zhao, and J. Paradiso, "Energy efficient control of polychromatic solid-state lighting using a sensor network," Proc. SPIE **7784**, 105–114 (2010).
15. W. Pierpoint, "Equi-visibility lighting control system", United States Patent 4,273,999 (1981)

#245953 Received 14 Jul 2015; revised 18 Sep 2015; accepted 29 Sep 2015; published 16 Oct 2015
© 2015 OSA 16 Nov 2015 | Vol. 23, No. 24 | DOI:10.1364/OE.23.0A1564 | OPTICS EXPRESS A1564

ATTENTION ¡

Pages 183 to 192 of the thesis, containing the article mentioned above, are availables at the editor's web https://www.osapublishing.org/oe/abstract.cfm?uri=oe-23-24-a1564